Direct measurement of the W boson mass in e^+e^- collisions at LEP

Front cover This event was recorded by DELPHI on the 21st of April 2000 at a LEP centre-of-mass energy of 204 GeV (run 109140, event 1323). Five distinct jets are clearly visible. The event is compatible with the production of a pair of W bosons followed by a fully hadronic decay.

Back cover An illustration of four different stages of the W mass analysis. The bottom plot displays the energy flow of the 5-jet event shown on the front cover. The other three plots correspond to a WW event with significant ISR radiation, obtained from Monte Carlo simulation. From bottom to top: (1) the experimental Ideogram, reflecting the mass information extracted from the energyflow; (2) a two-dimensional Breit-Wigner distribution; and (3) the likelihood curve (green) as a function of the W mass for this event, extracted from a convolution of the experimental Ideogram and the Breit-Wigner function. The analysis included an event-by-event ISR treatment. Without this treatment the curve indicated by the yellow dashed line would have been obtained instead.

Direct measurement of the W boson mass in e^+e^- collisions at LEP

ACADEMISCH PROEFSCHRIFT

TER VERKRIJGING VAN DE GRAAD VAN DOCTOR
AAN DE UNIVERSITEIT VAN AMSTERDAM,
OP GEZAG VAN DE RECTOR MAGNIFICUS PROF. DR. J. J. M. FRANSE
TEN OVERSTAAN VAN EEN DOOR HET COLLEGE VOOR PROMOTIES INGESTELDE
COMMISSIE, IN HET OPENBAAR TE VERDEDIGEN IN DE AULA DER UNIVERSITEIT
OP WOENSDAG 5 SEPTEMBER 2001 TE 10.00 UUR

door

Martijn Pieter Mulders

geboren te Katwijk aan Zee

Promotor: Prof. Dr. J.J. Engelen
Universiteit van Amsterdam (UvA), Amsterdam
Co-Promotor: Dr. N.J. Kjær
European Organization for Nuclear Research (CERN), Genève

Faculteit der Natuurwetenschappen, Wiskunde en Informatica

The work described in this thesis is part of the research programme of the 'Nationaal Instituut voor Kernfysica en Hoge–Energie Fysica (NIKHEF)' in Amsterdam, the Netherlands. The author was financially supported by the 'Stichting voor Fundamenteel Onderzoek der Materie (FOM)', which is funded by the 'Nederlandse Organisatie voor Wetenschappelijk Onderzoek (NWO)'.

ISBN: 90-6464-800X

Contents

Preface

I wonder why. I wonder why.
I wonder why I wonder.
I wonder *why* I wonder why
I wonder why I wonder!

R.P. Feynman

(from "Surely You're Joking, Mr. Feynman!")

Sooner or later — typically at a birthday party or at the doorstep of the employment office — every particle physicist has to face the question "why?". Why bother about the properties of particles and forces at scales so small that no useful application can be expected from it in the foreseeable future?

The correct answer to this question would be that the scientific research performed at physics laboratories like CERN is driven by *curiosity*. This answer is honest and consistent, and will probably satisfy the average tax-payer and scientist. However, it will not convince people whose curiosity is confined to what the stock-market is going to do tomorrow. The truly materialistic tax-payer will always fail to see the profit, while on the other end of the spectrum the more philosophically inclined scientist, like Richard Feynman, keeps wondering... Where does curiosity come from, and what use does it have?

So why wonder?

This question also bears some relevance to the measurement of the mass of the W particle, presented in this work. It left me pondering and wondering from time to time. Until I found an answer that seems to make a lot of sense to me. It is at least an attractive metaphor and I have the feeling that it might be more than just that:

The idea is that the essence of life is the creation of order in matter and knowledge. And this is exactly what science is all about. To be alive is to be curious. *Not* to be curious and supportive of the activities employed at CERN is possible, but inconsistent with being alive (as a human being, that is). To explain that, one first has to go back to a basic and remarkable difference between life and the star dust that we are made of: *entropy*.

The Second Law of thermodynamics states that in every closed system entropy, or disorder, should increase. Generally the natural course of things is that information 'smears out', and disorder increases unless countermeasures are taken. The fate of the universe is disarray.

Life, however, plays a clever trick. It comes with a pattern that contains enough order to maintain that order and even increase and expand it. We can increase or decrease order at will.

Living organisms can sustain their low entropy by eating nutritious (= low entropy), high calorie food or, at the beginning of the ecological cycle, absorbing energy from the Sun. Indeed, as long as somewhere else (in our Sun) entropy increases more than it decreases locally (inside the organism), life is physically possible. In some sense it resembles a phase transition — metaphorically speaking, at least. When under the right conditions, perhaps by pure chance, atoms form a first pattern of life, it can grow and multiply and spread order like a condensation-kernel starts the formation of a cloud. A life ends when the ordered pattern is broken beyond the point of self-repair, after which the natural loss of order sets in again and the atoms return to dust.

In the early days of life on Earth, the forms of life most successful in using energy to create order were the ones with the most optimal mix between stability and ability to evolve (limited life-span, combined with a good, but not perfect reproductive system). Natural selection, though not infallible, provided an ever present driving force, leading to more and more intricate patterns and complex forms of life.

It is all about order and information. Somewhere during the evolution of life, a crucial advantage started developing, not to rely completely on inheritance of information through the patterns contained in organic molecules, but to develop senses and some degree of consciousness to process and react to the information received. Now this is where *curiosity* comes in, as an incentive to gather information by other means than inheritance. Increasing complexity of the nerve systems to process the information from the senses went hand-in-hand with the development of brains. Where primitive brains still are largely pre-programmed by instincts, more evolved brains like human brains allow for abstract *thinking*, freedom of choice and *creativity* to come up with new *ideas*, being only partly influenced by emotions and instincts. The flexibility of thought, fed by information from the senses, opens a new world of possibilities to reduce entropy.

This is not the full story. People talk and share ideas. And in ever increasing scale and speed. Today we live in a complex, global society, in which order and disorder are organised at a global scale. Through communication and cooperation new ideas and knowledge can be developed at a rate far beyond the capability of the individual. But also in the development of new ideas a balance has to be found... a balance between stability (order) and the ability to evolve through a natural selection principle. The most successful system developed to date to achieve that balance in the ordering of ideas is known as the scientific method. It provides a set of rules and traditions, knowledge of varying degrees of certainty, and a method to select the good ideas from the bad ideas: scepticism and experimental falsification. This way of thinking — when followed properly — is the best way we currently have of improving our knowledge of the world surrounding us.

At CERN the battle against entropy is fought in several ways, and at an impressive scale. It is not only a shining example of curiosity-driven scientific research. Some of the world's largest and most complicated machines have been and are being built there, converting energy directly into well controlled, low entropy conditions needed to extend our senses and probe matter at the scale of W and Z particles and beyond. Together with the complex research performed at CERN this requires the cooperation of thousands of physicists from all over the world and the combined resources of the 20 European member states (and seven observers), all jointly focused at the same goal. It is not just coincidence that an unprecedented new world-wide way of communication was invented in the process: the World Wide Web. CERN can without doubt be called one of the crowning achievements of life in the battle against entropy.

After this introduction it may be clear that the research presented here is a miracle of cooperation, which would not have been possible without the help of many others. First of all this includes the many people that have contributed to DELPHI. When I first learned that about 500 physicists were working on the same experiment, I got scared. But to my pleasant surprise the DELPHI collaboration turned out to be a nice and open society with room for personal input and ideas. Very fruitful and pleasant was the collaboration inside the W mass analysis team with Chris Parkes, Roberto Chierici, Alessandra Tonazzo, Ahmimed Ouraou, Arnoud Duperrin, Laurent Simard, guided by Klaus Mönig, Rasmus Møller, Peter Renton and others. Jörgen D'Hondt and Joana Montenegro, thanks for taking over my analysis and good luck with its further development!

During my 19 months stay at CERN it was fascinating to contribute to the operation of the experiment. During the many pit-meetings I learned that it is not easy to keep a complicated machine like DELPHI running. It was fun to take care of the Inner Detector, knowing that Duncan Reid and André Augustinus always were around as a backup in case things would really get serious. In general I liked to do central shifts in the DELPHI control room. It was cool to be right there when the data came in, and to keep an eye on the detector. Night shifts could be boring, though. But this was not always the case, depending on the other two people who made up the shift crew. I still remember the shift with Thomas Alderweireld and Lena Leinonen, when we figured out how to play CD's on the CD-ROM players of the sub-detector workstations and danced Tango to stay awake.

It is my pleasure to thank my direct supervisors Jan Timmermans and Niels Kjær. Their sincere attempts to familiarise me with the delights of the French kitchen and the world of wine tasting were enjoyable but, especially the latter, only partly successful. Fortunately the teaching in other subjects was more effective: Jan taught me carefully how not to blow up the Inner Detector of DELPHI while being on shift. And from Niels I learned all I needed to know about measuring the W mass. His experience with statistics, insight in special features of the DELPHI detector and remarkable supply of creative ideas made physics analysis a lot of fun. I enjoyed very much the way in which we could communicate new concepts and ideas with surprisingly few words, leading to a smooth and productive collaboration. On many occasions this formed a striking contrast with the long time-scale and challenge involved in convincing other people, especially beyond the small circle of DELPHI W physics colleagues. Which, on the other hand, justified repeated meetings in the framework of the LEP2 WW workshops in Crete and Lisbon, which I found very stimulating.

I am grateful to my promotor Jos Engelen, for his confidence and support. I was impressed by his quick and efficient handling of my thesis, which applies also to Jan and Niels, who did a thorough job checking the first and second version of the manuscript. Finally I would like to thank Eric Laenen, Stefan Groot Nibbelink, Joana Montenegro, Marco van Leeuwen, Maarten Bruinsma, Robert Sekulin and Duncan Reid for reading parts of the thesis and giving valuable suggestions.

In the background Jan van Eldik and colleagues in the computing support group played a crucial supporting role, providing useful scripts, preventing most computer problems and being always available to solve the few remaining ones that slipped through. Not an easy task given the complexity of the DELPHI reconstruction and analysis software. Many thanks.

I was quite fortunate to have Ivo van Vulpen, Martin Blom, Edik Boudinov and Joana Montenegro as fellow PhD students and Peter Kluit as the new group leader in the DELPHI group at NIKHEF. You all contributed in your own ways to a very good atmosphere.

For great memories of dinners, skiing and snow-boarding adventures, hikes, parties, barbecues, wind-surfing and salsa courses, movies, a beautiful apartment in Ferney-Voltaire, Florian, nice times in Prevessin, coffee-breaks, silly chats, deep discussions, fitness during lunch-times, Hiiuma, kiik, kama and vobla I would like to thank Frank and Ramona, Martijn and Merian, Daniel and Joana, Sandra and Jord, Ann and André, Edik and Hanna, Tasja and Frank, Ivo and Julia, Martin and Cathelijne, Chiara and Maarten, Tim and Vanessa, Katja and Nick, Bert and Tanja, Simon, Michiel, Rutger, Henrique, Jukka, Ari, Oli and Isabel, Kaia and Rego and Saali.

For those friends and family who would have liked to see me more often than they did during the last few years: the size of this book, if not its contents, may tell you why. And last but certainly not least I would like to thank my sister Marloes for the fun we always have and my parents, whose encouragement and unconditional support has always been very important to me,

Martijn Mulders.

Amsterdam, July 2001

Introduction

In some fundamental respects W bosons are identical to photons (light particles). One major difference, however, is that W bosons are quite heavy while photons are massless. The measurement of the mass of the W boson is the subject of this thesis. With a mass of about $1.43 \cdot 10^{-25}$ kg they are almost 86 times as heavy as a proton. This large W mass is part of the reason that W bosons are not so 'visible' in daily life, compared to photons. The other reason is that their lifetime is short: $3.2 \cdot 10^{-25}$ seconds. Nevertheless their existence plays an important role in our current understanding of the universe. W bosons are the carriers of the Weak nuclear force.

Because of the large mass of the W boson, high energies are needed to produce them in a particle collider. After the prediction of the existence of the W boson and its neutral partner, the Z boson, at the end of the 1960s, it was not until 1983 that the W and Z bosons were actually produced for the first time at the proton-antiproton collider (SPS) at the European Laboratory for particle physics (CERN) in Geneva. In 1989 the largest scientific instrument ever built, the Large Electron Positron collider (LEP) at CERN, was switched on. During the first years (LEP1 phase) it was used to produce millions of Z bosons and study their properties. Subsequently the energy was increased and in 1996 the WW production threshold was passed, so that the properties of W bosons could be studied as well.

The subject of this thesis is the measurement of the mass of the W boson directly from the invariant mass of its decay products, using the DELPHI detector at LEP. The combination with the results of the other 3 collaborations at LEP will yield a direct measurement of the W mass more precise than ever before, thus allowing important tests of the Standard Model and also enabling an improved prediction of the mass of the elusive Higgs particle, the only particle in the Standard Model that has not yet been observed.

The theoretical motivation of the measurement will be elucidated in a slightly more quantitative manner in chapter 1, while chapters 2 and 3 deal with the more experimental aspects of the production, decay and observation of W bosons at LEP. Chapter 2 focuses on the relevant physics processes and phenomenological models used to describe them. This includes final state gluon radiation, jet fragmentation and possible final state cross-talk between the W bosons in hadronic final states. Furthermore the 'line-shape' of the W boson is defined here, used to define the W mass and the width observables. The aim of this chapter and of chapter 3, describing LEP and the DELPHI detector, is to highlight the main physics processes and experimental properties that are vital to understand and control the measurement.

The following chapters are dedicated to a detailed description of the analysis techniques used. The methods developed for this thesis have been (and still are) the baseline analysis for the DELPHI results in the fully hadronic channel. This thesis therefore details the evolution and final version of this analysis which includes several novel techniques in an 'Ideogram' framework. First in Chapter 4 a few basic analysis tools are reviewed, namely jet clustering, constrained fit, Monte Carlo reweighting and the Jackknife method. Chapter 5 describes how these basic analysis tools were combined to construct the Ideogram analysis. It will give an overview of the development of the analysis by briefly outlining the different versions employed by DELPHI to analyse the data sets at 172, 183 and 189 GeV. The final analysis, identical to the 189 GeV version, is presented in a comprehensive manner in Chapter 6. In addition to the measurement of the W mass and width, a method to measure the difference m_{W^+} - m_{W^-} is also proposed. Furthermore a feasibility study of a similar approach in the semileptonic channel is presented but with less detail.

A crucial part of the W mass analysis is the treatment of systematic errors. A careful study is presented in chapter 7, including the main conclusions obtained from a new and highly sensitive technique based on Mixed Lorentz Boosted Z boson events (MLBZ).

The final results on W mass, width and the difference between the masses of the W^+ and the W^- bosons are presented in chapter 8, and a conclusion and outlook are given. Appendix A contains a detailed discussion of the MLBZ method and its results.

The work presented in this thesis has taken place from 1996 to 2001. Some of the results have already been published [1, 2, 3, 4, 5], while the analysis method has been described in some detail in [6].

Chapter 1

The W boson in the Standard Model

The Standard Model (SM) describes all known elementary particles and their interactions through the Strong, Weak and Electromagnetic force. Its fundamental constituents are the integer spin bosons and spin-1/2 fermions listed in Table 1.1 and 1.2. Central to the model is the idea that the interactions are manifestations of an underlying fundamental gauge symmetry, given by the symmetry group $SU(3)_C \otimes SU(2)_L \otimes U(1)_Y$. The condition that the theory is invariant under local gauge transformations of this symmetry group requires the existence of so-called gauge bosons: the intermediate vector bosons of Table 1.1, which act as messengers of the corresponding force.

vector bosons	spin	interaction	mass (GeV/c^2)
γ (photon)	1	Electromagnetic	0
W$^+$,W$^-$	1	Weak (charged current)	$\approx$ 80
Z^0	1	Weak (neutral current)	$\approx$ 90
g (gluon)	1	Strong	0
H (Higgs)	0	Yukawa coupling	$>$ 114

Table 1.1: *Bosons of the Standard Model. The non-zero masses listed are just meant as an indication. Their values are not predicted by the Standard Model.*

The W boson is one of the gauge bosons: it is the charged gauge boson of the Weak interaction. As the principal aim of this thesis is the measurement of the mass of the W boson, this chapter will focus on the ElectroWeak (EW) sector of the Standard Model, which describes how the W and the Z boson acquire mass through spontaneous breaking of the $SU(2)_L \otimes U(1)_Y$ symmetry mentioned above, while the photon — the gauge boson of Quantum Electro Dynamics (QED) — remains massless.

The $SU(3)_C$ part of the symmetry of the Standard Model is associated with the strong nuclear force. Quantum Chromo Dynamics (QCD) is the corresponding gauge theory and its gauge bosons are massless gluons. Although QCD is not the primary concern of the measurement presented here, the phenomenology of the strong force does have interesting consequences for the experimental aspects of the analysis, to be discussed in more detail in the next chapter.

The EW theory as it is known today was formulated by Weinberg in 1967 and by Salam in 1968 who incorporated the idea of unification of Glashow [7]. This theory, commonly called the Glashow-Weinberg-Salam model, was built with the help of the gauge principle and incorporated the mechanism of spontaneous symmetry breaking of local (gauge) symmetries proposed by Higgs, Englert and Brout in 1964 [8]. The important proof of renormalisability of (non-Abelian) gauge theories with and without spontaneous symmetry breaking was provided by the work of 't Hooft and Veltman, completed in 1971 [9].

The Standard Model has been tremendously successful in making precise predictions that have all been in agreement with experimental tests performed to date. All fermions of the Standard Model, listed in Table 1.2, have been observed. They are all spin-1/2 fermions called quarks and leptons. The quarks have a colour charge and feel the strong force, while the leptons do not. They come in three families. At LEP, the number of families has been established to be three [10], and the couplings of the W and the Z boson follow precisely the behaviour predicted by the group structure of the Standard Model.

Fermions	Generation						Q	I_3
	1		2		3			(left-handed)
Leptons	ν_e		ν_μ		ν_τ		0	1/2
	e^-	(electron)	μ^-	(muon)	τ^-	(tau)	-1	-1/2
Quarks	u	(up)	c	(charm)	t	(top)	2/3	1/2
	d	(down)	s	(strange)	b	(bottom)	-1/3	-1/2

Table 1.2: *Fermions of the Standard Model, and their quantum numbers corresponding to electric charge (Q) and the third component of weak isospin (I_3) for the left-handed chirality state (a particle's right-handed component always has $I_3 = 0$). All fermions have a corresponding anti-fermion partner and additionally (anti-)quarks exist in 3 species of different colour charge.*

The Higgs mechanism will be the subject of section 1.1 as it gives rise to a lowest order prediction of the W mass (section 1.2); then the effects of higher order radiative corrections are discussed (section 1.3) followed by a brief discussion of the mass mystery and possible theories beyond the Standard Model (section 1.4).

1.1 EW symmetry breaking

As mentioned already, the postulated underlying symmetry of EW interactions is given by $SU(2)_L \otimes U(1)_Y$. The $U(1)_Y$ gauge invariance requires the introduction of a neutral massless field B_μ. The B field couples to fermions with a strength g' according to the particle's weak hypercharge Y defined as

$$Y = 2(Q - I_3) \tag{1.1}$$

where Q is the electric charge (in units of e) and I_3 the third component of the weak isospin I as shown in Table 1.2. To satisfy $SU(2)_L$ gauge invariance three massless fields $\mathbf{W}_\mu$ are introduced, where two fields are charged, and the third field is neutral. These $\mathbf{W}_\mu$ fields couple to left handed chirality states with a strength g.

The physical W bosons are related to these fields as

$$W^\pm_\mu = \frac{1}{\sqrt{2}}(W^1_\mu \mp iW^2_\mu) \tag{1.2}$$

while in order to comply with the experimental fact that the physical Z boson and photon couple both to left- and right-handed fermions the corresponding fields must be orthogonal linear combinations of the $\mathbf{W}$ and B fields:

$$\begin{aligned} A_\mu &= \sin\theta_W W^3_\mu + \cos\theta_W B_\mu \\ Z_\mu &= \cos\theta_W W^3_\mu - \sin\theta_W B_\mu \end{aligned} \tag{1.3}$$

where θ_W is called the Weinberg weak mixing angle. The well-known coupling strength of the photon, $e = \sqrt{4\pi\alpha}$, gives the following constraint for the coupling strengths:

$$e = g\sin\theta_W = g'\cos\theta_W \tag{1.4}$$

The gauge bosons described above are massless. The weak force, however, is known to be a short-range interaction, which means that its intermediate vector bosons need to be heavy. One way to introduce masses without spoiling the gauge invariance is spontaneous symmetry breaking through the Higgs mechanism. In its minimal form, a single weak isospin doublet of complex scalar fields is needed:

$$\Phi = \begin{pmatrix} \phi^+ \\ \phi^0 \end{pmatrix} \equiv \begin{pmatrix} (\phi_1 + i\phi_2)/\sqrt{2} \\ (\phi_3 + i\phi_4)/\sqrt{2} \end{pmatrix} \tag{1.5}$$

where the ϕ_i are real fields. When the potential energy associated with this field is given by

$$V(\Phi) = \mu^2|\Phi|^2 + \lambda|\Phi|^4 \tag{1.6}$$

with parameters $\mu^2 < 0$ and $\lambda > 0$, the potential does not obtain its minimal value (ground state) for a zero value of the field, but for

$$|\Phi|^2 = -\frac{\mu^2}{2\lambda} \equiv \frac{1}{2}v^2 \tag{1.7}$$

where v is known as the vacuum expectation value. By choosing one possible minimum on the circle defined by equation (1.7), e.g. $\phi_1 = v$ and $\phi_2 = \phi_3 = \phi_4 = 0$, and postulating that this represents the ground state of the vacuum, the $SU(2)_L \otimes U(1)_Y$ symmetry is broken leaving only the $U(1)_{\mathrm{em}}$ symmetry of QED. One obtains one massive scalar field of mass $\sqrt{2\lambda v^2}$ which is called the Higgs field H, and three massless particles, known as Goldstone bosons. For a particular choice of the gauge, the three degrees of freedom of the Goldstone bosons disappear and effectively give mass to the three vector bosons, while the photon remains massless. This leads to the following mass predictions:

$$\begin{aligned} m_W &= \frac{1}{2}vg \\ m_Z &= \frac{v}{2}\sqrt{g^2 + g'^2} \\ m_\gamma &= 0 \\ m_H &= \sqrt{2\lambda v^2} \end{aligned} \tag{1.8}$$

As a by-product, the Higgs field gives masses to the fermion fields through a Yukawa coupling. For each fermion a Yukawa coupling strength g_f can be derived from its observed mass m_f as:

$$m_f = \frac{g_f v}{\sqrt{2}} \tag{1.9}$$

Two remarks should be made here. First it should be noted that although the Higgs mechanism gives precise predictions for the vector boson masses, the Yukawa couplings g_f are free parameters.

Second, the mass eigenstates of the quarks are not the same as the weak eigenstates listed in Table 1.2. By convention, this is represented by a rotation of the 'down-type' quark mass eigenstates given by the unitary Cabibbo-Kobayashi-Maskawa mixing matrix V_CKM:

$$\begin{pmatrix} d' \\ s' \\ b' \end{pmatrix} = \begin{pmatrix} V_{ud} & V_{us} & V_{ub} \\ V_{cd} & V_{cs} & V_{cb} \\ V_{td} & V_{ts} & V_{tb} \end{pmatrix} \begin{pmatrix} d \\ s \\ b \end{pmatrix} \tag{1.10}$$

where the current experimental 90% confidence limits on the V_CKM matrix elements, using constraints from unitarity and assuming three generations, are [11]:

$$\begin{pmatrix} 0.9742-0.9757 & 0.219-0.226 & 0.002-0.005 \\ 0.219-0.225 & 0.9734-0.9749 & 0.037-0.043 \\ 0.004-0.014 & 0.035-0.043 & 0.9990-0.9993 \end{pmatrix} \tag{1.11}$$

The diagonal elements of V_CKM are close to unity, while the off-diagonal elements are small. Thus weak interactions between quarks of the same family are favoured, while interactions between families are said to be 'Cabibbo suppressed' (by a factor $\sim |V_{ij}|^2$).

1.2 W mass prediction at Born level

The mechanism of spontaneous symmetry breaking presented in the previous section does not fix the W mass, but it provides a set of well-defined relations between the W mass and other parameters of the Standard Model. In this section a 'tree level' (also called 'Born level') prediction of the W mass is discussed, using only lowest order expressions. In the next section the effects of higher order corrections are discussed.

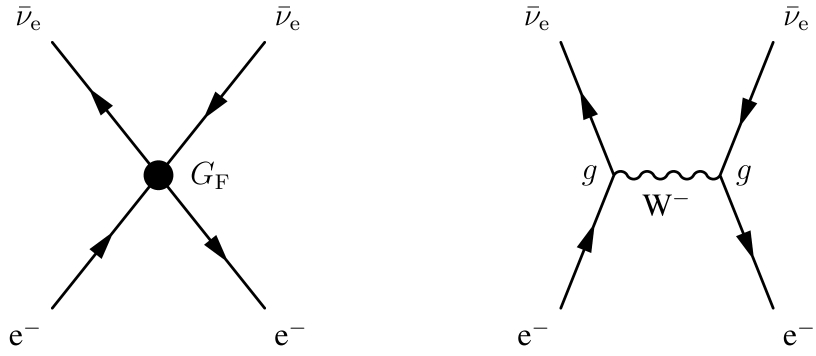

Figure 1.1: *The representations of an electron neutrino interaction as a contact interaction (left), or via the exchange of an intermediate vector boson (right) must provide equivalent descriptions in the limit of low momentum transfer.*

In order for the definition of the Fermi coupling constant G_F to agree with the Standard Model description in the limit of small momentum transfer (as illustrated in Figure 1.1), the following relation should hold:

$$\frac{G_\mathrm{F}}{\sqrt{2}} = \frac{g^2}{8m_\mathrm{W}^2} = \frac{1}{2v^2} \tag{1.12}$$

Using relation (1.4) and the expression for the finestructure constant $\alpha = e^2/4\pi$, the following predictions for the W boson and Z boson mass can be derived:

$$m_\mathrm{W}^\mathrm{tree} = \cos\theta_\mathrm{W} \cdot m_\mathrm{Z}^\mathrm{tree} = \frac{1}{\sin\theta_\mathrm{W}}\sqrt{\frac{\pi\alpha}{G_\mathrm{F}\sqrt{2}}} \tag{1.13}$$

The Fermi constant G_F can be obtained [12] from the measured muon lifetime to be

$$G_\mathrm{F} = (1.16637 \pm 0.00001) \cdot 10^{-5}\ \mathrm{GeV}^{-2} \tag{1.14}$$

corresponding to a vacuum expectation value

$$v = 246\ \mathrm{GeV} \tag{1.15}$$

The fine-structure constant α is known most precisely from the measurement of the anomalous magnetic moment of the electron. Its current best value is [13]:

$$\alpha^{-1} = 137.03599976 \pm 0.00000050 \tag{1.16}$$

The observation of neutral current processes in neutrino scattering by the Gargamelle collaboration in 1973 [14], 11 years after the existence of neutral current weak interaction had been predicted, was the first firm indication that the Standard Model was correct. In the following years a first value of $\sin^2\theta_\mathrm{W}$ could be derived from the observed ratio between neutral current and charged current scattering, thus enabling the first numerical predictions of the weak boson masses:

$$\begin{aligned} m_\mathrm{W}^\mathrm{tree} &= 78\ \mathrm{GeV}/c^2 \\ m_\mathrm{Z}^\mathrm{tree} &= 89\ \mathrm{GeV}/c^2 \end{aligned} \tag{1.17}$$

The subsequent discovery of the $\mathrm{W}^\pm$ and Z gauge bosons at the SPS collider at CERN in 1983 [15] was a great triumph and definitive confirmation of the validity of the SM. The observed masses reported in Stockholm (from electron decays only [16]) were in remarkable agreement with the predicted values:

$$\begin{aligned} m_\mathrm{W} = \quad & 80.9 \pm 1.5 \pm 2.4 \quad \mathrm{GeV}/c^2\ \text{(UA1)} \\ & 83.1 \pm 1.9 \pm 1.3 \quad \mathrm{GeV}/c^2\ \text{(UA2)} \\ m_\mathrm{Z} = \quad & 95.6 \pm 1.4 \pm 2.9 \quad \mathrm{GeV}/c^2\ \text{(UA1)} \\ & 92.7 \pm 1.7 \pm 1.4 \quad \mathrm{GeV}/c^2\ \text{(UA2)} \end{aligned} \tag{1.18}$$

with statistical (first) and systematic (second) errors quoted separately.

Rho parameter

The ρ parameter was introduced in 1975 by Ross and Veltman [1] to summarise their argument [17] that the ratio between m_{W} and m_{Z} depends on the structure of the Higgs fields. At tree level its definition as

$$\rho \equiv \frac{m_{\mathrm{W}}^2}{m_{\mathrm{Z}}^2 \cos^2\theta_{\mathrm{W}}} \tag{1.19}$$

makes ρ equal to 1 for the simplest version of the Higgs mechanism involving only a single weak isospin doublet, as described in the previous section. In this formula $\cos^2\theta_{\mathrm{W}}$ should be extracted from an independent measurement, e.g. the ratio between eν and e$\bar{\nu}$ scattering cross-sections. If other Higgs multiplets with weak isospin $> 1/2$ and a significant vacuum expectation value were to exist, it would modify the ρ parameter. The observed value of ρ close to unity is an indication that the SM Higgs sector indeed consists of a single doublet, or at least excludes several other *a priori* possibilities.

W$^+$ and W$^-$ mass difference

In the Standard Model, W$^+$ and W$^-$ are eachother's anti-particles. Therefore, as in any relativistic quantum field theory, they must have equal masses. This is true to all orders in perturbation theory, otherwise CPT symmetry would be violated. The strictest experimental limits on mass differences between particle and anti-particle have been obtained in the neutral Kaon sector [11]:

$$|m_{\mathrm{K}^0} - m_{\overline{\mathrm{K}}^0}|/m_{\mathrm{average}} < 10^{-18} \tag{1.20}$$

by experiments studying $\mathrm{K}^0 - \overline{\mathrm{K}}^0$ mixing. As the W$^+$ and W$^-$ bosons are charged particles, such mixing could never occur. Therefore an experimental determination has to rely on a direct measurement of the W$^+$ and W$^-$ mass separately, leading to a relatively large error on the difference. Currently the world-average is based on the measurement of the W mass by CDF [18]:

$$(m_{\mathrm{W}^+} - m_{\mathrm{W}^-})/m_{\mathrm{average}} = -0.002 \pm 0.007 \tag{1.21}$$

This mass difference can in principle also be extracted from the LEP2 data. This thesis includes a feasibility study of such a measurement, exploring the possible experimental challenges and estimating the precision that can be obtained at LEP.

[1] Though originally, in [17], the new parameter was called 'β'.

1.3 Radiative corrections

With the ever increasing precision of the experimental tests of the Standard Model, the accuracy of tree level relations discussed so far is no longer sufficient. This can be illustrated considering the combined W mass result obtained at $\mathrm{p\bar{p}}$ colliders (CDF, D0 and UA2 [19]): $m_{\mathrm{W}} = 80.452 \pm 0.062$ GeV/c^2, which using the tree level relation (1.13) corresponds to $\sin^2\theta_{\mathrm{W}}{}^{\mathrm{naive}} = 0.2147 \pm 0.0004$ and a Z^0 boson mass $m_{\mathrm{Z}}{}^{\mathrm{naive}} = 90.788 \pm 0.055$ GeV/c^2, clearly in disagreement with the precise measurement of the Z^0 mass performed at LEP1:

$$m_{\mathrm{Z}}{}^{\mathrm{LEP}} = 91.1875 \pm 0.0021 \text{ GeV/c}^2 \tag{1.22}$$

The difference is more than 7 times the experimental error, showing that first order calculations are no longer sufficient to describe the experimental results. It turns out, however, that it is non-trivial to take into account higher order diagrams.

When doing higher order perturbative calculations in the framework of the Standard Model, involving the summation over all (∞) virtual intermediate states, infinities arise. Already at the level of individual diagrams the calculation of the amplitude yields infinite results. This appears to be in contradiction with the experimental fact that the physical observables to be predicted by the theory are finite.

Fortunately, however, the Standard Model is a gauge theory and thus is a *renormalisable* theory which means that it is possible, with some mathematical trickery, to absorb these infinities in the fundamental coupling constants and masses order by order. When a careful job is done of expressing physical predictions only in terms of physically measurable parameters, the infinities disappear and the resulting calculations can, in principle, be performed to any order in perturbation theory.

The physics at an ordinary scale turns out to be insensitive to the infinities that occur in such very high energy virtual processes, related to a small number of affected parameters that are in fact physically unobservable.

The resulting relations between observables are modified with respect to the tree level relations. Thus the full calculation taking into account higher order diagrams and applying the renormalisation procedure leads to 'radiative corrections' of the SM predictions [20].

A particularly useful set of experimental observables currently used in fits of the EW Standard Model consists of the Z^0 pole mass m_{Z}, the fine structure constant α, and the Fermi coupling constant G_{F}, with currently measured values already given in equations (1.14), (1.16) and (1.22). These parameters have been measured independently with high precision.

This thesis reports a direct measurement of the W boson mass m_{W}, which is another fundamental Standard Model observable. Its measured value is to be compared to the Standard Model prediction which, written in terms of m_{Z}, α, and G_{F}, including radiative corrections, is given by:

$$m_{\mathrm{W}}^2 = \frac{1}{2} m_{\mathrm{Z}}^2 \left(1 + \sqrt{1 - \frac{4}{m_{\mathrm{Z}}^2} \left(\frac{\pi\alpha}{\sqrt{2} G_{\mathrm{F}}} \right) \cdot \frac{1}{1 - \Delta r}} \right) \tag{1.23}$$

In this formula all modifications due to higher order diagrams have been absorbed in the Δr term, whose value can be calculated when the parameters of the Standard Model, including the masses of all fermions and bosons, are known. For $\Delta r = 0$ and the tree level definition of the weak mixing angle $\sin^2\theta_{\mathrm{W}} = 1 - m_{\mathrm{W}}^2/m_{\mathrm{Z}}^2$, it reduces to the tree level relation (1.13) shown before.

This definition of $\sin\theta_{\mathrm{W}}$ is the 'on-shell' definition. After the introduction of higher-order corrections, however, this definition is no longer unique. Other definitions exist, the most optimal choice depending on the renormalisation prescription that is used. Table 1.3 gives a short list of popular schemes. In the modified minimal subtraction ($\overline{\mathrm{MS}}$) scheme, the mixing angle is defined as $\sin^2\hat{\theta}_{\mathrm{W}}(\mu) \equiv \hat{g}'^2(\mu)/[\hat{g}'^2(\mu)+\hat{g}^2(\mu)]$, where the renormalisation scale μ is chosen to be equal to m_{Z}. The advantage of this definition is a smaller dependence of the dominant quadratic correction due to the top quark mass, which explains the smaller uncertainty quoted. The third definition, the 'effective' mixing angle, is convenient for the interpretation of forward-backward asymmetries measured at the Z pole (see e.g. the Z parameter fits done by the EW working group [10]).

Renormalisation scheme	notation for $\sin^2\theta_{\mathrm{W}}$	SM value (from SM fit)
On-shell	${s_{\mathrm{W}}}^2$	0.22302 ± 0.00040
$\overline{\mathrm{MS}}$	${\hat{s}_{\mathrm{Z}}}^2$	0.23117 ± 0.00016
Effective angle	${\bar{s}_{\mathrm{f}}}^2$	0.23147 ± 0.00016

Table 1.3: *Several popular renormalisation schemes and the corresponding definition of the weak mixing angle (see text). The small differences between the values for* $\sin^2\theta_{\mathrm{W}}$ *are mainly due to corrections depending on* m_{H} *and* m_{t}.

In order to make the different contributions to Δr visible it can be decomposed into the following terms:

$$\Delta r = \Delta\alpha - \rho_{\mathrm{t}}\frac{\hat{c}_{\mathrm{Z}}^2}{\hat{s}_{\mathrm{Z}}^2} + \Delta r_{\mathrm{Higgs}} + \Delta r_{\mathrm{vertex}} + \Delta r_{\mathrm{box}} + \Delta r_{\mathrm{rem}} \tag{1.24}$$

where the different terms are briefly discussed below. A rigorous treatment of all corrections in the framework of one renormalisation scheme — let alone a comparison of different schemes — is outside the scope of this thesis. Instead in the following paragraphs a brief outline is given, concentrating on the three corrections most relevant for the interpretation of the W mass measurement: the ρ_{t} and the $\Delta r_{\mathrm{Higgs}}$ terms because of their relevance for the top quark and Higgs boson mass, and the $\Delta\alpha$ term since it involves one of the dominant uncertainties on the calculation of Δr. The $\Delta r_{\mathrm{vertex}}$, Δr_{box} and Δr_{rem} terms are also important, but will not be discussed here. Their numerical values have been calculated to sufficient precision.

Fermionic loop corrections

Radiative corrections to the self-energy of the weak vector bosons include fermion loop corrections of the type shown in Figure 1.2. These corrections are different for the W and the Z boson, leading to changes in the ratio of the observable W mass and the Z mass. It can be shown that at the one-loop level such corrections correspond to a change of the ρ parameter equal to:

$$\Delta\rho^{(1)}_{(\mathrm{f}_1,\mathrm{f}_2)} = \frac{CG_{\mathrm{F}}}{8\sqrt{2}\pi^2}\left(m_1^2 + m_2^2 - \frac{4}{m_1^2 m_2^2}\cdot\ln\frac{m_1}{m_2}\right) \geq \frac{CG_{\mathrm{F}}}{8\sqrt{2}\pi^2}(\Delta m)^2 \tag{1.25}$$

for each weak SU(2) fermion doublet (f_1, f_2), where C is 3 (1) for a colour triplet (singlet). This effect vanishes when the difference of the masses Δm goes to zero, which is to good approximation the case for all known fermion doublets except for the top-bottom quark pair. Neglecting the mass (≈ 5 GeV$/c^2$) of the bottom quark, the following radiative correction to the ρ parameter due to the top quark mass is obtained:

$$\rho_{\rm t} \equiv \frac{3G_{\rm F}}{8\sqrt{2}\pi^2} m_{\rm t}^2 \approx 0.009520 \cdot (m_{\rm t} \ / \ 174.3 \ {\rm GeV}/c^2)^2 \tag{1.26}$$

This quadratic dependence on $m_{\rm t}$, enhanced by a factor $1/\tan^2\theta_W$ as shown in equation (1.24), constitutes the dominant contribution to Δr. As this correction becomes larger for increasing values of $m_{\rm t}$, it was possible to constrain the top quark mass within an allowed mass window using the precision EW measurements performed at LEP1, even before the top quark was discovered at the Tevatron collider in 1995 [21]. With the current EW precision data available [11], the SM prediction for $m_{\rm t}$, without using the direct measurement, is $m_{\rm t} = 168.2^{+9.6}_{-7.4}$ GeV$/c^2$, or for a Higgs mass fixed to 100 GeV/c^2, $m_{\rm t} = 172.2 \pm 4.0$ GeV$/c^2$, both in stunning agreement with the directly observed value: 174.3 ± 5.1 GeV$/c^2$.

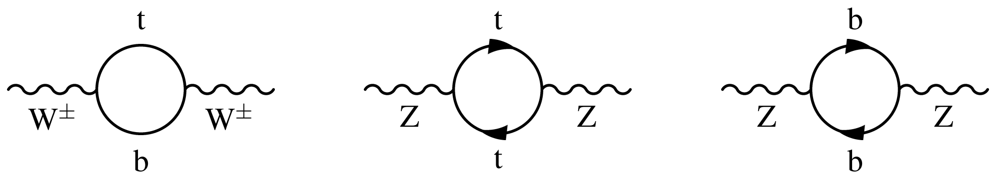

Figure 1.2: *Self-energy corrections to the W propagator (left) and Z propagator (centre and right) loop. Here only the one-loop level diagrams involving top and bottom quarks are shown.*

Bosonic loop corrections

Bosonic loop corrections are all much smaller than the quadratic $m_{\rm t}$ contribution. Figure 1.3 shows a one-loop correction to the W and Z self energies that is of particular experimental interest, because it involves the SM Higgs boson. According to the Veltman screening theorem, the leading correction for a Higgs boson heavy compared to $m_{\rm W}$ is logarithmic in $m_{\rm H}$ and of the following form:

$$\begin{aligned} \Delta r_{\rm Higgs} &\approx \frac{\sqrt{2}G_{\rm F}m_{\rm W}^2}{16\pi^2} \cdot \frac{11}{3}\left(\ln\frac{m_{\rm H}^2}{m_{\rm W}^2} - \frac{5}{6}\right) \\ &\approx 0.002474 \cdot \ln\left(\frac{m_{\rm H}}{100\ {\rm GeV}/c^2}\right)^2 - 0.000981 \end{aligned} \tag{1.27}$$

The small size of $\Delta r_{\rm Higgs}$ and the fact that it only depends on the logarithm of the Higgs mass requires that the other terms be known to good precision in order to be able to constrain $m_{\rm H}$ indirectly on the basis of EW precision measurements.

Vacuum polarisation and the running of alpha

The largest of the remaining terms in equation (1.24) is the $\Delta\alpha$ term defined by:

$$\alpha(m_{\rm Z}^2) = \frac{\alpha(0)}{1-\Delta\alpha} \tag{1.28}$$

Figure 1.3: *A one-loop radiative correction to the W and the Z propagators involving the Higgs boson.*

which describes the change in the running coupling constant α going from the Thomson scale ($Q^2 \approx 0$), where α is accurately known, to the Weak physics scale ($Q^2 \approx m_{\mathrm{Z}}^2$). As in the case of the Z and the W, the photon propagator is modified by fermion loops. The contributions from different known fermions pairs have been calculated separately:

$$\Delta\alpha = \Delta\alpha_{\mathrm{leptons}} + \Delta\alpha_{\mathrm{5quarks}} + \Delta\alpha_{\mathrm{top}} \tag{1.29}$$

Until recently the largest uncertainty on $\Delta\alpha$ (and consequently on Δr) came from the $\Delta\alpha_{\mathrm{5quarks}}$ term involving the light quarks, dominated by the experimental errors on the $\mathrm{e^+e^-} \to$ hadrons cross-section in the low Q^2 region between 1 GeV and 7 GeV. Recent measurements at the $\mathrm{e^+e^-}$ collider BES in Beijing [22], however, have improved the situation and allowed an update of the 'experimental' evaluation of $\Delta\alpha_{\mathrm{5quarks}}$ [23], giving:

$$\Delta\alpha_{\mathrm{5quarks}} = 0.02761 \pm 0.00036 \tag{1.30}$$

Complementary results have been obtained from theoretical calculations based on the assumption that perturbative QCD can be used down to a scale of 1.8 GeV. A recent theory-driven evaluation, used as input for the PDG 2000 EW fit [11], predicts $\Delta\alpha_{\mathrm{5quarks}}$ to be [24]

$$\Delta\alpha_{\mathrm{5quarks}} = 0.02776 \pm 0.00020 \tag{1.31}$$

so that the corresponding values for $\Delta\alpha$ and $\alpha(m_{\mathrm{Z}}^2)$ become [11]:

$$\Delta\alpha = 0.0664 \pm 0.0002 \;\; ; \quad \alpha(m_{\mathrm{Z}}^2) = (127.938 \pm 0.027)^{-1} \tag{1.32}$$

1.3.1 SM prediction for the W mass

Thus, applying a SM fit to all indirect data including the measured value of the top quark mass, a current 'best' SM value of Δr is given by [11]:

$$\Delta r = 0.0357 \pm 0.0014 \tag{1.33}$$

Substituting this value of Δr in equation (1.23) gives:

$$m_{\mathrm{W}} = 80.373 \pm 0.024 \ \mathrm{GeV}/c^2 \tag{1.34}$$

which is in excellent agreement with the combined result from the direct measurements by CDF, D0 and UA2 [19]:

$$m_{\mathrm{W}} = 80.452 \pm 0.062\ \mathrm{GeV}/c^2 \tag{1.35}$$

The LEP2 data will provide an independent, direct measurement of the W mass with a precision to match the uncertainty of the indirect prediction. This will be discussed further in chapter 8, together with its implications for the indirect search of the Higgs boson.

1.3.2 The Rho parameter after renormalisation

It is clear that beyond tree level the definition of ρ as given in equation (1.19) requires a further specification of the definition of $\sin\theta_{\mathrm{W}}$ to be used. Obviously the on-shell definition of $\sin\theta_{\mathrm{W}}$, fixing $\rho = 1$ by construction, is out of the question. Here we will use the $\overline{\mathrm{MS}}$ definition of $\sin\theta_{\mathrm{W}}$ defining $\hat{\rho}$ as:

$$\hat{\rho} \equiv \left(\frac{m_{\mathrm{W}}}{m_{\mathrm{Z}}\hat{c}_{\mathrm{Z}}}\right)^2 \tag{1.36}$$

For this definition of $\hat{\rho}$ the one-loop correction involving the top quark takes the shape of the ρ_{t} expression (1.26) given before. Thus in the SM a deviation of $\hat{\rho}$ from 1 is expected:

$$\hat{\rho} \approx 1 + \rho_{\mathrm{t}} \tag{1.37}$$

When, apart from the dominant ρ_{t} term, contributions from bosonic loops and two-loop corrections involving the top-quark are also included, one obtains [11]:

$$\hat{\rho} = 1.0107 \pm 0.0006 \tag{1.38}$$

the main uncertainty coming from the allowed range on m_{t} and m_{H}. One can now define a new parameter, ρ_0, which probes new sources of $SU(2)$ symmetry breaking beyond the Standard Model:

$$\rho_0 \equiv \frac{m_{\mathrm{W}}^2}{m_{\mathrm{Z}}^2\hat{c}_{\mathrm{Z}}^2\hat{\rho}} \tag{1.39}$$

As $\hat{\rho}$ describes all known effects due to m_{t} and the Standard Model Higgs doublet, the SM expectation for ρ_0 is 1. Any deviation from unity would indicate new physics beyond the Standard Model.

1.4 Open questions on mass scales

The Standard Model has proven to be a surprisingly consistent, predictive and precise theory. Not only its qualitative (Z boson, Gargamelle neutral currents), but also the quantitative predictions turned out to be correct at tree level (UA1, UA2) and at the one-loop level (Top mass prediction). It has survived all scrutiny by experimental tests performed in the last 30 years. However, the model also has limitations and involved features that raise questions:

- Why is the number of generations (with light neutrinos) limited to exactly three?

- Where is the Higgs boson? The proposed Higgs mechanism has firmly been established as a possible model to accommodate masses in the Standard Model, but the corresponding Higgs particle has not (yet) been observed.

- Where does the apparently random mass hierarchy of fermions come from? The Standard Model does not predict the masses of the fermions, and the observed mass spectrum ranging from the very small (or zero) masses of the neutrinos via leptons (0.5 - 1,784 MeV/c^2) to quark masses (≈ 0.001 - ≈ 175 GeV/c^2) is puzzling.

- In the boson sector the masses of the Weak gauge bosons are nicely explained, but the Higgs boson mass is not predicted and the value indicated indirectly by the Standard Model fits seems to be 'un-natural' from a theoretical point of view. It is very difficult to ensure such a low mass of the Higgs if no theory beyond the Standard Model exists up to the Planck energy scale, because higher order corrections due to top quark loops and self-interactions of the Higgs easily lead to divergences and spoil the renormalisability of the theory. Unless the Higgs mass is in a narrow band (shown in Figure 1.4), the SM can only be a low-energy effective theory promising 'new' physics already below a scale of ≈ 1 TeV.

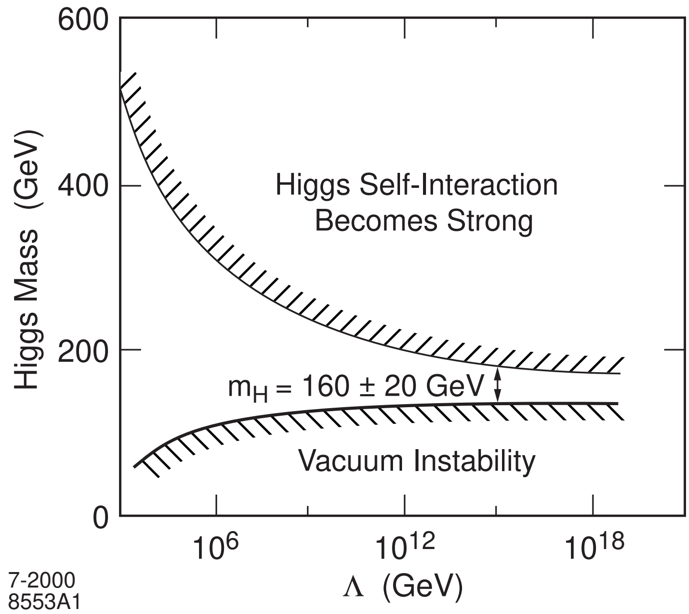

Figure 1.4: *The energy scale up to which EW perturbation theory converges depends on the mass of the Higgs particle. The upper region is forbidden because there the self-interactions of the Higgs particle become strong. The lower region is forbidden because the vacuum itself becomes unstable (picture taken from [25]).*

- Even if the Higgs mass turns out to be in the above-mentioned window with a Standard Model possibly valid up to the Planck scale, the (philosophical) question remains why the EW scale and the Planck scale are so different. This 'hierarchy problem' seems fundamentally linked to the question of unification of the Standard Model and gravitation.

These and other questions inspire particle physicists to develop new theories and models such as Supersymmetry and String theories with compactified higher dimensions. But as long as no supersymmetric particles or other non-SM physics effects have been established, these theories beyond the Standard Model remain pure speculation.

The direct measurement of the W mass presented in this thesis will help to narrow down the predicted mass region in which to search for the SM Higgs boson. In the coming decade the establishment of the Higgs mechanism and further investigation of its precise properties will be one of the major topics in particle physics and will almost certainly lead to new insights in the enigma related to the generation and scales of masses of elementary particles. The next collider in line to search for the Higgs particle is the Tevatron, which will be followed by the Large Hadron Collider (LHC) at CERN, whose start is foreseen in 2006 and whose large energy range will cover the full allowed range of the Higgs boson mass.

Chapter 2

W pair production at LEP

The crossing of the WW production threshold in July 1996 marked the beginning of the LEP2 phase. The first LEP2 energy was chosen to be 161 GeV, just above 2 times the W mass, at that time known to 160 MeV/c^2 precision from direct measurements and predicted with an accuracy of about 50 MeV/c^2 from a global SM fit to LEP1 and SLC data. Figure 2.1 shows the behaviour of the WW production cross-section as a function of the $\mathrm{e}^+\mathrm{e}^-$ centre-of-mass energy.

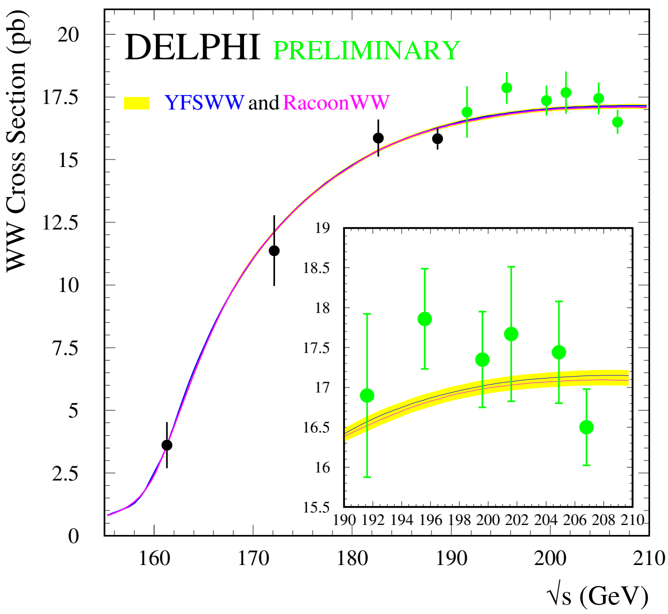

Figure 2.1: *DELPHI measurements of the* $\mathrm{e}^+\mathrm{e}^- \rightarrow \mathrm{W}^+\mathrm{W}^-$ *production cross-section compared with the Standard Model prediction given by the YFSWW [26] and RacoonWW [27] programs. The shaded band indicates the uncertainty on the theoretical calculations. Results for* $\sqrt{s} > 190$ *GeV are preliminary.*

W pair production

The production of on-shell (i.e. stable) W bosons already demonstrates some of the most important features of W pair production at LEP, as will be discussed in section 2.1. The W pair events thus produced have allowed measurements of the W mass via two different methods:

- The threshold measurement, based on a SM fit to the cross-section near threshold.
- The direct kinematic reconstruction: deriving the W mass from the invariant mass of its decay products.

The cross-section method was used at $\sqrt{s}$ =161 GeV since it has its optimal statistical sensitivity at the threshold. At all other energies, however, direct reconstruction is the preferred method. Its performance is rather independent of the centre-of-mass energy, as long as it is at least a few GeV above threshold to allow both W bosons to be on-shell. This thesis concerns a direct measurement based on the 172 GeV, 183 GeV and 189 GeV DELPHI data sets, covering approximately 1/3 of the available statistics.

W decay

The W boson can decay either into a lepton and a neutrino or into a quark anti-quark pair, followed by subsequent hadronisation into stable particles observed as jets. The combination of 2 W's in one event thus leads to 3 different event topologies, with the following branching ratios:

- 45.6% fully-hadronic ($q\bar{q}q\bar{q}$)
- 43.9% semi-leptonic ($q\bar{q}l\nu$)
- 10.5% fully-leptonic ($l\nu l\nu$)

The doubly resonant production of W bosons, followed by their decay, gives rise to a double Breit-Wigner shape of the differential cross-section as a function of the two W boson invariant masses. It is the shape of this differential cross-section which is used to extract the W mass. This is discussed in more detail in section 2.2.

QCD and jets

At LEP, QCD processes are purely restricted to the final state, after the hard scale EW process has taken place and only if quarks were produced. Quarks are never observed as individual particles. Due to QCD confinement, the hadronic decay gives rise to jets of particles in the final state. Section 2.5 will concentrate on the phenomenological aspects of the radiation of gluons and the formation of jets. QCD is also responsible for the main source of background processes in the fully hadronic channel, to be discussed in section 2.6.

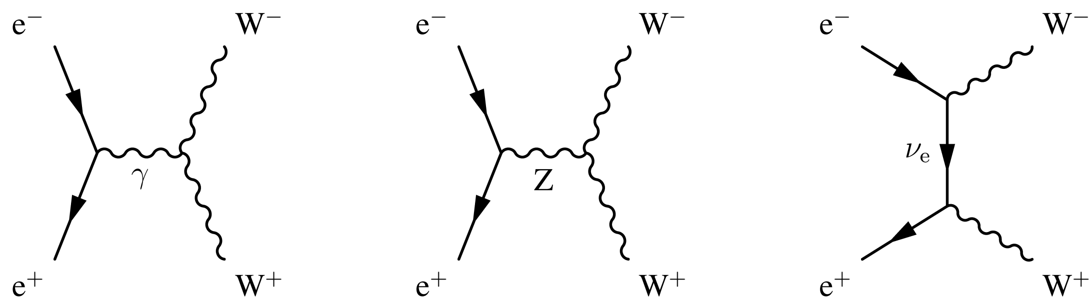

Figure 2.2: *Dominant lowest order Feynman diagrams for the process* $\mathrm{e^+e^-} \rightarrow W^+W^-$.

Other phenomenological aspects

The reconstruction of the invariant mass of the decay products is based on the crucial property of each event that at all times total energy and momentum are conserved. This is also true for complex decay processes like the hadronic decay into jets. In chapter 4 to 6 it will be explained how, using jet clustering and a constrained fit, even in those complex final states the invariant mass of the W bosons can be measured and improved considerably using the knowledge of energy and momentum conservation.

In the majority of the events, the constraints give a vast improvement. But when, occasionally, an Initial State Radiation (ISR) photon escapes undetected inside the beam-pipe, the constraints are incomplete and lead to an erroneous value of the fitted mass. It is therefore important to understand this effect with sufficient precision. Fortunately it is well described by QED (section 2.3) and included in the Monte Carlo generators (section 2.4).

Another possible complication emanates from Final State Interferences (FSI) between the W bosons. When such cross-talk occurs, the simple picture of two bosons decaying independently no longer holds, and the direct correspondence of the invariant mass of the decay products with the invariant mass of the W bosons is lost. These possible cross-talk effects are discussed in section 2.7.

2.1 On-shell W pair production at LEP

The three dominant diagrams for the production of stable W bosons at LEP are shown in Figure 2.2. This set of three Charged Current diagrams is often referred to as 'CC03'. The corresponding tree level amplitude can be written as [29]:

$$\mathcal{M}(\sigma, \lambda, \bar{\lambda}) = \mathcal{M}_\gamma + \mathcal{M}_\mathrm{Z} + \mathcal{M}_\nu \tag{2.1}$$

where the e^- and e^+ helicities are given by $\sigma/2$ and $-\sigma/2$ (in the massless limit $m_\mathrm{e} \ll \sqrt{s}$) and λ and $\bar{\lambda}$ denote the W^- and W^+ helicities, which can have values -1, 0 or 1 as the W bosons are massive particles with spin 1.

Choosing the z-axis along the e^- flight direction, and the x-axis along the W^- transverse momentum, the leading angular dependences can be expressed in terms of the d^{J_0} functions [11]

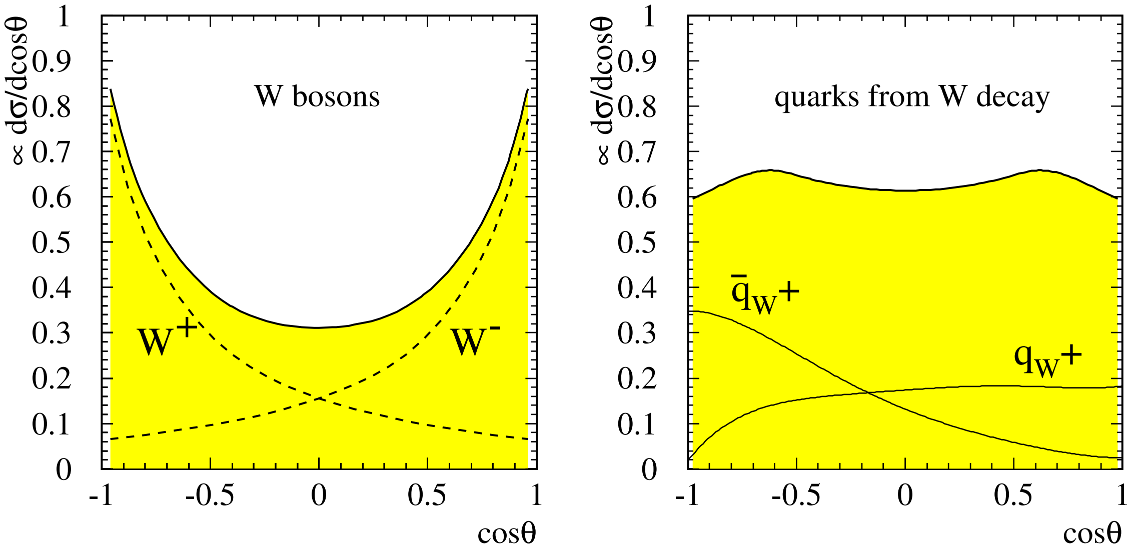

Figure 2.3: *Distribution of cosθ, where θ is the production angle of the W bosons (left), from EXCALIBUR [28] simulation at $\sqrt{s}$= 189 GeV. While the W production is clearly peaked in the forward directions, the distribution of the fermions after the decay of the W bosons (next section) remains almost independent of the polar angle (right plot).*

shown in Table 2.1, with the reduced matrix elements $\tilde{\mathcal{M}}$ defined in such a way that:

$$\begin{aligned}
\mathcal{M}(\sigma,\lambda,\bar{\lambda};\theta) &= \sqrt{2}\sigma e^2 \left[\tilde{\mathcal{M}}_\gamma + \tilde{\mathcal{M}}_\mathrm{Z} + \tilde{\mathcal{M}}_\nu(\theta)\right] d^{J_0}_{\sigma,\lambda-\bar{\lambda}}(\theta) \\
\tilde{\mathcal{M}}_\gamma &\equiv -\beta A_{\lambda\bar{\lambda}} \\
\tilde{\mathcal{M}}_\mathrm{Z} &\equiv +\beta A_{\lambda\bar{\lambda}} \left[1 - \delta_{\sigma,-1}\frac{1}{2\sin^2\theta_\mathrm{W}}\right] \frac{s}{s-m_\mathrm{Z}^2} \\
\tilde{\mathcal{M}}_\nu &\equiv \delta_{\sigma,-1}\frac{1}{2\beta\sin^2\theta_\mathrm{W}} \left[B_{\lambda\bar{\lambda}} - \frac{1}{1+\beta^2-2\beta\cos\theta}C_{\lambda\bar{\lambda}}\right]
\end{aligned} \tag{2.2}$$

where $\beta = \sqrt{1-4m_\mathrm{W}^2/s}$ is the W velocity, θ is the production angle of the W bosons with respect to the positive z axis, δ_{ij} is the Kronecker delta function, and $J_0 = \max(1, |\lambda - \bar{\lambda}|) = 1, 2$ is the minimum angular momentum contributing to a given helicity combination. The coefficients $A_{\lambda\bar{\lambda}}$, $B_{\lambda\bar{\lambda}}$ and $C_{\lambda\bar{\lambda}}$ are given in Table 2.1.

Just above threshold ($\beta \ll 1$) the differential cross-section is given by [30]:

$$\frac{\mathrm{d}\sigma}{\mathrm{d}\cos\theta} = \frac{\alpha^2}{s}\frac{\beta}{4\sin^4\theta_\mathrm{W}}\left[1 + 4\beta\cos\theta\frac{3\cos^2\theta_\mathrm{W}-1}{4\cos^2\theta_\mathrm{W}-1} + \mathcal{O}(\beta^2)\right] \tag{2.3}$$

where the leading term $\propto \beta$ comes from the t-channel ν exchange diagram only. Thus, for small values of β the differential cross-section is essentially angular independent, while for increasing values of $\sqrt{s}$ other angular dependent terms become important.

$\Delta\lambda$	$(\lambda\bar{\lambda})$	$A_{\lambda\bar{\lambda}}$	$B_{\lambda\bar{\lambda}}$	$C_{\lambda\bar{\lambda}}$	$d^{J_0}_{\sigma,\Delta\lambda}$
± 2	$(+-),(-+)$	0	0	$2\beta\sqrt{2}$	$\lambda\,\sin\theta(1-\lambda\cos\theta)/2$
$+1$	$(+0),(0-)$	2γ	2γ	$2(1+\beta)/\gamma$	$(1+\sigma\cos\theta)/2$
-1	$(0+),(-0)$	2γ	2γ	$2(1-\beta)/\gamma$	$(1-\sigma\cos\theta)/2$
0	$(++),(--)$	1	1	$1/\gamma^2$	$-(\sigma\sin\theta)/\sqrt{2}$
0	(00)	$2\gamma^2+1$	$2\gamma^2$	$2/\gamma^2$	$-(\sigma\sin\theta)/\sqrt{2}$

Table 2.1: *Coefficients of the helicity amplitudes and the d-functions corresponding to equation (2.3). In the table γ is the relativistic factor $\gamma \equiv (1-\beta^2)^{-1/2}$, with β and θ as defined in the text.*

The differential cross-section as a function of the production angle θ is one of the main input variables for the study of the couplings of the vector bosons among themselves (Trilinear Gauge Couplings, TGC). For the W mass measurement it is not important, but the knowledge of this distribution does play a minor role in the analysis, providing extra information in the choice of the correct jet pairing (section 6.4, page 101). The overall angular distribution for $\sqrt{s}$ =189 GeV is shown in Figure 2.3.

The total Born cross-section has a threshold behaviour proportional to β as shown in Figure 2.4 where the 6 interference terms (from the square of the matrix element separated in the 3 terms shown in equation (2.1)) are shown separately. At high energies the individual terms diverge, but the total cross-section is well behaved, thanks to the precise Gauge cancellations prescribed by the Standard Model.

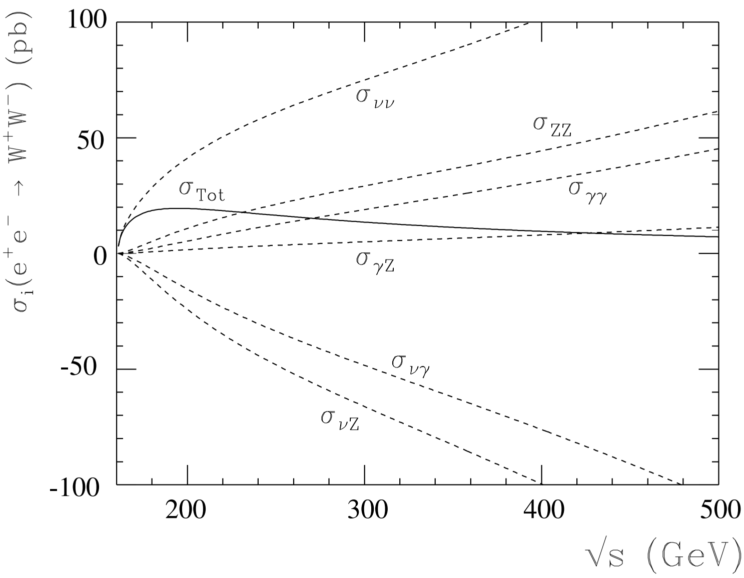

Figure 2.4: *The $e^+e^- \to W^+W^-$ production cross-section as a function of $\sqrt{s}$. The partial cross-sections corresponding to the 6 interference terms from the CC03 Born level diagrams are shown separately.*

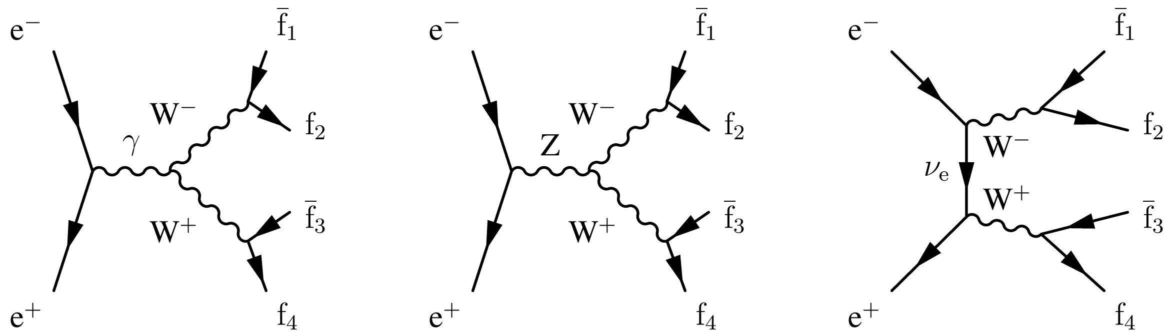

Figure 2.5: *Dominant lowest order diagrams for the process* $\mathrm{e^+e^-} \rightarrow \mathrm{W^+W^-} \rightarrow \mathrm{\bar{f}_1 f_2 \bar{f}_3 f_4}$.

2.2 Unstable W's and 4-fermion production

In the previous section the production of stable W bosons was described. In reality, however, W bosons are unstable particles whose properties are analysed only through their decay products. It is therefore important to take the whole 4-fermion production process into account and describe the W bosons as resonances with a finite width, leading to the following expression for the leading-order cross-section for off-shell $\mathrm{W^+W^-}$ production:

$$\sigma(s) = \int_0^s ds_1 \int_0^{(\sqrt{s}-\sqrt{s_1})^2} ds_2 \rho(s_1)\rho(s_2)\sigma_0(s, s_1, s_2) \tag{2.4}$$

where s_1 and s_2 are the virtualities of the two W bosons and σ_0 reduces to the on-shell Born cross-section for $s_1 = s_2 = m_\mathrm{W}^2$. The function $\rho(s)$ is described by a relativistic Breit-Wigner:

$$\rho(s) = \frac{1}{\pi} \frac{s}{(s - m_\mathrm{W}^2)^2 + m_\mathrm{W}^2 \Gamma^2(s)} \tag{2.5}$$

where $\Gamma(s)$ is given by:

$$\Gamma(s) \equiv \frac{s}{m_\mathrm{W}^2} \Gamma(m_\mathrm{W}^2), \text{ where } \Gamma(m_\mathrm{W}^2) \equiv \Gamma_\mathrm{W} \tag{2.6}$$

This definition of the Breit-Wigner function and corresponding decay width is called the 's-dependent width' or 'running width' definition. At LEP1 the Z lineshape was fitted according to this definition and the same convention is used for the presentation of LEP2 W mass results. An alternative definition, equally well motivated from a theoretical point of view, is the 'fixed width' definition:

$$\rho(s) = \frac{1}{\pi} \frac{\overline{\Gamma}}{\overline{m}} \frac{s}{(s - \overline{m}^2)^2 + \overline{m}^2 \overline{\Gamma}^2} \tag{2.7}$$

Near the pole both Breit-Wigner shapes are equivalent, provided that the mass and the width parameters satisfy the following transformation:

$$\overline{m} = m_\mathrm{W} \Big/ \sqrt{1 + \frac{\Gamma_\mathrm{W}^2}{m_\mathrm{W}^2}} \approx m_\mathrm{W} \left(1 - \frac{1}{2} \frac{\Gamma_\mathrm{W}^2}{m_\mathrm{W}^2}\right) \approx m_\mathrm{W} - 26.9\ \mathrm{MeV}/c^2 \tag{2.8}$$

$$\overline{\Gamma} = \Gamma_\mathrm{W} \Big/ \sqrt{1 + \frac{\Gamma_\mathrm{W}^2}{m_\mathrm{W}^2}} \approx \Gamma_\mathrm{W} \left(1 - \frac{1}{2} \frac{\Gamma_\mathrm{W}^2}{m_\mathrm{W}^2}\right) \approx \Gamma_\mathrm{W} - 0.7\ \mathrm{MeV}/c^2 \tag{2.9}$$

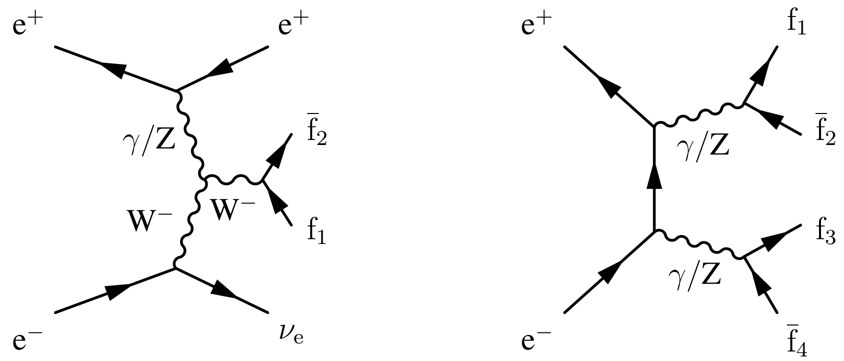

Figure 2.6: *Example of a single W production diagram (left) and a neutral current doubly-resonant ZZ process (right). These diagrams interfere with WW diagrams leading to the same 4-fermion final states.*

The width Γ_{W} is predicted by the Standard Model. At Born level, neglecting the masses of the fermions which are all small except for the top quark and the bottom quark, the width of the W boson is calculated as:

$$\Gamma_{\mathrm{W}}^{\mathrm{Born}} = \sum_{i,j} \Gamma_{\mathrm{W}f_i,f_j} = \sum_{i,j} N_C^f \frac{\alpha}{6} \frac{m_{\mathrm{W}}}{2\sin^2\theta_{\mathrm{W}}} |V_{ij}|^2 \approx \frac{3\alpha m_{\mathrm{W}}}{2\sin^2\theta_{\mathrm{W}}} \tag{2.10}$$

where the sum includes the 3 leptonic decay modes (with $N_C^f = 1$ and $|V_{ij}| = \delta_{ij}$) and all decays into quarks with $m_{f_i} + m_{f_j} < m_{\mathrm{W}}$. This excludes decay modes that contain a top quark, and therefore reduces the occurrence of bottom quarks in the decay through the small values of the CKM matrix elements $|V_{ub}| \approx 0.004$ and $|V_{cb}| \approx 0.04$ (section 1.1). With a colour factor $N_C^f = 3$ the three dominating contributions to the decay width become: $\Gamma_{\mathrm{W}1,\nu} \approx \Gamma_{\mathrm{Wu,d}} \approx \Gamma_{\mathrm{Wc,s}} \approx \frac{1}{3}\Gamma_{\mathrm{W}}$. A prediction of Γ_{W} slightly more precise than equation (2.10) is given by the improved Born approximation [30]:

$$\Gamma_{\mathrm{W}} \approx \frac{3G_{\mathrm{F}} m_{\mathrm{W}}^3}{2\pi\sqrt{2}} \left(1 + \frac{2\alpha_s(m_{\mathrm{W}}^2)}{3\pi}\right) \approx \left(\frac{m_{\mathrm{W}}}{80.35\ \mathrm{GeV}/c^2}\right)^3 \cdot 2.09\ \mathrm{GeV}/c^2 \tag{2.11}$$

with a precision better than 0.5%. This is more than accurate enough for our purposes, since the direct measurement of the W width presented here has a statistical precision of 7%.

The CC03-like 4-fermion diagrams shown in 2.5 do not form a complete subset of Feynman diagrams, since other leading order diagrams can lead to the same final state. Two examples of such diagrams that are not of the doubly-resonant form, $\mathrm{e^+e^-} \to \mathrm{W^+W^-} \to \bar{\mathrm{f}}_1\mathrm{f}_2\bar{\mathrm{f}}_3\mathrm{f}_4$, are shown in Figure 2.6. These 'single W' and ZZ diagrams contribute to (pseudo) backgrounds for the analysis presented here. To take this into account all leading order EW diagrams producing WW-type 4-fermion final states were included in the MC simulation (section 2.4). The presence of ZZ background is relevant for the W width measurement, but the effects of 4-fermion backgrounds on the W mass measurement are negligible [1].

[1]Except in the case of the $\mathrm{q\bar{q}e\nu}$ channel, where mass shifts up to 50 MeV/c^2 were observed [31].

It should be mentioned that the inclusion of the finite width of the W also has important effects for the cross-section. The behaviour near threshold becomes more smooth, and the total cross-section decreases by about 5%. These effects are of no importance for the direct W mass measurement, however.

2.3 Radiative corrections

The leading order EW diagrams discussed so far did not include any higher order corrections. In particular photonic (QED) corrections can play an important role. Corrections to be considered are: Initial State Radiation (ISR) of photons from the incoming e^+ and e^-; the exchange of virtual photons between the charged W bosons (Coulomb correction); and Final State Radiation (FSR) of photons from the 4 fermions in the final state.

The FSR photons can generally be combined with the lepton or jet they belong to, and do not play an important role in the analysis presented here. Therefore this will not be discussed further. The Coulomb correction (see Figure 2.7) can be included as a correction to the Born cross-section [32] $\approx \frac{\alpha}{v}\delta_{\mathrm{Coul}}$, where v is the relative velocity of the two W bosons. This correction becomes important near the WW production threshold where it has a singularity ($v \to 0$). The width of the W reduces the singularity at threshold to an effect of about 6% on the total cross-section, falling off with increasing $\sqrt{s}$ to about 2% at 190 GeV.

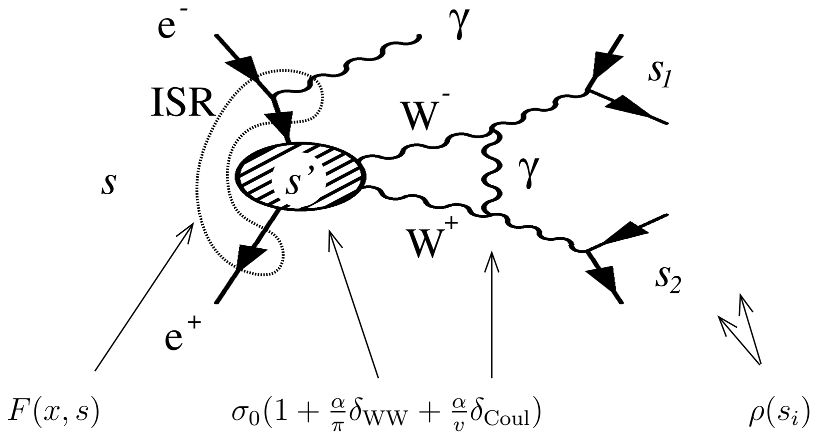

Figure 2.7: *Illustration of radiative corrections to the off-shell WW cross-section.*

Initial State Radiation

The most important correction to WW production comes from Initial State Radiation. ISR photons can carry away a significant amount of energy from the incoming electron and positron, thus reducing the effective centre-of-mass energy $\sqrt{s'}$ available for the hard scattering process. If the constraints used in the W mass measurement assume that the full centre-of-mass energy $\sqrt{s}$ is available, the reconstructed mass is shifted by

$$\Delta m \approx \langle E_\gamma \rangle m_{\mathrm{W}} / \sqrt{s} \tag{2.12}$$

where the average radiated ISR photon energy $\langle E_\gamma \rangle$ varies from 1 to 3 GeV in the $\sqrt{s}$ range from 170 to 200 GeV. To good approximation the correction due to the emission of real photons in the initial state can be written as the product of a 'radiator function' and a cross-section modified by weak corrections (by a factor $\equiv (1 + \delta_{\mathrm{WW}})$) — this is called factorisation. A convenient way to include the photonic corrections is by means of the 'structure function' formalism [28, 33]. In this method, the probability that the colliding electron (positron) has a longitudinal momentum fraction x_1 (x_2) is described by a structure function, and the leading-order cross-section for off-shell $\mathrm{W}^+\mathrm{W}^-$ production (2.4) is modified to:

$$\begin{aligned} \sigma(s) &= \int_0^s ds_1 \int_0^{(\sqrt{s}-\sqrt{s_1})^2} ds_2 \rho(s_1)\rho(s_2) \\ &\cdot \int_0^{x_{\max}} dx F(x,s)\sigma_0(s', s_1, s_2)\left(1 + \frac{\alpha}{\pi}\delta_{\mathrm{WW}} + \frac{\alpha}{v}\delta_{\mathrm{Coul}}\right) \end{aligned} \tag{2.13}$$

where x is defined by $s' = (1-x)s$ and the radiator function $F(x,s)$ is given by [32]:

$$\begin{aligned} F(x,s) &= \beta x^{\beta-1}\left[1 + \frac{3}{4}\beta - \frac{\beta^2}{24}\left(\frac{1}{3}\ln\left(\frac{s}{m_{\mathrm{e}}^2}\right) + 2\pi^2 - \frac{37}{4}\right)\right] - \beta\left(1 - \frac{x}{2}\right) \\ &+ \frac{\beta^2}{8}\left[4(2-x)\ln\left(\frac{1}{x}\right) + \frac{1+3(1-x)^2}{x}\ln\left(\frac{1}{1-x}\right) - 6 + x\right] \end{aligned} \tag{2.14}$$

with

$$\beta = \frac{2\alpha}{\pi}\left(\ln\left(\frac{s}{m_{\mathrm{e}}^2}\right) - 1\right) \tag{2.15}$$

Alternative methods to describe the ISR spectrum are the QED parton shower (QEDPS [34]) and the YFS exponentiation method [30, 35]. All these methods are able to describe the ISR spectrum with great precision, corresponding to an uncertainty of just a few MeV/c^2 on the W mass [36]. The numerical importance for the W mass depends on the beam energy via the available phase space for ISR radiation. This corresponds to the integration limit $x_{\max}$ in equation (2.13) and is graphically illustrated in Figure 2.8.

Non-factorisable $\mathcal{O}(\alpha)$ corrections

In the recent LEP200 MC workshop, however, one of the main topics of discussion was the necessity also to take non-factorisable corrections into account. Ideally one would like to take into account the complete set of $\mathcal{O}(\alpha)$ electroweak corrections. For the on-shell case the $\mathcal{O}(\alpha)$ corrections have been calculated, but for the much more complicated off-shell case this work has not been completed so far. As in WW events — contrary to Z^0 events at LEP1 — charged particles are present during the whole reaction, virtual photons can connect at all places in the diagrams, leading among others to these non-factorisable corrections. These corrections were found to be responsible for a 2% change in the predicted WW production cross-section. A possible effect of 10 MeV on the W invariant mass peak was reported in a theoretical study based on RacoonWW [27], which remains to be confirmed with a (more) realistic W mass analysis.

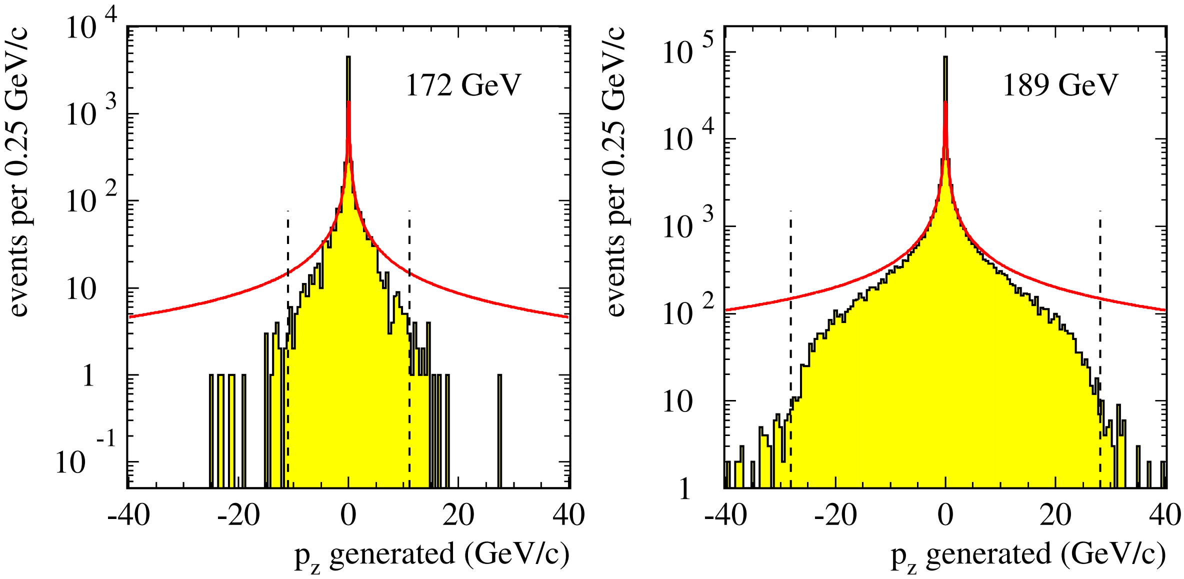

Figure 2.8: *The z momentum of the 4-fermion system due to the recoil from ISR photons as generated by PYTHIA simulation at 172 GeV (left) and EXCALIBUR simulation at 189 GeV (right). The distributions are compared to the leading term $\beta x^{\beta-1}$ from equation (2.14), indicated by the solid line. The phase space available when both W bosons are on-shell, $\sqrt{s'} > 2m_{\mathrm{W}}$, is indicated by the dashed lines.*

2.4 ElectroWeak simulation models

Models to simulate the EW physics processes described above have been implemented in different programs, which can be divided into two distinct classes:

Semi-analytical programs such as GENTLE and BBC [36] are designed to do the most precise calculations, incorporating (almost) all ideas available in the literature. They provide precise theoretical calculations of specific physics processes.

Monte-Carlo event generators are more suitable for the experimental situation. By generating events with simulated particles and typically interfaced to hadronisation packages (next section) and full detector simulation (next chapter), they enable the investigation of all experimental aspects relevant for a physics analysis. Due to the extra complications induced by the requirement to generate (large numbers of) events in a reasonable amount of computing time, these MC generators do not always reach the same theoretical precision as the semi-analytical programs. Recently, however, W-physics generators like YFSWW [26] and RacoonWW [27] have managed to include state-of-the-art theoretical knowledge in a generator.

In the analysis presented here, EXCALIBUR [28] was used as main Monte Carlo generator to simulate the 4-fermion signal (WW + ZZ). It takes all leading order 4-fermion diagrams into account. In order to treat the large number of possible diagrams and their interferences efficiently, EXCALIBUR makes use of helicity amplitude techniques which work under the assumption of massless fermions. Internally the program uses the fixed-width Breit-Wigner definition, but the standard DELPHI interface routine takes care of the transformation (2.9), ensuring that all physics results correspond to the running-width definition. For the inclusion of ISR, the default treatment in EXCALIBUR is based on the structure function approach according to (2.13), producing only collinear photons. For final states without e^+e^- pairs, however, the DELPHI implementation includes ISR with finite transverse momentum using the QEDPS [34] package.

This covers the simulation of 4 fermions (plus photons). However, for final states containing (anti-)quarks this is not the end of the story. In those events QCD plays a striking role. But it has been shown that QCD graphs, except for FSR from $\mathrm{q\bar{q}}$ pairs, do not interfere with the EW graphs to any sizeable extent, and are therefore treated separately with standard Monte Carlo QCD programs, to be discussed in the next section.

2.5 QCD phenomena and jet formation

The quark and anti-quark produced in the hadronic decay of a W boson W$\rightarrow \mathrm{q\bar{q}}$ are never observed as free particles; due to colour confinement they give rise to jets of particles observed in the detector. At high energy scales the fragmentation of the $\mathrm{q\bar{q}}$ pair into high energy partons (gluons and $\mathrm{q\bar{q}}$ pairs) is described — in principle — by *perturbative* QCD. At lower energy scales, soft gluon radiation is less well described (the *non-perturbative* phase), and has to be modelled using phenomenological models. In the last phase, the partons produced have to form stable final state particles — the hadrons, leptons and photons that can be detected in the detector, as two or more jets (per W boson). This fragmentation process is depicted in figure 2.9.

In WW events the starting configuration of the fragmentation process is well defined: a $\mathrm{q\bar{q}}$ pair with a centre-of-mass energy of $\sqrt{s_{\mathrm{q\bar{q}}}} \sim m_{\mathrm{W}}$. The probability for the radiation of a single gluon can be calculated perturbatively. The exact $\mathcal{O}(\alpha_s)$ result is given by:

$$\frac{d^2\sigma}{dx_1 dx_3} = \frac{2\alpha_s}{3\pi}\frac{x_1^2 + x_3^2}{(1-x_1)(1-x_3)} \tag{2.16}$$

where x_1 and x_3 are the energy fractions of the quark and anti-quark after emission, defined as $x_i \equiv 2E_i/\sqrt{s_{\mathrm{q\bar{q}}}}$ in the centre-of-mass system of the original $\mathrm{q\bar{q}}$ pair. A useful effective approximation, which has been used in some models and in several QCD studies [37], is given by:

$$\frac{d\sigma}{dk_T^{\mathrm{gluon}}} \sim \frac{\alpha_s(k_T^{\mathrm{gluon}})}{k_T^{\mathrm{gluon}}} \tag{2.17}$$

where the transverse momentum of the gluon k_T^{gluon} is defined with respect to the original $\mathrm{q\bar{q}}$ pair. The differential cross-section becomes infinitely large when either the gluon is collinear with one of the outgoing quarks (either x_1 or x_3 becomes 1), or the gluon momentum goes to zero (both x_1 and x_3 approach 1). In both cases k_T^{gluon} approaches zero. If the gluon is required to be well-separated — experimentally observable as a separate jet ($k_T^{\mathrm{gluon}} > y_{\mathrm{cut}}$) — the divergences can be integrated out, and the corresponding cross-section for the emission of an extra gluon

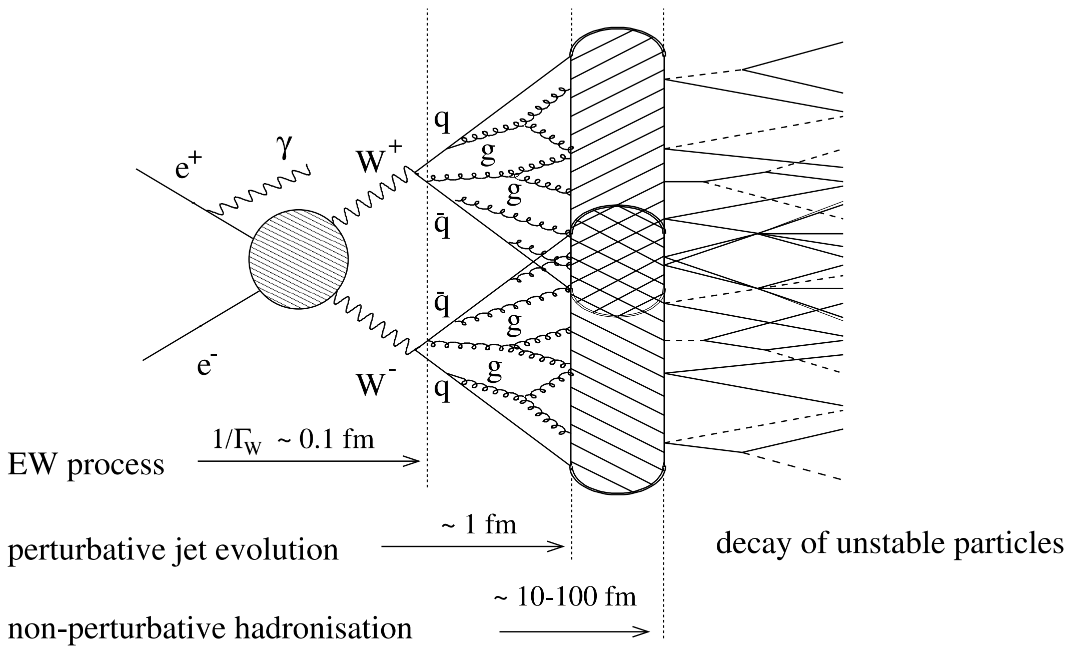

Figure 2.9: *Schematic illustration of the jet fragmentation process (see text).*

is suppressed approximately by a factor α_s. The value of α_s ranges between ≈0.1 and ≈0.3 depending on the transverse momentum scale of the gluon. With two W bosons the probability to see an extra jet doubles, leading to a sizeable fraction of 5-jet WW events. Indeed in 30% - 50% of the events at least one extra jet is seen, depending on the jet resolution $y_{\rm cut}$ chosen (section 5.4.3, Figure 5.7). Examples of such multi-jet events are shown and will be discussed later; e.g. in pictures 3.9 and 4.1.

The subsequent radiation of additional gluons down to the typical scale of hadrons (~ 1 GeV), cannot be calculated exactly using perturbative QCD. Instead one has to rely on phenomenological models, implemented in Monte Carlo programs. Fortunately these models have been tested and tuned with great precision exploiting the 4 million hadronic Z^0 events (per experiment) produced at LEP1. Only a fraction of the tuned parameters have real physical meaning. So to a certain extent these models can be regarded as 'templates', which through optimization on Z^0 data have come to reproduce the Z^0 decays to a high precision. It is important to stress that the models are built in such a way that they are able to predict the evolution from the scale of the Z^0 (91.2 GeV) to the W (80.4 GeV) with very high and reliable precision. The Monte Carlo programs used deal with the jet formation in the following three stages (as illustrated in Figure 2.9):

1. To describe the perturbative emission of high energy gluons JETSET [38], ARIADNE [39] and HERWIG [40] implement a Parton Shower (PS) approach. They all apply the dipole formula (2.16) for the emission of the first (i.e. highest k_T) gluon. In ARIADNE the emission continues according to the dipole formula (with analogous expressions for the emission from qg and gg dipoles), while in the other programs the Parton Shower is based on repetitive emission from single partons: $\mathrm{q} \to \mathrm{q}g$, $g \to \mathrm{q}\bar{\mathrm{q}}$, and $g \to gg$. The Colour Dipole

Model (CDM) approach used in ARIADNE is formulated in terms of Lorentz invariants and reproduces the experimentally observed angular ordering of gluons in a natural way. The other programs have to add the angular ordering conditions 'by hand' in order to avoid considerable double-counting and emission of too many gluons. These MC programs do not only cover the parton evolution but also the competing FSR from quarks and anti-quarks. Since $\alpha_{\rm s} > \alpha_{\rm QED}$, it effectively means that the QED FSR is suppressed. The final effect of this feature is very small, because the final jet properties are not very sensitive to the type of radiation responsible for the parton shower.

2. Several different models exist to describe the non-perturbative phase. The JETSET program uses the Lund string model, where the partons produced in the perturbative Parton Shower are connected by colour strings. When this string breaks up, hadrons are formed with a width of the momentum distribution transverse to the string direction of the order of 0.3 GeV/c. Numerous tunable parameters ensure that a good description of the data can be obtained. The colour dipoles produced by ARIADNE are also interfaced to the Lund string model.

   Another approach, employed by the HERWIG MC program, is the cluster fragmentation model. In this model the remaining gluons are made to decay into $\rm q\bar{q}$ pairs, which form colourless clusters of different masses. Depending on their mass these clusters can decay into clusters of smaller mass or directly into hadrons. Both the string model and the cluster fragmentation model are well able to reproduce most of the available experimental data.

3. Finally resonances and particles that have been produced, if unstable, decay into stable particles. Here decay tables are used that contain masses, branching ratios, quantum numbers etc. of the particles.

The program used in the main analysis to describe the jet fragmentation is JETSET 7.409 with PS, tuned with $\rm Z^0$ events from DELPHI LEP1 data [41]. The DELPHI-tuned HERWIG fragmentation and ARIADNE CDM approaches have been considered as well, to study possible systematic effects.

2.6 QCD background

Not only WW signal, but also background can have 4 jets. In fact the most significant irreducible background for the WW signal in the $\rm q\bar{q}q\bar{q}$ channel is formed by $\rm e^+e^- \rightarrow Z(\gamma) \rightarrow q\bar{q}gg(\gamma)$, where the hadronic decay of the Z boson obtains a ($\geq$)4-jet signature due to the radiation of two high k_T final state gluons. The $\rm q\bar{q}\gamma$ cross-section, with σ $\approx$100 pb, is more than 10 times larger than the $\rm q\bar{q}q\bar{q}$ cross-section (Figure 2.1). However, the requirement that two hard gluons be radiated supresses this background by two orders in $\alpha_{\rm s}$. In practice about 1/50 of the total $\rm q\bar{q}\gamma$ cross-section is selected in the $\rm q\bar{q}q\bar{q}$ channel. The corresponding O($\alpha_{\rm s}^2$) matrix elements have been calculated, but in this analysis the QCD background was simulated using PYTHIA 5.722 + JETSET 7.409 with PS, with an estimated uncertainty of about 5% on the 4-jet rate in terms of the accepted cross-section.

Fortunately the influence of such processes on the W mass measurement is small. The effect of the uncertainty in cross-section and possible deviations in differential distributions ('shape') are taken into account in the systematics studies in chapter 7.

2.7 Final State Interference phenomena

One aspect of the fragmentation models that cannot be tested and tuned on Z^0 events is the possible final state cross-talk between the two W systems. In the $\mathrm{q\bar{q}q\bar{q}}$ channel the two decaying hadronic systems can have a significant space-time overlap, since the distance between the decay vertices ($1/\Gamma_\mathrm{W} \sim 0.1$ fm) is much smaller than the typical hadronisation size of 1-10 fm. This means that cross-talk between the two decaying hadronic systems cannot be excluded. The precise mechanism and significance of these effects, however, is largely unknown. In that respect LEP2 provides a beautiful laboratory to study the interaction of two super-imposed hadronising systems in a clean environment.

The two final state cross-talk phenomena of interest are Bose-Einstein Correlations and Colour Reconnection. Their physics background and possible effect on the W mass measurement will be discussed in the following.

Bose-Einstein Correlations

Correlations within pairs or multiplets of identical bosons in the final state are a well-known quantum-mechanical phenomenon. In astronomy, it is known as the Hanbury Brown-Twiss (HBT) effect for incoherent emission of photons (e.g. from stars). The analogous effect has been observed in hadronic, heavy ion and $\mathrm{e^+e^-}$ collisions. However, in most observations except for the heavy-ion collisions, source sizes of ≈ 1 fm are seen, which appears (too) small compared to the event size at the time of hadron formation (typically several fm).

An alternative model, in the framework of the Lund string model, was proposed by Andersson and Ringnér [42]. In this model the correlations follow as a coherent effect related to the symmetrisation of the quantum-mechanical amplitude for particle production from the Lund string. Its predictions are in agreement with the expected source size and correlation strength seen in Z^0 events. A fundamental prediction of the model is that only bosons from the same string are subjected to BEC, which means that this type of BEC does not lead to cross-talk between W bosons, unless Colour Reconnection happens at parton level.

Experimentally the correlations can be observed by investigating two-particle correlations between like-sign pions. By comparing the correlations in $\mathrm{q\bar{q}q\bar{q}}$ events with the correlations in a reference sample of mixed $\mathrm{q\bar{q}l}\nu$ events, a model-independent measurement can be performed. Recent results from all four LEP experiments show that the correlations between W bosons are strongly suppressed compared to correlations within W (or Z^0) bosons. In fact no evidence for correlations between W's is seen at all [43]. This could be an indication in favour of the coherent scenario.

This means that BEC from different W bosons might come only from the incoherent HBT effect, which occurs at a larger length scale. Therefore the effect on the mass measurement is expected to be small. Unfortunately the coherent BE model has not yet been implemented in a MC generator. The other models available are not based on quantummechanics, but implement in various ways the enhancement of identical bosons that form pairs close in phase space. Such effects could change the way the decay products of the W bosons are mixed in the jet reconstruction, and thus affect the W mass measurement. This will be addressed in more detail in chapter 7.

Colour Reconnection

Cross-talk via the strong interaction is known as Colour Reconnection (CR). The effect is expected to enhance particle production in phase space regions 'outside' the EW W bosons, and reduce it inside the W boson domains. This would actually change the invariant mass of the decay systems of the supposed W bosons. As mentioned already QCD does not provide a well-defined description of this effect, but several observations can be made:

Perturbative QCD: Since the W bosons are typically separated by a distance $1/\Gamma_{\mathrm{W}}$ at the time of decay, only virtual gluons with an energy less than Γ_{W} can participate in the cross-talk. For the leading perturbative CR the exchange of two colour-matched gluons is required, giving an additional suppression factor of $\alpha_{\mathrm{s}}^2/(N_{\mathrm{C}}^2\text{-}1)$, where $N_{\mathrm{C}} = 3$ is the number of colours in QCD. Therefore the effect from CR in the perturbative phase is expected to be small and indeed calculations have shown that the consequence for the measurement of the W mass is below 5 MeV/c^2 [44].

Non-perturbative QCD: Hadronisation at distance scales $\sim$ 1 fm is not independent. Coherent gluon emission from both hadronic systems is to be expected, leading to final state interference. To study CR effects in the non-perturbative phase, one has to rely on the available phenomenological models. These models are not directly based on first principles, but implement CR in a semi-classical way inside existing fragmentation models (JETSET, HERWIG and ARIADNE all have a built-in CR option).

As mentioned already, LEP2 provides interesting data for dedicated studies of Colour Reconnection effects themselves. These studies are ongoing [45], and will hopefully lead to an improved understanding of the physics, and give constraints on the models to be used.

Possible effect of cross-talk on the W mass measurement

More details about the different phenomenological models and experimental constraints will be presented in chapter 7, together with their predicted effects on the W mass measurement. In principle all predictions and models that have not been proven to be wrong are taken seriously. The effects of BEC appear to be less severe than CR. In both cases our understanding of the models and the experimental measurements of the effect is improving, but currently they still constitute major contributions to the systematic uncertainty in the $\mathrm{q\bar{q}q\bar{q}}$ channel.

Chapter 3

Experimental set-up

3.1 The LEP collider

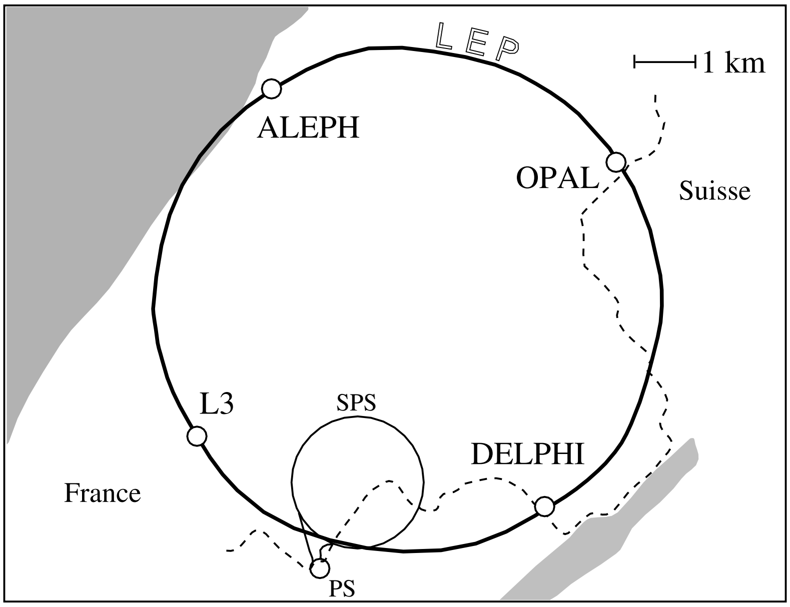

Figure 3.1: *Schematic view of the CERN site at the border between Switzerland and France, situated between the Jura mountains and the Geneva airport (shaded in grey).*

The Large Electron Positron (LEP) collider was built and operated by the European Organisation for Nuclear Research (CERN) in Geneva; its geographical location is shown in Figure 3.1. The electrons and positrons are produced and accelerated in a chain of accelerators before being injected into the LEP main ring, illustrated in Figure 3.2. First of all the LEP Injector Linacs (LIL) produce electrons and positrons and accelerate them to 600 MeV. The Electron Positron Accumulator collects the electrons and positrons in bunches which are accelerated to 3.5 GeV in the Proton Synchrotron (PS). Before injecting the bunches into the LEP main ring, the Super Proton Synchrotron (SPS) accelerates them to 22 GeV. The electrons and positrons are collected in four

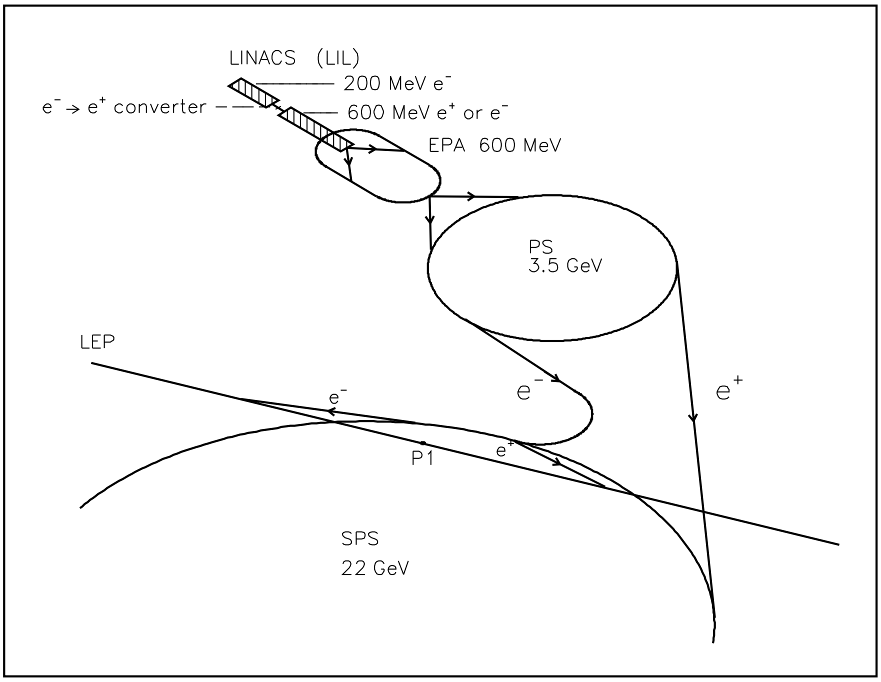

Figure 3.2: *Schematic drawing of the LEP* e^+e^- *injection and accelerator set-up.*

bunches inside LEP, increasing their number until the maximum beam current is reached. Then the LEP RF voltages are increased, accelerating the electrons and positrons to physics energies. When the beam reaches stable conditions at the correct energy, the superconducting quadrupole magnets a few metres away from the interaction points focus the beams in the interaction region. As soon as 'colliding beams' settings are declared, the collaborations ramp up the voltages of their detectors and start recording data of the physics processes that occur each time an e^- and e^+ collide. A 'fill' of electrons and positrons can typically be kept inside LEP for several hours until the beam is dumped and the whole procedure is repeated from the beginning.

The LEP ring is located in an almost circular tunnel, on average 100 m below the surface. In eight regions the tunnel is straight over a distance of a few hundred metres. In four of these straight sections, large underground halls house the detectors that are operated by the 4 LEP collaborations: ALEPH, DELPHI, L3 and OPAL. The particles travel inside a vacuum pipe, surrounded by magnets to keep them in their orbit and radio frequency (RF) cavities to accelerate them. During the first years (LEP1) copper cavities were used, allowing centre-of-mass energies around the Z^0 peak, while during the LEP2 phase superconducting cavities were installed every year, reaching centre-of-mass energies up to 209 GeV in 2000 — the final year of LEP running. The RF cavities are needed not only for acceleration, but also to continuously replenish the energy that is lost 'in orbit' due to the synchrotron radiation emitted by the electrons and positrons moving through the LEP magnetic field. The radiated power for a relativistic particle is given by

$$P_{\mathrm{radiated}} = \frac{q^2 c}{6\pi\epsilon_0} \frac{\gamma^4 \beta^4}{\rho^2} \tag{3.1}$$

where $\gamma = E_{\mathrm{beam}}/m_e$, q denotes the charge of the particle and ρ is the local bending radius.

The velocity of the electrons and positrons in the LEP beam is very close to the speed of light, $\beta \equiv v/c \approx 1$, and assuming that the local bending radius inside all magnets is constant the energy loss is equal to:

$$E_{\text{loss}} = 8.85 \times 10^{-5} \frac{E^4_{\text{beam}}}{\rho} \text{ MeV (per turn)} \tag{3.2}$$

where E_{beam} is given in GeV and ρ in km. This corresponds to ≈ 2 GeV per turn at $\sqrt{s} = 200$ GeV. The accelerating RF cavities are located in the straight sections while the bending field is concentrated in the arc sections, so the energy of the particles is not constant along the circumference of LEP, but shows a saw-tooth like dependence with variations in energy of about $E_{\text{loss}}/4 \sim 600$ MeV. Such variations in energy can be monitored and have been accurately modelled. The results of a simulation are shown in Figure 3.3.

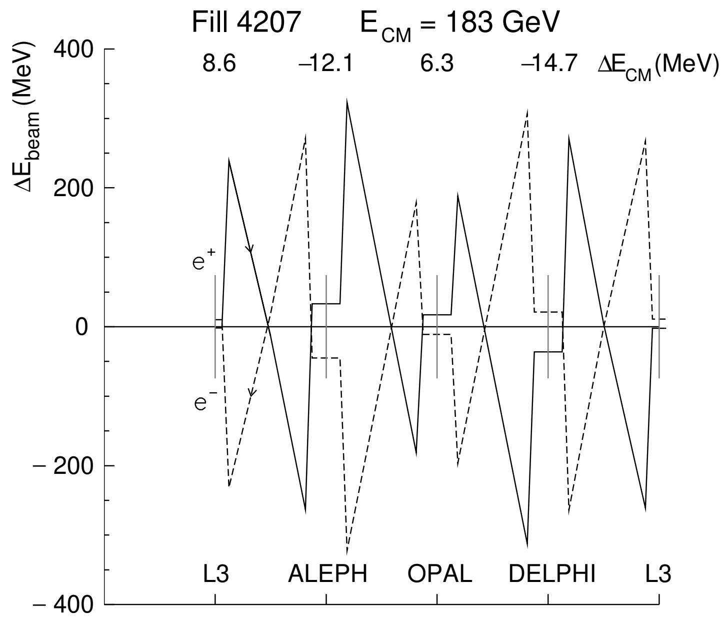

Figure 3.3: *The energy 'saw-tooth' (see text) for a typical RF configuration at a centre-of-mass energy of 183 GeV. The variations in energy are shown separately for the electron beam (dotted line) and positron beam (solid line).* $\Delta E = 0$ *corresponds to the average LEP energy [46] for this fill.*

LEP beam energy model

A precise knowledge of the LEP energy scale is of crucial importance for the W mass (and Z mass) measurements because the centre-of-mass energy is used in the analyses to set the mass scale. Hence the relative variations of energy along the circumference of LEP (or at least in the Interaction Points (IP) where the experiments are situated) and as a function of time have to be understood with an MeV-level precision, two or three orders of magnitude better than the amplitude of the energy variation discussed above. Furthermore the absolute scale has to be calibrated with similar accuracy.

The LEP Beam Energy Model describes all relative variations in energy taking into account the precise RF and magnet configuration at all times. Additionally it includes small corrections in order to reach a systematic precision better than 2 MeV at the Z^0 peak [10]. An example of the kind of effects which need to be taken into account is the gravitational pull of the Moon and Sun distorting the Earth's crust and thereby periodically changing the circumference of the LEP ring by approximately ± 0.5 mm. In Figure 3.4 the measured effect on the LEP beam energy is compared to the prediction from a geological model.

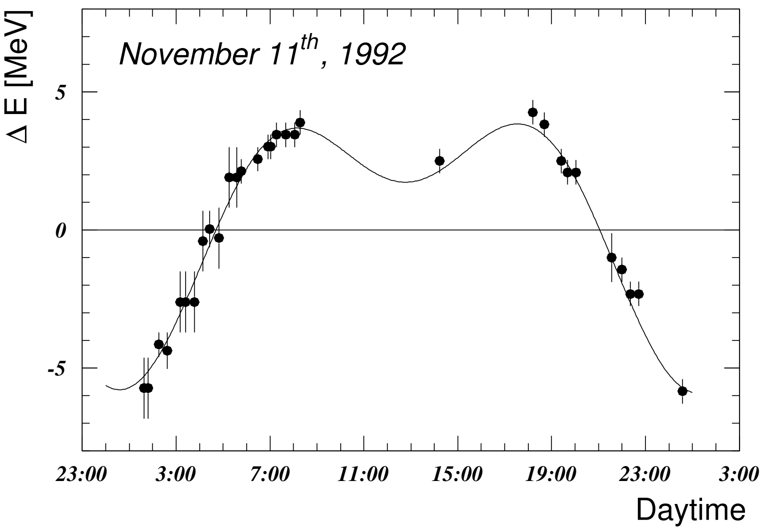

Figure 3.4: *The shift of the LEP beam energy during a full Moon tide. The measured energy is compared to the prediction from a geological model [47].*

Resonant Depolarisation

The calibration of the absolute energy scale is based on the method of Resonant De-Polarisation (RDP). The emission of synchrotron radiation leads to the build-up of transverse beam polarisation in $\mathrm{e}^+\mathrm{e}^-$ storage rings. Application of a small RF magnetic field perpendicular to the LEP bending field will rotate the spins of the electrons in the beam, and destroy the polarisation, provided the applied RF frequency matches the natural spin precession frequency which is proportional to the beam energy:

$$\nu = \frac{g_\mathrm{e} - 2}{2} \frac{E_\mathrm{beam}}{m_\mathrm{e} c^2} \tag{3.3}$$

where $(g_\mathrm{e} - 2)/2$ is the electron anomalous magnetic moment and m_e is its mass. Using this method a precision better than 1 MeV has been achieved.

Energy calibration at LEP2

Unfortunately, for beam energies at LEP2 a direct calibration using the RDP technique is not possible, because at energies above 60 GeV transverse polarisation does not build up (due to the increased beam energy spread). Instead, one has to rely on magnetic extrapolation. In 1997 sixteen Nuclear Magnetic Resonance (NMR) probes were installed in the arc sections of LEP to continuously monitor the local magnetic bending fields. These probes were calibrated with RDP energy measurements in the region between 41 and 61 GeV, and were then used to determine the beam energy during physics conditions by means of a linear extrapolation. A similar magnetic extrapolation can be done using the flux loop system that is installed in the LEP dipole magnets, covering 96.5% of the total bending field. This measures the change of the bending field through magnetic induction during magnet cycling. A comparison of these two methods showed a difference of about 10-15 MeV for a beam energy of 94.5 GeV. This extrapolation uncertainty constitutes the largest contribution to the systematic error quoted by the LEP energy working group. Numerous other possible sources of systematics have been studied and are taken into account. For illustrative purposes the complete list of error contributions is shown in Table 3.1; a precise description can be found in [46].

Source	Error [MeV]			Correlation
	1997	1998	1999	
Extrapolation from NMR–polarisation:				
NMR rms/$\sqrt{N}$ at physics energy	10	8	11	100%
Variations from calibration procedure	5	4	3	0%
Flux-loop test of extrapolation:				
NMR flux-loop difference at physics energy	20	15	15	100%
Field not measured by flux loop	5	5	5	100%
Polarisation systematic	1	1	1	100%
e^+e^- energy difference	2	2	2	100%
Optics difference	4	6	4	50%
Corrector effects	3	4	2	50%
Tide	1	1	1	100%
Initial dipole energy	2	1	1	0%
Dipole rise modelling	1	1	1	100%
IP specific corrections ($\delta E_{\mathrm{CM}}/2$):				
RF model	4	4	5	100%
Dispersion	1	1	1	50%
Total	25	20	21	

Table 3.1: *List of contributions to uncertainty on the LEP beam energy calibration [46].*

In order to reduce this significant systematic uncertainty, the LEP Energy Working Group has been working on alternative methods to cross-check the energy extrapolation:

- The LEP spectrometer project:
  In 1998 one of the LEP dipole magnets was replaced by a high quality steel dipole with a particularly well known magnetic field, with two arms of high precision beam position monitors as shown in Figure 3.5. By measuring very precisely the direction of the beam before and after the magnet, the beam energy E_{beam} can be derived from the bending angle θ via the relation
  $$\theta \propto \frac{\int B\mathrm{d}s}{E_{\mathrm{beam}}} \tag{3.4}$$
  where $\int B\mathrm{d}s$ is the integral over the magnetic field. When the ongoing study of systematic effects is finished, the aim is to achieve an uncertainty on the beam energy of 10-15 MeV at physics energies, which can be extrapolated back in time to improve the energy calibration during the whole LEP2 program.

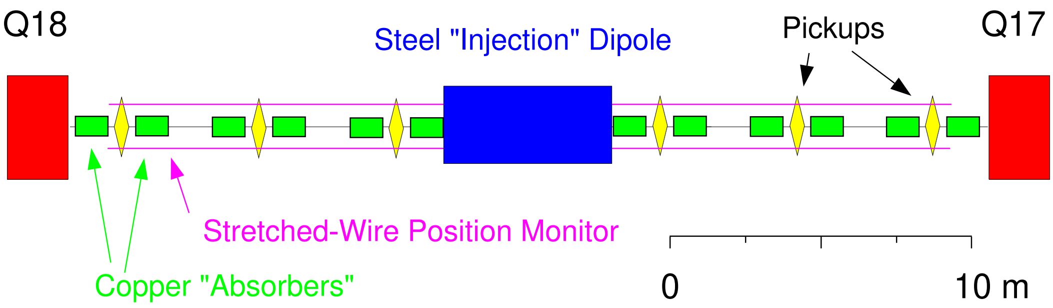

Figure 3.5: *Layout of the LEP spectrometer set-up*

- Energy determination based on energy loss measurements:
  A complementary approach to high energy calibration is to use observables that are sensitive to the energy loss per turn. As this energy loss is proportional to E^4_{beam}, a suitable observable would be very sensitive to the physics energy scale. One of the most promising observables turns out to be the synchrotron tune Q_s, defined as the ratio between the synchrotron oscillation frequency Ω and the revolution frequency of particles in LEP:
  $$Q_s \equiv \frac{\Omega}{\omega_{\mathrm{rev}}} \tag{3.5}$$
  The revolution frequency is fixed (11.249 kHz), while Ω depends on the settings of the accelerator. Among other parameters, Ω depends to first approximation on the amplitude of the effective total RF cavity voltage V_{RF}, with the following dependence:
  $$Q_s^2 \propto \frac{1}{E_{\mathrm{beam}}}\sqrt{e^2V^2_{\mathrm{RF}} - E^2_{\mathrm{loss}}} \tag{3.6}$$
  By fitting the measured Q_s as a function of V_{RF} the beam energy scale can be extracted. Work in progress indicates that the systematics of this measurement (using a more refined model) can be controlled to the level of 15 MeV.

- Experimental determination:
  Experiments have used events containing a radiative return to the Z resonance ($e^+e^- \rightarrow Z\gamma \rightarrow f\bar{f}\gamma$), where the ISR photon escaped undetected along the beam, to reconstruct the Z boson mass using the beam energy as constraint. Comparing the newly measured m_Z with the precise measurement performed at LEP1, an extra cross-check on the extrapolation is obtained [48]. It is still uncertain whether measurements of this type will yield results of sufficient precision.

It is hoped that the ongoing evaluation of these independent cross-checks will reduce the final uncertainty on the extrapolation from the lower energy, where RDP calibration is possible, to LEP2 energy scales. The currently quoted error on the LEP beam energy is one of the major contributions to the systematic uncertainty on the W mass measurement, as will be discussed in more detail in chapter 7.

Energy Spread

The energy calibration described above determines the average energy of the beam. From event to event, however, the actual e^+e^- centre-of-mass energy $\sqrt{s} = 2 \cdot E_{\mathrm{beam}}$ shows a statistical random variation due to the natural energy spread σ_E of electrons and positrons in the beam. This spread can be predicted for certain settings of the beam optics, energy and RF frequency shift, or derived from the longitudinal size of the interaction region σ_z^{IP} that can be measured by the experiments, via the relation

$$\frac{\sigma_E}{E_{\mathrm{beam}}} \propto \omega_{\mathrm{rev}} Q_s \sigma_z^{\mathrm{IP}} \tag{3.7}$$

This corresponds to a typical spread in $\sqrt{s}$ of the order of 200 MeV. More detailed numbers are given in section 7.2 where also the consequences for the W mass and width measurement are discussed. Due to its statistical nature the spread is not worrying for the mass measurement, but its potential bias on the width measurement has to be considered.

Luminosity

Another important collider parameter is the luminosity. The instantaneous luminosity is related to the number of particles that cross the collision region per unit of (transverse) area per second. The event rate $\dot{N}$ of a physical process with a cross-section σ_{proc} is proportional to the luminosity $\mathcal{L}$:

$$\dot{N} = \mathcal{L} \cdot \sigma_{\mathrm{proc}} \tag{3.8}$$

The number of events available for physics analysis is therefore determined by the luminosity, integrated over the period of data taking:

$$\int_{\Delta t} \mathcal{L} \mathrm{d}t = \frac{N}{\sigma_{\mathrm{proc}}} \tag{3.9}$$

As the cross-sections for typical processes studied at LEP are usually expressed in pb (where 10^{12} pb $= 1$ b $\equiv 10^{-28}$ m^2), the integrated luminosity is often quoted in units of inverse cross-section such as pb^{-1}. A high integrated luminosity is desirable to obtain the best statistical precision on a measurement or increase the reach of a particle search. LEP has surpassed all expectations by delivering ≈ 800 pb^{-1} of integrated luminosity to each of the LEP experiments during the LEP2 program, where the original aim was 500 pb^{-1} per experiment. The most precise determination of the luminosity at LEP was obtained by measuring the rate of small angle Bhabha scattering ($e^+e^- \rightarrow e^+e^-$) events, for which the cross-section is high and accurately known, using a detector with well-defined geometrical acceptance (the STIC in the case of DELPHI, see page 42). The precise knowledge of the integrated luminosity does not play an essential role in the analysis presented in this thesis.

3.2 The DELPHI detector

The DELPHI (DEtector with Lepton, Photon and Hadron Identification) detector was designed as a general purpose detector with coverage of almost the full 4π solid angle. An overview of the detector and its sub-systems is shown in Figure 3.7. The detector consists of a cylindrical 'barrel' part and two end-caps covering 'forward' regions (only one of which is shown in Figure 3.7). Both the diameter and overall length of the detector are about 10 m, and the design is symmetrical in the $z = 0$ plane, with the coordinate system as defined in Figure 3.6.

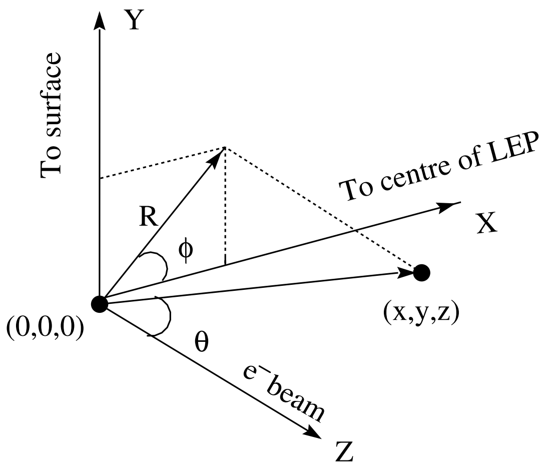

Figure 3.6: *In the standard DELPHI coordinate system, the origin is the nominal interaction point, which coincides with the geometrical center of the detector. The z axis points along the flight direction of the beam electrons, the x axis in the horizontal plane towards the centre of LEP, and the y axis points upwards. Cylindrical coordinates (R,ϕ,θ) are defined with respect to the Cartesian system in the usual way.*

In the design of DELPHI special emphasis was put on charged particle identification. In particular the Ring Imaging CHerenkov (RICH) detectors provide particle identification capabilities unique among the 4 LEP experiments. Also the high precision silicon Vertex Detector provides excellent identification of b-quark jets through secondary vertex reconstruction. However, the analysis presented here did not exploit DELPHI's extended particle identification capabilities. In the fully hadronic channel, b-tagging is used in the event selection, but it does not play an essential role. The information from the RICH detectors is not used at all in this analysis.

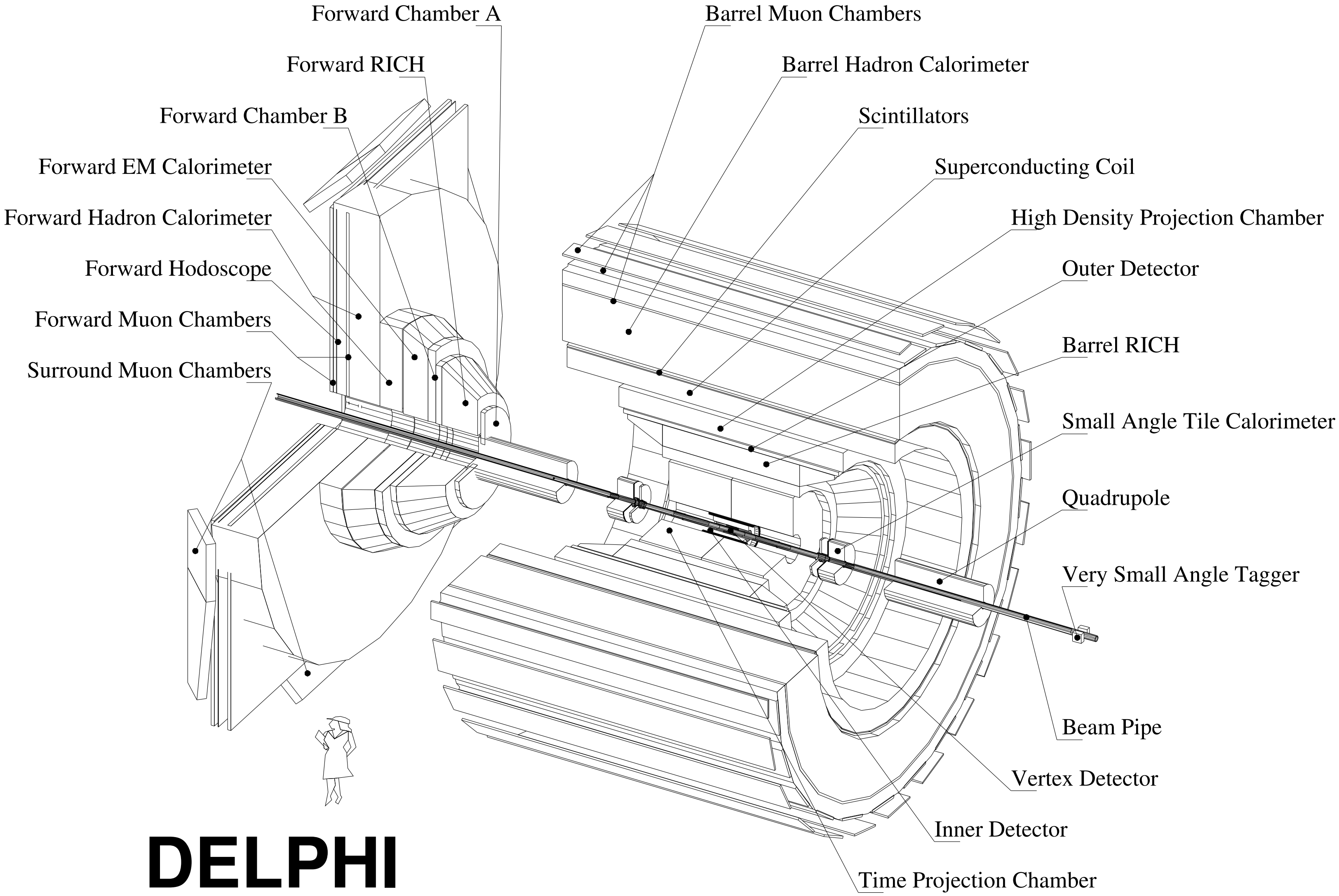

Figure 3.7: *Overview of the DELPHI detector .* .

The W mass measurement relies mainly on the reconstruction of jets and identification of occasional isolated (ISR) photons. In the $\mathrm{q\bar{q}l}\nu$ channel also the measurement of isolated high-momentum leptons is needed. These functions all rely on tracking (for the detection of charged particles) and calorimetry (for the detection of both charged and neutral particles):

Tracking: The DELPHI tracking system in the barrel region consists of four detectors at different radii centered at the beam axis. They are surrounded by a superconducting solenoidal coil with an inner diameter of 5.2 m and a length of 7.5 m providing a homogeneous magnetic field of 1.23 Tesla aligned along the z axis. The bending radius of charged particle tracks in the magnetic field as recorded by the DELPHI tracking detectors can thus be used to measure the momentum/charge ratio of the corresponding particle. The system consists of the Vertex Detector (VD), Inner Detector (ID), Time Projection Chamber (TPC) and the Outer Detector (OD). Out of these detectors the main tracking device is the TPC, which is able to reconstruct 3D tracks with good resolution over a large volume.

The inclusion of the RICH system inside the tracking volume limited the volume available for other tracking systems, in particular the TPC. Hence, in order to have precise tracking with adequate lever arm for the precise reconstruction of high momentum tracks, an additional layer of tracking (i.e. the Outer Detector) was included outside the RICH but still inside the solenoid magnetic field.

Also in the forward regions ($11^\circ \leq \theta \leq 33^\circ$ and $147^\circ \leq \theta \leq 169^\circ$) a tracking detector is placed before (Forward Chambers A, FCA) and just after (Forward Chambers B, FCB) the Forward RICH. The outer layer of DELPHI consists of the Barrel, Forward and Surround muon chambers (MUB, MUF and SMC).

Calorimetry: The DELPHI electromagnetic calorimeters are the High density Projection Chamber (HPC) located in the barrel on the inside of the solenoid, and the lead-glass Forward ElectroMagnetic Calorimeter (FEMC) in the end-caps. The Hadron Calorimeter (HAC) is an iron-gas sampling calorimeter integrated in the iron return yoke of the solenoid, covering the whole polar angle between 10° and 170°. On both sides of the interaction region, about 2 m away, the Small angle Tile Calorimeter (STIC) encloses the beam-pipe, covering the polar angle regions between about w° and 10°. This electromagnetic calorimeter is also used for the luminosity measurements based on small angle Bhabha scattering.

More details about the DELPHI sub-detectors can be found in [49]. Here we concentrate on the aspects most relevant to the W mass measurement. After a brief overview of some further points concerning the DELPHI data processing in the next paragraph, section 3.4 concentrates on the reconstruction of muons, electrons and photons. A separate section 3.5 is dedicated to the reconstruction of jets and energyflow, which play a dominant role in the W mass measurement.

3.3 Trigger, data stream and simulation

The DELPHI trigger system consists of four levels. The first two levels are fully electronic and synchronised with the beam crossing (every 22 μs), making their trigger decision within 3.5 μs and 40 μs respectively. The third and fourth levels are slower (software based) and asynchronous with the beam. The trigger efficiency for semi-leptonic and fully hadronic WW events selected by the analysis is practically 100% with respect to the efficiency for the Bhabha events used to define the integrated luminosity.

Online system For all events passing the trigger, the DELPHI data acquisition system collects the raw digitized data from the event buffers from each of the sub-detector systems. The data is written to disk and then stored on magnetic tape for later analysis. Information about the status of the subdetectors and LEP, calibration constants relevant for data reconstruction, or other specific conditions at a given moment are kept in a database.

Offline system The DELPHI reconstruction program DELANA [50] reconstructs particles by applying pattern recognition and track fitting to combine information from different sub-detectors. It also uses the information stored in the database. Some particle identification is done already at this stage and a basic event classification is performed. The output from DELANA is stored on magnetic Data Summary Tapes (DST), from where it is available for physics analysis.

The analysis presented here relied on the standard DELPHI software packages PHDST [51] for reading data from the DST, SKELANA [52] providing a convenient analysis framework and WWANA [53] for its routines aimed at the identification of isolated leptons in W pair events.

Alternatively, the working of the DELPHI detector can be simulated using the DELphi SIMulation program DELSIM [54]. Applied to simulated particles produced by a Monte Carlo generator this package simulates the detailed response of the DELPHI detector to the particles traversing the detector, taking granularity, resolution and efficiencies of the detector into account. The output of DELSIM is in raw data format, to be analysed further by DELANA in an identical manner to the real data.

3.4 Reconstruction of leptons and photons

In this section a short description is given of the standard tools used for the identification of leptons in the $\mathrm{q\bar{q}l}\nu$ channel and of isolated (ISR) photons:

electrons and photons are identified and distinguished using the REMCLU (Reconstruction of ElectroMagnetic CLUsters) software package [55]: electrons are identified as a track in the central tracking chamber whose extrapolation points to a shower in the electromagnetic calorimeter, without associated activity in the hadron calorimeter. The ratio of the shower energy E and the measured track momentum p is expected to be close to 1 (compared to $E/p < 0.05$ for muons), and the REMCLU package makes an empirical combination of the two to obtain a best estimate of the electron energy, with a resolution between $\approx 5\%$ and

$\approx 15\%$, depending on the electron energy and the polar angle. Both the identification and the energy resolution are hampered by interactions that electrons can have before reaching the calorimeters, especially in the forward region.

Photons are also treated by REMCLU, being identified as electromagnetic clusters without an associated track. Complications arise from photon conversion into e^+e^- pairs before the calorimeter. About 40% of all photons convert before reaching the HPC, including about 7% even before reaching the TPC, thus creating visible tracks.

muons can be identified with excellent efficiency by their minimum ionising signature in the calorimeters, complemented with at least one hit in the muon chambers. Their momentum can be measured with a good resolution of about 3% in the momentum range of interest (20 - 70 GeV/c).

taus decay before reaching the detector, producing at least one additional neutrino. As the neutrino cannot be detected only the direction of the momentum can be determined with reasonable precision; not its magnitude. Therefore the contribution of the tau lepton to the reconstruction of the invariant mass of the W bosons is negligible. However, for the selection of $\mathrm{q\bar{q}}\tau\nu$ events the identification of the tau is essential. Besides that, especially for decay modes with more than one visible particle in the tau final state, it is crucial to distinguish and separate the decay products of the tau from the hadronic decay of the other W boson. For the $\mathrm{q\bar{q}l}\nu$ study the standard WWANA tau treatment was used, basically identifying the tau lepton as the lowest multiplicity jet in a 3-jet configuration.

3.5 Reconstruction of jets: energyflow

The reconstruction of jets plays a dominant role both in the $\mathrm{q\bar{q}q\bar{q}}$ and the $\mathrm{q\bar{q}l}\nu$ channel. As jets contain both neutral and charged particles, a combination of tracking and calorimetry is needed for the optimal measurement of the jet energy and direction. Typically the particles inside a jet are close to each other in the detector, which further complicates the reconstruction. The detector response for different types of particles can briefly be summarised as follows:

- Neutrinos escape without detection;

- Charged particles are generally measured with excellent efficiency and good momentum resolution. The momentum resolution can be estimated on a particle-by-particle basis from the track fit using the known resolution of the different sub-detectors involved;

- Neutral hadrons and photons are generally reconstructed on the basis of calorimetric information only. The resolution on the measured energy has to be estimated on a statistical basis, and is typically significantly worse than the resolution for charged particles. The vicinity of other (charged) particles inside jets further complicates the association of the measured showers to the corresponding particle.

Sources of energyflow mis-reconstruction

The ability of the detector to correctly reconstruct the energy and direction of jets will from now on be called 'energyflow' response.

The overall jet 4-momentum is determined simply as the sum of the 4-momenta of the particles. The errors on the momenta of individual particles are not taken into account, since preliminary studies using such an approach did not show a clear improvement. The underlying reason is that the effect of the measurement resolution of correctly measured particles is small compared to the uncertainty induced by particles that are mis-reconstructed or not reconstructed at all.

Instead a simple parameterisation of the jet energy resolution can be extracted from the data (see next paragraph) and used to estimate the average jet energy resolution as a function of the jet direction (see the left hand plot in Figure 3.8, and section 4.2).

DELPHI energyflow

The energyflow resolution and efficiency vary depending on the direction of the jet, because the detector is not perfectly homogeneous. Although the DELPHI detector hermetically covers more than 99$\%$ of the solid angle and about 98$\%$ with full tracking, some weak regions exist, especially in the electromagnetic calorimetry. These are:

- $\theta \simeq 90°$
  In this region the midwall of the TPC causes a small loss in efficiency.

- $\theta \simeq 40°$ and $\theta \simeq 140°$
  The gap between the barrel and the end-caps contains a significant amount of dead material in the form of cables. The gap in polar angle between the HPC and the FEMC ranges from $35°$ to $42°$ (and from $138°$ to $145°$, corresponding to $0.74 < |\cos\theta| < 0.82$).

- $\phi \simeq 7.5° + (n-1) \cdot 15°, n = 1 \ldots 24$
  Close to the ϕ cracks between the 24 HPC modules the electromagnetic showers are less well contained, and energy is also deposited in the hadron calorimeter. This makes a correct reconstruction of particle energies more complicated.

The plot in Figure 3.8 shows the reconstructed energy of jets as a function of cos(θ) and as a function of ϕ, for 2-jet Z^0 events from the calibration runs in 1998. For these events the jet energies are known to be equal to E_{beam} ($\approx$ 45.6 GeV), so the corresponding energyflow efficiency can be calculated directly as $E_{\mathrm{measured}}/E_{\mathrm{beam}}$. Some of the weak regions discussed above are visible as dips in the efficiency. Also a clear trend is seen towards lower efficiencies in the forward directions. This is due to the reduced redundancy of the forward tracking and, more importantly, the increased amount of material in front of the calorimeters. But even though the resolution and efficiency are poorer, the jets are not lost. Where tracking ceases in the very forward region, calorimetry takes over and it is still possible to design algorithms to recover the measurement of forward jets. This is important, because even though the forward region covers a small fraction of the solid angle, with 4 or 5 jets in a single event a non-negligible chance exists that this region will contain at least one jet.

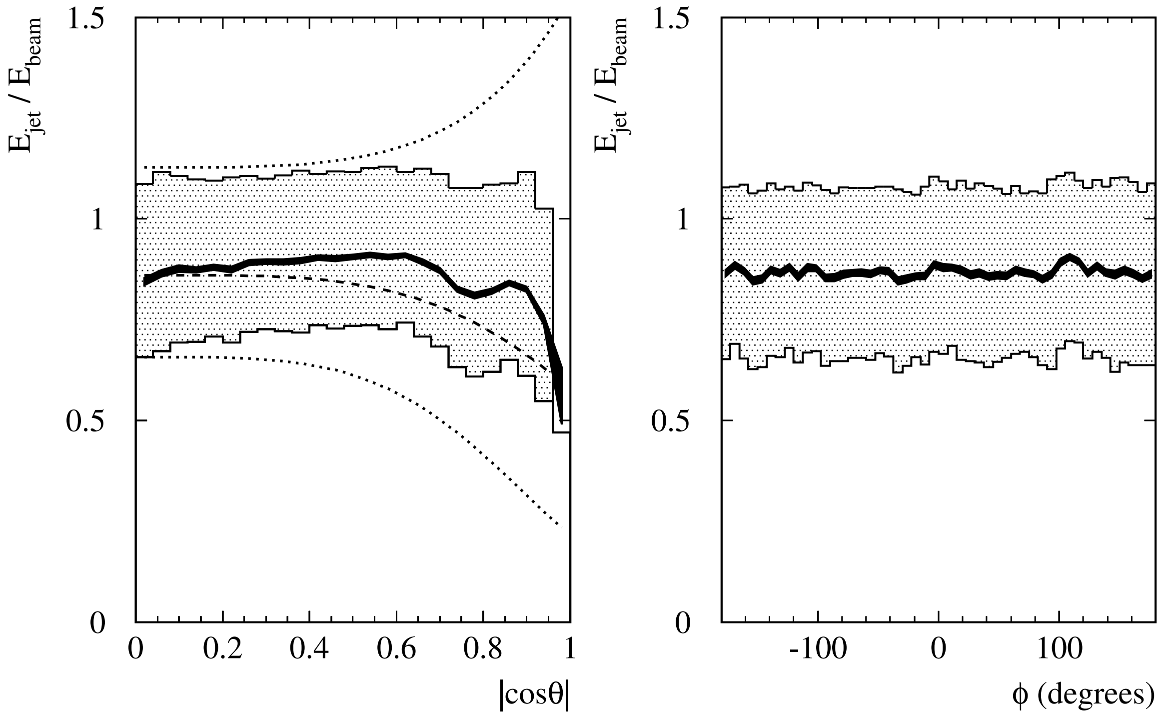

Figure 3.8: *Jet energy reconstruction efficiency as a function of the fitted polar (left) and azimuthal angles (right) of the jet. The black band indicates the average jet energy efficiency, while the shaded area corresponds to the energy resolution per jet. Resolution and average were extracted as the RMS spread and average value of the* a *parameter defined as* $a \equiv \ln(E_{\rm beam}/E_{\rm jet})$ *in the spirit of the constrained fit parameterisation to be discussed in section 4.2. The weak region around* $|\cos\theta| \approx 0.77$ *(see text) is visible as a dip in the energyflow efficiency. The* ϕ *cracks are too narrow to be seen in the jet energyflow. The dashed line (left) indicates the 'expected' energyflow efficiency and the dotted lines the one standard deviation error band as a function of* θ *used as input for the constrained fit (the* $a_0(\theta)$ *and* $\sigma_{a_j}(\theta)$ *parameters in equation (4.14)).*

B-tagging

For specific analyses involving the study of heavy-quark production, DELPHI has developed the combined b-tagging algorithm AABTAG [56]. It combines several pieces of information in order to separate b-quark jets from light-quark jets. It searches for signs of long-lived B mesons, using the impact parameters of each track and calculating the probability that all tracks originated from the primary vertex. Whenever a secondary vertex can be reconstructed, additional information like the invariant mass of the decay products is used. Although this b-tag did not play a crucial role in the analysis, it is used in the event selection (see page 90) and some of the systematic studies (appendix A).

3.6 Visualising the energyflow

In order to visualise the often complicated energyflow structure of hadronic multi-jet events, a new type of event display was introduced in DELPHI. This energyflow plot is used by the VINCENT [57] (Visual INterface to Constrained fit and ENergyflow Tool) program and is also part of the standard DELPHI event display program DELGRA [58].

The VINCENT program is an interface to the Monte Carlo simulation in which the user can see on an event-by-event basis how the energyflow develops while having access to all relevant information at generator level. Figure 3.9 shows an example of the production of a simulated fully hadronic WW event at $\sqrt{s} = 189$ GeV in four successive stages:

- The first plot (top left) shows the 4 fermions (quarks and anti-quarks) generated by EXCALIBUR. The $\mathrm{q\bar{q}}$ pair originating from one of the W bosons is encircled by the dashed line.
- The second plot (top right) shows the resulting partons generated by the Parton Shower (see section 2.5), including the radiation of hard gluons.
- The third plot (bottom left) displays all the stable particles that emerge from the hadronisation process. The sum of momenta and the energy are still conserved, and at generator level it is still possible to identify which particles should belong to which W boson (not shown). An ideal detector would measure all these particles with perfect resolution.
- The last plot displays the particles that are reconstructed after applying the full DELSIM detector simulation and the DELANA reconstruction program.

It is instructive to see that already at the perturbative stage of hard gluon radiation the final energyflow pattern of the event is determined. Already at that stage it would be difficult — without the dashed line — to see which decay products originated from which W boson. The hadronisation process and the detector response do not change the pattern significantly. Even though many of the low-momentum (especially neutral) particles are lost and some fake particles are reconstructed, in general the energyflow pattern is rather well reconstructed. Several of the jets have lost some energy, but a jet clustering algorithm (see next chapter) should recognise each of the jets.

This demonstrates that it is possible to reconstruct the energy flow pattern of hadronic events (though not with perfect resolution and efficiency), and that the hard gluon radiation poses a bigger challenge to the analysis of this event than the detector response. Quantitative analysis has shown that this is typically the case for hadronic WW events [59].

The basic tools that are used for the further treatment of the energyflow through jet clustering and constrained fits are discussed in the next chapter.

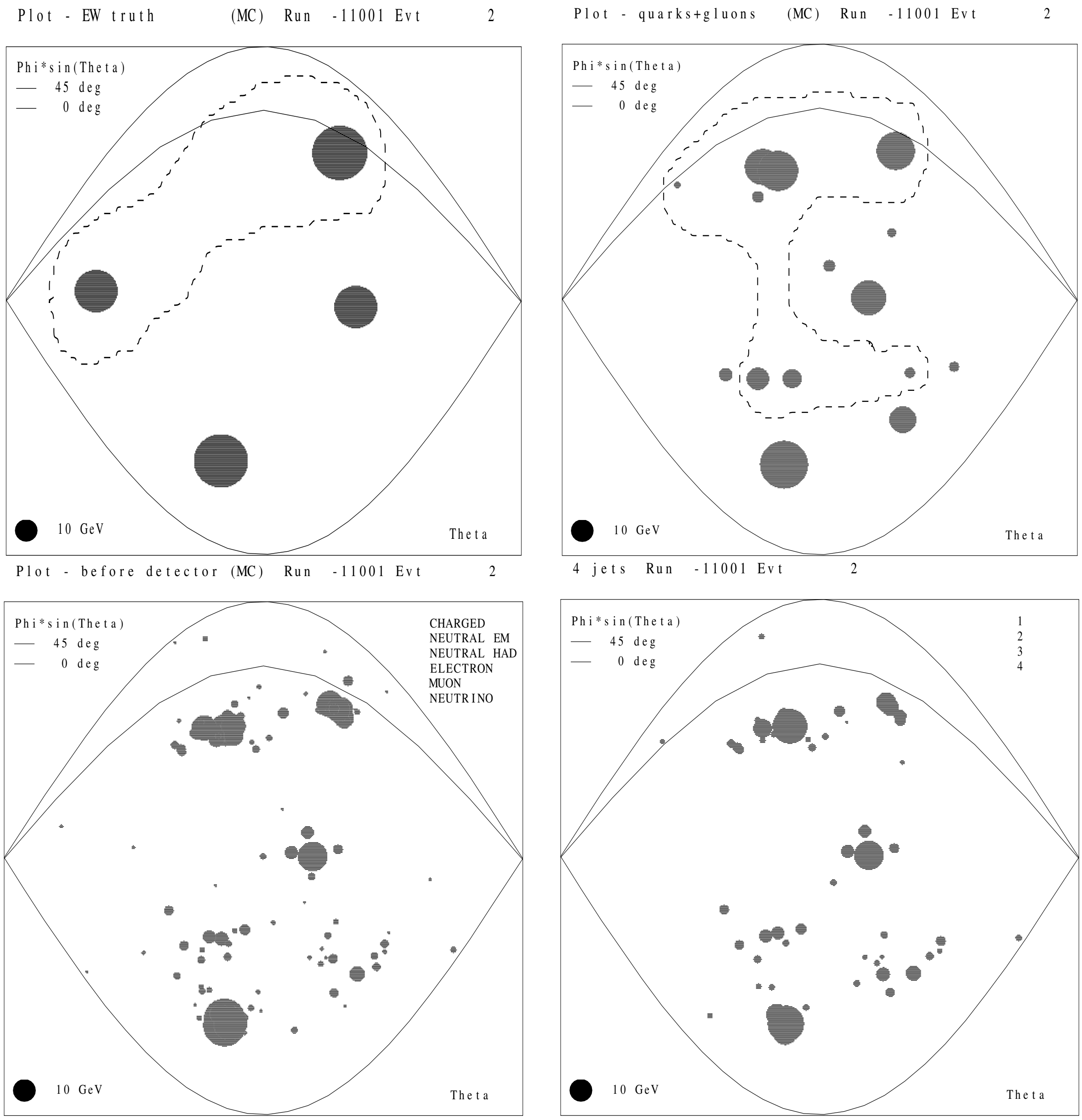

Figure 3.9: *Simulation of a $\sqrt{s} = 189$ GeV* $\mathrm{q\bar{q}q\bar{q}}$ *event in four stages (see text). The energyflow plots should be read in the following way: The surface of each dot is proportional to the particle energy, and the position of the dot marks the (θ, ϕ) direction of its momentum. The angle θ is plotted on the horizontal axis (from 0 to π) and ϕ is plotted on the vertical axis, multiplied by* $\sin\theta$.

Chapter 4

Basic analysis techniques

The purpose of this chapter is to introduce the basic analysis techniques that were used in the W mass analysis presented in this thesis. The following techniques are discussed:

Jet finding algorithms (section 4.1) used to identify and analyse hadronic decay products of the W bosons.

A constrained fit (section 4.2) to improve the measurement of the invariant mass beyond the detector resolution using the knowledge of the initial $e^+ e^-$ state prepared by LEP.

Monte Carlo reweighting (section 4.3); a technique widely used to change the properties of samples of Monte Carlo events after they have been generated.

The Jackknife method (section 4.4); a resampling technique to determine statistical errors.

These are simple, conventional techniques that are all (maybe with the exception of the Jackknife) widely used by particle physicists. The next chapter will describe how these 'standard' analysis techniques were further developed and combined in an unconventional way to create the 2D Ideogram analysis that is presented in detail in chapter 6.

4.1 Jet finding

Unlike in QCD studies, where jet finding is a fundamental necessity to define infra-red and collinear safe observables that can be measured experimentally, in W mass measurements the definition of jets is optional. An option which turns out to be very convenient, because it reduces the number of objects in the event while avoiding (as much as possible) mixing up the decay products of the two W bosons — a difficult task especially in fully hadronic final states.

The two practical advantages of reducing the number of objects in the event are:

- It minimises the number of parameters to be fitted in a constrained fit (typically 3 times the number of particles and/or jets; to be discussed in section 4.2).
- In the $q\bar{q}q\bar{q}$ channel, one of the main challenges is to separate the hadronic decay products of the W^+ and the W^- boson. In an event with n_j objects (particles or jets), the number of

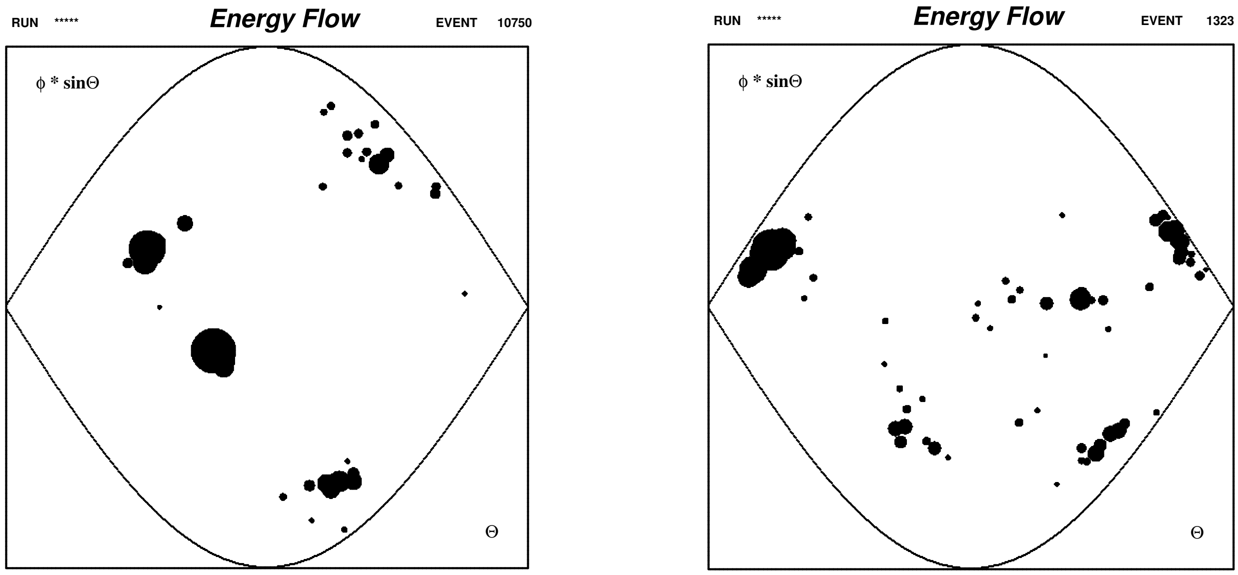

Figure 4.1: *Example of* $q\bar{q}q\bar{q}$ *events with a clear 4-jet (left) and 5-jet structure (right). Both are events from DELPHI data.*

possible assignments n_{pair} of the objects to the two W bosons with at least two objects in each W boson (needed to form a high mass boson) is equal to

$$n_{\mathrm{pair}} = 2^{n_j - 1} - n_j - 1 \tag{4.1}$$

so that a reduction of n_j to 4 or 5 jets is required to avoid unacceptable combinatorial complications.

Clearly, the major concern in the case of $q\bar{q}q\bar{q}$ events is that particles from different W bosons might be mixed in a single jet, making a correct subsequent separation of the two hadronic systems impossible. This complication plays a minor role in QCD analyses of single hadronic systems like the hadronic decay products of a single Z boson, for which most jet finding algorithms were originally developed. On the other hand, the requirement that the process has to be well-defined in terms of QCD theory does not play a role here, as long as the Monte Carlo simulation gives a satisfactory description of the fragmentation process, in terms of the results from the jet finding procedure.

Jet clustering algorithms

In most (but not all) W pair events the jets can easily be recognised by eye. In Figure 4.1 two examples of events with a clear jet structure are shown. To devise an algorithm that can do the same is less trivial and as a consequence many different jet finding algorithms have been developed. In e^+e^- physics the jet finding algorithms most commonly used are 'clustering' algorithms in which pairs (or triplets; see below) of particles are successively merged in order of increasing transverse momentum or a similar 'distance' measure. This procedure is continued until a pre-defined jet resolution or a desired number of jets is reached. The following three clustering algorithms have been studied and were used in the analysis presented here:

- DURHAM [60] (also known as 'k_T' clustering algorithm): In DURHAM the distance measure used to determine the order of clustering is the normalised effective transverse parton momentum y_{ij} defined as

$$y_{ij} = 2(1 - \cos\theta_{ij})\min(E_i^2, E_j^2)/E_{\text{vis}}^2 \tag{4.2}$$

  where θ_{ij} is the angle between the two particles or clusters i and j with energies E_i and E_j and E_{vis} is the total visible energy in the event. There are different ways to choose the 4-momentum of the resulting cluster. In all clustering algorithms used in this thesis the so-called 'E-scheme' was adopted, defining the resulting 4-momentum as the sum of the original 4-momenta: $\mathbf{p}_{ij} = \mathbf{p}_i + \mathbf{p}_j$. This procedure is repeated over and over again until the smallest y_{ij} becomes larger than the jet resolution parameter y_{cut}, chosen to be 0.002 in the analysis discussed here. The clusters that are left at this final stage are called 'jets'.

- The 'Cambridge' algorithm CAMJET [61] is a development of the DURHAM algorithm with the following two changes:

  - while the y_{ij} measure defined in (4.2) is still used as jet resolution parameter, the ordering variable used to choose the pair of clusters to be combined next is just the angle between the two clusters: min$(1 - \cos\theta_{ij})$.
  - an additional feature is that whenever the two clusters to be combined have a y_{ij} larger than y_{cut}, the cluster with the smallest energy of the two is removed from the event and saved as a jet ('soft gluon freeze out').

  These improvements with respect to DURHAM were designed to reduce the risk of 'junk-jet' formation, i.e. the gathering of soft gluons into a stand-alone jet instead of assigning them to the leading parton they originated from. As the gathering of soft gluons into 'junk-jets' increases the risk of clustering soft decay products from two different W bosons into one jet, the reduction of this effect is also expected to slightly help the W mass measurement.

- DICLUS (also called ARCLUS) is designed differently [62]. Inspired by the Colour Dipole model (as used in the ARIADNE [39] program) it combines *triplets* of clusters into *pairs*. In some sense the underlying physics idea is to reverse the colour dipole cascade, where gluons are emitted from pairs of colour-connected partons. The ordering variable used in DICLUS is a Lorentz invariant transverse momentum $p_\perp$ defined for an emitted parton i with respect to the two emitting partons j and k as

$$p_{\perp i(jk)}^2 = \frac{(s_{ij} - (m_i + m_j)^2)(s_{ik} - (m_i + m_k)^2)}{s_{ijk}} \tag{4.3}$$

  where s_{ij} and s_{ik} (s_{ijk}) are the squared invariant masses of two (three) partons. For events with more than 40 particles first a pre-clustering was done based on angles reducing the number of particles to 40, in order to keep the combinatorics down to an acceptable level.

Comparative study

Each of these three clustering algorithms is suitable for the W mass measurement, as they all have a good jet finding performance. To compare their performances for the W mass, in Table 4.1 and Figure 4.2 some benchmark numbers and plots are shown.

algorithm	Energyflow Separation for best pairing				W mass	
	Generator level		Analysis level		bias	relative
	$\langle\epsilon_{\text{sep}}\rangle$	$\epsilon_{\text{sep}} > 0.7$	$\langle\epsilon_{\text{sep}}\rangle$	$\epsilon_{\text{sep}} > 0.7$	(MeV/c^2)	resolution
DURHAM	0.81	76%	0.59	49%	177 ± 27	1.000
CAMJET	0.82	80%	0.61	52%	146 ± 26	0.985
DICLUS	0.72	56%	0.48	32%	181 ± 27	1.011
'Best of 3'	0.86	87%	0.70	62%	-	-
Ideogram-combined					162 ± 26	0.958

Table 4.1: *Comparison of DURHAM with the other clustering algorithms (see text), forcing all selected events to 4 jets. For each clustering algorithm both the average energyflow separation ϵ_{sep} is quoted and the fraction of events with a value of ϵ_{sep} larger than 0.7. The quoted W mass bias and resolution were obtained with the 183 GeV DELPHI analysis (see section 5.4.2) using the corresponding clustering algorithm.*

In order to have a well-defined clustering efficiency in the Monte Carlo study, the detector simulation was drastically simplified to an efficiency depending on the angle θ_j with the beam as used in the next section (e.g. equation (4.9), a beampipe causing a zero efficiency for $|\cos\theta_j| > 0.9986$, and a minimum momentum detection threshold of 300 MeV/c). In this way, the unambiguous origin of each particle was maintained, making it possible to define a 'separation efficiency' for each event and each jet pairing as

$$\epsilon_{\text{sep}} \equiv \left| \frac{\sum E_{\text{right}} - \sum E_{\text{wrong}}}{\sum E_{\text{right}} + \sum E_{\text{wrong}}} \right| \tag{4.4}$$

where $\sum E_{\text{right}}$ and $\sum E_{\text{wrong}}$ represent the sum of the energies of the particles that are assigned to the correct and the wrong W boson respectively. The 'best' jet pairing will give the best energyflow separation and the highest value of ϵ_{sep}. Thus the maximum value of ϵ_{sep} for each event is a measure of the clustering performance in that particular event. Similarly the jet pairing algorithm can be used that is also applied in the real W mass analysis (where Monte Carlo information about the origin of each particle is not available) to compare the clustering efficiencies under realistic analysis conditions. By definition the value of ϵ_{sep} has to be in the range $0 \leq \epsilon_{\text{sep}} \leq 1$, where $\epsilon_{\text{sep}} = 1$ corresponds to a perfect jet clustering and correct jet pairing, while $\epsilon_{\text{sep}} = 0$ means that for this clustering and chosen jet pairing 50% of the energyflow is assigned correctly to its parent W boson while 50% is assigned to the wrong W boson. For scores worse than that, it is more appropriate to swap the labels 'right' and 'wrong' by taking the opposite jet pairing; hence the absolute value.

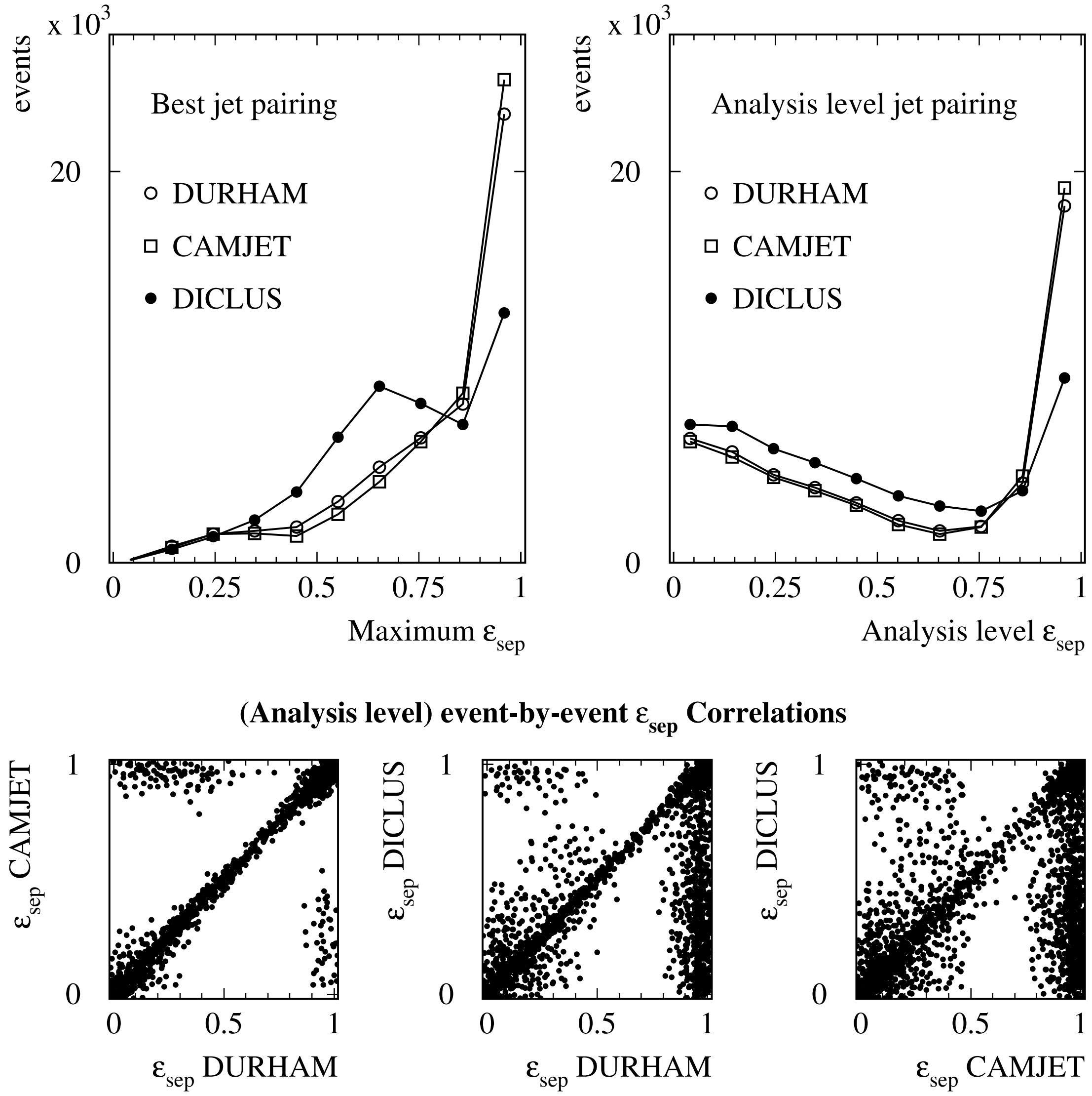

Figure 4.2: *Monte Carlo simulation study of the jet clustering performance. For 3 different clustering algorithms the energy flow separation performance (see text) is shown choosing the jet pairing with the best separation (top left) and for the jet pairing with the highest pairing probability in the W mass analysis (top right). The three lower plots show that for most events the performance of the 3 clustering algorithms is highly correlated, while for some ambiguous events the performances show remarkable differences.*

The omission of a realistic detector simulation in this study is believed to be non-critical, as earlier studies have shown that the main effect on the determination of the W mass takes place in the soft and hard gluon radiation phase, combined with the superposition of the two hadronic systems (see e.g. [59]).

Conclusions

Table 4.1 shows that the Cambridge algorithm performs slightly better than DURHAM, which in turn performs quite a bit better than DICLUS. The most interesting conclusion that can be drawn, however, is that for a certain class of ambiguous events the clustering result is quite uncorrelated between the 3 clustering algorithms (visible as off-diagonal points in the correlation plots shown in Figure 4.2). A method to identify such ambiguities and the possibility to take them into account constructively would give access to a possible improvement of up to 10% in efficiency for 'correctly clustered' events.

We will see later that Ideograms are able to provide both of these two features (see page 76 and beyond).

4.2 Constrained fit

The RMS spread in the beam energies of LEP is typically 0.1%. This is two orders of magnitude more precise than the experimental resolution with which the overall momentum and energy of the final state can be measured (for final states without neutrinos and initial states without significant ISR radiation). It is standard practice to use conservation of energy and momentum to transfer this knowledge to the final state by means of a constrained fit.

Constraints used

For a given $\sqrt{s} = 2E_{\mathrm{beam}}$ conservation of energy and momentum provide 4 constraints. By allowing for the possibility of one unseen energetic ISR photon collinear with the beam one arrives at the most general set of constraints used in this thesis:

$$\begin{aligned}
\sum_{i=1}^{n_{\mathrm{elements}}} p_x^i &= 0 \\
\sum_{i=1}^{n_{\mathrm{elements}}} p_y^i &= 0 \\
\sum_{i=1}^{n_{\mathrm{elements}}} p_z^i &= -p_z^\gamma \\
\sum_{i=1}^{n_{\mathrm{elements}}} E^i &= \sqrt{s} - |p_z^\gamma| \qquad (4.5)
\end{aligned}$$

where p_z^γ denotes the unknown momentum of the hypothetical ISR photon in the z direction and the sums include all other particles in the event. Thus, the inclusion of the ISR hypothesis effectively reduces the number of constraints to three.

Dividing the elements of the event in two heavy objects (e.g. W bosons), additional constraints can be introduced, leading to the sets of constraints shown in Table 4.2 — all used in the analysis presented here. If the final state contains a neutrino (e.g. as in $W^+W^- \rightarrow q\bar{q}l\nu$) three constraints are needed to reconstruct the neutrino, and formally the number of constraints in the fit is reduced by three.

	Extra constraints in addition to (4.5)	
	including possibility of ISR	excluding possibility of ISR (default)
E,p only	none "3C fit"	$p_z^\gamma = 0$ "4C fit"
equal mass	$m_1 = m_2$	$m_1 = m_2$ "5C fit" $p_z^\gamma = 0$
both masses	$m_1 = m_0$ $m_2 = m_0$	$m_1 = m_0$ "6C fit" $m_2 = m_0$ $p_z^\gamma = 0$

Table 4.2: *Different sets of constraints used in addition to the general constraints (4.5).*

Description of the fitting program

The constrained fit used throughout this thesis is available inside DELPHI as the PUFITC+ package [63]; a versatile event fitting program which allows the user to fit almost any configuration of jets and/or leptons with a variety of kinematic constraints. The program uses Lagrange multipliers to satisfy the constraints imposed while searching for a minimum χ^2 solution. The minimization is done in an iterative procedure using analytically calculated first and second-order derivatives.

The input to the fit consists of the measured elements (jets, charged lepton and neutrino). Each element is characterized by 3 parameters. Muons and electrons are defined by their measured direction and momentum or energy. The neutrino in $W^+W^- \to q\bar{q}l\nu$ events is not observed at all and therefore 'absorbs' 3 constraints and therefore 3 degrees of freedom in the fit. Tau leptons and jets are parameterized slightly differently (see below). The χ^2 is defined in the usual way:

$$\chi^2 = \sum_{i=1}^{n_y} \frac{(y_i^{\mathrm{fit}} - y_i^{\mathrm{meas}})^2}{\sigma_{y_i}^2} \tag{4.6}$$

where y_i are the fitting parameters and the number of parameters n_y equals 3 times the number of observed elements (jets, leptons). The estimated errors on the measured parameters σ_{y_i} are supplied by the user.

As discussed in the previous chapter, tau leptons and jets both have relatively large measurement uncertainties on the energy. In the case of the tau this is due to the fact that its decay contains at least one neutrino. Therefore a fit parameterisation is used that ensures that the fit is well behaved and that the fitted energy cannot become negative:

$$\mathbf{p}_j^{\mathrm{fit}} = \exp(a_j)\mathbf{p}_j^{\mathrm{meas}} + b_j\mathbf{p}^{b_j} + c_j\mathbf{p}^{c_j} \tag{4.7}$$

where $\mathbf{p}_j^{\mathrm{meas}}$ is the measured jet (or tau) momentum, and $\mathbf{p}^{b_j}$ and $\mathbf{p}^{c_j}$ are unit vectors of length 1 GeV/c, chosen in the transverse plane orthogonal to each other and to $\mathbf{p}_j^{\mathrm{meas}}$ as shown in figure 4.3. The corresponding χ^2 is given by

$$\chi_j^2 = \frac{(a_j - a_0)^2}{\sigma_{a_j}^2} + \frac{b_j^2}{\sigma_{b_j}^2} + \frac{c_j^2}{\sigma_{c_j}^2} \tag{4.8}$$

where a_0 represents the expected loss of energy (typically $\approx 15\%$ for jets).

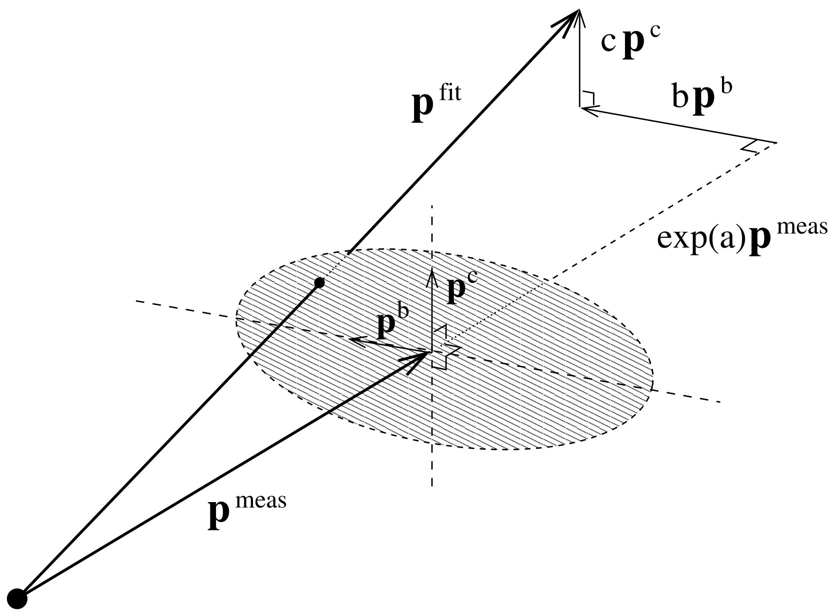

Figure 4.3: *Parameterisation used for jets (and tau leptons) in the constrained fit.*

For jets, the standard choice of jet errors, based on energyflow studies using Z^0 events like the one that was presented in section 3.5, is as follows:

$$\begin{aligned} a_0 &= 0.15 + 0.40 \cdot \cos^4\theta_j \\ \sigma_{a_j} &= 0.15 + 0.40 \cdot \cos^4\theta_j \\ \sigma_{b_j} &= \sigma_{c_j} = (1.0 + 0.6 \cdot \cos^4\theta_j) \cdot 1.62 \end{aligned} \tag{4.9}$$

where θ_j is the polar angle of the momentum of jet j with respect to the z axis (= beam direction). For taus, a first fit is done with large errors:

$$\begin{aligned} a_0 &= 1 \\ \sigma_{a_j} &= 10 \\ \sigma_{b_j} &= \sigma_{c_j} = 0.5 \end{aligned} \tag{4.10}$$

in order to determine the missing mass in the tau decay (depending on the number of neutrinos in the tau decay), which is then used to estimate the transverse errors on the tau for a second fit:

$$\sigma_{b_j}^2 = \sigma_{c_j}^2 = \frac{E_m(E_{\text{fit}} - E_m)m_\tau^2 - E_{\text{fit}}(E_{\text{fit}} - E_m)m_m^2 - \frac{1}{2}(m_\tau^2 - m_m^2)^2}{2(\text{GeV}/c)^2 p_m^2} \tag{4.11}$$

with a minimum σ of 0.1, where the subscript m means ‘measured’, fit means ‘fitted’, and m_τ is the tau mass 1.784 GeV/c^2. It should be noted, however, that in a $\mathrm{W}^+\mathrm{W}^- \to \mathrm{q\bar{q}}\tau\nu$ event the tau lepton plays a negligible role in fitting the W invariant mass, due to its large measurement errors.

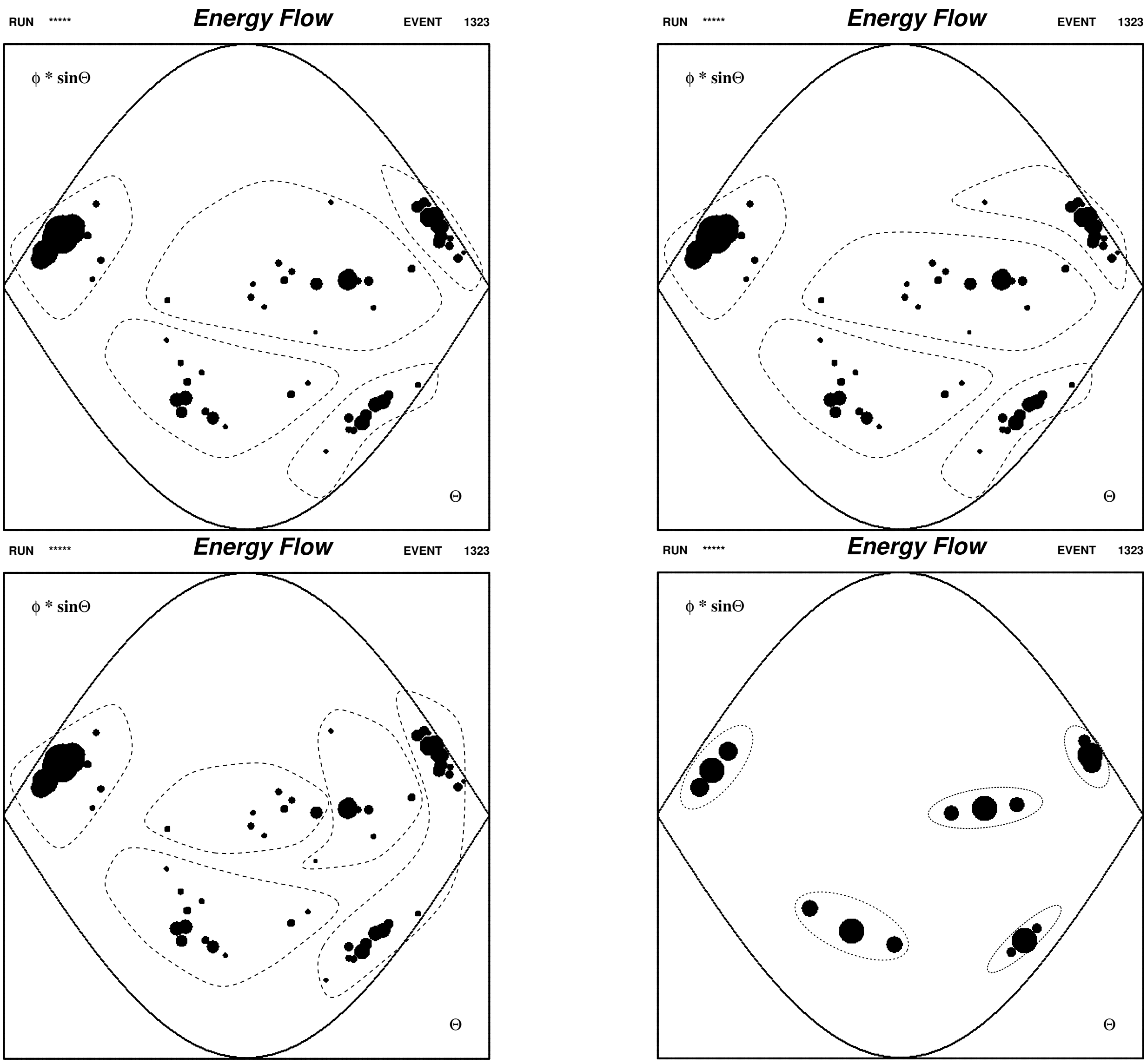

Figure 4.4: *The clustering of the 5-jet event from Figure 4.1 according to DURHAM (top left), CAMJET (top right) and DICLUS (bottom left). The jets as found by DURHAM are shown in the bottom right plot. For each jet not only the energy flow corresponding to the energy of the jet is shown, but also the directions $\mathbf{p}_j^{\mathrm{meas}} \pm B_b \mathbf{p}_b$, with the surface of the blob proportional to B_b, thus indicating the direction in which the jet was found to be broadest.*

Asymmetric transverse jet errors

The correct treatment of jet errors is more critical. Due to gluon radiation jets can have some elongated shape in the plane transverse to their momentum, as is clearly the case for the jets in the events shown in Figure 4.1 and 4.4.

As the main loss of energy flow information is due to missing particles, it can be expected that the transverse measurement error is largest in the direction in which the jet is broadest. Therefore, an improved estimate of the transverse errors was made in 3 steps:

- The direction in which the jet is broadest had to be determined. This was done by projecting the momenta of all the particles belonging to a jet to the plane perpendicular to the overall jet momentum and diagonalising the 2-dimensional momentum tensor $\mathcal{T}_{\beta\gamma}$ defined as:

$$\mathcal{T}_{\beta\gamma} = \sum_{j=1}^{n_{\text{particles}}} p_\beta^j p_\gamma^j \tag{4.12}$$

  where p_β^j and p_γ^j are the two components of the momentum of particle j in the transverse jet plane. The eigenvectors $\mathbf{p}_b$ and $\mathbf{p}_c$ give the directions in which the jet was broadest and slimmest, and the corresponding eigenvalues B_b and B_c are used as a measure of broadness. The result of this procedure is illustrated in Figure 4.4 (bottom right).

- In order to be able to use the directions thus obtained, the constrained fit should allow the user to choose the transverse jet directions $\mathbf{p}^{b_j} = \mathbf{p}_b$ and $\mathbf{p}^{c_j} = \mathbf{p}_c$ according to which the errors σ_{b_j} and σ_{c_j} are to be defined. It turned out to be trivial to add this option to the PUFITC program.

- In order to get a rough estimate of the energy that was missed in each jet, for every event first a 4C fit was performed with standard transverse errors as given in equations (4.9). The difference of the fitted and the measured energy for each jet $E_{j\text{miss}}$ was retained for later fits.

For all subsequent constrained fits in the event, improved asymmetric transverse jet errors were defined as follows for the semi-leptonic channel:

$$\begin{aligned}
a_0 &= 0.15 + 0.40 \cdot \cos^4\theta_j \\
\sigma_{a_j} &= 0.15 + 0.40 \cdot \cos^4\theta_j \\
\sigma_{b_j}^2 &= 0.2 + 1.0\ (\text{GeV}/c)^{-2} \cdot B_b \frac{\sqrt{1\text{GeV} \cdot E_j^{\text{m}} + E_{j\text{miss}}^2}}{E_j^{\text{m}}} \\
\sigma_{c_j}^2 &= 0.2 + 1.0\ (\text{GeV}/c)^{-2} \cdot B_c \frac{\sqrt{1\text{GeV} \cdot E_j^{\text{m}} + E_{j\text{miss}}^2}}{E_j^{\text{m}}}
\end{aligned} \tag{4.13}$$

and for the fully-hadronic channel:

$$\begin{aligned}
a_0 &= 0.15 + 0.40 \cdot \cos^4\theta_j \\
\sigma_{a_j} &= 0.27 + 0.72 \cdot \cos^4\theta_j \\
\sigma_{b_j}^2 &= 0.36 + 1.8\ (\text{GeV}/c)^{-2} \cdot B_b \frac{\sqrt{1\text{GeV} \cdot E_j^{\text{m}} + E_{j\text{miss}}^2}}{E_j^{\text{m}}} \\
&\quad +0.036\ (\text{GeV}/c)^{-4} \cdot B_b^2 \\
\sigma_{c_j}^2 &= 0.36 + 1.8\ (\text{GeV}/c)^{-2} \cdot B_c \frac{\sqrt{1\text{GeV} \cdot E_j^{\text{m}} + E_{j\text{miss}}^2}}{E_j^{\text{m}}} \\
&\quad +0.036\ (\text{GeV}/c)^{-4} \cdot B_c^2.
\end{aligned} \tag{4.14}$$

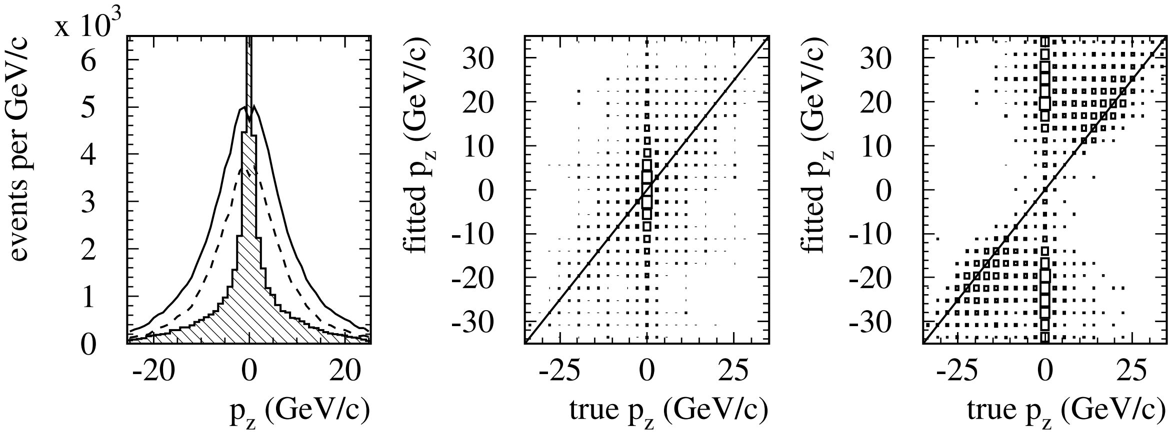

Figure 4.5: *Illustration of the $p_z^\gamma = 0$ constraint, based on 189 GeV EXCALIBUR simulation. For fully hadronic WW events, the generated p_z of the 4-fermion centre-of-mass system is plotted in the shaded histogram (left). The central bin (see text) exceeds the vertical scale. The solid line shows the fitted p_z when the $p_z^\gamma = 0$ constraint is not used, and the dashed line idem but only for those events with a generated p_z in the central bin. The other plots show the fitted p_z as a function of the generated p_z without further cuts (middle) and applying the additional requirement that the fitted p_z is more than 3 sigma away from 0 GeV/c (right).*

The effect of using jet broadness in the fit

The main improvement observed was a reduction of the tails in pull distributions plotting b_j/σ_{b_j} and c_j/σ_{c_j}. A statistically significant improvement in W mass resolution, however, was never proven.

The effect of including ISR in the constraints

The ISR constraint defined in formula (4.5), is useful to determine how well the measured event is balanced around 0 in the z direction, at the level of the measurement resolution. As shown in Figure 4.5, however, the average resolution on p_z^γ is much worse (≈ 9 GeV/c) than the typical p_z imbalance caused by ISR photons. At 189 GeV, 67% of the WW events have a generated $|p_z| < 0.5$ GeV/c and 85% have $|p_z| < 5$ GeV/c, in agreement with the radiator function mentioned in section 2.3. This means that for the majority of the events the additional $p_z^\gamma = 0$ constraint is a good constraint to use.

For the small fraction of the events with a collinear ISR photon with an energy exceeding 5 to 10 GeV/c, the W mass reconstruction can be improved by including the ISR hypothesis. However, to implement this in the W mass analysis is non-trivial because these events are often indistinguishable from badly reconstructed events without ISR. An approach that was found to be succesful will be described in section 5.4.3.

Another application of the ISR hypothesis is the determination of the effective centre-of-mass energy $\sqrt{s'}$, discussed in the next paragraph.

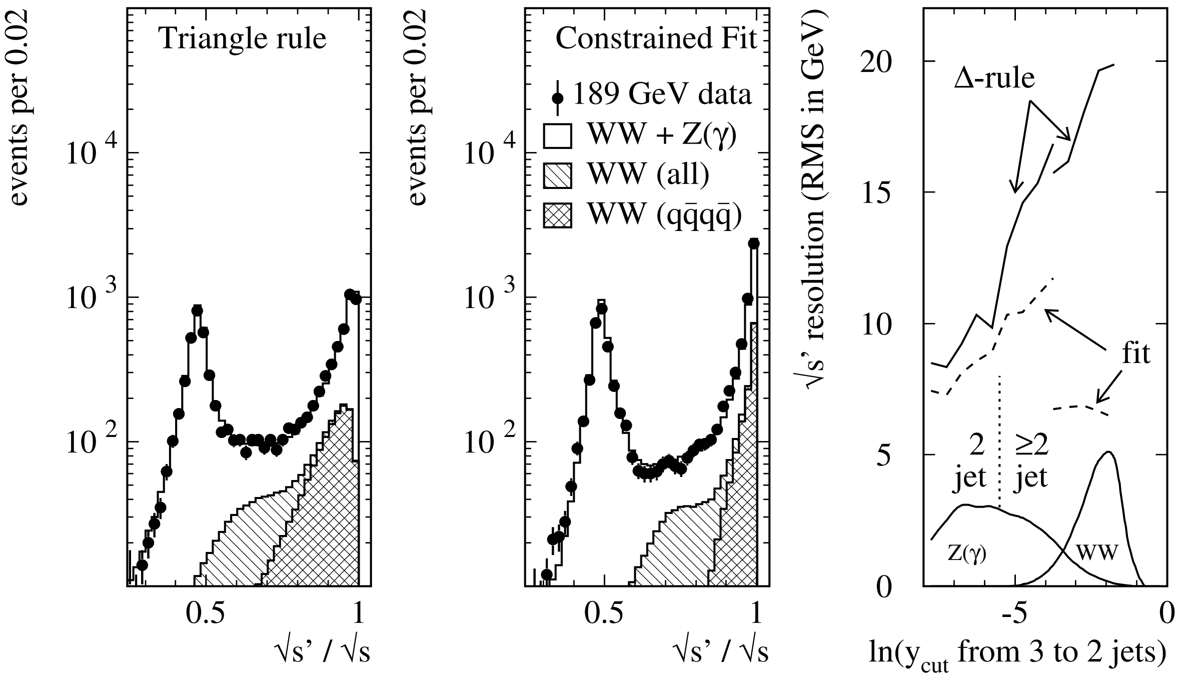

Figure 4.6: *Comparison of the determination of $\sqrt{s'}$ using either the Triangle rule (left) or a constrained fit with the 'natural' number of jets (middle). The right-hand plot shows the $\sqrt{s'}$ resolution for the Triangle rule (solid line) and the constrained fit (dashed) as a function of the value of $y_{\rm cut}$ that would be required to force the event in a 2-jet configuration. The fixed value of $y_{\rm cut}$ used in the main W-mass analysis is indicated by the vertical, dotted line. For low values of $y_{\rm cut}$ on-shell Z(γ) events were selected with a reconstructed value of $\sqrt{s'}$ below 110 GeV, while in the high $y_{\rm cut}$ region WW events where used, requiring the reconstructed $\sqrt{s}$ to be above 161 GeV. The deterioration of the resolution as $y_{\rm cut}$ increases is worse for the Triangle rule.*

The effect of acknowledging the 'natural' number of jets

The 3C fit with ISR hypothesis is well suited for the experimental determination of $\sqrt{s'}$, which is an important event observable in many LEP2 analyses. As shown in Figure 4.6, at LEP2 energies about half of the hadronic events have a $\sqrt{s'}$ around the Z peak after the emission of an energetic ISR photon (so-called 'radiative return to the Z' events). One way to reconstruct $\sqrt{s'}$ is to cluster all events into 2 jets and then apply 3-body kinematics (the 'triangle rule') where the 3$^{\rm rd}$ particle is the photon which is either observed in the detector or assumed to have escaped inside the beam-pipe. Using the constraints from energy and momentum conservation the jets can thus be rescaled, keeping the directions fixed, and the resulting invariant mass of the jet system is taken as estimate of $\sqrt{s'}$ (see Figure 4.6).

A better solution is to cluster the event in the 'natural' number of jets, i.e. the number of jets that remains when the clustering process is continued until a fixed $y_{\rm cut}$ is reached, followed by a constrained fit including all jets, detected photon(s) and an additional hypothetical photon inside the beam-pipe. In Figure 4.6 the improvement is clearly visible, especially for fully hadronic W events. An additional advantage is that the constrained fit returns a χ^2, providing information about the goodness-of-fit.

In the analysis of W events the use of the 'natural' number of jets is advantageous as well, but partly for different reasons (there the whole situation is a bit more complicated). This will be the subject of chapter 5.

4.3 Monte Carlo reweighting

Another useful analysis technique is the Monte Carlo reweighting approach. The Monte Carlo events that are normally used all have equal weight (=1). By reweighting every generated event with an a posteriori weight w_i, a Monte Carlo sample can be made to 'mimic' a Monte Carlo sample with different generated properties, e.g. a different W mass, provided the statistics are sufficient. In the W mass measurements of the other LEP experiments Monte Carlo reweighting plays a central role [64, 65] (see section 5.1). For the results presented in this thesis it is used for some cross-checks and the final calibration of the W boson width measurement.

The penalty that has to be paid for reweighting is that by giving different weights to events, statistical fluctuations are amplified, and statistical information is not optimally distributed for the newly obtained distributions. It is convenient to express this loss of statistical significance in terms of an *equivalent number* of 'non-weighted' events n_{eqv}:

$$n_{\mathrm{eqv}} \equiv \frac{\left(\sum_{i=1}^{n} w_i\right)^2}{\sum_{i=1}^{n} w_i^2} = \frac{(n \cdot \langle w \rangle)^2}{n \cdot (\mathrm{var}(w) + \langle w \rangle^2)} = n \cdot \frac{\langle w \rangle^2}{\mathrm{var}(w) + \langle w \rangle^2} \tag{4.15}$$

where $\langle w \rangle$ is the average event weight, and $\mathrm{var}(w)$ the variance. When all weights are equal (no reweighting), the number of equivalent events n_{eqv} is equal to n. Otherwise, the statistical significance deteriorates for increasing spread in the event weights. Therefore, by minimising the spread of the event weights, one can optimise the use of statistical information. This is a useful insight, because there can be some freedom in the choice of the event weights (as exploited in the 3$^{\mathrm{rd}}$ method mentioned below).

Three formulas for calculating the event weights have been implemented in the framework of the analysis presented in this thesis, for obtaining a reweighted Monte Carlo sample corresponding to a W mass and width $m_{\mathrm{W}}^{\mathrm{new}}$ and $\Gamma_{\mathrm{W}}^{\mathrm{new}}$ from a sample generated using $m_{\mathrm{W}}^{\mathrm{old}}$ and $\Gamma_{\mathrm{W}}^{\mathrm{old}}$:

1. *Breit-Wigner reweighting*
   For each generated event i the boson masses m_1^i and m_2^i are retained, and the event weights are calculated using running-width Breit-Wigner functions (as in equation (2.5)):

   $$w_i = \frac{\mathrm{BW}(m_1^i, m_{\mathrm{W}}^{\mathrm{new}}, \Gamma_{\mathrm{W}}^{\mathrm{new}}) \cdot \mathrm{BW}(m_2^i, m_{\mathrm{W}}^{\mathrm{new}}, \Gamma_{\mathrm{W}}^{\mathrm{new}})}{\mathrm{BW}(m_1^i, m_{\mathrm{W}}^{\mathrm{old}}, \Gamma_{\mathrm{W}}^{\mathrm{old}}) \cdot \mathrm{BW}(m_2^i, m_{\mathrm{W}}^{\mathrm{old}}, \Gamma_{\mathrm{W}}^{\mathrm{old}})} \tag{4.16}$$

   The advantage of this method is that the calculation of the weights is fast. The main drawback is that it does only take into account the CC03 doubly resonant WW diagrams, and not all 4-fermion diagrams generated by the EXCALIBUR Monte Carlo generator.

2. *Matrix element reweighting*
   A similar approach can be used using the full matrix elements calculated by EXCALIBUR.

In this case the 4-momenta $\mathbf{p}_j$ of the 4 fermions are used as input, and the weights are calculated as follows:

$$w_i = \frac{|\mathcal{M}(\mathbf{p}_{\mathrm{f1}}, \mathbf{p}_{\mathrm{f2}}, \mathbf{p}_{\mathrm{f3}}, \mathbf{p}_{\mathrm{f4}}, m_{\mathrm{W}}^{\mathrm{new}}, \Gamma_{\mathrm{W}}^{\mathrm{new}})|^2}{\left|\mathcal{M}(\mathbf{p}_{\mathrm{f1}}, \mathbf{p}_{\mathrm{f2}}, \mathbf{p}_{\mathrm{f3}}, \mathbf{p}_{\mathrm{f4}}, m_{\mathrm{W}}^{\mathrm{old}}, \Gamma_{\mathrm{W}}^{\mathrm{old}})\right|^2} \tag{4.17}$$

These matrix elements take into account all generated 4-fermion diagrams (WW-like and ZZ-like). It turns out that the difference with the results obtained with the BW weights is negligible in most cases. A practical disadvantage is the increased amount of CPU time needed.

3. *Optimised choice of weights*
When samples were generated with different m_{W}^k the above formulae can still be used, using for each event the values of m_{W}^k and Γ_{W}^k with which this particular event was generated. An improved choice of weights, however, can reduce the spread of the weights while giving an equivalent reweighting result with reduced statistical fluctuations. This choice is based on the philosophy that equivalent events, i.e. events with identical 4-fermion configurations (barring infinitesimal differences), should have equal weights. This can be achieved using the following definition of weights:

$$w_i = \frac{\mathrm{p}(\mathbf{p}_{\mathrm{f1}}, \mathbf{p}_{\mathrm{f2}}, \mathbf{p}_{\mathrm{f3}}, \mathbf{p}_{\mathrm{f4}}|m_{\mathrm{W}}^{\mathrm{new}}, \Gamma_{\mathrm{W}}^{\mathrm{new}}) \sum_k n_k/\sigma_{\mathrm{new}}}{\sum_k \mathrm{p}(\mathbf{p}_{\mathrm{f1}}, \mathbf{p}_{\mathrm{f2}}, \mathbf{p}_{\mathrm{f3}}, \mathbf{p}_{\mathrm{f4}}|m_{\mathrm{W}}^k, \Gamma_{\mathrm{W}}^k) n_k/\sigma_k} \tag{4.18}$$

where $\mathrm{p}(\mathbf{p}_{\mathrm{f1}}, \mathbf{p}_{\mathrm{f2}}, \mathbf{p}_{\mathrm{f3}}, \mathbf{p}_{\mathrm{f4}}|m_{\mathrm{W}}^{\mathrm{new}}, \Gamma_{\mathrm{W}}^{\mathrm{new}})$ is the differential cross-section to generate an event with 4-fermion configuration $\mathbf{p}_{\mathrm{f1}}, \mathbf{p}_{\mathrm{f2}}, \mathbf{p}_{\mathrm{f3}}, \mathbf{p}_{\mathrm{f4}}$ given a new W mass and width, while the $\mathrm{p}(\mathbf{p}_{\mathrm{f1}}, \mathbf{p}_{\mathrm{f2}}, \mathbf{p}_{\mathrm{f3}}, \mathbf{p}_{\mathrm{f4}}|m_{\mathrm{W}}^k, \Gamma_{\mathrm{W}}^k)$ signify the 'original' differential cross-sections for the original samples k with n_k generated events each, normalised with the overall cross-sections σ_k and σ_{new}. For these differential cross-sections a BW can be used (as in formula (4.16)) or the full matrix element squared (equation (4.17)).

Of the three methods mentioned above the third is the most optimal in the case that samples with different generator parameters are combined. The effect is illustrated in Figure 4.7 for the realistic case where 3 large Monte Carlo samples have been generated with W masses 79.35, 80.35 and 81.35 GeV/c^2.

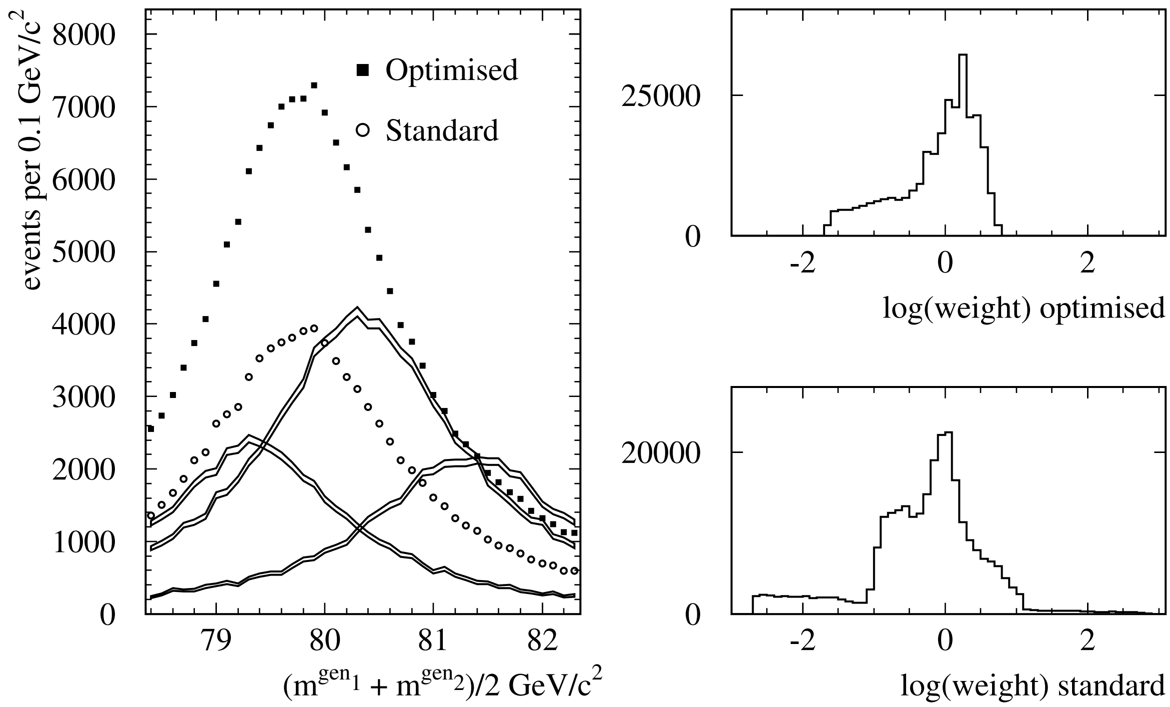

Figure 4.7: *The average invariant mass distribution of the two W bosons per event is plotted for the 3 main samples of 189 GeV WW Monte Carlo with generated m_W 79.35, 80.35 and 81.35 GeV/c^2. Also the combined distributions are shown, after reweighting to m_W=79.85 GeV/c^2 using either the standard method (no.1) or the optimised method (no.3) with BW weights (see text). Both reweighted distributions are normalised to their equivalent number of events. Also the distributions of weights used are shown for the optimised case (top right) and the standard case (bottom right).*

4.4 The Jackknife method

Finally the Jackknife, a non-parametric resampling technique related to the Bootstrap method, is an easy-to-use and powerful method to determine statistical errors on complicated quantities when the underlying probability distribution and/or internal correlations are unknown or (too) complicated to be taken into account with conventional statistical techniques [66].

Let X be an observable extracted from a sample of n independent events:

$$X = \mathrm{F}(\{\text{sample}\}) \tag{4.19}$$

where F can be a complicated analysis procedure (e.g. using events more than once). And let X_i be defined as the same observable when event no. i would have been removed from the sample:

$$X_i = \mathrm{F}(\{\text{sample}\} - \text{event no. } i) \tag{4.20}$$

and the influence Δ_i of event no. i as

$$\Delta_i \equiv X_i - X. \tag{4.21}$$

The numerical evaluation of Δ_i can be elaborate when the computation of X is involved. In our case X is always estimated from the minimum of a 1-dimensional likelihood curve, which makes the numerical estimation trivial. The Jackknife estimate of the variance of X then follows directly from the sum of the squares of the Δ_i:

$$\mathrm{var}(X) = \frac{n-1}{n} \sum_{i=1}^{n} \Delta_i^2. \tag{4.22}$$

This simple formula is useful for the determination of statistical uncertainties in systematics studies. In fact, for many of the small systematics effects reported in chapter 7 and the MLBZ results presented in Appendix A the Jackknife method was succesfully applied to determine their statistical significance. The Jackknife was also used to evaluate errors on errors which is essential for the assessment of analysis optimisations.

Chapter 5

Historical account

The aim of this chapter is to give a historical overview of the developments and key new ideas that led to the realization of the main analysis presented in this thesis. Starting from the 'Yellow Book approach' (section 5.1) several new ideas are introduced including a 5-jet treatment (section 5.2) and the Ideogram technique with its development from a 1D convolution in the 172 GeV analysis to a fast 2D convolution at 189 GeV (section 5.3). In the last section (5.6) a few words are spent on the role that Jackknife and MLBZs have played in the studies of systematic errors. A comprehensive description of the main analysis is given in the next chapter.

5.1 Yellow Book approach

The different methods for the direct measurement of the W mass as proposed at the 1995 'Physics at LEP2' workshop [67] were all based on the following approach:

1. Event selection and jet clustering in 4 jets ($\mathrm{q\bar{q}q\bar{q}}$ channel) or 2 jets + lepton ($\mathrm{q\bar{q}l}\nu$ channel)

2. Full kinematic event reconstruction extracting 1 or 2 masses per event

3. A fit to the obtained mass spectrum, using one of the following four methods proposed:

   (a) fitting the mass spectrum with a 'simple' *analytical function*, followed by calibration using Monte Carlo simulation.

   (b) the *convolution method*, where the underlying physics function (or differential cross-section $\frac{\mathrm{d}^2\sigma(s;m_\mathrm{W},\Gamma_\mathrm{W})}{\mathrm{d}m_1\mathrm{d}m_2}$) is used as a fitting function, taking into account the effects of the detector by convolution. The prediction of the reconstructed invariant masses $(\overline{m}_1,\overline{m}_2)$ is thus given by:

$$\frac{\mathrm{d}^2\sigma(s;m_\mathrm{W},\Gamma_\mathrm{W})}{\mathrm{d}\overline{m}_1\mathrm{d}\overline{m}_2} = \int \mathrm{d}m_1 \int \mathrm{d}m_2\, \mathrm{G}(s;\overline{m}_1,\overline{m}_2,m_1,m_2) \cdot \frac{\mathrm{d}^2\sigma(s;m_\mathrm{W},\Gamma_\mathrm{W})}{\mathrm{d}m_1\mathrm{d}m_2} \quad (5.1)$$

   The yellow report does not give any guidelines of how to choose the Green's function $\mathrm{G}(s;\overline{m}_1,\overline{m}_2,m_1,m_2)$, which is obviously the most involved part of this method. This approach in fact is a special case of method (a), with a slightly more restricted and therefore less arbitrary choice of the fitting function. Also in this method a calibration using Monte Carlo simulation is needed.

(c) *Monte Carlo interpolation*. Monte Carlo samples with different values of ${m_{\mathrm{W}}}^{\mathrm{MC}}$ and ${\Gamma_{\mathrm{W}}}^{\mathrm{MC}}$ are generated and processed with the same event selection and kinematic fit as the data. Then for each of the samples the compatibility of the invariant mass spectrum with the mass spectrum obtained with real data is determined (e.g. using a binned maximum likelihood fit). Interpolation of the likelihood (or χ^2) in the (${m_{\mathrm{W}}}^{\mathrm{MC}}$,${\Gamma_{\mathrm{W}}}^{\mathrm{MC}}$) grid then gives the fitted value of m_{W} or Γ_{W} automatically correcting for all possible biases due to mass reconstruction and experimental cuts, provided they are described by the Monte Carlo.

(d) *Monte Carlo reweighting*. Same as (c), but using a Monte Carlo reweighting technique as described in section 4.3 to produce the samples with different values of ${m_{\mathrm{W}}}^{\mathrm{MC}}$ and ${\Gamma_{\mathrm{W}}}^{\mathrm{MC}}$ from a single (or just a few) samples of generated Monte Carlo events, which is more efficient and more flexible.

Example of a Yellow Book analysis

For illustrative purposes a simple implementation of such an analysis, based on method (d) and only including the $\mathrm{q\bar{q}q\bar{q}}$ channel, is described in the following. This 'reference' Yellow Book analysis consists of:

- Event selection:
  Identical to the $\mathrm{q\bar{q}q\bar{q}}$ selection of the main analysis described in chapter 6. The DURHAM jet clustering algorithm is used to cluster these events in 4 jets.

- Full kinematic event reconstruction:
  A 5C equal mass constrained fit is performed as described for the main analysis. Out of 3 possible jet pairings the one with lowest χ^2 is chosen. Thus one mass per event is extracted and plotted as in Figure 5.1.

- Fit to the obtained mass spectrum using Monte Carlo reweighting and a binned maximum likelihood fit, based on Poissonian statistics in each bin. The Monte Carlo events are reweighted changing the W mass in steps of 0.1 GeV/c^2 and the likelihood given by

  $$\Delta\chi^2 = 2\sum_j \left[N_j^{\mathrm{MC}} - N_j^{\mathrm{data}} + N_j^{\mathrm{data}} \cdot \ln(N_j^{\mathrm{data}}/N_j^{\mathrm{MC}})\right] \tag{5.2}$$

  is calculated and plotted (see Figure 5.1), where N_j^{data} and N_j^{MC} are the number of selected data events and Monte Carlo events respectively in bin no.j. From the likelihood curve the mass and error on the mass are derived in the usual way by fitting a parabola as shown in Figure 5.1.

  To good approximation this method is unbiased, since all known reconstruction biases (e.g. due to experimental cuts and detector efficiencies and resolution) are automatically corrected for by the Monte Carlo simulation.

This analysis is only a simplified approach, meant to quantify some of the effects discussed in the next sections.

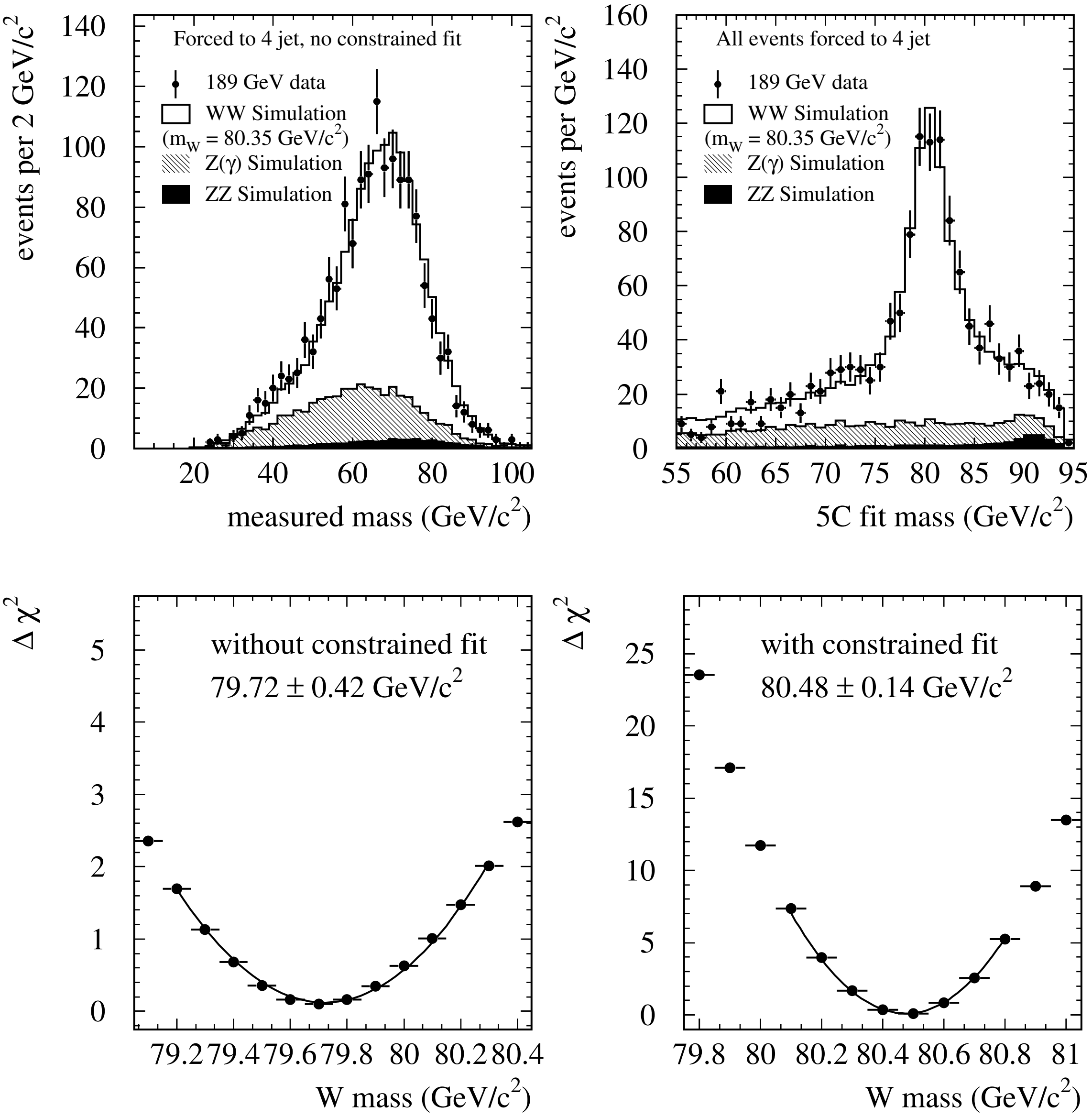

Figure 5.1: *Fully-hadronic mass spectrum showing the invariant mass from the 'best' (= lowest χ^2_{5C}) jet pairing in each event, before (top left) and after (top right) a 5C constrained fit, illustrating the improvement in resolution. The bottom plots show the corresponding likelihood curves obtained from a binned maximum likelihood fit of reweighted Monte Carlo to the 189 GeV DELPHI data shown in Figure 5.1. The errors quoted are the statistical errors obtained from the parabolic fit to the likelihood curves shown.*

Other analyses

All m_{W} measurements based on 172-189 GeV data published to date by the other LEP experiments [64, 65] are improved variations of the Yellow Book analysis, in the sense that they are all based on a Monte Carlo reweighting fit of a mass spectrum to the data. Technical improvements were made to the Monte Carlo reweighting fits and the performance of the measurements was improved by optimising event selection, the development of better jet pairing algorithms, and attempts to further improve the constrained fit. A few examples of such developments are:

- ALEPH: 4C fit + energy scaling instead of 5C fit, extracting two masses per event instead of one
- L3: neural network for event selection, improved handling of the binning in the global fit, and a separate fit of the second best jet pairing
- OPAL: improved event selection and choice of jet pairing using multivariate likelihood discriminants, and (at 189 GeV) a separate treatment for 4-jet and 5-jet events

The development of analysis methods is still ongoing: In the recent WW physics at LEP2 Workshops [68] results were presented not only on the study of systematic uncertainties, but also on the continuing effort to further improve the mass extraction methods. OPAL has been working on a convolution method similar to the one presented in this thesis, and L3 reported about an investigation of a separate treatment for 5-jet events, also pioneered by the work presented here. A totally different approach is being pursued by ALEPH, based on a 3-dimensional reweighting technique in the semi-leptonic channels, where the main challenge is to control the danger of instabilities in the fit when the limited Monte Carlo statistics is spread out in 3 dimensions.

5.2 5-jet events... a first attempt

The first attempt back in 1996 to improve the statistical treatment of the events beyond the Yellow Book approach, was to treat 5-jet events as 5-jet events. In about 30% to 50% of the selected WW events (depending on the jet resolution variable $y_{\rm cut}$) more than 4 jets are visible, due to the radiation of final state gluons with high k_T (see section 2.5). Obviously, as was the case with the determination of $\sqrt{s'}$ (section 4.2, page 60), by acknowledging the apparent energy-flow structure including the 'natural' number of jets one should be able to extract more detailed and correct statistical information from the event.

But here the situation is more complex: In addition to the advantage of having a more correct model of the event, also the energyflow separation $\epsilon_{\rm sep}$ will improve, provided that an effective algorithm can be designed to choose the correct jet pairing. As the number of possible jet pairings increases from 3 in a 4-jet event to 10 in a 5-jet event, it becomes more challenging to find the correct jet combination. An optimal treatment has to balance two pieces of information:

1. the distance of the closest jets (equivalent to the DURHAM $\rm y_{cut}$ used to distinguish a 4-jet from a 5-jet event)
2. a jet pairing criterion; in our simple example just the pairing with the lowest $\chi^2_{\rm 5C}$ (i.e. smallest difference of the two measured boson masses).

The traditional approach applies these two measures sequentially: first measure no.1 is used to reduce the number of jets from 5 to 4, followed by criterion no.2. In our analysis we chose to use the $1/k_T$ dependence as discussed in 2.5 as a natural measure to estimate the relative probability for each jet pairing that the fifth jet was radiated with the observed k_T with respect

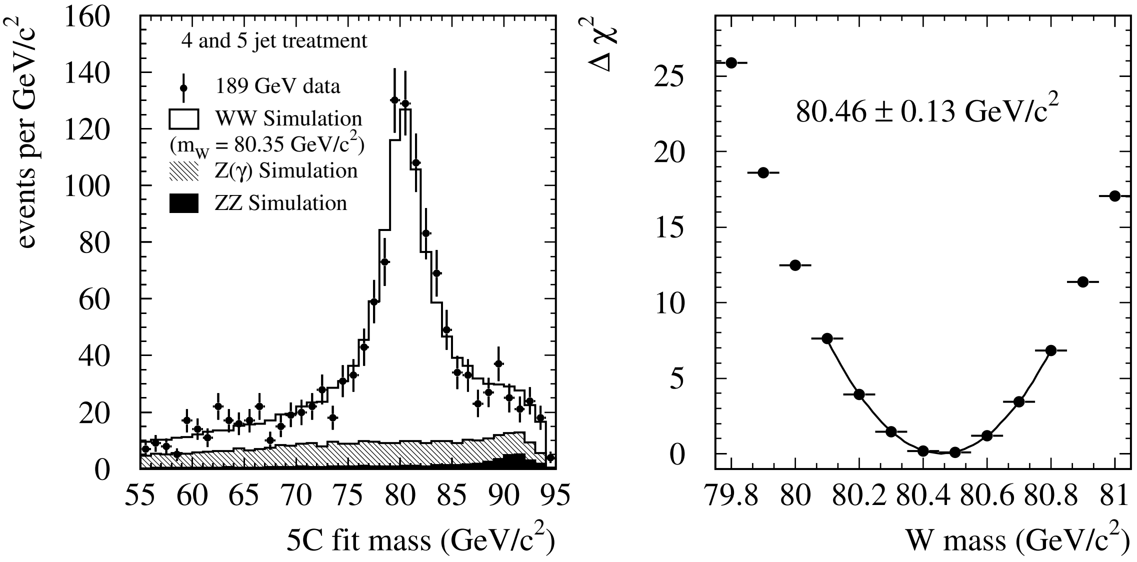

Figure 5.2: *Fully-hadronic mass spectrum (left) showing the fitted mass from the 'best' (see text) jet pairing in each event with 4-jet events treated as 4-jet and 5-jet events treated as 5-jet and the corresponding likelihood curve and fitted mass (right) using the Monte Carlo reweighting fit described in section 5.1.*

to its corresponding parent quark jets. The $p \propto 1/k_T$ probability was transformed to a χ^2 using $\chi^2_{k_T} = -2 \cdot \ln(p)$, and the jet pairing with the lowest overall χ^2 was then further used in the analysis:

$$\chi^2_{\text{tot}} = \chi^2_{5\text{C}} + \chi^2_{k_T} \tag{5.3}$$

thus combining both pieces of information on an equal footing. This straight-forward 5-jet treatment resulted in a visible improvement of a few percent as Figure 5.2 compared to 5.1 shows.

This 5-jet study proved that a further refinement of the Yellow Book approach could lead to modest improvements in the statistical sensitivity. More important was the fact that it highlighted as main limitation of the analysis the representation of each WW event by just one fitted mass, inevitably forcing a trade-off between a more detailed and correct description of the event ambiguities and the resulting increased difficulty in making the right 'choice'. The solution, not to make a choice at all, emerged from an entirely different analysis approach: the *Ideogram technique*.

5.3 The Ideogram technique

The basic idea of the Ideogram technique is to abandon the analysis paradigm based on a lineshape fit of the global invariant mass spectrum, and change to event-by-event likelihoods describing the full ambiguity of the mass information in each event as correctly as possible. By taking into account the full mass ambiguity the limitation of 'choosing' the correct solution is avoided. The full information is carried on to the combined likelihood of the overall event sample, where ambiguities that could not be resolved on the event level become easy to solve, as the signal clearly stands out w.r.t. the background of 'wrong' solutions.

Statistics background

Though originally conceived on the basis of sheer common sense, the Ideogram analysis technique can be derived directly from Bayesian inference principles, starting from very basic statistics rules, namely the *sum rule*:

$$\mathrm{p}(X|I) + \mathrm{p}(\overline{X}|I) = 1 \tag{5.4}$$

and the *product rule*:

$$\mathrm{p}(X, Y|I) = \mathrm{p}(X|Y, I) \cdot \mathrm{p}(Y|I) \tag{5.5}$$

where X, Y and I are *Boolean* variables or propositions that can either be *true* or *false* and $\mathrm{p}(X|Y)$ signifies the probability that X is true, *given* that Y is true. The comma stands for the logical conjunction 'AND', while $\overline{X}$ is the negation of X, i.e. the proposition that X is false. Related to the sum rule equation (5.4) is the principle of *marginalisation*, either used in discrete form:

$$\mathrm{p}(X|I) = \sum_i \mathrm{p}(X, H_i|I), \tag{5.6}$$

where the different propositions H_i should be mutually exclusive and form a complete set, or as a continuous integration:

$$\mathrm{p}(X|I) = \int_{-\infty}^{\infty} \mathrm{p}(X, a|I) da \tag{5.7}$$

where a is a so-called *nuisance parameter*, i.e. a parameter that is not of primary interest for the measurement. A result that follows directly from the basic equations (5.4) and (5.5) is Bayes' Theorem:

$$\mathrm{p}(m_{\mathrm{W}}|\textit{event}, I) = \frac{\mathrm{p}(\textit{event}|m_{\mathrm{W}}, I) \cdot \mathrm{p}(m_{\mathrm{W}}|I)}{\mathrm{p}(\textit{event}|I)} \tag{5.8}$$

where m_{W} stands for the parameter to be measured, I encompasses all underlying assumptions, and *event* stands for the observed data. This theorem turns out to be very useful to describe the process of scientific inference. If one is interested in parameter estimation the normalisation constant $\mathrm{p}(\textit{event}|I)$ which does not depend on the parameter to be measured can be omitted. Also the 'Bayesian prior' $\mathrm{p}(m_{\mathrm{W}}|I)$ is often chosen to be flat, which is certainly a good choice for a statistically well-behaved precision measurement like the W mass analysis. Technically this reduces the procedure to a standard *maximum likelihood* approach:

$$\mathrm{p}(m_{\mathrm{W}}|\textit{event}, I) \propto \mathrm{p}(\textit{event}|m_{\mathrm{W}}, I) \tag{5.9}$$

where the proportionality sign indicates that whereas the posterior probability density function $\mathrm{p}(m_{\mathrm{W}}|\textit{event}, I)$ is normalised the relative likelihood function $\mathrm{p}(\textit{event}|m_{\mathrm{W}}, I)$ is not. In practice this does not matter. In order to determine the W mass (or width) and the statistical uncertainty it is sufficient to obtain a relative likelihood curve (or likelihood ratio) which is the product of all relative event likelihood curves $\mathrm{p}(\textit{event}|m_{\mathrm{W}}, I)$ that are calculated for each event as a function of m_{W} (or Γ_{W}). The absolute WW cross-section is kept fixed which is a good approximation in the m_{W} range of interest, to be cross-checked later by doing a full Monte Carlo calibration. In principle *event* includes the complete set of observations connected to the event *event*, but in practice the likelihood can only be evaluated for a limited number of observables. Moreover, the only way to take into account complicated jet fragmentation and detector acceptance and resolution effects with sufficient precision is to rely on Monte Carlo simulation; either directly or indirectly, as a final calibration of the analysis.

Limitations of the 'black box' Monte Carlo reweighting approach

As was shown in the previous sections (5.1 - 5.2) a straightforward way to obtain the likelihood function p$(event|m_{\rm W}, I)$ is to represent the event *event* just by its 5C fitted mass $m_{\rm fit}^{\rm 5C}$ and estimate the probability distribution of $m_{\rm fit}^{\rm 5C}$ using Monte Carlo simulation directly:

$$\mathrm{p}(event|m_{\rm W}, I) = \mathrm{p}_{\mathcal{MC}}(m_{\rm fit}^{\rm 5C}|m_{\rm W}, I). \tag{5.10}$$

In fact the Monte Carlo histograms shown in Figure 5.1 and 5.2 give precisely this likelihood as a function of $m_{\rm fit}^{\rm 5C}$ for the corresponding analyses and a given W mass of 80.35 GeV/c^2. The Monte Carlo reweighting technique can be used to determine the best available estimate of the relative likelihood for other values of $m_{\rm W}$. In fact this is exactly (an event-by-event version of) the 'Monte Carlo reweighting' analysis described before in section 5.1.

The main drawback of this method is that including more than one observable (e.g. also the error $\sigma_{m_{\rm fit}^{\rm 5C}}$ on the fitted mass $m_{\rm fit}^{\rm 5C}$) would require the available Monte Carlo events to be distributed in more than one dimension in observable space. For an increasing number of dimensions this quickly reaches the limits of the available statistics. In practice above 2 or 3 dimensions technical problems arise because statistical fluctuations in the coverage of the observable space can no longer be neglected. When these statistical limitations start playing a significant role this will lead in most cases to incorrect results and possibly to an underestimation of the statistical error if this is not taken into account.

Ideogram construction of the event likelihood

An analytically constructed likelihood does not have this limitation. In principle the Ideogram approach allows for the inclusion of all available event information taking into account all observables that are believed to be relevant. To include more event specific information the Ideogram method relies on a physics and statistics model to analytically evaluate expression (5.9) further and construct the event likelihood without using Monte Carlo simulation. This can be done to varying degrees of sophistication.

The first insight exploited in the Ideogram analysis is the fact that the event likelihood p$(event|m_{\rm W}, I)$ consists to a good approximation of two independent parts that can essentially be factorised (Figure 5.3). In statistical language, this factorisation is done by marginalisation. Using equation (5.7) and the product rule (5.5) the event likelihood p$(event|m_{\rm W}, I)$ can be written as:

$$\begin{aligned} \mathrm{p}(event|m_{\rm W}, I) &= \iint \mathrm{p}(event, \vec{m}'|m_{\rm W}, I)\ d\vec{m}' \\ &= \iint \mathrm{p}(event|\vec{m}', m_{\rm W}, I) \cdot \mathrm{p}(\vec{m}'|m_{\rm W}, I)\ d\vec{m}' \\ &\approx \iint \mathrm{p}(event|\vec{m}', I) \cdot \mathrm{p}(\vec{m}'|m_{\rm W}, I)\ d\vec{m}'. \end{aligned} \tag{5.11}$$

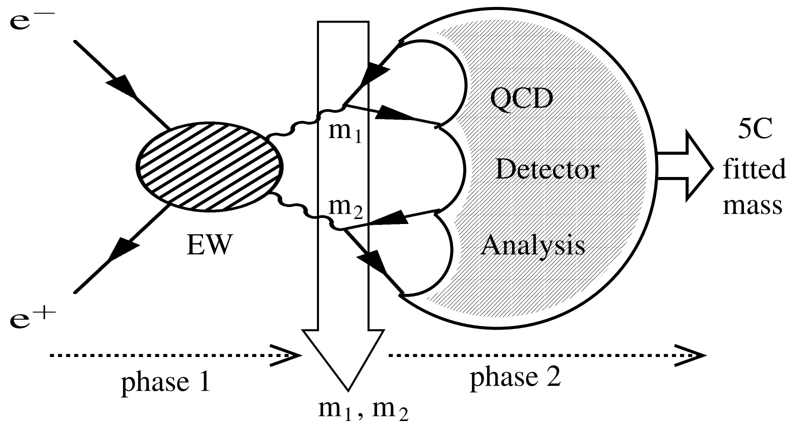

Figure 5.3: *A schematic representation of the generation of a single WW event in two phases: the production of two W bosons with masses m_1 and m_2, followed by their decay, detection and analysis resulting in a fitted mass $m_{\rm fit}^{\rm 5C}$.*

Here the integration has to be performed over the whole physically allowed range of values of $\overrightarrow{m}'$, with $\overrightarrow{m}'$ representing the *'true invariant masses (m_1, m_2) of the two objects in the event that are supposed to be W bosons'*. The last step in equation (5.11) reveals the motivation for separating these two factors: to a good approximation the $m_{\rm W}$ mass dependence is concentrated in the physics function $\mathrm{p}(\overrightarrow{m}'|m_{\rm W}, I)$ while the other factor $\mathrm{p}(\textit{event}|\overrightarrow{m}', I)$ only depends on the kinematics observed in the event.

The (QED + EW) physics part of the process $\mathrm{p}(\overrightarrow{m}'|m_{\rm W}, I)$ describing the production of two W bosons with masses m_1 and m_2, is well defined. The differential cross-section is contained in equation (2.4) in chapter 2, and can be written to a good approximation as the product of two running-width Breit-Wigner functions (2.5) and a two-dimensional phase space function:

$$\begin{aligned} \mathrm{p}(\overrightarrow{m}'|m_{\rm W}, I) &\approx \mathrm{S}(\overrightarrow{m}'|m_{\rm W}, \Gamma_{\rm W}, \sqrt{s}) \equiv \\ \mathrm{BW}(m_1|m_{\rm W}, \Gamma_{\rm W}) &\cdot \mathrm{BW}(m_2|m_{\rm W}, \Gamma_{\rm W}) \cdot \frac{1}{s}\sqrt{(s - m_1^2 - m_2^2)^2 - 4m_1^2 m_2^2} \end{aligned} \tag{5.12}$$

The evaluation of the experimental resolution function $\mathrm{p}(\textit{event}|\overrightarrow{m}', I)$ relies on approximations, where the aim is to describe the main features of the likelihood as correctly as possible. The resulting description of $\mathrm{p}(\textit{event}|\overrightarrow{m}', I)$ is what is referred to as 'Ideogram' throughout this thesis.

One indispensable ingredient in the calculation of the experimental Ideogram is the constrained fit. The likelihood to observe the jets (and possible lepton) seen in the event for a given pair of true invariant masses $\overrightarrow{m}'$ is estimated by the goodness-of-fit probability of a 6C kinematic fit:

$$\mathrm{p}(\textit{event}|\overrightarrow{m}', I) = p_{\rm 6C}^{\rm fit}(\text{jets (+ lepton)}|\overrightarrow{m}', \sqrt{s}) \tag{5.13}$$

where the two boson masses given by $\overrightarrow{m}'$ are fixed by the constraints.

As an example, for a $\mathrm{q\bar{q}l}\nu$ event *event* represented by the 4-momenta of the observed jets and lepton this would result in the following likelihood expression:

$$\mathrm{p}(\textit{event}|m_{\rm W}, I) = \iint p_{\rm 6C}^{\rm fit}(\text{ jets + lepton }|\overrightarrow{m}', \sqrt{s}) \cdot \mathrm{S}(\overrightarrow{m}'|m_{\rm W}, \Gamma_{\rm W}, \sqrt{s})\ d\overrightarrow{m}'. \tag{5.14}$$

The integral can be evaluated in one or two dimensions for $\overrightarrow{m}'$. A one-dimensional model assuming equal masses of the two W bosons works well for most events, and often the resulting 6C goodness-of-fit as a function of the equal mass m' even turns out to be close to a Gaussian with a maximum for m' $=m^{5C}_{\text{fit}}$ and a width equal to the error $\sigma_{m^{5C}_{\text{fit}}}$ estimated by the constrained fit. For some $\mathrm{q\bar{q}l}\nu$ events, however, this is not at all the case as will be discussed later in section 5.5.

In the $\mathrm{q\bar{q}q\bar{q}}$ channel the situation is slightly more complicated: there a jet pairing must be chosen to define to which combination of jets the mass constraints $\overrightarrow{m}'$ in the 6C kinematic fit apply. As discussed before the correct jet pairing can never be identified with certainty. This lack of knowledge is a key feature of of the $\mathrm{q\bar{q}q\bar{q}}$ resolution function $\mathrm{p}(\mathit{event}|\overrightarrow{m}', I)$ and can be taken into account using discrete marginalisation (equation (5.6)) to sum over all possible jet pairing hypotheses H^{pair}_j, and then applying the product rule (equation (5.5)) as was done before:

$$\begin{aligned}
\mathrm{p}(\mathit{event}|\overrightarrow{m}', I) &= \sum_{j=1}^{n_{\text{pair}}} \mathrm{p}(\mathit{event}, H^{\text{pair}}_j|\overrightarrow{m}', I) = \\
&= \sum_{j=1}^{n_{\text{pair}}} \mathrm{p}(H^{\text{pair}}_j|\overrightarrow{m}', I) \cdot \mathrm{p}(\mathit{event}|H^{\text{pair}}_j, \overrightarrow{m}', I) = \\
&= \sum_{j=1}^{n_{\text{pair}}} p_j \cdot p^{\text{fit}}_{\text{6C}}(\mathit{event}|\overrightarrow{m}', H^{\text{pair}}_j, \sqrt{s})
\end{aligned} \tag{5.15}$$

where the probabilities $p_j = \mathrm{p}(H^{\text{pair}}_j|\overrightarrow{m}', I)$ of the different jet pairings can be determined to different levels of sophistication, as will be discussed in more detail later.

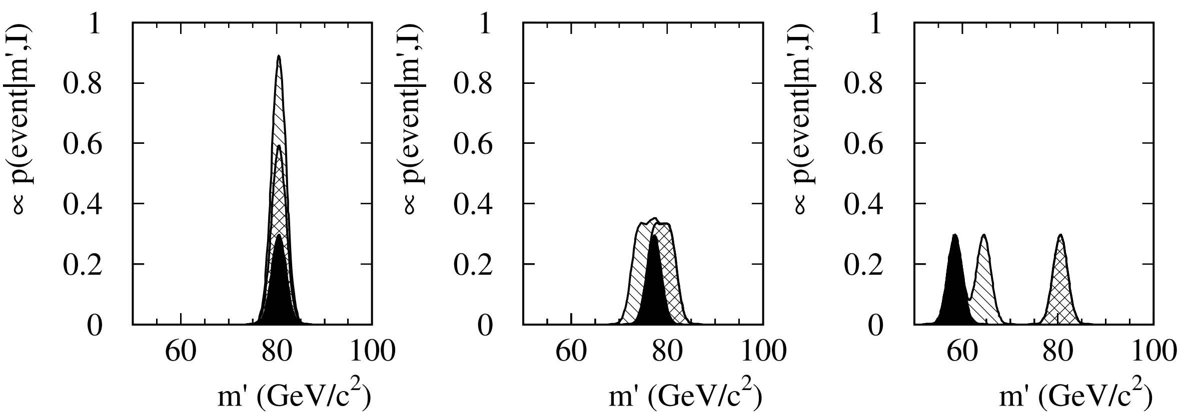

Figure 5.4: *Some examples of Ideograms are shown, for different hypothetical 4-jet events. For all events the 3-fold jet-pairing ambiguity is the same, but the resulting knowledge about the true boson mass m' is fundamentally different.*

In order to illustrate the non-trivial effect of jet-pairing ambiguities on the mass information in an event, Figure 5.4 shows the Ideograms for 3 hypothetical 4-jet events, using an equal-mass Gaussian approximation. For simplicity in this example the sigmas are all taken to be equal and the weights given to each of the three jet pairings is chosen equal to 1/3. In each event the correct pairing has a solution close to 80 GeV/c^2, while the wrong jet pairings have maxima for more-or-less random values of the mass m'. The effect of the jet pairing ambiguity on the mass is fundamentally different for each of the 3 cases:

1. If all pairings happen to give the same mass, the jet-pairing uncertainty does not matter at all. As a consequence this event contains the same information about m_{W} as an event without any ambiguity.

2. When the masses are rather close, the approximate value of the correct mass is known, but the ambiguity cannot be resolved and the net effect is a deterioration of the mass resolution for this event.

3. If, however, the masses are well separated, a broad range of possible masses should be considered for this event. By retaining this ambiguity in the event likelihood curve, however, this ambiguity will automatically become irrelevant when the addition of other events will unambiguously reveal the approximate location of the real W mass among the (almost) uniformly distributed background of wrong jet pairings. Effectively, for an event like this, the jet pairing ambiguity does not affect the mass resolution but it does reduce the weight (typically $\propto 1/(n_{\mathrm{pair}})$ of the signal peak w.r.t. to the background hypothesis (to be introduced later).

Thus, by describing the full ambiguity, the Ideogram method is able to take into account all possible jet pairings, and the fact that only one pairing per event can be correct. When more jet pairings are included, the weight per jet pairing is decreased accordingly, making sure that the integral over the signal probability stays normalised w.r.t. the background.

The extension from 3 jet pairings in a 4-jet event to 10 jet pairings in a 5-jet event is natural; the sum over 3 pairings is simply replaced by a sum over 10 pairings. To improve the analysis further, additional information can be used to determine the relative probabilities of the jet pairings p_j. Ambiguities of a different nature can be included by adding more hypotheses using discrete marginalisation as before.

Including the estimated event purity

One additional ambiguity that is included in all Ideogram analyses is the question whether the event originated from a WW signal interaction, or some kind of background physics process. For background processes the expected mass distribution $\mathrm{p}(\vec{m}'|m_{\mathrm{W}}, I)$ of the two identified heavy objects in the event is not given by a Breit-Wigner, but rather by some background shape $\equiv \mathrm{B}(\vec{m}'|I)$ which does not depend on m_{W} and can be extracted from Monte Carlo simulation. Applying discrete marginalisation, formula (5.11) can be expanded to:

$$\begin{aligned} &\mathrm{p}(\textit{event}|m_{\mathrm{W}}, I) \approx \\ &\iint \mathrm{p}(\textit{event}|\vec{m}', I) \cdot \Big[\mathcal{P}_{\mathrm{event}} \cdot \mathrm{S}(\vec{m}'|m_{\mathrm{W}}, I) + (1-\mathcal{P}_{\mathrm{event}}) \cdot \mathrm{B}(\vec{m}'|I)\Big] \; d\vec{m}' \end{aligned} \tag{5.16}$$

where the event purity $\mathcal{P}_{\mathrm{event}}$ signifies the probability that the event was a WW signal event, estimated for each event using observables that are — as much as possible — uncorrelated with the mass information $\vec{m}'$ (or m_{W}). In this manner the analysis takes into account the fact that 'pure' events are likely to contain useful W mass information, while this is unlikely to be the case for background-like events. The Ideogram function $\mathrm{p}(\mathit{event}|\overrightarrow{m}', I)$ is evaluated as described before, where the number of hypotheses to be included depends on the analysis channel. The evolution of the Ideogram analysis along these lines will be discussed further in section 5.4 and 5.5.

Comparison with the Convolution method

The integration over the invariant masses introduced in equation (5.11) appears similar to the Yellow Book convolution (formula (5.1)), but this similarity is misleading. One difference is that the Ideogram integration is performed over the 'true' invariant masses in the event instead of the reconstructed invariant mass. Furthermore, the Ideogram idea is to calculate event-by-event likelihoods rather than constructing a function to be fitted to the overall mass spectrum. Finally, a characteristic and distinctive feature of the Ideogram method is the sum over different hypotheses.

Resulting event likelihood curves

The posterior likelihood curves are multi-modal, showing typically more than one maximum (A few examples are shown in Figures 5.8 and 6.15.). They are numerically stored in logarithmic form:

$$L_{\mathit{event}}(m_{\mathrm{W}}) \equiv -2 \cdot \ln(\mathrm{p}(m_{\mathrm{W}}|\mathit{event}, I)) \tag{5.17}$$

and kept for further analysis involving standard maximum likelihood techniques.

Conclusion

The Ideogram technique presented here introduced a new approach in the direct measurement of the W mass based on the analytical construction of event-by-event likelihood curves, allowing for the inclusion of more information specific to each event.

Such an event-by-event approach is advantageous because W events come in different qualities. Some beautiful 4-jet events give a clear clustering, obvious jet pairing and good mass resolution. Those events give excellent information about the W mass. Other events are more ambiguous and effectively contain less reliable or less precise mass information. By taking this large event-by-event variation into account as correctly as possible, the final uncertainty on the W mass can be reduced significantly.

5.4 Evolution of fully-hadronic Ideograms in DELPHI

5.4.1 1D Ideograms at 172 GeV

The W mass measurement based on the 172 GeV DELPHI data [1] was the first published application of the Ideogram analysis, introducing a 5-jet treatment and taking into account

- All possible jet pairings. A 1-dimensional convolution was used. Each jet pairing was represented by a Gaussian resolution function, the mean being equal to the mass obtained from a 5C equal mass fit, with a sigma equal to the estimated error from the constrained fit. In principle each of the jet pairings has equal *a priori* probability. However, in this

1-dimensional approach the compatibility of each jet pairing with the equal mass hypothesis had to be put in via additional weights: the relative probabilities of the different jet pairings were derived from the mass difference determined with a 4C fit (without equal mass constraint). The theoretically expected distribution for the mass difference of the two W bosons was used to obtain the relative probability for each jet pairing. Additionally, for 5-jet events, each jet pairing was weighted according to an additional relative probability $1/k_T$ as described in section 5.2.

- The event purity. The expected mass distribution for the background was approximated by a flat function times a 1-dimensional phase space function. For each event the purity $\mathcal{P}_{\rm event}$ was estimated as a function of a discriminating variable $D \equiv \theta^{\rm jj}_{\rm min} \cdot E^{\rm jet}_{\rm min}$, the product of the smallest angle between 2 jets and the minimum jet energy in a 4-jet configuration. The Ideogram was calculated as the sum of the WW and the background hypothesis as in equation (5.16).

5-jet treatment

In this analysis a $y_{\rm cut}$ value of 0.004 was used, giving 5 or more jets in approximately 30% of the selected W events.

Adding jet broadness to PUFITC

This was also the first time that the improved error-parameterisation with transverse jet-broadness errors was used, as described in the previous chapter (see section 4.2).

5.4.2 2D Ideograms at 183 GeV

With two W bosons to be fitted, it is more natural and more convenient to do a 2-dimensional convolution. Equation (5.11) can easily be interpreted as such, by letting $\vec{m}'$ represent the combination of the two invariant masses in the event m_1 and m_2. For each combination of masses (m_1,m_2) a 6C constrained fit is done, and the χ^2 from the fit used to derive a goodness-of-fit probability $\propto \exp(-\Delta\chi^2/2)$ as a function of the two masses. The sum of the probability distributions for these jet pairings (Figure 5.5) is then convoluted with a 2D Breit-Wigner of the two W bosons. The advantages of the 2-dimensional approach are:

- No equal mass assumption is needed.
- No relative jet pairing weights have to be used. The solutions in which the two masses prefer to be close to each other will automatically obtain the largest weight by the convolution with a finite width Breit-Wigner
- The background distributions tend to be more flat in 2-dimensional phase space, which makes it more correct to make the assumption that the background is flat (multiplied by a 2D phase space function), which simplifies the likelihood expressions.

Of course in 5-jet events with 10 jet pairings the $1/k_T$ additional weights are still used to take into account the gluon radiation probability.

Further improvements that were developed for the 183 GeV publication [2] are the following:

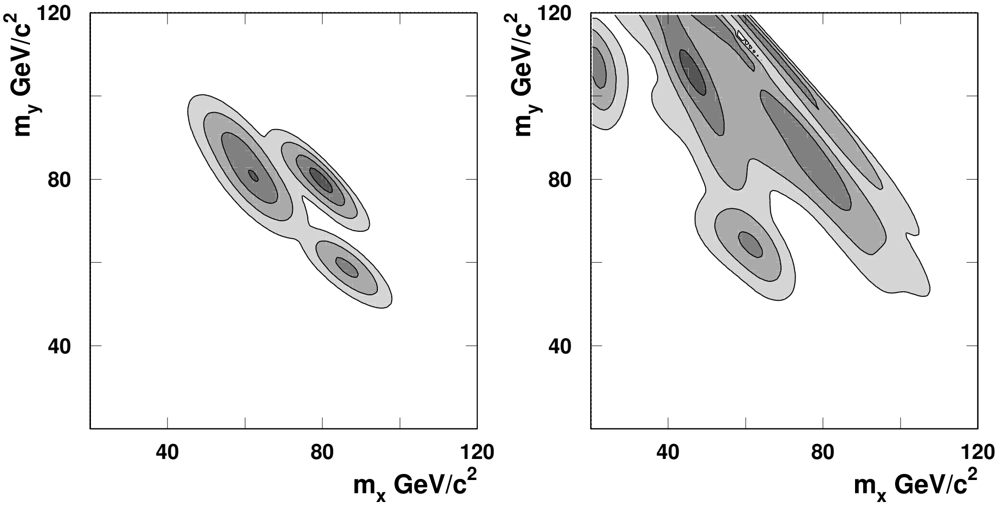

Figure 5.5: *Example of 2D Ideograms as used to analyse the 183 GeV data [2] for a simulated 4-jet event (left) and a 5-jet event (right).*

Improved ISR treatment in the event selection

In order to have a more accurate treatment of ISR in the event selection, especially for photons inside the detector acceptance, SPRIME, a standard DELPHI package, was adopted in the analysis to identify ISR photons inside the detector. Soon it was realised, however, that the kinematic treatment in this package was far from optimal for events with more than two jets (as discussed already in section 4.2 on page 60). Therefore a new algorithm was written, based on a constrained fit with the 'natural' number of jets. The new algorithm was published [5] and used in this analysis as part of the updated DELPHI SPRIME(+) package.

Jet charge

As W bosons are produced preferably in the same direction as the electron with the same electrical charge, and the difference in charge between the W^+ and the W^- is 2e, there is some experimental information in the measured jet charges that can be used to improve the jet-pairing. This will be explained in more detail in chapter 6.

Clustering ambiguity treatment

In the previous chapter (section 4.1) it was shown that different jet clustering algorithms, though giving similar clustering performance on a whole sample of events can give strikingly different clustering results on an event-by-event basis for those events where clustering is ambiguous.

The Ideogram method is well equipped to identify this kind of ambiguity and take it into account in the statistical analysis. By repeating the ideogram construction for three different clustering algorithms (DURHAM, Cambridge and DICLUS), and simply adding the three ideograms with equal weight, a combined ideogram is obtained that contains information about the clustering ambiguity of the event. If an event has clearly resolved jets, all three algorithms will find the same jets, and hence give identical ideograms. In this case the combined ideogram will be identical to the original 'DURHAM' ideogram. Alternatively, if the jet clustering is ambiguous, the ideograms produced using the three different algorithms may differ and lead to a combined ideogram in which the invariant mass information is smeared out. This takes into account more correctly the mass reconstruction ambiguity in such events.

Effectively this identification of ambiguous events will give more weight to unambiguous events, and on average improve the extraction of mass information from the overall event sample. This simple but effective idea led to an improvement of $4\pm1\%$ on the W mass resolution.

5.4.3 Fast 2D Ideograms at 189 GeV

The final improvements to the 2D Ideogram analysis, accepted for publication [3] as analysis of DELPHI 189 GeV data and presented in full in chapter 6, were the following:

Improved ISR treatment in mass reconstruction

With increasing centre-of-mass energy the Initial State Radiation increases almost linearly with the available phase space ($\propto \sqrt{s} - 2m_{\mathrm{W}}$). In most cases the ISR photon escapes undetected down the beampipe, which leads to a z-momentum imbalance and a reduction of the effective centre-of-mass energy, not taken into account in the standard constraints. At 189 GeV this has a significant effect on both resolution and bias in the reconstructed mass in about 20% of the events.

Several attempts to take into account ISR on an event-by-event basis in the analysis failed due to the non-Gaussian nature of the radiated ISR photon energy (see for example Figure 5.6). It turned out to be too difficult to use a first principle approach based on semi-analytical integration combining the *a priori* probability with the detector resolution effects that are Gaussian around the origin, but not in the tails where ISR starts to have a noticeable effect.

In the end a more pragmatic, Monte Carlo-based approach was found to be successful: for those events with fitted p_z^{fit} more than 1.5 σ_{p_z} away from zero, ideograms were reconstructed both for the hypothesis that there was significant ISR, and that there was no significant ISR. The relative probabilities of the two hypotheses to be true were extracted from the Monte Carlo simulation as a function of $|p_z^{\mathrm{fit}}|/\sigma_{p_z}$, and the weighted sum of the two ideograms was used in the analysis.

At 189 GeV this ISR treatment was thus applied to 16% of the events, leading to a 15% improvement in W mass resolution for those events. The other events remained unaffected. The overall positive mass bias caused by ISR was reduced from 353 to 290 MeV/c^2 (at 189 GeV). The treatment of ISR will become more important with increasing $\sqrt{s}$. One of the advantages of this event-by-event approach is that the correction automatically increases when there are more events with collinear ISR radiation. Therefore it will slightly reduce possible ISR systematic effects as well.

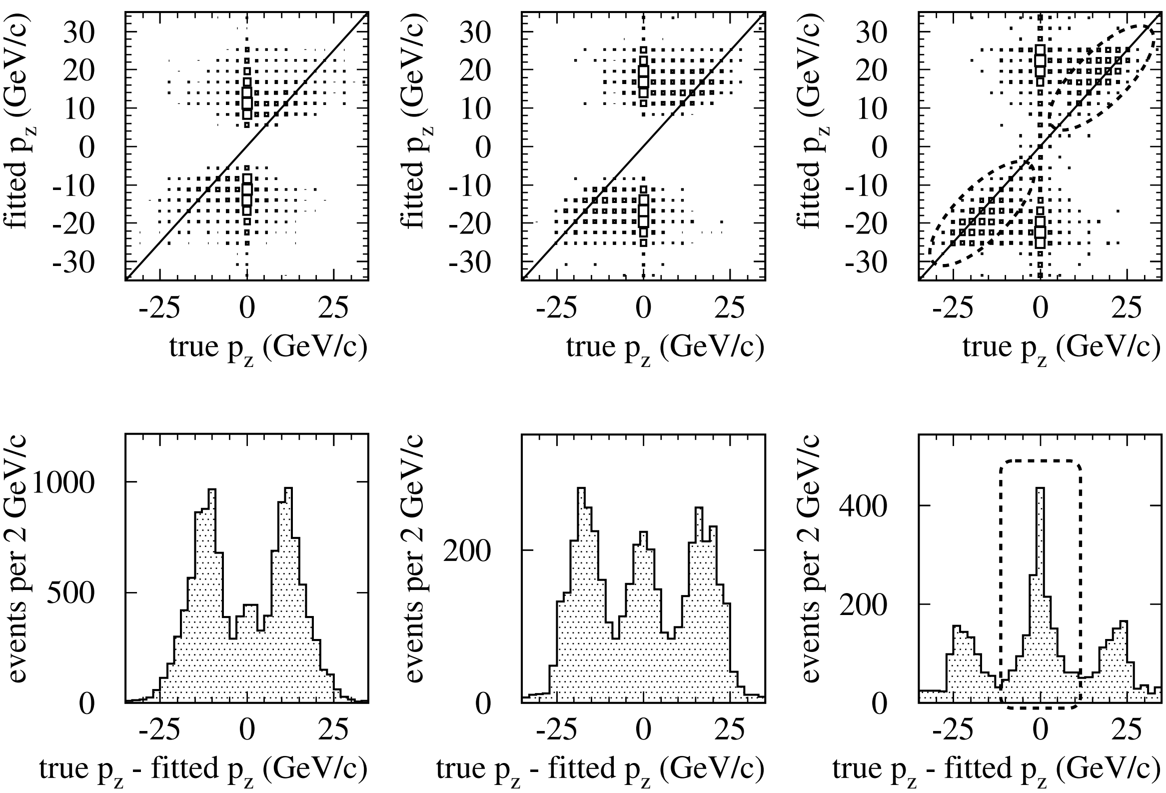

Figure 5.6: *Events with a fitted p_z^γ far away from zero are either badly reconstructed, or had an energetic ISR photon collinear with the beam. In these plots the fitted p_z is compared to the generated p_z (from 189 GeV EXCALIBUR simulation), for selected WW events with a fitted $|p_z^\gamma|/\sigma_{p_z}$ between 1.5 and 2.5 (left), 2.5 and 3.5 (middle) and more than 3.5 (right). The fraction of events with true ISR (encircled with the dashed lines) increases for higher values of $|p_z^\gamma|/\sigma_{p_z}$.*

Faster Ideograms

Perhaps the most significant improvement introduced was a technical one: a small sacrifice in resolution led to a gain in speed of the analysis of a factor 10, by

- reverting to 4C instead of 6C ideograms, using the correlation between the masses as found by the 4C constrained fit, and assuming a 2D Gaussian resolution function for each jet pairing. This reduced the number of fits from $\mathcal{O}(30)$ to one kinematic fit per jet pairing, clustering algorithm and ISR hypothesis.

- introducing a cut on the event purity at 25%. This reduced the number of events to be analysed by 23%, while affecting mass resolution and bias by only 1% and less than 1 MeV/c^2 respectively.

This improvement played a crucial role in speeding up the further development and testing of the analysis. Furthermore it enabled the analysis of systematic effects on millions of simulated events, necessary for an optimal estimation of the systematic errors.

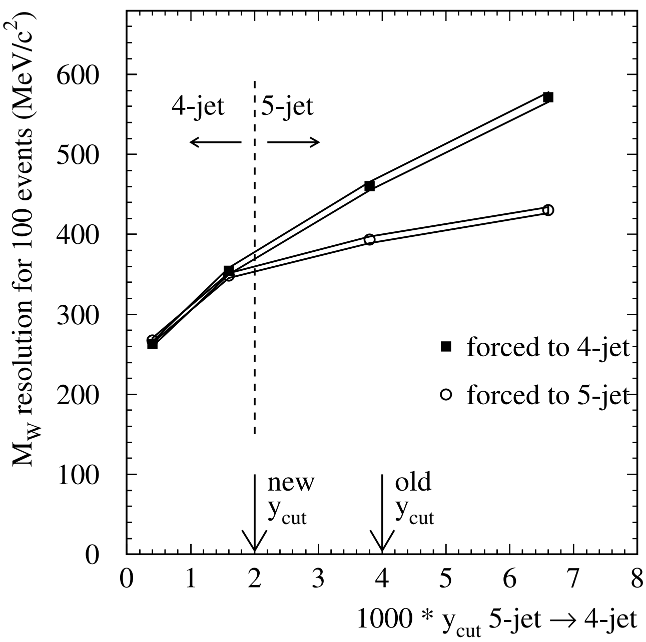

Figure 5.7: *The statistical mass resolution is shown as a function of the* $y_{\rm cut}$ *going from 5 to 4 jets in 4 bins of approximately equal statistics, either when the events are treated as 4-jet (solid squares) or as 5-jet (open circles). The resolution was determined using 189 GeV WW simulation for Poissonian samples with average benchmark size of 100 events. The statistical uncertainty is indicated by the error band. As expected the resolution deteriorates for increasing values of* $y_{\rm cut}$*. This deterioration can be reduced significantly, however, by treating 5-jet events as 5-jet. The plot also shows that for clear 4-jet events the 5-jet treatment performs almost as well as the 4-jet treatment, which proves that also there the 1/*k_T *weight works satisfactorily (creating a smooth transition from the 5-jet to the 4-jet regime).*

Other final 'adjustments' at 189 GeV

- Improved D variable
  The D variable (to be defined later, on page 90), used to discriminate the 4-fermion signal from 2-fermion background, was slightly improved by not only taking into account the lowest jet energy and smallest inter-jet angle, but also the second-smallest energy and angle, thus probing both the difference between 4-jet and 3-jet and the distinction between 3-jet and 2-jet topologies. This improved the optimum product of selection efficiency and purity by about 3% without mass bias.

- Smaller value of $y_{\rm cut}$
  In preparations for the 1999 WW Crete Workshop — in response to inquiries made by OPAL — it was found that an additional gain in resolution would be possible by increasing the fraction of events fitted as 5-jet (see Figure 5.7). This was implemented by reducing the $y_{\rm cut}$ value from 0.004 to 0.002. The fraction of 5-jet events thereby increased from 30% to 50% of the selected WW events. A further reduction of $y_{\rm cut}$ would only increase the

amount of CPU time needed without improvement in the mass resolution.

- Improved background description
  Cross-checks of the shape of the $\mathrm{q\bar{q}}\gamma$ background in the 2D reconstructed mass plane revealed that the shape is actually more flat than had been thought previously. In fact a completely flat description instead of a 2D phase space function turned out to be a better description and gave a small improvement in W mass resolution.

- Introduction of a soft anti-b-tag cut to reduce the background from heavy flavour ZZ events (by 17%) and the QCD backgrounds nearly without loss of WW events, exploiting the fact that the decay of $W \to bq$ is Cabibbo suppressed (section 2.2, page 23).

A further description of this analysis and its results is given in chapter 6-8.

5.5 Application to the semi-leptonic channel

In the $\mathrm{q\bar{q}l}\nu$ channel the mass information per event is less affected by ambiguities than in the $\mathrm{q\bar{q}q\bar{q}}$ channel, as jet clustering and jet pairing do not play a role in separating the decay products of the two W bosons. However, the missing neutrino introduces a new challenge. Depending on the decay angles of the two W bosons the topology of the final state can differ. In some configurations the neutrino causes a larger uncertainty on the fitted mass than in other configurations. This results in a large spread from event to event in the W mass resolution. In order to take the event resolution into account, the published DELPHI results are based on a method that is similar to the 1D ideogram approach — using 1D Gaussian event resolutions and the event purity in calculating likelihood curves for each event [1, 2, 3].

Semi-Leptonic Ideograms

It was realised for the first time at the LEP2 workshop [67] that in some events the missing neutrino can even lead to *double* solutions in the constrained fit, visible as double minima in the χ^2 as function of the mass in an equal mass fit.

Also here the Ideogram method is a natural way to take into account such non-Gaussian resolution functions. First studies with a 2D Ideogram method showed that the convolution of a 2D Breit-Wigner with such a double kinematic solution can even lead to a *triple* ambiguity in the W mass likelihood, as illustrated in Figure 5.8.

To demonstrate the power of 2D ideograms in the semi-leptonic channel in the following chapter also a semi-leptonic 2D Ideogram analysis is described. In this analysis an extra ambiguity is taken into account, viz. the hypotheses that the observed electron or muon either was a direct decay product of a W boson, or just one of the decay products of the tau in a $\mathrm{q\bar{q}}\tau\nu$ event, in which case the constrained fit is slightly different due to the special treatment of the tau.

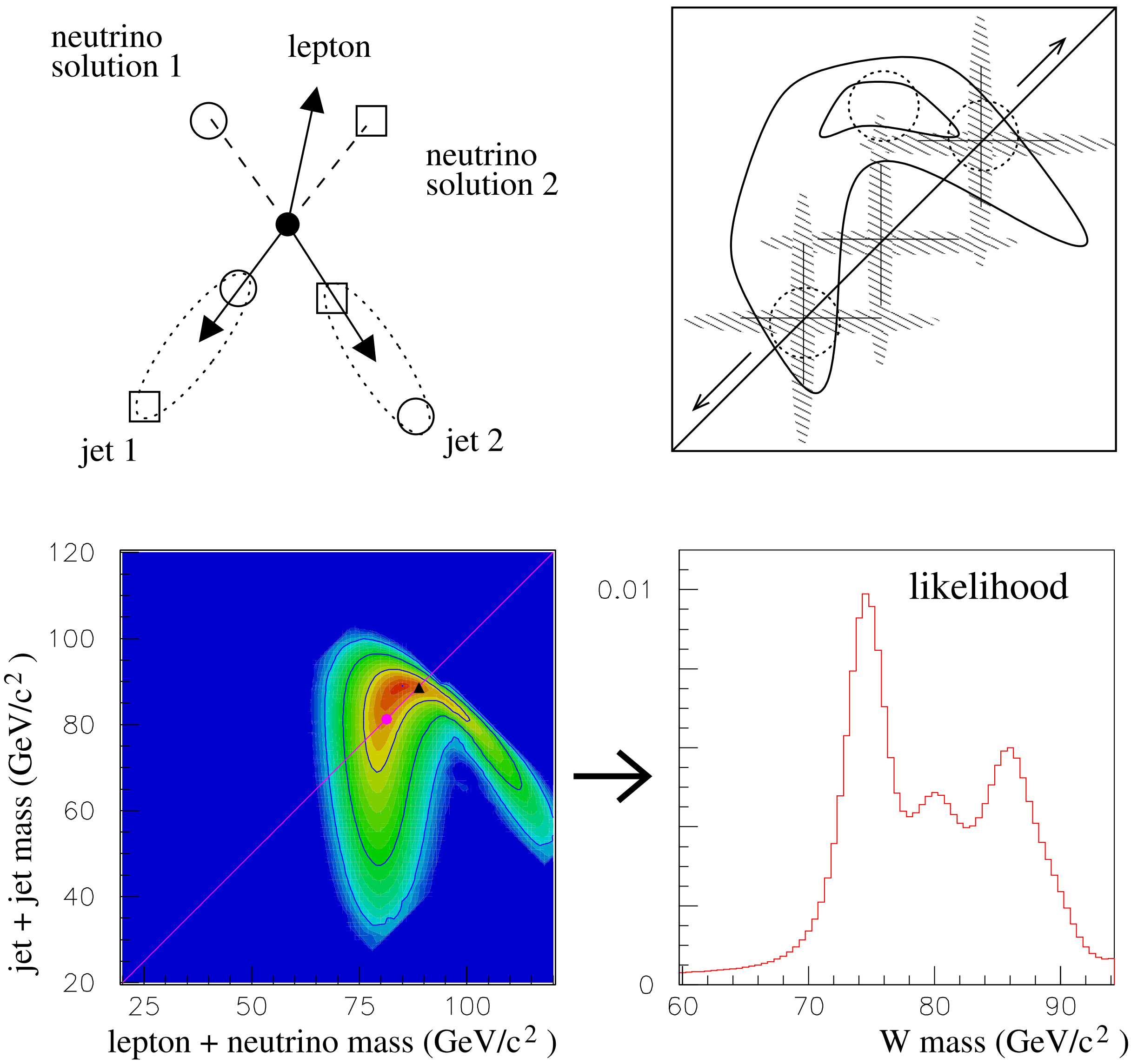

Figure 5.8: *Example of a semi-leptonic 2D Ideogram (bottom left), and the event W mass likelihood curve derived from it (bottom right). In this event the ideogram has a clear non-Gaussian shape, and three maxima are visible in the likelihood curve. The maxima occur for the three values of m_W for which the BW has the largest overlap with the boomerang shaped maximum in the Ideogram (illustrated in the top right plot). For those three cases the region of most significant overlap is indicated by a dashed circle. The boomerang shape is believed to originate from multiple solutions for the reconstruction of the neutrino due to the relatively large errors on the jet energies (top left).*

5.6 Systematics, Jackknife and MLBZ method

All of the W mass analyses discussed in this chapter rely either directly or indirectly on Monte Carlo simulation to correct for detector effects, experimental cuts and statistical approximations made. Imperfections in the Monte Carlo simulation will therefore cause systematic errors in each of these analyses, and the different analyses are expected to have very similar sensitivity to most of these systematic effects.

The addition of the 189 GeV data brought the LEP combined statistical error on the W mass down to the level of the quoted systematic errors. Therefore, extensive studies have been made to better understand possible systematic effects, as described in detail in chapter 7. Regarding this systematics study, in this historical account, two aspects should be mentioned: the use of the Jackknife and the development of the MLBZ method.

Event likelihood curves and the Jackknife

For the W mass measurement systematic effects have to be studied and controlled at the level of a few MeV/c^2. Using the 'brute force' approach, for each possible systematic effect a large number of Monte Carlo events would have to be generated to obtain such a precision: with a typical W mass resolution of about 3 GeV/c^2 per event $\mathcal{O}(1 \text{ million})$ $\mathrm{q\bar{q}q\bar{q}}$ events are needed to reach a precision of 3 MeV/c^2 per effect per channel. The precision of complicated systematic studies therefore easily becomes limited by statistics.

Fortunately, many systematics effects can be studied in a much more powerful and efficient way, applying the (small) systematic disturbance to a sample of generated Monte Carlo events, and taking the difference in fitted W mass with and without applying the effect. By keeping the 4-fermion configurations of the events fixed, this approach can give statistically very precise results. In fact, in most cases the statistical error turns out to be proportional to the size of the effect, which is a most desirable property. But the problem is how to determine the statistical precision, now that the samples with and without systematic effect have become correlated.

It turns out that the Jackknife method (see section 4.4) is an excellent solution to this problem. Especially in combination with event-by-event likelihood curves the Jackknife method provides a convenient and quick way to determine the statistical error on the shift in W mass between two samples containing the same events.

The ability to determine the statistical significance of results found in the systematics studies was a great advantage leading more quickly to more complete and more precise results with modest Monte Carlo requests. The Jackknife method was used in most of the numbers quoted in chapter 7 and played a crucial role to determine the precision of results obtained with the MLBZ method.

MLBZ

With the addition of the 189 GeV data the systematic uncertainty due to possible imperfections in the jet fragmentation modelling emerged as the dominating systematic error quoted on the combined LEP W mass measurement.

The MLBZ method was developed to study a possible systematic effect related to jet reconstruction directly from the data, using hadronic Z^0 events.

The basic idea is to take pairs of hadronic Z^0 events from the Z^0 calibration runs that are taken every year, boost them in opposite direction and then superimpose them emulating a 4-jet hadronic WW event (see Figure 5.9). The W mass analysis is applied directly to these 'Mixed

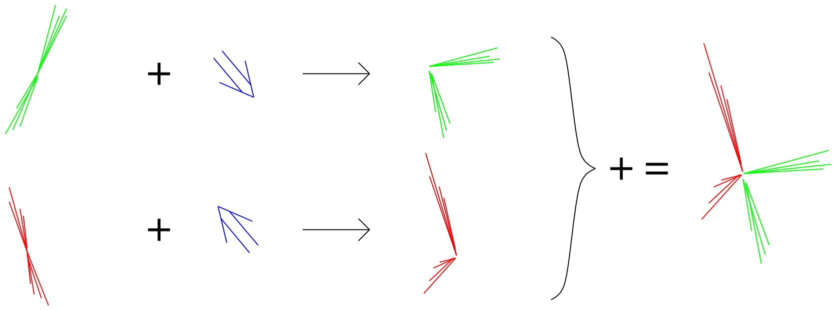

Figure 5.9: *Illustration of the basic principle of the MLBZ method.*

Lorentz Boosted Z^0' events in order to measure the 'Z boson mass' This can be done on data and Monte Carlo simulation separately, and the difference of the measured mass (rescaled to the W mass scale) is a measure of the systematic error on the W mass due to jet reconstruction. A detailed example of an implementation of the MLBZ method is given in Appendix A and its results and interpretation are summarised in chapter 7.

Chapter 6

2D Ideogram analysis

In this chapter a comprehensive description is given of the 2D Ideogram analysis, applied to all DELPHI LEP2 data taken at 172, 183 and 189 GeV. Both the fully-hadronic and semi-leptonic channel are used. The analysis of the fully-hadronic channel presented here has been published in the DELPHI 189 GeV W mass paper [3]. The application to the semi-leptonic channel should be regarded as a feasibility study to show that the 2D Ideograms are suitable for use in the semi-leptonic channel as well.

The analysis is described in the following steps:

- The choice of data sets and run quality selection is discussed in section 6.1
- The selection of events and treatment of particles, which is different for
  - the fully-hadronic channel (section 6.2)
  - and the semi-leptonic channel (section 6.3)
- The construction of an event ideogram containing all measured kinematical information about the event (section 6.4).
- The extraction of an event likelihood curve from the ideogram through analytical convolution (6.5).
- The calibration of the analysis using Monte Carlo simulation (6.6).
- Cross-checks of the statistical properties (6.7).
- Summary (6.8).

6.1 Data sets used

Data run quality selection

The analysis described here was applied to DELPHI data taken in the period from October 1996 to November 1998 at the centre-of-mass energies shown in Table 6.1. Since DELPHI had a policy to only record data when at least a minimum configuration of the DELPHI sub-detectors was operational, the data on tape is generally of good quality. More than 99% of the data on tape was used in the fully-hadronic analysis, requiring the TPC data taking to be $> 90\%$ efficient per run file, and checking the DELANA status flag for TPC data acquisition and high-voltage for each event. For the semi-leptonic channel additional requirements were put on the operational state of the calorimeters, requiring the HPC and the EMF to be $> 95\%$ efficient. During the 1997 data taking, a known problem in the HPC electronics caused a small fraction ($\sim$0.85 %) of the events to have no HPC information at all. All events ($\mathrm{q\bar{q}q\bar{q}}$ and $\mathrm{q\bar{q}l}\nu$) were rejected that could possibly have been affected by this.

	Luminosity weighted mean $\sqrt{s}$ (GeV)	$\int \mathcal{L}$ (pb^{-1}) $\mathrm{q\bar{q}q\bar{q}}$	$\int \mathcal{L}$ (pb^{-1}) $\mathrm{q\bar{q}l}\nu$
October-November 1996	172.3	10.0	10.0
July-November 1997	182.7	53.4	51.9
May-November 1998	188.6	157.4	153.0

Table 6.1: *DELPHI data sets on which the results in this thesis are based*

Monte Carlo simulation

Monte Carlo (MC) generators were used to produce simulated event samples at the nominal centre-of-mass energies corresponding to each of the data sets mentioned above. The main generator for WW-like and ZZ-like 4-fermion final states was EXCALIBUR, while $\mathrm{q\bar{q}}\gamma$ background processes were simulated using PYTHIA. Both generators were interfaced with DELPHI-tuned JETSET fragmentation (section 2.5), supplemented by the full DELSIM detector simulation (section 3.3). The reference samples used for the calibration of the analysis and checks of the statistical performance are listed in Table 6.2.

6.2 Fully-hadronic event selection

Particle reconstruction

Not all reconstructed particles in the events that are read from DST are of good quality. Since the optimal treatment of dubiously reconstructed tracks and energy clusters depends on the type of physics analysis, a customised particle selection is required at analysis level. For the fully-hadronic W mass analysis the November 1999 version of the DELPHI analysis software was used with the following standard particle selection criteria for LEP2 hadronic analyses:
For charged particles:

- track momentum $|\mathbf{p}| > 200$ MeV/c
- relative momentum error $\Delta|\mathbf{p}|/|\mathbf{p}| < 1$

	$\sqrt{s}$ (GeV)	m_W (GeV/c^2)	$\int \mathcal{L}$ (fb^{-1})
PYTHIA WW	172.0	80.35	1.15
		79.85	1.37
		78.35 - 83.35	13 $\times$ 0.17
		79.35, 80.85, 81.35	3 $\times$ 0.20
PYTHIA ZZ			1.68
PYTHIA $q\bar{q}\gamma$			0.519
EXCALIBUR 1.06 WW/ZZ	183.0	80.35	7.20
		79.35	7.18
		81.35	7.17
PYTHIA $q\bar{q}\gamma$			3.589
EXCALIBUR 1.08 WW/ZZ	189.0	80.35	18.52
		79.35	10.08
		81.35	10.11
PYTHIA $q\bar{q}\gamma$	188.0*		9.418
* this MC sample was generated at the start of the year when the average LEP centre-of-mass energy for this run (188.6 GeV) was not yet precisely known.			

Table 6.2: *DELPHI simulation sets used for the analysis in this thesis.*

- impact parameter in $r\phi < 4$ cm
- impact parameter in $z \cdot \sin\theta < 4$ cm
- track length > 30 cm, i.e. rejecting tracks with only ID and VD hits associated.

For neutral particles:

- To distinguish genuine energy deposits from detector noise, a minimum energy was required depending on the calorimeter (500 MeV in the HPC, 400 MeV in the FEMC, 900 MeV in the HAC and 300 MeV in the STIC).

In addition to these standard quality criteria an extra cut was applied to eliminate possible energy depositions from off-momentum beam electrons [70],

- rejecting all particles with a polar angle outside the range $3° < \theta < 177°$

and a special treatment was included to protect the analysis against particles reconstructed with an unphysically high momentum ($p > E_{\rm beam}$). Studies have shown that the 'straight' tracks reconstructed in such cases are often indeed caused by charged particles of fairly high momentum. Therefore charged particles with a momentum larger than 60 GeV/c were rescaled to 10 GeV/c — a value based on the momentum spectrum of particles in a hadronic event. Furthermore charged particles with a momentum between 10 and 60 GeV/c and a relative momentum error larger than 0.3, were rescaled to 10 GeV/c, and for neutral particles any excess of associated energy above 100 GeV was discarded.

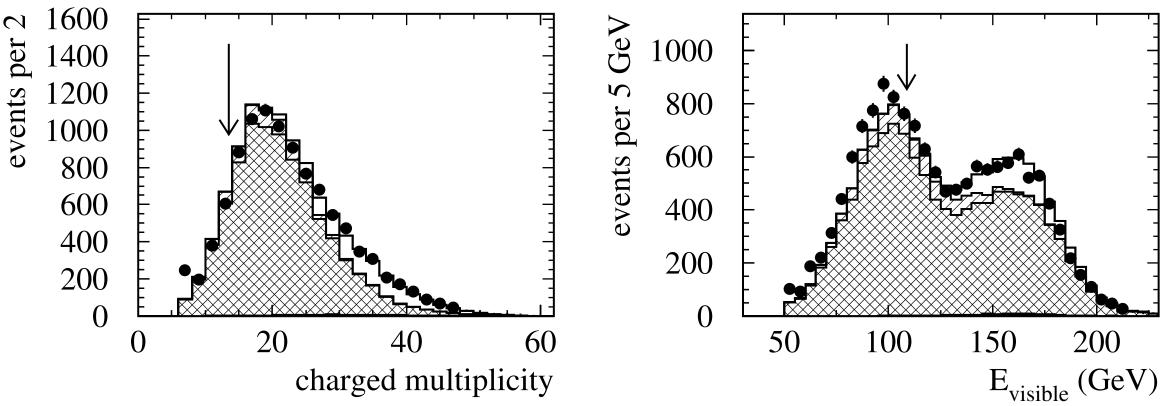

Figure 6.1: *The hadronic pre-selection cuts, shown for 189 GeV data and MC. In the plot of the charged multiplicity (left) only the cut on the visible energy (right) was used and vice versa. The corresponding legend is shown in Figure 6.2.*

Event selection

For the fully-hadronic channel a rather simple event selection based on sequential cuts was used, aiming for a reasonable purity without loss of efficiency for W events that contain useful mass information and without introducing correlations with the mass. The purity of the selection is not crucial for the analysis, because later the likelihood will include the estimated event purity on an event-by-event basis.

First of all a sample of hadronic events was selected requiring more than 13 charged particles and a total visible energy exceeding $0.575\sqrt{s}$ (Figure 6.1). Then the following cuts were applied, the effects of which are illustrated in Figure 6.2:

- A jet clustering was done using the DURHAM algorithm with a y_{cut} fixed to 0.002. All jets were required to be of 'good quality', defined by the following two criteria:
  - an invariant mass of the jet larger than 1 GeV/c^2
  - at least 3 particles

  If necessary, clustering was continued to a higher value of y_{cut} until all resulting jets satisfied these criteria.

- Events with less than 4 jets were rejected and events with 6 jets or more were re-clustered to 5 objects.

- The effective centre-of-mass energy $\sqrt{s'}$ was estimated using the SPRIME+ package (section 5.4.2, page 77) and was required to be larger than $\sqrt{s} - 28$ GeV, mainly in order to remove $\mathrm{q\overline{q}}\gamma$ background from 'radiative returns to the Z'. To improve the purity of the photon identification inside SPRIME+, only candidate photons with less than 3 particles within a cone of opening angle 25.8° = arccos(0.9) were considered to be ISR photons.

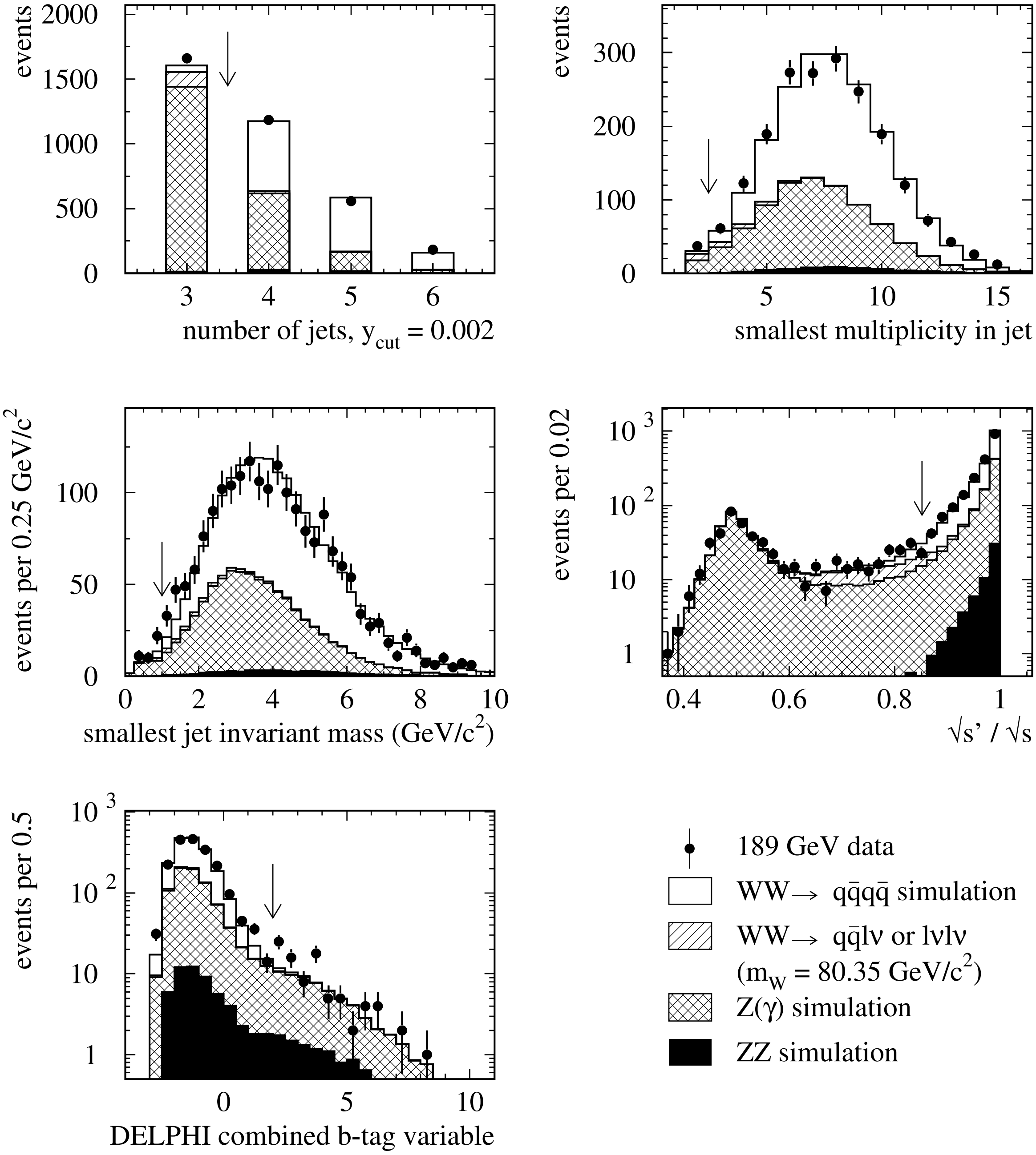

Figure 6.2: *The main* $q\bar{q}q\bar{q}$ *event selection cuts. The sample shown consists of 189 GeV data and MC. In each of the plots all event selection cuts are used, except for the cut on the variable that is shown and without cut on the estimated purity (section 6.2).*

- Events containing clear b-quark candidates were rejected, requiring the DELPHI combined b-tag variable (section 3.5, page 46) to be smaller than 2.0. This cut removed 16.9% of the ZZ and 6.4% of the $q\bar{q}\gamma$ background while reducing the signal efficiency by only 0.2% (numbers for $\sqrt{s} = 189$ GeV).

As visible in Figure 6.2 these cuts are quite loose, i.e. they were chosen to allow a high efficiency for WW$\rightarrow q\bar{q}q\bar{q}$ events (92.3±0.3% at $\sqrt{s} = 189$ GeV).

4C kinematic fit

A 4C kinematic fit was applied to the remaining events, enforcing conservation of energy and momentum. In all fits asymmetric transverse jet errors were used, following the procedure explained in section 4.2.

Event purity

The fitted jets define the topological variable D_{pur} that is used to distinguish 4-fermion from 2-fermion(+ 2 hard gluons) final states and estimate the purity of the event (ZZ events also have a 4-fermion signature and are treated as signal without W mass information).

$$D_{\mathrm{pur}} = \theta^{\mathrm{fit}}_{\mathrm{jj4}} \cdot E^{\mathrm{fit}}_{\mathrm{j4}} \cdot \sqrt{\frac{\theta^{\mathrm{fit}}_{\mathrm{jj3}} \cdot E^{\mathrm{fit}}_{\mathrm{j3}}}{100\,\mathrm{rad}\cdot\mathrm{GeV}}} \tag{6.1}$$

where $E^{\mathrm{fit}}_{\mathrm{j4}}$ and $E^{\mathrm{fit}}_{\mathrm{j3}}$ are the smallest and the one-but-smallest fitted jet energies and $\theta^{\mathrm{fit}}_{\mathrm{jj4}}$ and $\theta^{\mathrm{fit}}_{\mathrm{jj3}}$ are the smallest and one-but-smallest fitted angle between two jets. D_{pur} tends to be high for 4-fermion processes and low for 2-fermion processes as gluon radiation at low angles and small energies is preferred. The purity, i.e. the signal-to-(signal+background) ratio $P^{4\mathrm{f}}(D_{\mathrm{pur}})$, is fitted as a function of D_{pur} as shown in Figure 6.3 using a simple parametrisation given by

$$P^{4\mathrm{f}}(D_{\mathrm{pur}}) = \frac{(\mathrm{A}\cdot D_{\mathrm{pur}})^2 + (\mathrm{B}\cdot D_{\mathrm{pur}})^3}{1 + (\mathrm{A}\cdot D_{\mathrm{pur}})^2 + (\mathrm{B}\cdot D_{\mathrm{pur}})^3} \tag{6.2}$$

resulting in the fitted parameters shown in Table 6.3.

	4-jet		5-jet	
$\sqrt{s}$	A [GeV^{-1}]	B [GeV^{-1}]	A [GeV^{-1}]	B [GeV^{-1}]
172 GeV	0.06091	0.04821	0.09844	0.04644
183 GeV	0.05679	0.08075	0.09463	0.07718
189 GeV	0.03458	0.09266	0.08870	0.07920

Table 6.3: *Fitted parameters for the purity parameterisation given by equation (6.2) at different centre-of-mass energies.*

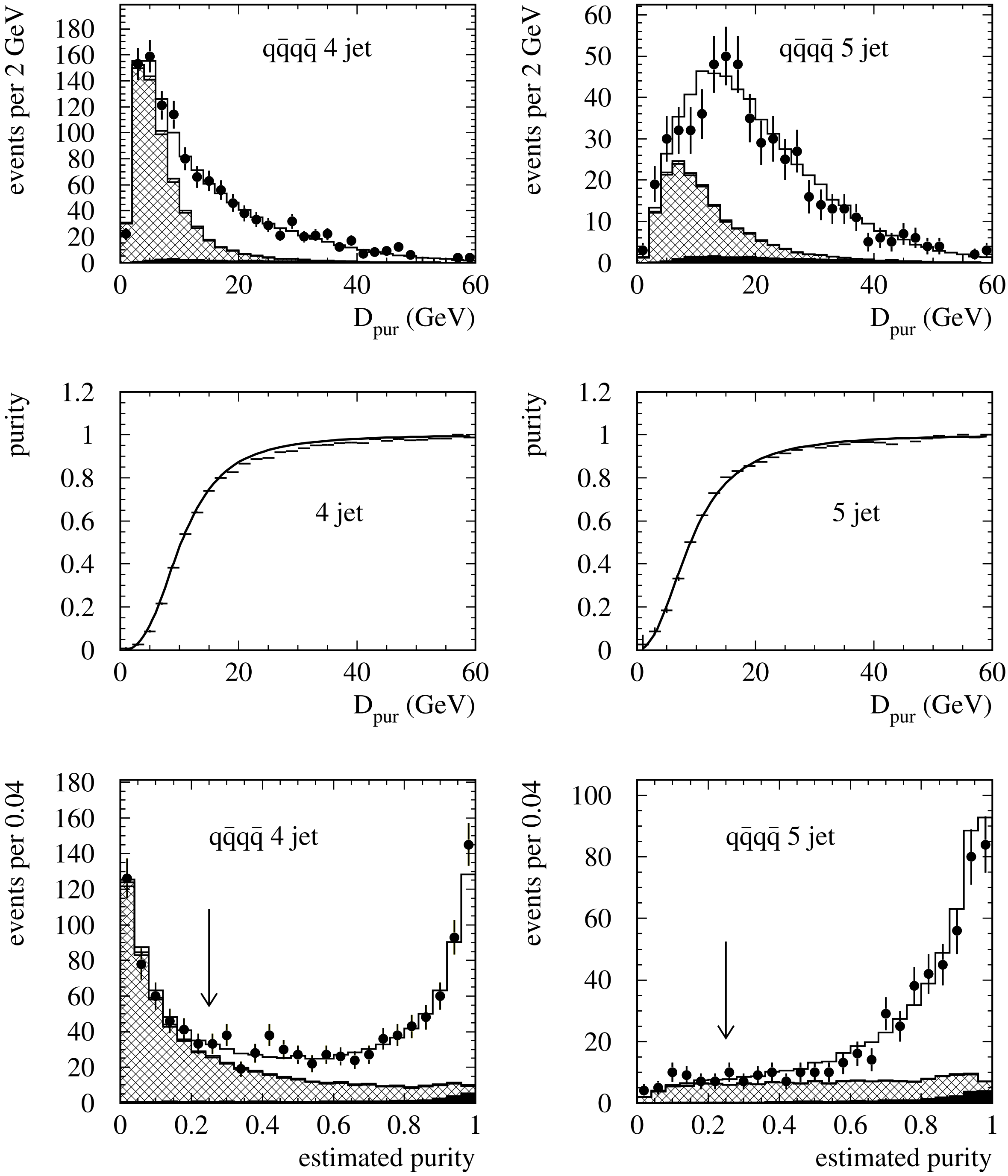

Figure 6.3: *Distribution of the $D_{\rm pur}$ variable for 4-jet (top left) and 5-jet (top right) events separately, for 189 GeV data and MC. The legend is the same as in Figure 6.2. In the middle plots the parameterisations of the $P^{\rm 4f}(D_{\rm pur})$ purity are plotted, used to extract the estimated event purity, for which the resulting distributions are shown in the bottom plots. The arrows indicate the final cut in the* $\mathrm{q\bar{q}q\bar{q}}$ *event selection.*

- As a final $q\bar{q}q\bar{q}$ cut all events with an estimated purity P^{4f} below 25% were rejected (see Figure 6.3). This hardly affects the analysis as events with low estimated purity already obtain a low effective weight in the W mass measurement, but it reduces the use of computing resources, proportional to the number of selected events, by 23%.

All remaining events were then used to extract the W mass, provided that at least one of the equal-mass constrained fits (next section) converges. A small fraction of the events for which this turned out not to be the case were kept in the sample, but obtained a flat likelihood curve. The numbers of selected events and the expectation from Monte Carlo are listed in Table 6.4, and Figure 6.4 shows a few distributions of relevant variables of the selected events.

	$\sqrt{s}$ (GeV)		
Event Type	172	183	189
$q\bar{q}q\bar{q}$	51.2	342.2	1112.7
$q\bar{q}e\nu$	0.3	1.4	4.2
$q\bar{q}\mu\nu$	0.3	1.0	2.5
$q\bar{q}\tau\nu$	0.4	2.5	8.0
Other 4f	0.0	0.0	0.0
$q\bar{q}\gamma$ and other 2f	19.7	123.7	346.9
Total	71.9	470.9	1474.2
Data	73	505	1481
$q\bar{q}q\bar{q}$ efficiency	86.6 %	87.8 %	89.7 %
$q\bar{q}q\bar{q}$ purity	71.2 %	72.7 %	75.5 %

Table 6.4: *Expected number of selected events in the* $q\bar{q}q\bar{q}$ *channel according to simulation at different centre-of-mass energies compared to the number of events selected from data.*

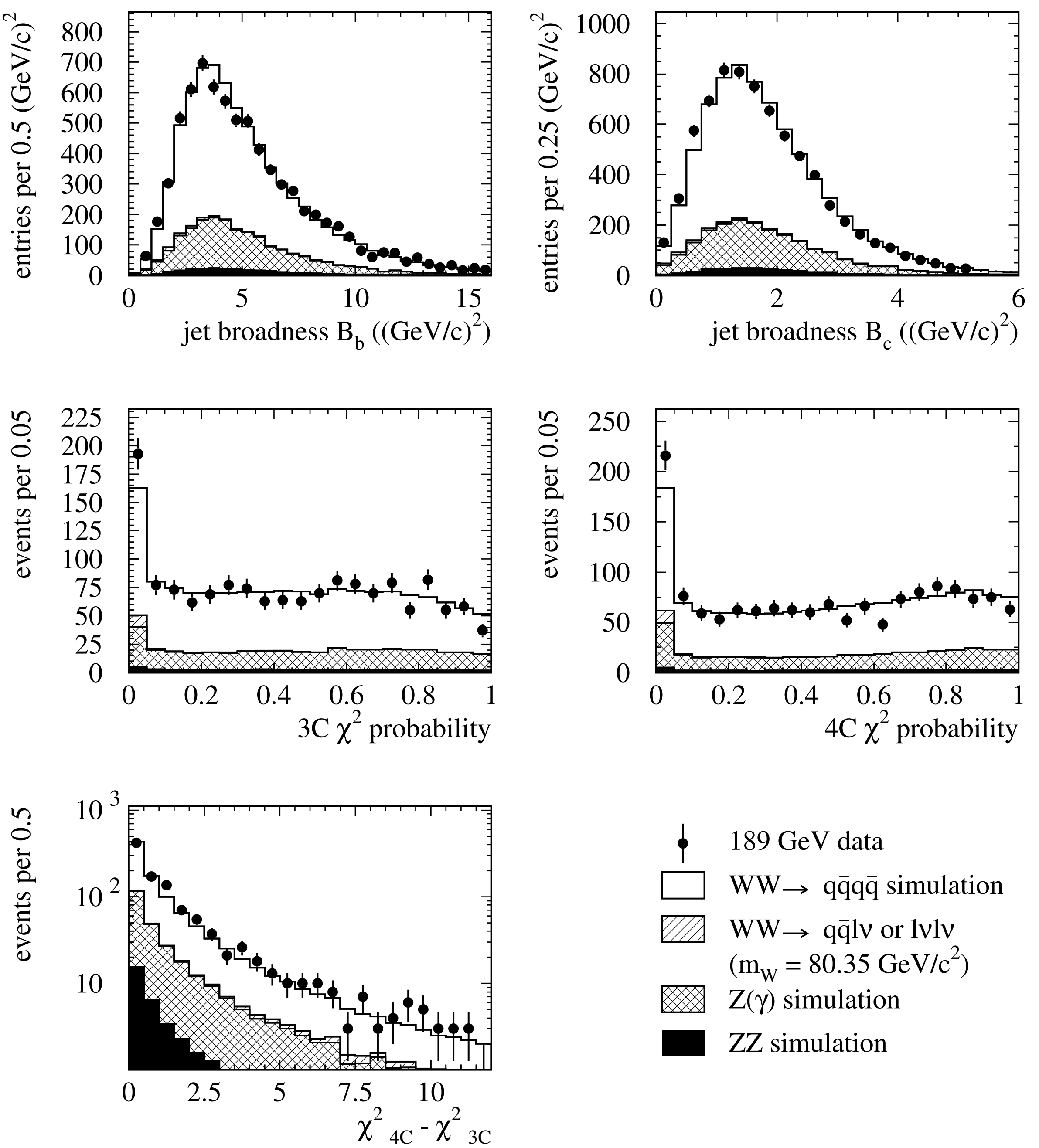

Figure 6.4: *Distribution of some relevant* q$\bar{q}$q$\bar{q}$ *event variables, for 189 GeV data and MC. The jet broadness values B_b and B_c are the eigenvalues of the momentum tensor given in equation (4.12). The 3C and 4C χ^2's refer to the constrained fits with and without the assumption of an unseen ISR photon in the beam-pipe. A large difference $\chi^2_{4C} - \chi^2_{3C}$ indicates an imbalance of momentum in the z direction, most likely caused by ISR, a neutrino, or bad reconstruction of the event.*

6.3 Semi-leptonic event selection

Particle reconstruction

The feasibility study for Ideograms in the semi-leptonic channel was based on the analysis framework provided by the WW physics package WWANA 6.10 [53] using the standard SKELANA 2.0 particle selection [52].

Event selection

The event selection for the semi-leptonic channel was designed to be simple and optimised for a high 'inclusive' efficiency for all semi-leptonic channels combined. Cross-feed between the different semi-leptonic channels was not considered to be a special concern as this is taken into account in the analysis later. Lepton tags, energies and energy resolution were taken from the WWANA 6.10 package (section 3.4), and the events were treated as follows:

- Only events with a charged particle multiplicity between 4 and 40 were considered, to reduce the background from di-lepton events and fully-leptonic or fully-hadronic WW events.

- Lepton candidates were searched for in a polar angular range from 5° to 175°, satisfying either one (or both) of the following two signatures:

  - A single isolated track tagged as electron or muon with a momentum larger than 20 GeV/c, with an energy less than 10 GeV from other particles in a cone with a 10° opening angle, and an angle with the nearest jet larger than 5°.
  - A narrow, low-multiplicity jet (at most 5 particles of which at least 1 but at most 3 charged) obtained when clustering the event in 3 jets, with a minimum momentum of 5 GeV/c and satisfying the same isolation criteria as above.

- In case more than one lepton was found, the candidates were arranged in order of preference based on the product of momentum and isolation angle (w.r.t. the nearest charged track with momentum larger than 1 GeV/c).

- Events with at least one lepton candidate were classified as follows:

  - If one of the candidates was a muon the event was classified as $q\bar{q}\mu\nu$ event.
  - Otherwise if an electron candidate was available the event was treated as $q\bar{q}e\nu$.
  - Otherwise the event was classified as $q\bar{q}\tau\nu$.

For events passing the pre-selection, the hadronic part of the event (after excluding the lepton) was clustered in the natural number of jets. And finally only events were accepted with an estimated event purity $\mathcal{P}_{\text{event}}$ larger than 25%, where $\mathcal{P}_{\text{event}}$ signifies the estimated probability that it was a semi-leptonic WW event. Its calculation is discussed in the next paragraph.

Calculation of the semi-leptonic event purity

The purity was estimated using a likelihood ratio based on 10 event variables:

1. Charged multiplicity n_c
2. Sphericity $S \equiv \frac{3}{2}(\lambda_2 + \lambda_3)$, where λ_2 and λ_3 are the two smallest eigenvalues of the sphericity tensor
$$\mathbf{S}^{\alpha\beta} = \frac{\sum_i p_i^\alpha p_i^\beta}{\sum_i |p_i|^2} \tag{6.3}$$
3. Estimated effective centre-of-mass energy $\sqrt{s'}$
4. Size of the missing momentum $|\mathbf{p}_{\text{miss}}|$
5. The cosine of the polar angle of the missing momentum vector cosθ_{miss}
6. Size of the lepton momentum $|\mathbf{p}_{\text{lepton}}|$
7. Isolation angle θ_{iso} of the lepton with respect to the closest particle with an energy of more than 1 GeV
8. Product of the cosine of the polar angle of the lepton momentum and its charge: $Q_{\text{lepton}} \cdot$ cosθ_{lepton}
9. Fitted polar angle θ_{W^-} of the W$^-$
10. Angle between the two jets θ_{jj} when the event is forced into a 2 jets + lepton configuration

For each lepton channel the distributions of signal and background for each of these variables were normalised to 1, and the signal over background ratios $(\frac{s}{b})_i$ were plotted and parametrised. The overall signal-to-background likelihood ratio was then estimated using a simplified expression:
$$(\frac{s}{b})_{\text{total}} = \frac{\sigma_{\text{signal}}^{\text{acc}}}{\sigma_{\text{background}}^{\text{acc}}} \cdot \prod_{i=1}^{10} (\frac{s}{b})_i \cdot a_{\text{corr}} \tag{6.4}$$
where $\sigma_{\text{signal}}^{\text{acc}}$ and $\sigma_{\text{background}}^{\text{acc}}$ are the accepted cross-section for signal and background after the event pre-selection, and a_{corr} a correction factor to be determined by hand for each lepton channel and $\sqrt{s}$ in order to take into account part of the correlations between the likelihood variables. In absence of correlations a_{corr} should equal 1. From the overall signal to background ratio it is straightforward to calculate the estimated purity
$$\mathcal{P}_{\text{event}} = \frac{s}{s+b} = \frac{(\frac{s}{b})_{\text{total}}}{(\frac{s}{b})_{\text{total}} + 1} \tag{6.5}$$
In order to cross-check the result and determine a_{corr}, the $s/(s+b)$ ratio obtained from MC simulation (≡ 'true' purity) was plotted as a function of the estimated purity. As visible in Figure 6.5, the agreement between estimated and true purity is quite reasonable. The numerical values found for a_{corr} ranged from about 0.02 in the electron and tau channel to unity in the muon channel. Distributions of the variables used are shown in Figure 6.6, while Figure 6.7 shows the resulting

$(\frac{s}{b})_i$ parameterisations obtained for the tau channel as an example. Table 6.5 and 6.6 give an overview of the selection efficiencies and expected number of events determined using the Monte Carlo samples listed in Table 6.2.

process	Efficiency (%) for selection as muon	electron	tau	(not selected)
$q\bar{q}\mu\nu$	88.3	0.1	2.7	8.8
$q\bar{q}e\nu$	0.2	68.3	9.7	21.7
$q\bar{q}\tau\nu$	7.5	6.8	35.9	49.8
other 4f	0.1	0.2	0.6	98.8
$q\bar{q}\gamma$	0.0	0.4	0.5	99.1
process	Selection purity (%) in channel muon	electron	tau	
$q\bar{q}\mu\nu$	87.2	0.1	3.7	
$q\bar{q}e\nu$	0.2	74.8	14.2	
$q\bar{q}\tau\nu$	7.4	7.0	49.5	
other 4f	3.1	2.8	5.4	
$q\bar{q}\gamma$	2.0	15.3	27.2	

Table 6.5: *Selection efficiencies and purities for the* $q\bar{q}l\nu$ *channel at* $\sqrt{s} = 189$ *GeV*

Number of events	Expected	Observed in data
172 GeV μ-channel	18.3	17
e-channel	15.1	15
τ-channel	11.3	18
183 GeV μ-channel	114.9	129
e-channel	109.4	121
τ-channel	74.5	86
189 GeV μ-channel	373.7	338
e-channel	367.4	372
τ-channel	267.2	280

Table 6.6: *Number of events selected in the* $q\bar{q}l\nu$ *channel at different energies compared to the number of events expected from MC simulation.*

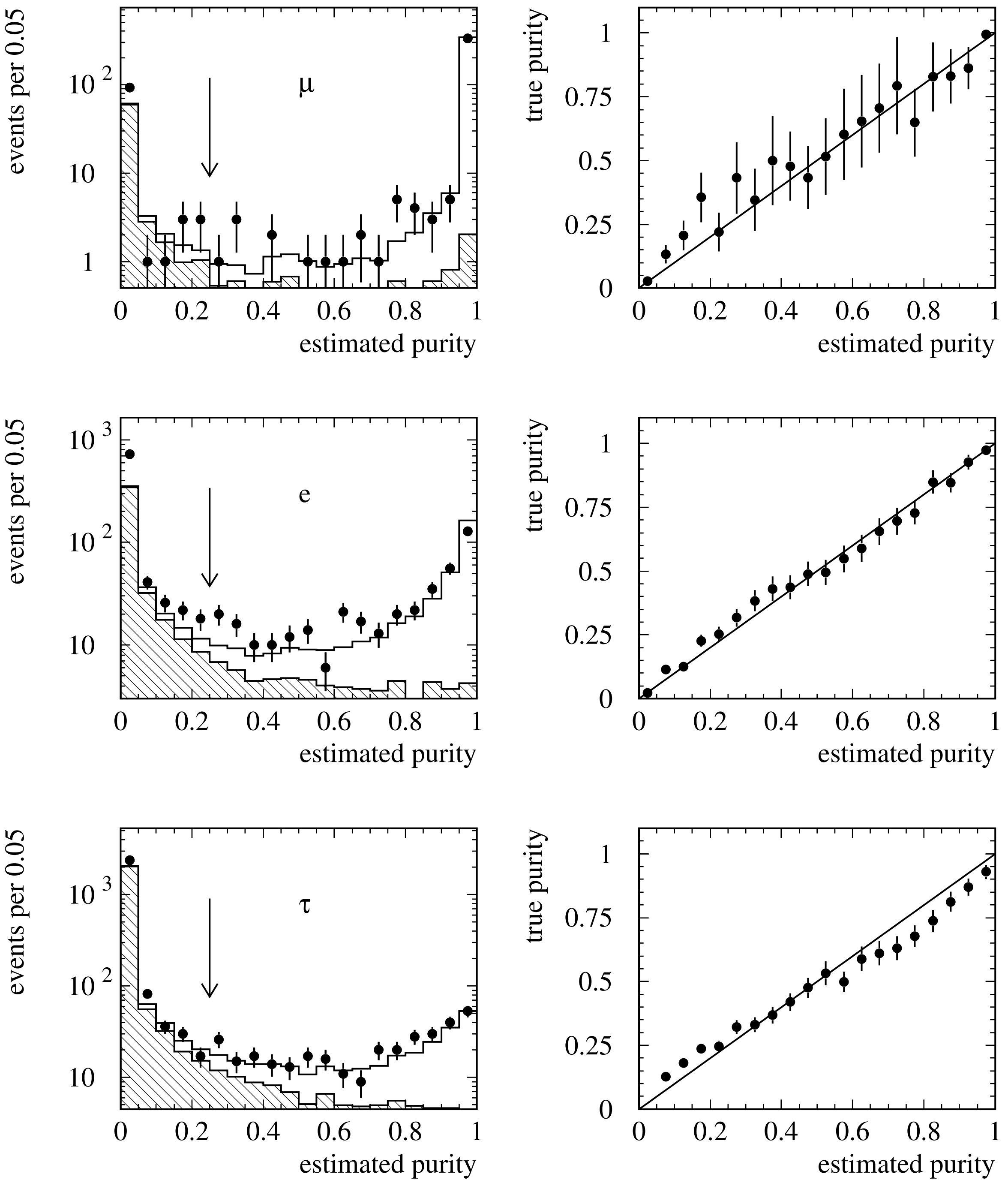

Figure 6.5: *Purity distributions obtained for the different channels at a centre-of-mass energy of 189 GeV.*

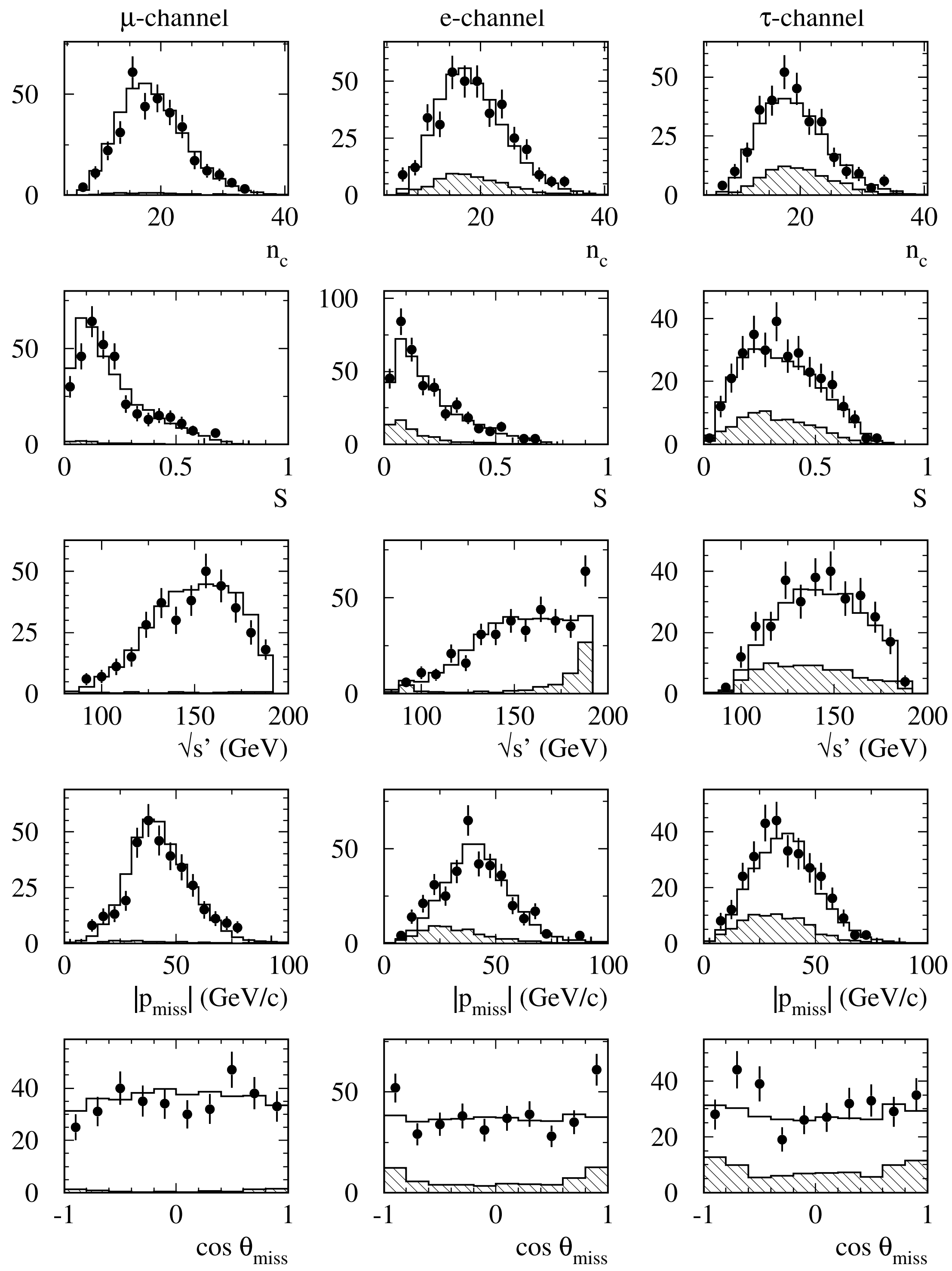

Figure 6.6: *Distributions of the variables used for the purity estimation in the* $\mathrm{q\bar{q}l}\nu$ *channels after full selection — including the final cut requiring* $\mathcal{P}_{\mathrm{event}} > 0.25$*. The points with error bars indicate 189 GeV data, while the histograms include Z*γ *(shaded) and WW+ZZ simulation.*

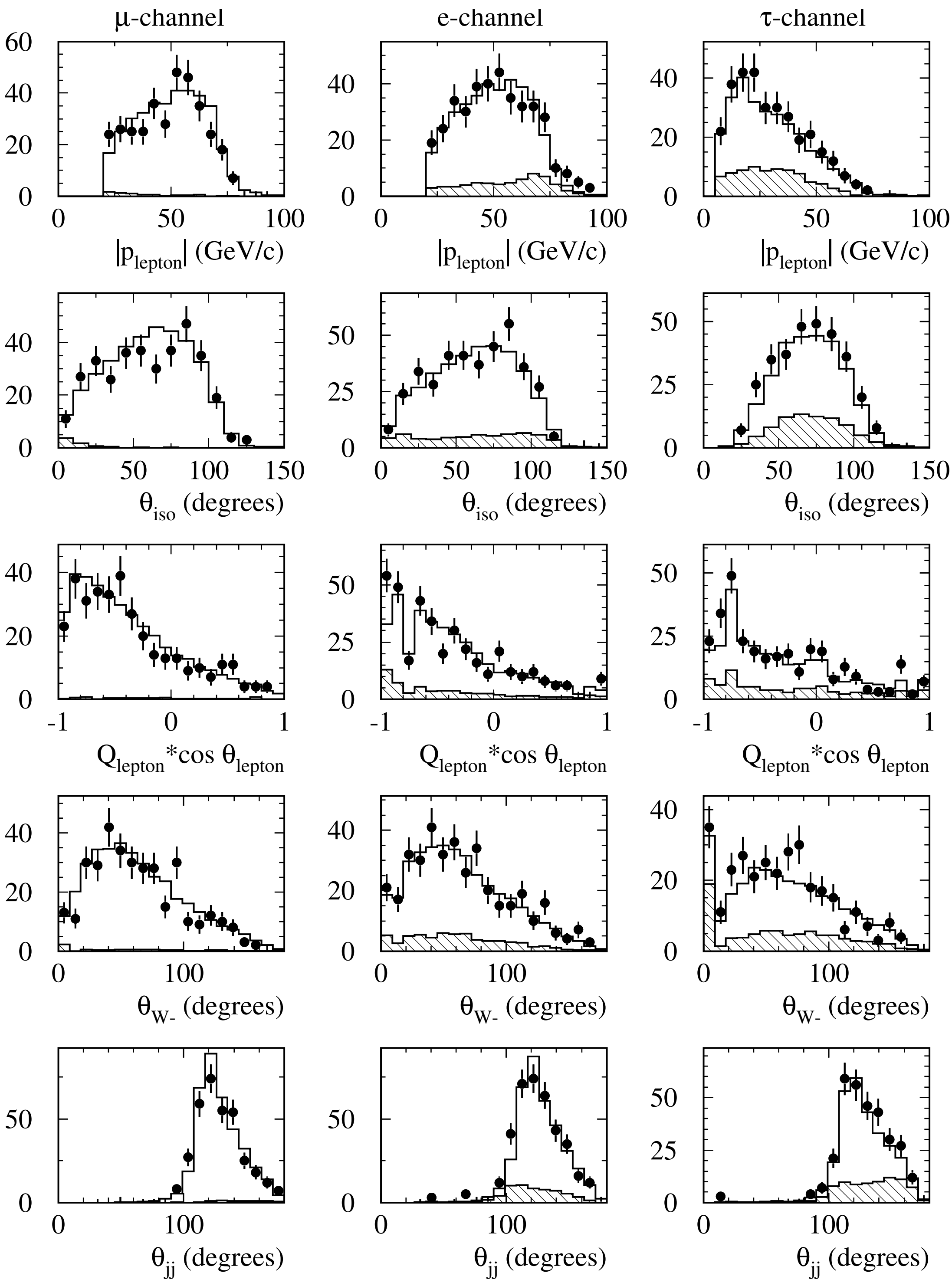

Figure 6.6, *cont'd*

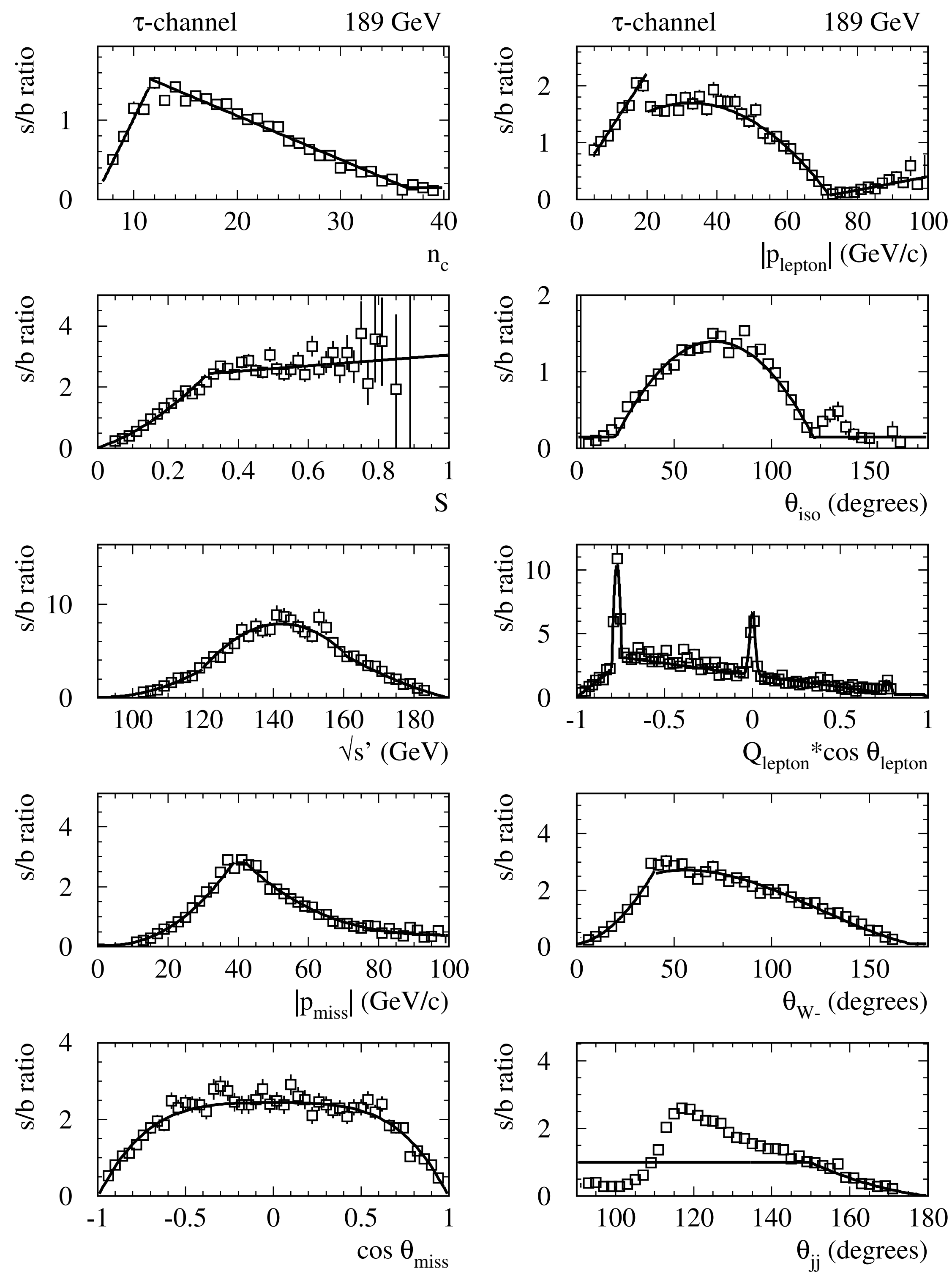

.

Figure 6.7: *The parameterisations of the likelihood ratios used in the calculation of the estimated purity in the tau channel at* $\sqrt{s} = 189$ *GeV. The parameterisation as a function of* θ_{jj} *was delibirately chosen such as not to follow the structure of the peak, because of its direct correlation with the W mass.*

6.4 Kinematical event reconstruction

Now that the events have been selected, their WW purity estimated, and the constrained fits have been prepared, the next step is to fully reconstruct the kinematics of the event under the assumption that two heavy vector bosons were produced with masses m_1 and m_2. The aim is to produce the 2-dimensional Ideogram $\mathrm{p}(event|\overrightarrow{m}', I)$ (equation (5.16)), representing the relative likelihood (from the goodness-of-fit) that the event is kinematically compatible with this assumption as a function of the two masses m_1 and m_2.

6.4.1 Equal-mass constrained fit

In order to obtain a first impression of the mass information in the events, 1-dimensional mass spectra are made using a 5C equal mass constrained fit. Both in the $\mathrm{q\bar{q}l}\nu$ and the $\mathrm{q\bar{q}q\bar{q}}$ channel more than one hypothesis is possible. For each hypothesis a 5C fit is performed and the most probable solution is plotted.

Fully-hadronic channel

For the 1-dimensional mass plot in the $\mathrm{q\bar{q}q\bar{q}}$ channel only the hypotheses without ISR and using the DURHAM clustering algorithm are considered, thus reducing the number of hypotheses to 3 possible jet pairings in a 4-jet event, and 10 in a 5-jet event. For each jet pairing k a constrained fit is performed, leading to a different $\chi^2_{5\mathrm{C},k}$ per pairing, depending on its compatibility with the equal-mass constraint. In addition to the $w_k^{\mathrm{gluon}} \equiv 1/k_T$ pairing probability for 5-jet events (section 5.2), jet charges Q^j_{jet} are used to further improve the choice of the correct jet pairing. The jet charge is defined as

$$Q^j_{\mathrm{jet}} \equiv \sum_{i=1}^{n^j_{\mathrm{c}}} q_i \cdot \left(\frac{|\mathbf{p}_{\|\mathrm{i}}|}{1\mathrm{GeV}/c}\right)^{\kappa} \tag{6.6}$$

with κ =0.5, and summing over all n_{c} charged particles i in jet no. j where q_i is the charge of particle no. i and $\mathbf{p}_{\|\mathrm{i}}$ its momentum parallel to the axis of jet j. For each jet pairing k the measured boson charges Q_k^{W1} and Q_k^{W2} are calculated as the sum over the jet charges in each W boson (see the distribution shown in Figure 6.8). The probability $\mathrm{p}_{\mathrm{W}^+}$ that W_1 corresponds to W^+ is extracted as a function of $\Delta Q_k \equiv Q_k^{\mathrm{W}_1} - Q_k^{\mathrm{W}_2}$. Then the distribution of the W^+ production angle $P_{\theta+}(\theta_{\mathrm{W}^+})$ (section 2.1) is used to determine the relative likelihood for each jet pairing:

$$w_k^{\mathrm{charge}} = \mathrm{p}_{\mathrm{W}^+}(\Delta Q_k) \cdot P_{\theta+}(\theta^k_{\mathrm{W}_1}) + (1 - \mathrm{p}_{\mathrm{W}^+}(\Delta Q_k)) \cdot P_{\theta+}(\pi - \theta^k_{\mathrm{W}_1}) \tag{6.7}$$

In Figure 6.9 one mass per event is plotted, choosing the jet pairing with the lowest $\chi^2_{\mathrm{total,q\bar{q}q\bar{q}}}$ where

$$\chi^2_{\mathrm{total,q\bar{q}q\bar{q}}} = \chi^2_{5\mathrm{C}} - 2 \cdot \ln(w_k^{\mathrm{charge}}) - 2 \cdot \ln(w_k^{\mathrm{gluon}}) \tag{6.8}$$

thus using the extra information from jet charge and hard gluon emission.

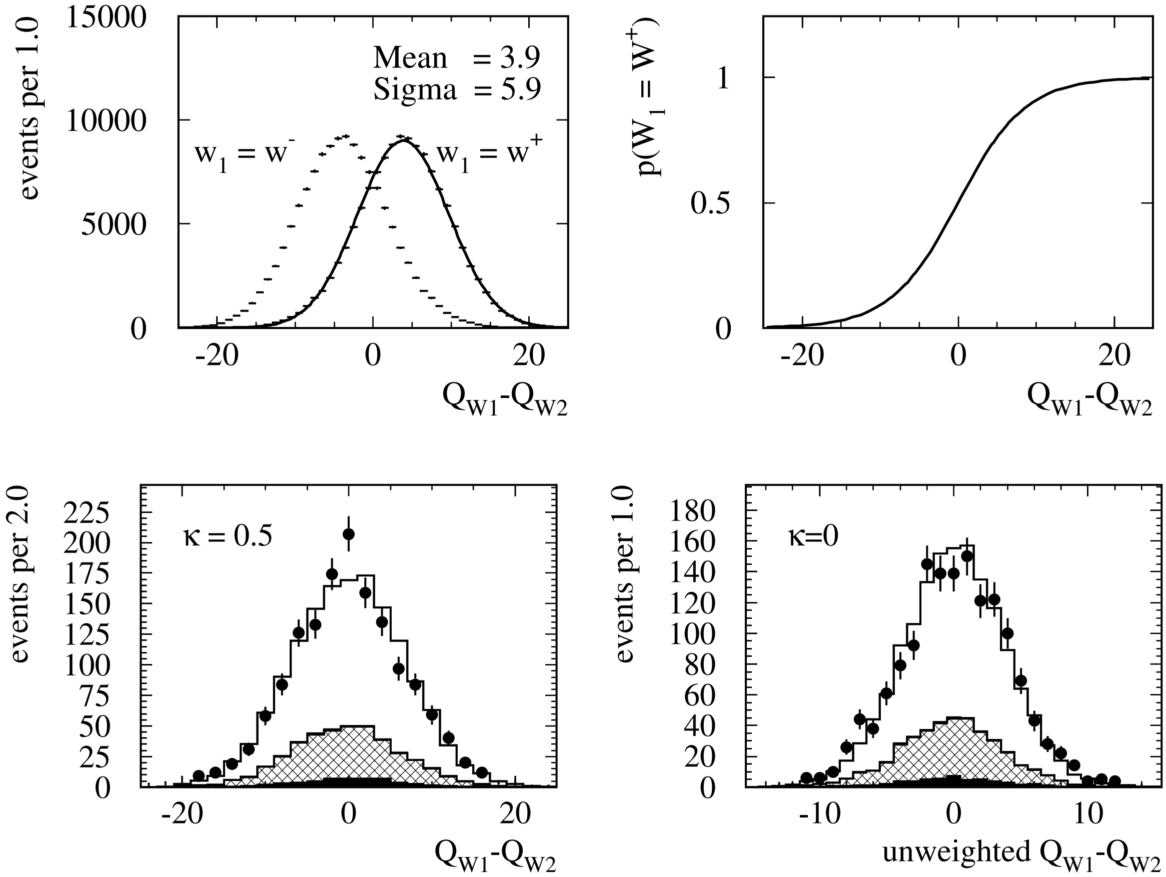

Figure 6.8: *The jet pairing closest to the true generated W bosons is chosen using MC information, and the distribution of measured charge difference of the respective bosons* $\Delta Q_{k\text{`correct'}}$ *is plotted for 189 GeV WW simulation and fitted with a Normal distribution (top left). The fitted Gaussian is used to calculate p*($\mathrm{W}_1 = \mathrm{W}^+$) *(top right), representing the probability that a supposed W boson with a measured charge difference* ΔQ_k *with respect to the other W boson in the event indeed is the positively charged W boson, provided the respective jet pairing* k *is the 'correct' jet pairing. The bottom plots contain the same distributions of* ΔQ_k *for data and MC, but choosing the most probable jet pairing in the analysis, without using generator level information.*

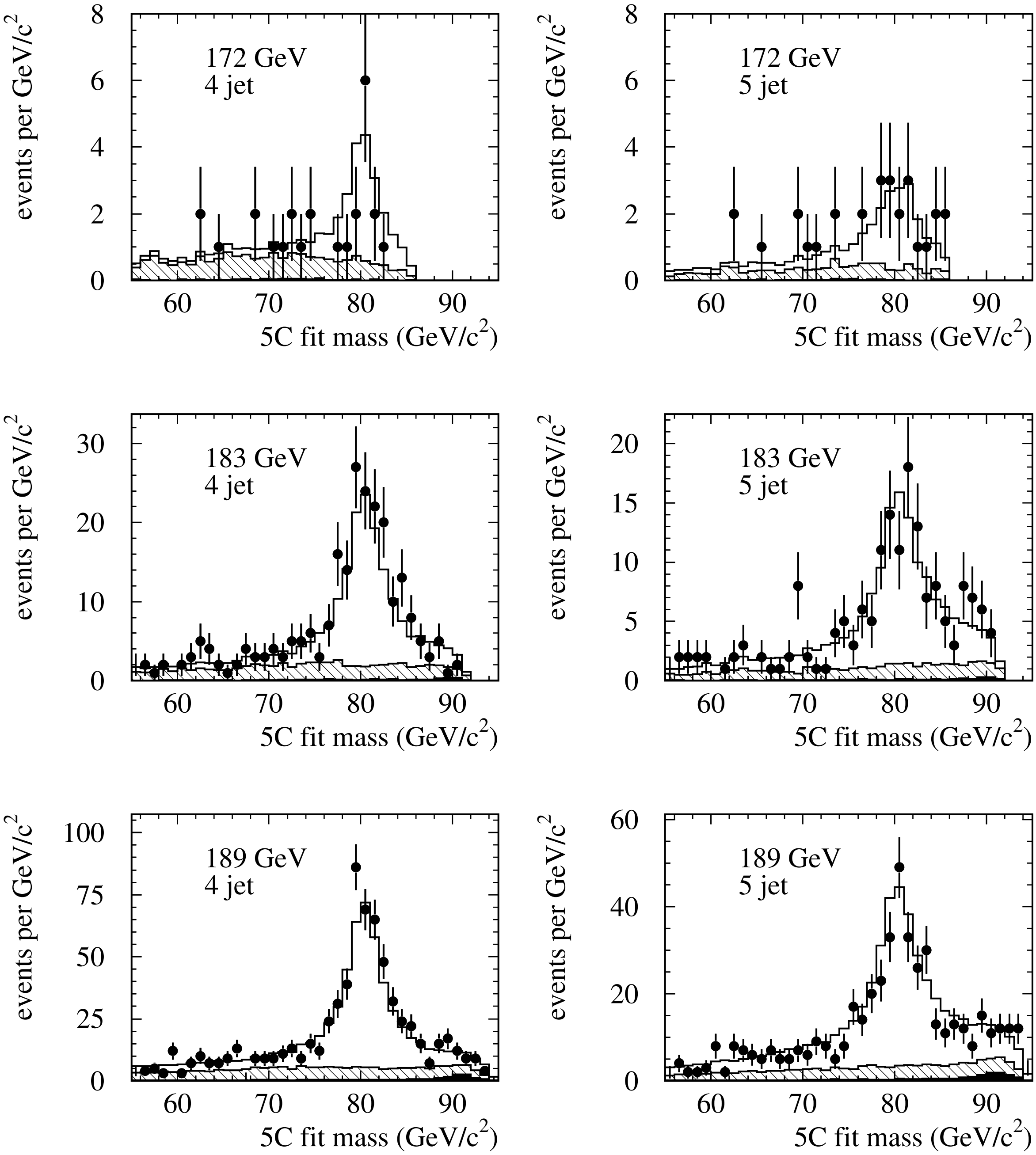

Figure 6.9: *Mass spectra from a constrained fit using an equal-mass constraint at different energies. The jet pairing is chosen that gives the lowest* $\chi^2_{\mathrm{total,q\bar{q}q\bar{q}}}$ *(equation (6.8)).*

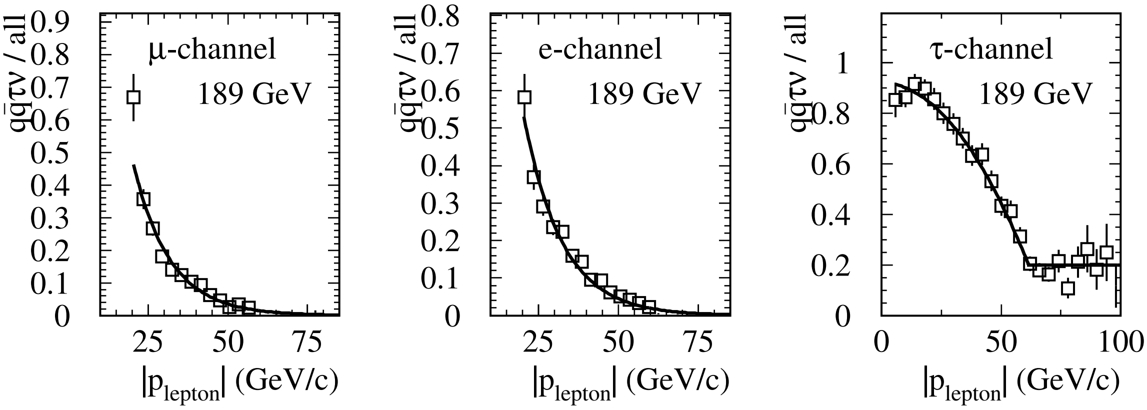

Figure 6.10: *The fraction of* $q\bar{q}\tau\nu$ *events in each of the* $q\bar{q}l\nu$ *channels after full selection shown as a function of the lepton momentum at 189 GeV. The functions shown were used to give relative weights to the tau and the non-tau hypotheses in the analysis.*

Semi-leptonic channel

As shown before (see Table 6.5) cross-feed occurs between the different $q\bar{q}l\nu$ channels. Whereas the cross-feed between the electron and the muon channel is small, this is not true between the tau channel and both of the other channels. Mis-identification of tau events as $q\bar{q}\mu\nu$ or $q\bar{q}e\nu$ is to be expected when the tau decays leptonically, resulting in an isolated electron or muon. Cross-feed in the opposite direction is dominated by electrons showering as a result of secondary interactions with 'dead' material at 90 degrees and in the gaps between barrel and endcaps (at 40 and 140 degrees), resulting in multiple tracks. When these are not recognised as an electron by the REMCLU package they might consequently be reconstructed as a tau jet. This effect is believed to be the cause of the narrow peaks in Figure 6.7 for the purity as a function of $Q_{\text{lepton}} \cdot \cos\theta_{\text{lepton}}$. To take this cross-feed into account, each event is fitted according to two hypotheses:

1. The lepton was a tau. In this case two additional neutrinos were lost, decreasing the kinematical information carried by the lepton. The constrained fit treats the lepton as a tau.
2. The lepton was an electron or a muon. In the $q\bar{q}e\nu$ and the $q\bar{q}\mu\nu$ channel the corresponding assumption for the lepton is used. In the $q\bar{q}\tau\nu$ channel, for this hypothesis the supposed tau candidate is defined as an electron in the fit.

The relative probability $w_k^{\tau/\text{non}-\tau}$ of each hypothesis $k = 1, 2$ to be correct is estimated as a function of the lepton momentum, using parameterisations extracted from MC simulation as shown in Figure 6.10 for $\sqrt{s} = 189$ GeV. An effective χ^2 is calculated as

$$\chi^2_{k,\text{total},q\bar{q}l\nu} = \chi^2_{5C,k} - 2 \cdot \ln(w_k^{\tau/\text{non}-\tau}) \tag{6.9}$$

and for each event the solution with the lowest $\chi^2_{k,\text{total},q\bar{q}l\nu}$ is plotted as in Figure 6.11 and 6.12.

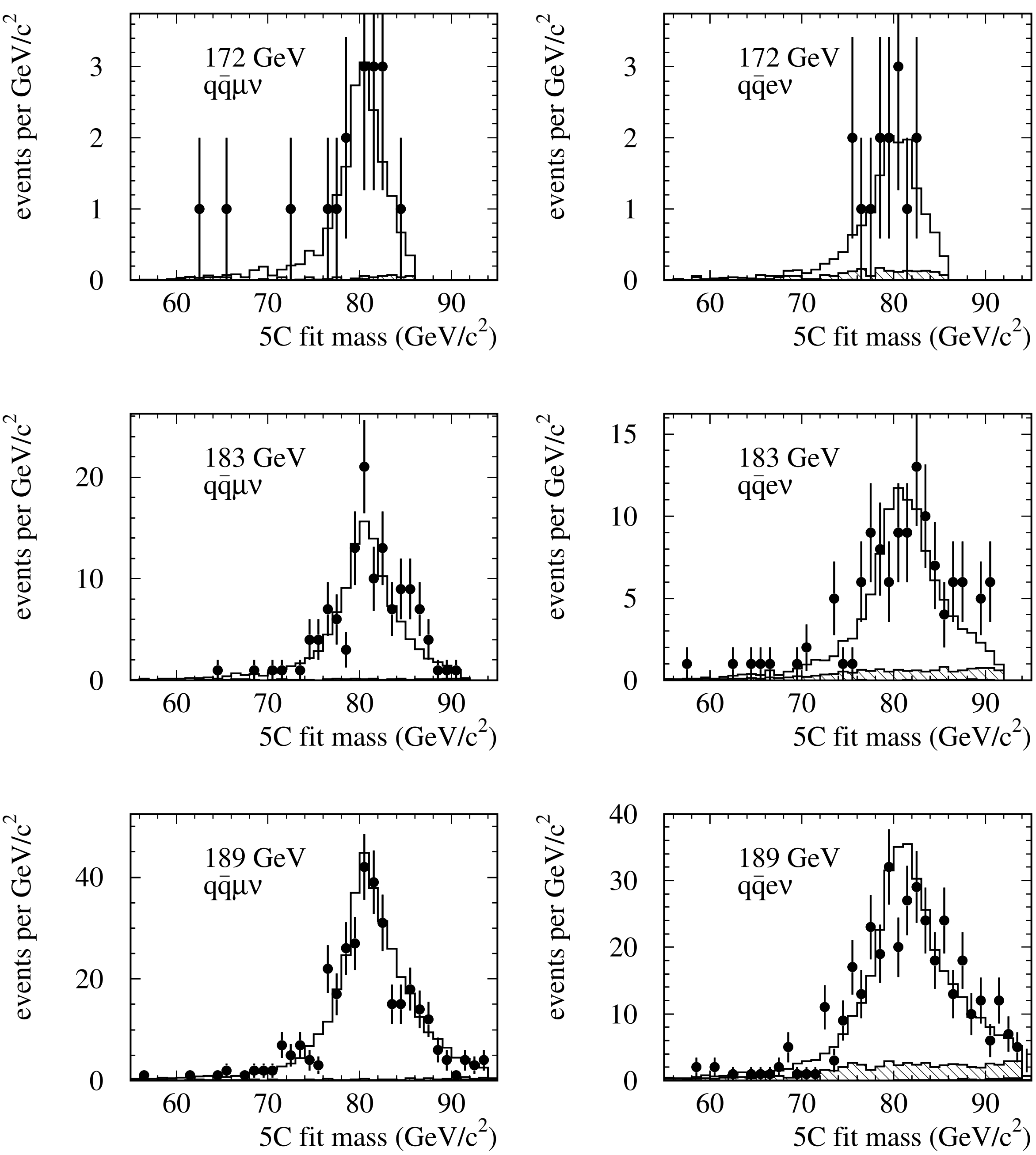

Figure 6.11: *Mass spectra from a constrained fit using an equal-mass constraint, for the semi-leptonic muon and electron channel at different energies.*

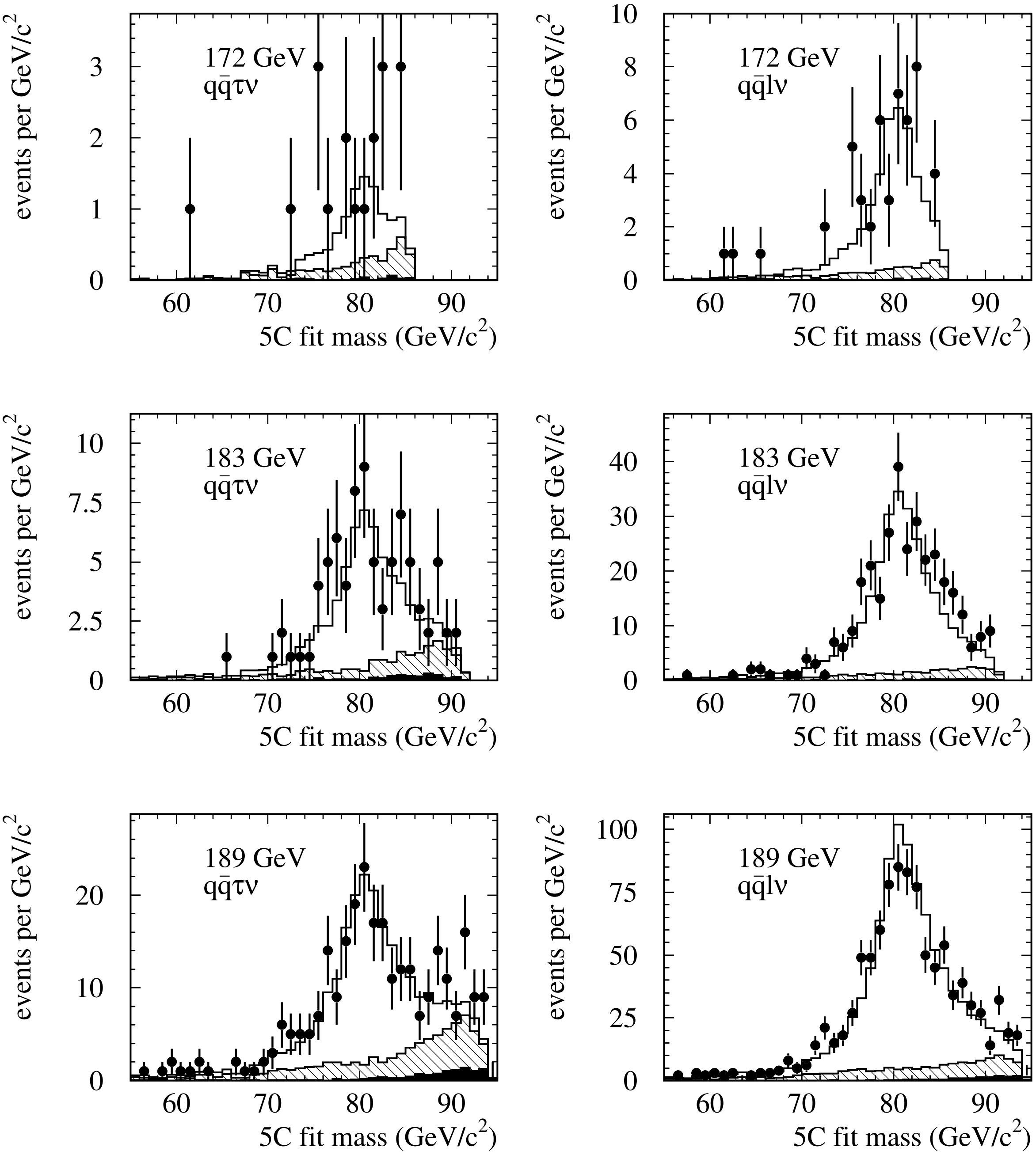

Figure 6.12: *Mass spectra from a constrained fit using an equal-mass constraint, for the tau channel (left) and all semi-leptonic channels combined (right) at different $\sqrt{s}$ energies.*

6.4.2 Calculating the 2D ideograms

As explained already in chapter 5 the Ideogram analysis does not use equal-mass plots to extract the W mass. Instead, for each event a W mass likelihood curve is computed, taking into account the full kinematic information about the two masses m_1 and m_2 of the W bosons in the event. The likelihood curve is extracted from a 2-dimensional ideogram representing the goodness-of-fit for each value of m_1 and m_2, obtained from kinematic constrained fits. The constrained fits all apply the error parameterisation given in equation (4.13) and (4.14), exploiting the information about jet broadness and undetected jet energy. The exact procedure depends on the analysis channel.

Fully-hadronic Ideogram

In case of a fully-hadronic event one ideogram is made for every jet pairing (max. 10), three clustering algorithms and a possible ISR hypothesis (additional factor 2), leading to a maximum of 60 ideograms per event.

The preferred way (proposed in section 5.3) to determine the likelihood that an event is compatible with two invariant masses m_1 and m_2 is by means of a 6C fit, as in equation (5.13), where both masses are fixed and used as constraints in the fit:

$$\mathrm{p}(\textit{event}|m_1, m_2, I) = p^{\mathrm{fit}}_{\mathrm{6C}}(\text{ jets }|m_1, m_2, \sqrt{s}, \sum \overrightarrow{p}) \tag{6.10}$$

To cover the region of interest in the 2-dimensional (m_1,m_2) mass plane, however, would require a large number of fits for each of the ideograms. Fortunately the constrained fit in the $\mathrm{q\bar{q}q\bar{q}}$ channel is well behaved and the corresponding ideogram can generally be described by a single, Gaussian solution. Therefore, the number of fits (and amount of CPU time needed) can be significantly reduced by using a Gaussian approximation based on a single 4C fit per ideogram.

For each of the (up to 60) hypotheses mentioned above a 4C fit is performed, rendering a χ^2_{4C}, two fitted boson masses m_1^{fit} and m_2^{fit}, the estimated errors on these masses σ_{m_1} and σ_{m_2} and the correlation coefficient ρ_{12}. Then the $\chi^2(m_1, m_2)$ as a function of the two masses m_1 and m_2 is approximated as

$$\chi^2_{\mathrm{hypothesis}}(m_1, m_2) \approx \chi^2_{4C} + (\mathbf{m} - \mathbf{m}^{\mathrm{fit}})^T \mathbf{V}^{-1} (\mathbf{m} - \mathbf{m}^{\mathrm{fit}}) \tag{6.11}$$

where

$$\begin{aligned}
\mathbf{V} &= \begin{pmatrix} \sigma^2_{m_1} & \sigma_{m_1}\sigma_{m_2}\rho_{12} \\ \sigma_{m_1}\sigma_{m_2}\rho_{12} & \sigma^2_{m_2} \end{pmatrix} \\
\mathbf{m} &= \begin{pmatrix} m_1 \\ m_2 \end{pmatrix} \\
\mathbf{m}^{\mathrm{fit}} &= \begin{pmatrix} m_1^{\mathrm{fit}} \\ m_2^{\mathrm{fit}} \end{pmatrix}
\end{aligned}$$

In case the 4C fit gives a χ^2_{4C} larger than the number of degrees of freedom NDF$= 4$, the whole ideogram $\chi^2_{\mathrm{hypothesis}}(m_1, m_2)$ is rescaled with a factor NDF$/\chi^2_{4C}$ in order to take into account non-Gaussian resolution effects, similar to the procedure used by the Particle Data Group. The $\chi^2_{4C}(m_1, m_2)$ distribution thus obtained is interpreted as a probability distribution:

$$P^{\rm qqqq}_{\rm hypothesis}(m_1, m_2)dm_1dm_2 \sim \exp\left(-\frac{1}{2}\chi^2_{\rm hypothesis}(m_1, m_2)\right) \tag{6.12}$$

and normalised on the kinematical region so that

$$\int_{m_{\rm min}}^{m_{\rm max}}\int_{m_{\rm min}}^{m_{\rm max}} P^{\rm qqqq}_{\rm hypothesis}(m_1, m_2)dm_1dm_2 = 1 \tag{6.13}$$

with $m_{\rm min} = 60$ GeV/c^2 and $m_{\rm max} = 110$ GeV/c^2 [1].

In the $\rm q\bar{q}q\bar{q}$ channel sufficient information is available to apply an ISR correction on an event-by-event level. As explained in section 5.4.3, for those events more than 1.5 sigma away from $p_z = 0$, additional ideograms are calculated for the hypothesis that an ISR photon escaped undetected in the beam-pipe. The relative probability $w^{\rm ISR}_j$ of the two hypotheses (j = 1, 2) was extracted from MC.

For the W mass measurement m_1 and m_2 are equivalent, and the choice of which of the two boson masses is assigned to m_1 and which to m_2 was arbitrary. Now in order to make the jet-charge information visible in the ideogram (and use it later to measure the difference between $m_{\rm W^+}$ and $m_{\rm W^-}$), the ideogram is 'symmetry broken' according to the calculated jet-charge weights:

$$\begin{aligned} P^{\rm W^+W^-}_{\rm hypothesis}(m_{\rm W^+}, m_{\rm W^-})dm_{\rm W^+}dm_{\rm W^-} &= \\ \left[\mathrm{p}_{\rm W^+}(\Delta Q_k)\cdot P^{\rm qqqq}_{\rm hypothesis}(m_1, m_2) + (1-\mathrm{p}_{\rm W^+}(\Delta Q_k)) \cdot P^{\rm qqqq}_{\rm hypothesis}(m_2, m_1)\right] dm_1dm_2 \end{aligned} \tag{6.14}$$

Since no equal-mass constraint is used the different jet pairings have an equal a-priory probability looking only at the energy and momentum constraints. Using the information from jet charge and gluon emission as described before, the ideograms for the different jet pairings are weighted and subsequently added to give the combined 'DURHAM' ideogram:

$$\begin{aligned} P^{\rm W^+W^-}_{\rm DURHAM}(m_{\rm W^+}, m_{\rm W^-})dm_{\rm W^+}dm_{\rm W^-} &= \\ \sum_{k=1}^{n_{\rm pairing}}\sum_{j=1}^{n_{\rm ISR}} w^{\rm charge}_k \cdot w^{\rm gluon}_k \cdot w^{\rm ISR}_j \cdot P^{\rm W^+W^-}_{\rm k,j}(m_{\rm W^+}, m_{\rm W^-})dm_{\rm W^+}dm_{\rm W^-} \end{aligned} \tag{6.15}$$

This ideogram was made using the jets found by the DURHAM clustering algorithm. In order to identify and empirically treat clustering ambiguities, this whole procedure is repeated using the CAMJET algorithm and the DICLUS algorithm (sections 4.1 and 5.4.2). The event is clustered again, forcing it into the same number of jets as found by the DURHAM algorithm, and the whole procedure described in this section (6.4) is repeated. Finally the (normalised) ideograms are added with equal weight, giving

$$\begin{aligned} \mathrm{p}(\textit{event}|\vec{m}', I)d\vec{m}' \sim P^{\rm q\bar{q}q\bar{q}}_{\rm TOT}(\vec{m}')d\vec{m}' &= \\ \frac{1}{3}\cdot\left[P^{\rm W^+W^-}_{\rm DURHAM}(\vec{m}') + P^{\rm W^+W^-}_{\rm CAMBRIDGE}(\vec{m}') + P^{\rm W^+W^-}_{\rm DICLUS}(\vec{m}')\right] d\vec{m}' \end{aligned} \tag{6.16}$$

with $\vec{m}' \equiv (m_{\rm W^+}, m_{\rm W^-})$. A few examples are shown in Figure 6.13.

[1] These values of $m_{\rm min}$ and $m_{\rm max}$ have been chosen such that CPU processing time is minimised while ensuring a numerically reliable result and a good calibration curve (section 6.6) in a reasonable W mass range e.g. from 75 to 85 GeV/c^2.

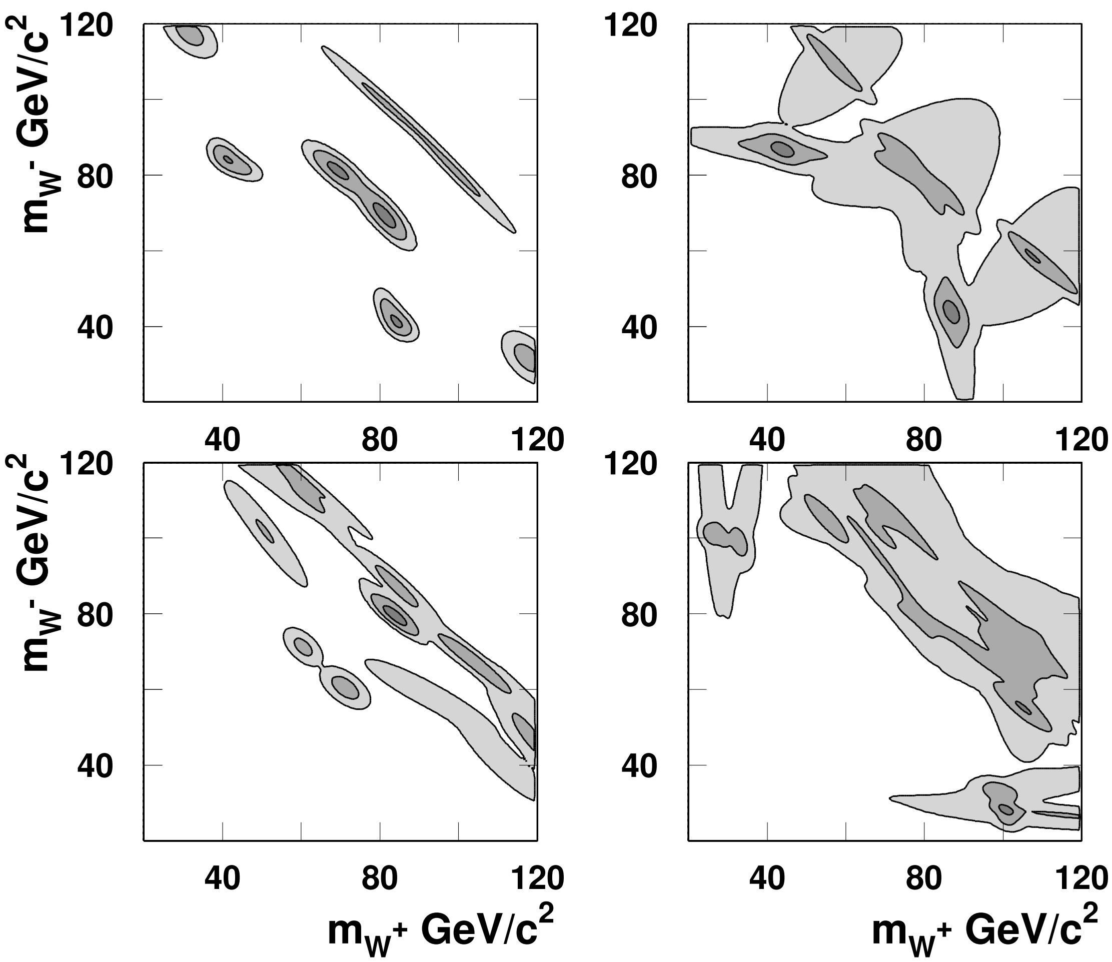

Figure 6.13: *Examples of Ideograms constructed for 4 different events from 189 GeV MC simulation. The two Ideograms at the right-hand side include the hypothesis of collinear ISR, while the other two events (left) are well balanced in p_z and were not treated with ISR hypothesis. The first three sigma contours are shown. The corresponding W mass likelihood curves are shown in Figure 6.15.*

Semi-leptonic Ideogram

In the $\mathrm{q\bar{q}l}\nu$ channel only two ideograms per event are made, corresponding to the tau and non-tau lepton hypotheses, as mentioned before (page 104). But while the number of hypotheses is smaller than in the $\mathrm{q\bar{q}q\bar{q}}$ channel, the construction of the $\mathrm{q\bar{q}l}\nu$ ideograms is more elaborate. Here the Gaussian approximation applied in the $\mathrm{q\bar{q}q\bar{q}}$ channel cannot be used, because in a significant fraction of the $\mathrm{q\bar{q}l}\nu$ events the presence of the invisible neutrino leads to involved non-Gaussian ideogram shapes and double solutions (see section 5.5). In this case the full $\chi^2_{6\mathrm{C}}$ from a 6C fit is needed.

To obtain the 6C fit χ^2 in the whole m_1, m_2 plane turned out not to be trivial. Especially in events with double solutions, near the boundary between the m_1, m_2 regions corresponding to the different solutions, convergence is an issue. Even if the fit converges it often requires an increased number of iterations and may converge to the 'second' solution, i.e. not the solution with the lowest χ^2 of the two for that particular (m_1, m_2) point.

Therefore a special interpolation algorithm was developed, which reduces the number of fits needed, improves the speed of the fits, enhances their rate of convergence and helps each fit to converge to the global χ^2 minimum instead of the 'second' solution. The technical details of this algorithm are described below:

- The 6C fits were performed on a rectangular grid in the (m_1+m_2) and (m_1-m_2) direction with a grid spacing decreasing towards the kinematical limit.
- The constrained fit package was altered to make it possible for the user to define the 'fitted' particle (= jets + lepton) 4-vectors to be used as a starting configuration for the iteration procedure in each fit. This feature offers the possibility to help the fit converge to the correct solution in a smaller number of iteration steps (see below).
- Starting with the (m_1, m_2) point found by a 4C fit leaving both masses free, fits were performed on the grid. Every next fitting point was randomly chosen from the neighbouring points of the point with the lowest χ^2_{6C} that had already been fitted and still had at least one 'free' (= not yet fitted) neighbour. As start of the new fit the fitted particle configuration of this lowest 6C χ^2 neighbouring point was used. For each succesful fit the particle configuration was saved and kept for later. When a fit did not converge, an unphysically high value $\chi^2 = 10,000$ was assigned. This step was repeated until no fitted point with a $\chi^2_{6C} < \chi^2_{4C} + 9$ with free neighbouring points remained.
- To obtain the χ^2 for an arbitrary point (m_1,m_2), a 10-point interpolation was applied when 10 neighbouring fits converged, otherwise a 3-point interpolation was used, or no value was returned at all.

This algorithm proved to be very successful. The resulting $\Delta\chi^2_{\mathrm{6C}}(m_1, m_2)$ distribution is transformed into a probability distribution analogously to the fully-hadronic channel:

$$P^{\mathrm{q\bar{q}l\nu}}_{\mathrm{hypothesis}}(m_1, m_2)dm_1dm_2 \sim \exp\left(-\frac{1}{2}\chi^2_{\mathrm{6C}}(m_1, m_2)\right) \tag{6.17}$$

followed by a normalisation of the ideogram as in equation (6.13):

$$\int_{m_{\min}}^{m_{\max}}\int_{m_{\min}}^{m_{\max}} P^{\mathrm{q\bar{q}l\nu}}_{\mathrm{hypothesis}}(m_1, m_2)dm_1dm_2 = 1 \tag{6.18}$$

on the same kinematical region defined by $m_{\min} = 60$ GeV/c^2 and $m_{\max} = 110$ GeV/c^2. Then the tau and the non-tau ideograms were weighted according to their relative probabilities $w_k^{\tau/\mathrm{non}-\tau}$ and summed to give the combined ideogram probability

$$\begin{aligned} \mathrm{p}(\mathit{event}|\vec{m}', I)d\vec{m}' &\sim \\ P^{\mathrm{q\bar{q}l\nu}}_{\mathrm{TOT}}(\vec{m}')d\vec{m}' &= \left[w_\tau^{\tau/\mathrm{non}-\tau}\cdot P^{\mathrm{q\bar{q}l\nu}}_{\tau}(\vec{m}') + w_{\mathrm{non}-\tau}^{\tau/\mathrm{non}-\tau}\cdot P^{\mathrm{q\bar{q}l\nu}}_{\mathrm{non}-\tau}(\vec{m}')\right]d\vec{m}' \end{aligned} \tag{6.19}$$

with $\vec{m}' \equiv (m_1, m_2)$. A few examples are shown in Figure 6.14.

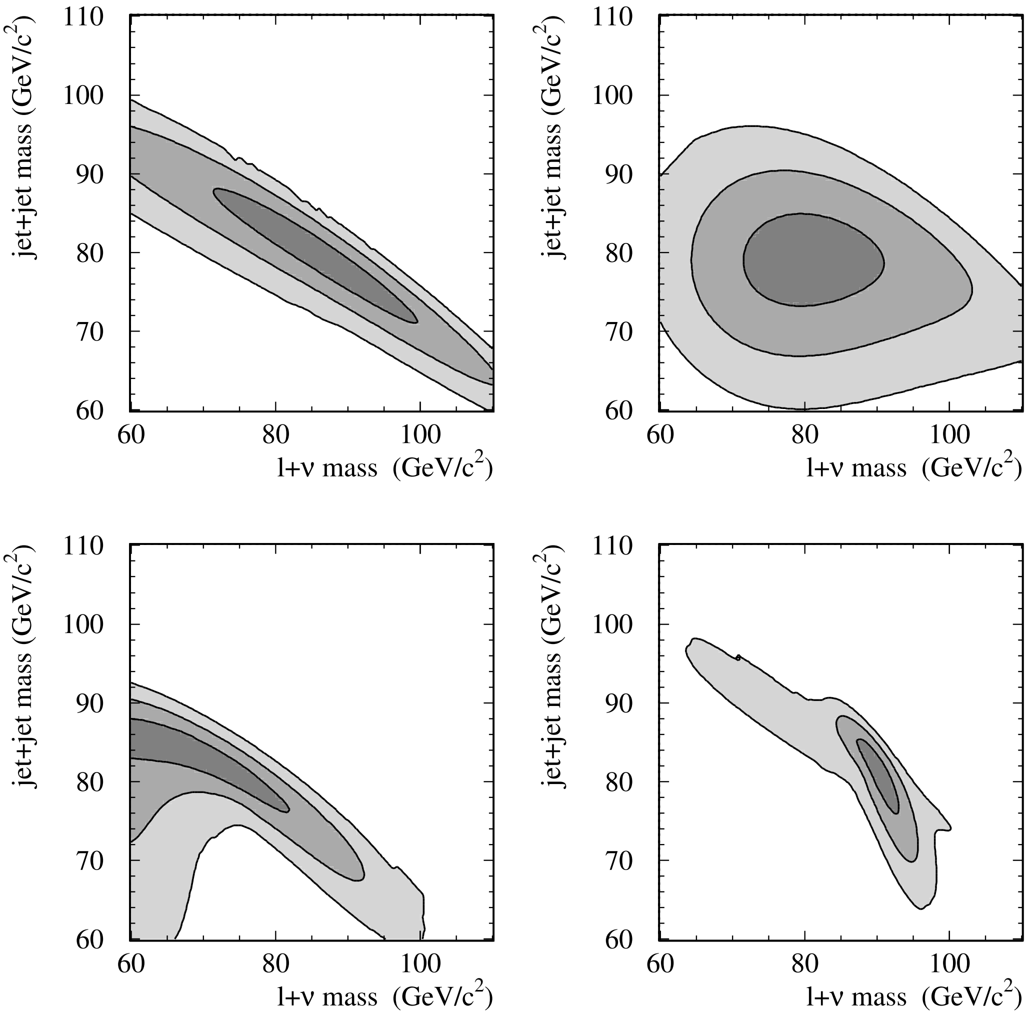

Figure 6.14: *Examples of Ideograms for typical* $\mathrm{q\bar{q}l}\nu$ *events, from MC simulation at* $\sqrt{s} = 189$ *GeV. The first 3 sigma contours of the probability density are shown. The variations in shape are related to different configurations of the lepton and the jets in the event. The distribution can be Gaussian and more or less elongated (top left and right), or non-Gaussian due to the double solution induced by the missing neutrino (bottom left) or when both lepton hypotheses (tau and non-tau) obtain a significant probability (bottom right).*

6.5 W mass, width and $\Delta\mathrm{m}_{\mathrm{W^+W^-}}$ extraction

For each event a likelihood curve $\mathcal{L}_{\text{event}}(m_{\mathrm{W}}, \Gamma_{\mathrm{W}})$ was extracted using equation (5.16):

$$\mathcal{L}_{\text{event}}(m_{\mathrm{W}}, \Gamma_{\mathrm{W}}) \equiv \tag{6.20}$$
$$\int_{m_{\min}}^{m_{\max}}\int_{m_{\min}}^{m_{\max}} P_{\mathrm{TOT}}^{\mathrm{q\bar{q}}xx}(\overrightarrow{m}') \cdot \Big[\mathcal{P}_{\text{event}} \cdot \mathrm{S}(\overrightarrow{m}'|m_{\mathrm{W}}, \Gamma_{\mathrm{W}}) + (1-\mathcal{P}_{\text{event}}) \cdot \mathrm{B}(\overrightarrow{m}')\Big] \; d\overrightarrow{m}'$$

where $P_{\mathrm{TOT}}^{\mathrm{q\bar{q}}xx}(\overrightarrow{m}')$ represents the Ideogram function $P_{\mathrm{TOT}}^{\mathrm{q\bar{q}q\bar{q}}}$ or $P_{\mathrm{TOT}}^{\mathrm{q\bar{q}l}\nu}$ described in the previous section. The measurement of m_{W} and the Γ_{W} is based directly on these likelihood curves. The extraction method of the difference of the W^+ and W^- is slightly more complicated and is discussed separately, later in this section.

Construction of the event likelihood

The physics probability density functions S and B in equation (6.20) are normalised to one. The background function is assumed to be flat $\mathrm{B}(\vec{m}') = \mathrm{B}$, while the signal function is the product of a phase space function and a factor containing Breit-Wigners:

$$\begin{aligned}\mathrm{S}(m_1, m_2, m_\mathrm{W}, \Gamma_\mathrm{W}) = &\frac{1}{s}\sqrt{(s - m_1^2 - m_2^2)^2 - 4m_1^2 m_2^2}\cdot \\ &\cdot \Big[\sigma^\mathrm{WW}_\mathrm{accept} \cdot \mathrm{BW}_\mathrm{WW}(m_1, m_2, m_\mathrm{W}, \Gamma_\mathrm{W}) \\ &+\sigma^\mathrm{ZZ}_\mathrm{accept} \cdot \mathrm{BW}_\mathrm{ZZ}(m_1, m_2, m_\mathrm{Z}, \Gamma_\mathrm{Z})\Big]\,, \end{aligned} \tag{6.21}$$

to be explained in more detail below; for the $\mathrm{q\bar{q}q\bar{q}}$ and the $\mathrm{q\bar{q}l}\nu$ channel separately:

- In the $\mathrm{q\bar{q}q\bar{q}}$ channel, the background function B describes the mass distribution expected from $\mathrm{q\bar{q}}\gamma$ background. The proper background distributions can be taken and parameterised from MC simulation, but it was found that for all practical purposes this function can be assumed to be flat on the region of integration. For analyses that use ideograms close to the kinematical limit [71] a more precise description is needed.

  The 4-fermion distribution contains a contribution from correct jet pairings and a contribution from wrong pairings, which also is assumed to be flat. The correct-pairing part contains relativistic Breit-Wigners for the WW and ZZ contribution, weighted according to their relative accepted cross-sections $\sigma^\mathrm{WW}_\mathrm{accept}$ and $\sigma^\mathrm{ZZ}_\mathrm{accept}$, extracted for every centre-of-mass energy from the MC simulation. This is actually a simplification of the more involved expression including the probability of the other jet-pairings to give the masses assumed to be wrong combinations. This simplification is only allowed if the wrong-pairing distribution is rather flat.

  Preliminary MC studies have shown that a proper inclusion of the wrong pairing background would improve the mass resolution by 1% or less. Event-by-event investigations of the jet structure show that not all $\mathrm{q\bar{q}q\bar{q}}$ events have a jet clustering which corresponds well to the parton shower truth. This was taken into account by reducing the effective purity of the events by a factor ϵ_clus. This procedure is justified by also this component of wrong pairings being very flatly distributed in the (m_1,m_2) plane. The effective event purity $\mathcal{P}_\mathrm{event}$ thus becomes $\mathcal{P}_\mathrm{event} = \epsilon_\mathrm{clus} \cdot P^\mathrm{4f}$ where P^4f was the estimated 4-fermion purity. A value of $\epsilon_\mathrm{clus} = 0.7$ was found to give good pull distributions for all of the centre-of-mass energies. The tuning procedure used to determine ϵ_clus is described in section 6.7.

- In the $\mathrm{q\bar{q}l}\nu$ channel a contribution from ZZ will not give a significant mass peak, as the fit hypothesis (jets, 1 lepton and 1 neutrino) is likely to be wrong, and the cross-section is small. Therefore $\sigma^\mathrm{ZZ}_\mathrm{accept}$ was taken to be zero in the likelihood expression. With only one possible jet pairing and a jet clustering that is less likely to cause problems that can affect the reconstructed mass, the effective event purity $\mathcal{P}_\mathrm{event}$ was defined to be equal to the estimated $\mathrm{q\bar{q}l}\nu$ purity obtained from equation (6.5).

The expression used for the 2-dimensional Breit-Wigner is the product of two 1-dimensional Breit-Wigners with s-dependent width (section 2.2):

$$\mathrm{BW}_{\mathrm{WW}}(m_1, m_2, m_{\mathrm{W}}, \Gamma_{\mathrm{W}}) = \mathrm{BW}_{\mathrm{W}}(m_1, m_{\mathrm{W}}, \Gamma_{\mathrm{W}}) \cdot \mathrm{BW}_{\mathrm{W}}(m_2, m_{\mathrm{W}}, \Gamma_{\mathrm{W}}) \tag{6.22}$$

with

$$\mathrm{BW}_{\mathrm{W}}(m, m_{\mathrm{W}}, \Gamma_{\mathrm{W}}) \propto \frac{\frac{\Gamma_{\mathrm{W}}}{m_{\mathrm{W}}} m^2}{(m^2 - m_{\mathrm{W}}^2)^2 + (m^2 \frac{\Gamma_{\mathrm{W}}}{m_{\mathrm{W}}})^2} \tag{6.23}$$

and a similar expression for the ZZ term $\mathrm{BW}_{\mathrm{ZZ}}(m_1, m_2, m_{\mathrm{Z}}, \Gamma_{\mathrm{Z}})$. Since the Breit-Wigners depend on the boson masses and decay widths m_{W}, Γ_{W}, m_{Z} and Γ_{Z}, the event likelihood (6.20) can be calculated as a function of these parameters by varying the corresponding parameter while ensuring that the BW functions stay normalised on the integration area.

The event likelihood $\mathcal{L}(m_{\mathrm{W}})$ is calculated in steps of 0.5 GeV/c^2 in m_{W} (0.4 GeV/c^2 for the $\mathrm{q\bar{q}l}\nu$ channel) and $\mathcal{L}(\Gamma_{\mathrm{W}})$ in steps of 0.2 GeV/c^2. Examples are shown in Figure 6.15.

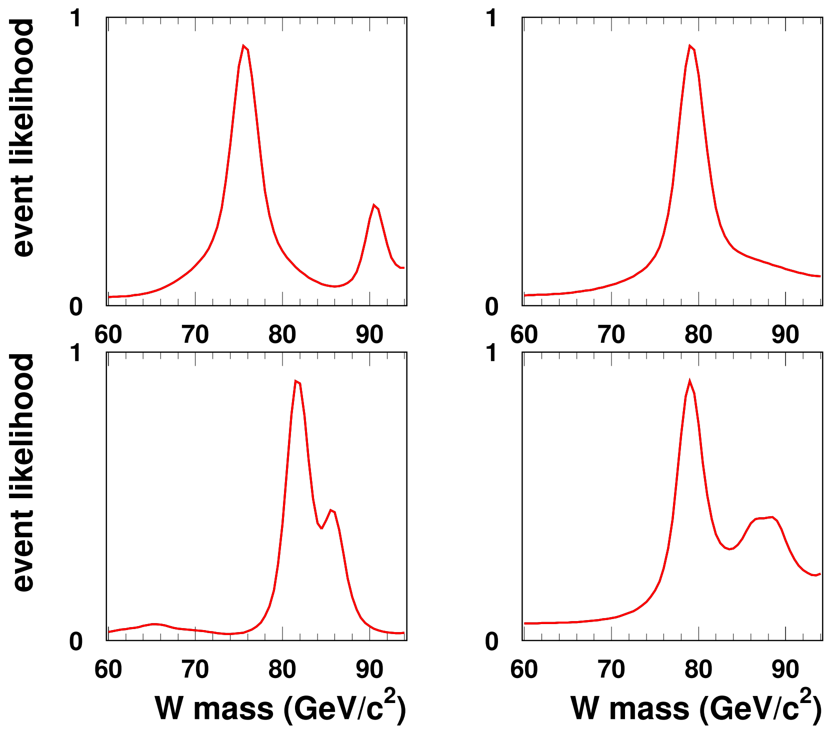

Figure 6.15: *Event likelihood curves corresponding to the Ideograms shown in Figure 6.13.*

The logarithms of the event likelihood curves

$$\begin{aligned} L_{\text{event}}(m_{\mathrm{W}}) &\equiv -2 \cdot \ln\left(\mathcal{L}_{\text{event}}(m_{\mathrm{W}})\right) \\ L_{\text{event}}(\Gamma_{\mathrm{W}}) &\equiv -2 \cdot \ln\left(\mathcal{L}_{\text{event}}(\Gamma_{\mathrm{W}})\right) \end{aligned} \tag{6.24}$$

are saved and kept for later combination and analysis.

Extraction of $\Delta m_{W^+W^-}$

For the measurement of the difference of the W^+ and the W^- boson masses also a 1-dimensional likelihood was extracted. The average W mass was fixed, and the W^+ and W^- masses in the 2D Breit-Wigner were varied according to: $m_{W^+} = 80.35\ \mathrm{GeV}/c^2 + \frac{1}{2}\Delta m_{W^+W^-}$ and $m_{W^-} = 80.35\ \mathrm{GeV}/c^2 - \frac{1}{2}\Delta m_{W^+W^-}$. By convoluting this with the W^+ W^- de-symmetrised ideograms in the $\mathrm{q\bar{q}q\bar{q}}$ channel the likelihood as a function of the difference of the masses $\Delta m_{W^+W^-}$ was extracted and saved in steps of 1 GeV/c^2. The effect on the measurement of fixing the average mass to 80.35 GeV/c^2 is negligible because the correlation between the sum of the masses and the difference of the masses should be extremely small, and because the sum of the masses is measured more than one order of magnitude more precisely than the difference. Any residual effect is taken into account in the estimation of the systematic errors.

A similar approach in the $\mathrm{q\bar{q}l}\nu$ channel would not be optimal, due to the fact that the resolution on the mass difference is significantly worse, while on the other hand the W^+/W^- separation is much better. For the $\Delta m_{W^+W^-}$ measurement in this channel a W mass likelihood $\mathcal{L}^{\tau}_{\mathrm{event}}(m_W)$ was extracted, using only the tau-hypothesis. By using the tau-hypothesis, the mass information extracted from the event is almost fully determined by the hadronic system, while the lepton is only used to determine the sign of the W bosons. Thus the W mass difference $\Delta m_{W^+W^-}$ can be measured by dividing the total event sample in a W^+ and a W^- sample and by then using the difference of the measured masses. Any remaining correlations inside the events are taken into account in the calibration of the analysis (section 6.6).

Overall likelihood

As the events are independent, the overall likelihood curve can be obtained by taking the product of the event likelihood curves, or equivalently, adding the negative log likelihood (or $\Delta\chi^2$) curves that were saved (see equation (6.24)), e.g. for the W mass:

$$\Delta\chi^2_{\mathrm{overall}}(m_W) \equiv L_{\mathrm{overall}}(m_W) = \sum_{event=1}^{n_{\mathrm{event}}} L_{\mathrm{event}}(m_W) \tag{6.25}$$

The 'bin' of m_W with the lowest value of $\Delta\chi^2_{\mathrm{overall}}$ is looked for, and a parabola is interpolated through this $\Delta\chi^2$ value and the neighbouring two bins. The error on the fitted mass is calculated from the second derivative at the minimum:

$$\sigma_{m_W^{\mathrm{fit}}} = \sqrt{\frac{2}{\alpha^2}} \qquad \text{with} \qquad \alpha = \left.\frac{\partial^2 L_{\mathrm{overall}}(m_W)}{\partial m_W^2}\right|_{m_W = m_{\mathrm{fit}}} \tag{6.26}$$

This is equivalent to the m_W range over which $\Delta\chi^2_{\mathrm{overall}}$ changes from 0 to 1 if the curve is parabolic which turns out to be a good assumption for the mass measurement in all channels at all energies. The fitted value for m_W will be called m_{fit} from now on.

In Figure 6.16 some examples of likelihood curves are shown. It was found for the measurement of the width, that the parabolic approximation could lead to numerical instabilities of the order of 3 MeV/c^2 due to the asymmetry in the likelihood curves. This was solved by using 3rd order polynomial interpolation through the 4 bins closest to the minimum in the Γ_W negative log likelihood curves.

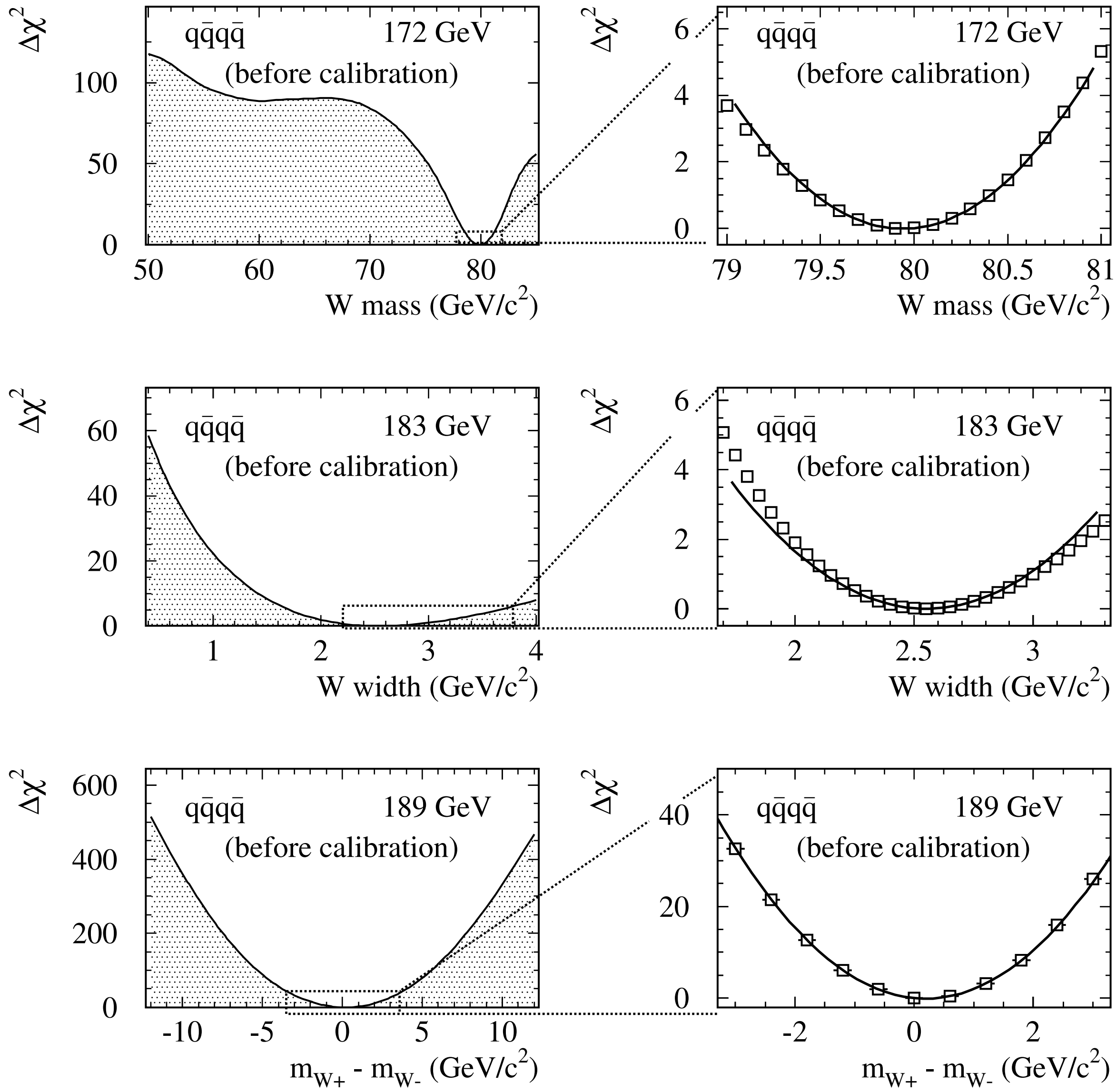

Figure 6.16: *Examples of overall likelihood curves obtained from data in the* qq̄qq̄ *channel. The curves for the W mass at 172 GeV, W width at 183 GeV and* $\Delta m_{W^+W^-}$ *at 189 GeV are shown before calibration (section 6.6). In each case the shape of the likelihood near the minimum is shown (right) compared to a parabolic fit to the bins surrounding the minimum. To produce these plots a smaller binsize than usual (text, page 113) was chosen. The W width likelihood is clearly asymmetric (see text).*

6.6 Final calibration using simulation

The mass thus obtained from the overall likelihood (6.25) relies on analytical event likelihood expressions based on energy and momentum conservation, a simplified jet-resolution parameterisation and a BW mass dependence modified by phase-space. Although these analytical likelihoods do not at all take into account the full complexity of the DELPHI detector and only partly correct for ISR, this 'raw' mass measurement turns out to be accurate to better than 1% (0.2% in the $\mathrm{q\bar{q}q\bar{q}}$ channel) over a broad $\sqrt{s}$ range, even without further calibration.

In order to reach the precision aimed for, however, Monte Carlo simulation is needed to correct for more complicated detector effects and the influence of 'higher order' physics effects like ISR radiation. The calibration can be done directly using MC reweighting or by using a linear transformation based on independent MC samples as described in the following two paragraphs.

Independent Samples at different generated mass

The MC samples listed in Table 6.2 were generated using different values of m_{W} in order to check how the bias on the measured W mass changes as a function of the W mass. The difference between the fitted and generated mass as a function of the generated mass is plotted (see Figure 6.17 and 6.18) and a slope a and bias b were obtained from a linear fit using the following relation:

$$m_{\mathrm{fit}} - m_{\mathrm{gen}} = a \cdot (m_{\mathrm{gen}} - 80.35 \text{ GeV}/c^2) + b \tag{6.27}$$

In all cases the fit is satisfactory, indicating that the calibration curve is consistent with being linear within MC statistics for all energies. Figure 6.19 shows the fitted bias and the slope as a function of $\sqrt{s}$. The increase of the positive bias with centre-of-mass energy is expected from ISR radiation. The ISR treatment in the $\mathrm{q\bar{q}q\bar{q}}$ channel (partly) corrects for this effect.

Continuous MC reweighting

The calibration curve can also be obtained without assuming a linear behaviour (or any other functional relation) by using a MC reweighting technique. The resulting reweighting curve compared to the straight line fit of the independent MC samples is shown in Figure 6.20. It provides an extra linearity cross-check for the W mass measurement.

For the Γ_{W} and the $\Delta m_{\mathrm{W^+W^-}}$ measurement MC reweighting was the only way to obtain the calibration curve, since only samples generated with $\Gamma_{\mathrm{W}} = 2.07$ GeV/c^2 and $\Delta m_{\mathrm{W^+W^-}} = 0$ were available. Figure 6.20 shows the calibration curve for the Γ_{W} measurement at 189 GeV as an example.

6.7 Checks of the statistical properties

Not only the fitted mass, also the error has to be cross-checked using Monte Carlo simulation, as the analytical likelihood expression used is only a simplification of the true (unknown) likelihood.

resampling

The analysis was applied many times on MC samples corresponding to the same integrated luminosity as the data in order to check whether the estimated statistical errors agreed with the spread in the measured quantity (m_{W}, Γ_{W}, $\Delta m_{\mathrm{W^+W^-}}$). In order to obtain a sufficiently precise result on this test, a large number of samples was needed. For n independent samples, the estimated

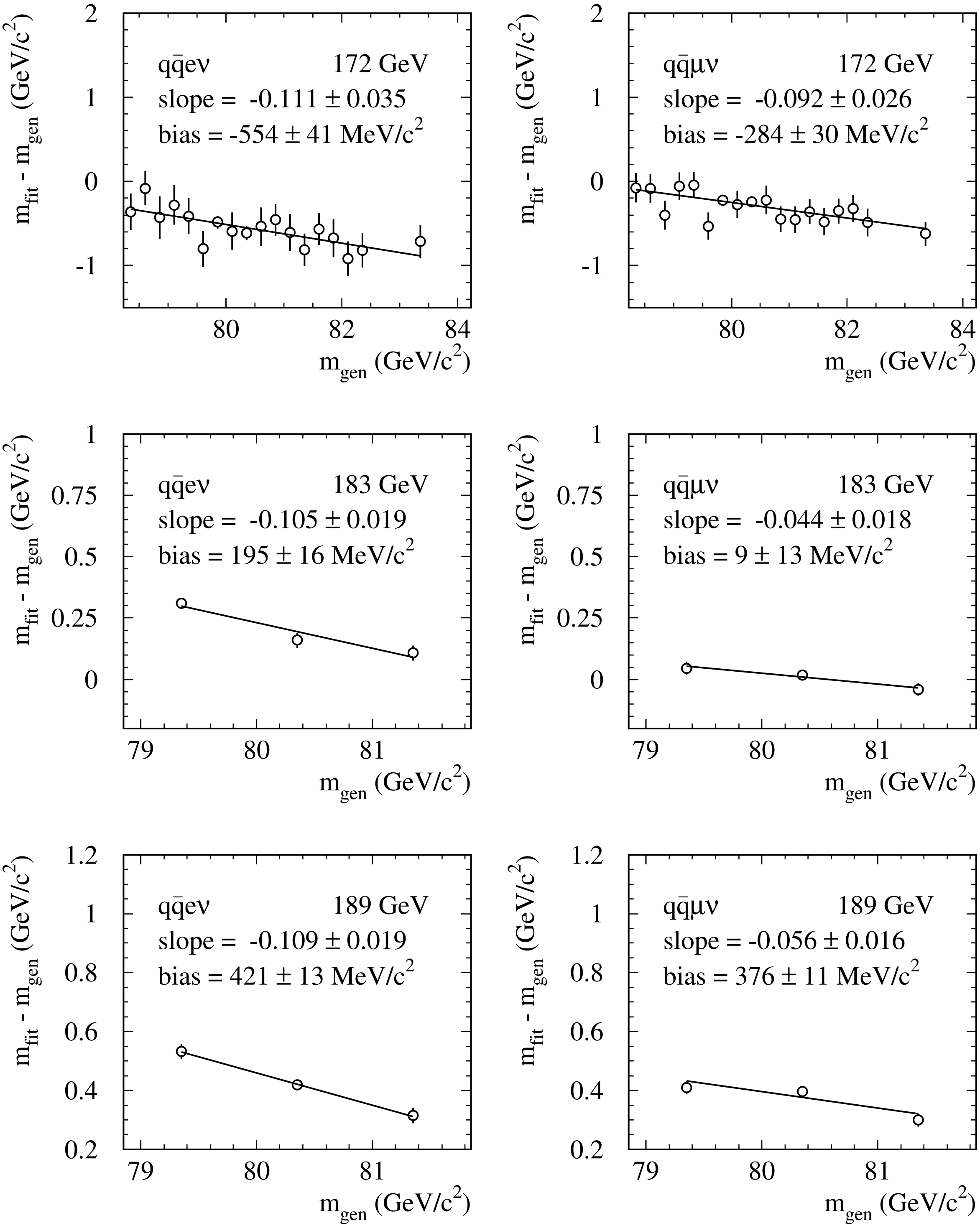

Figure 6.17: *Calibration curves for muon and electron channel showing the difference of the fitted mass $m_{\rm fit}$ and generated W mass $m_{\rm gen}$ as a function of the generated W mass. The definition of the fitted slope a and bias b is given in equation (6.27).*

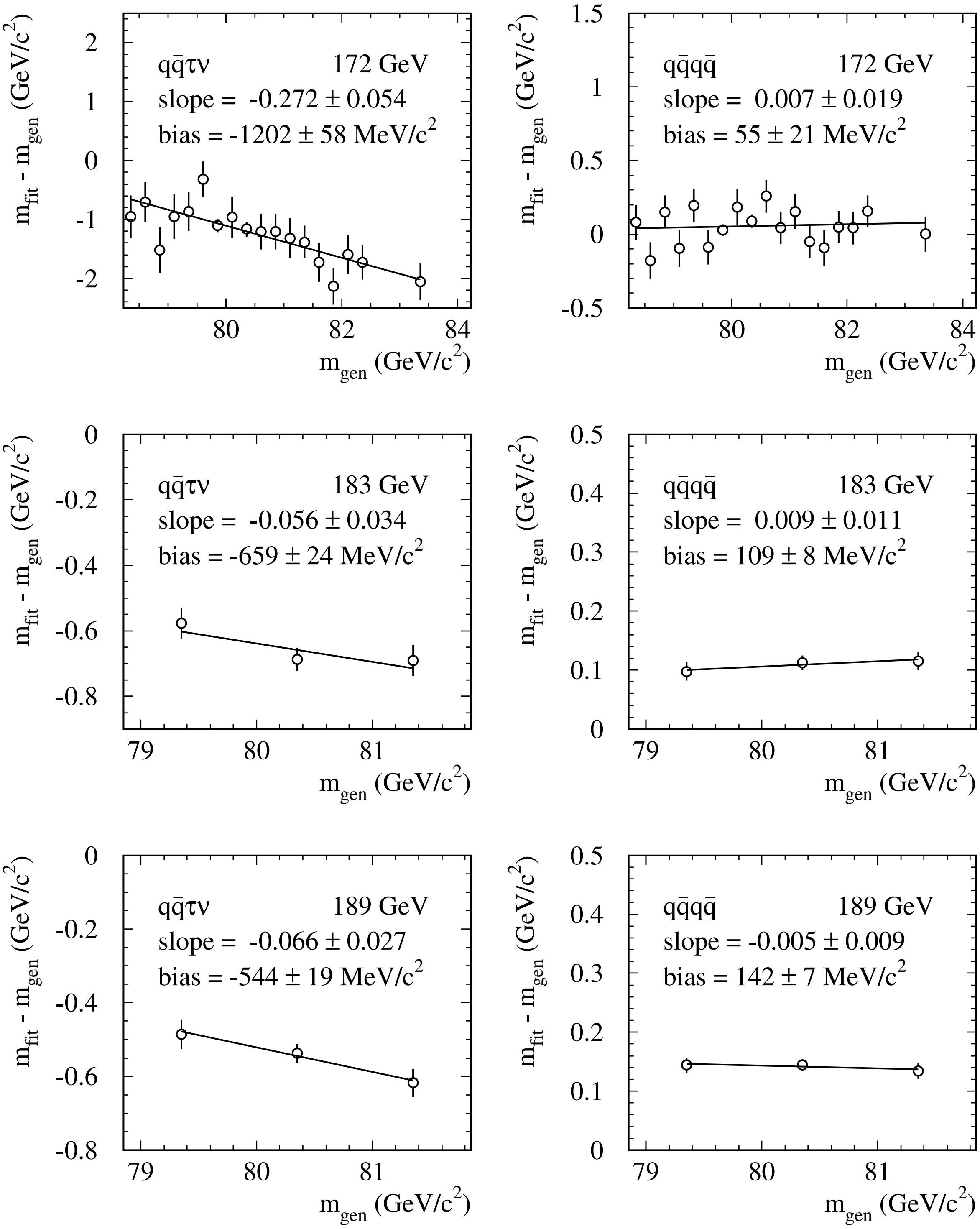

Figure 6.18: *Calibration curves for tau and hadronic channel. The definition of the fitted slope a and bias b is given in equation (6.27).*

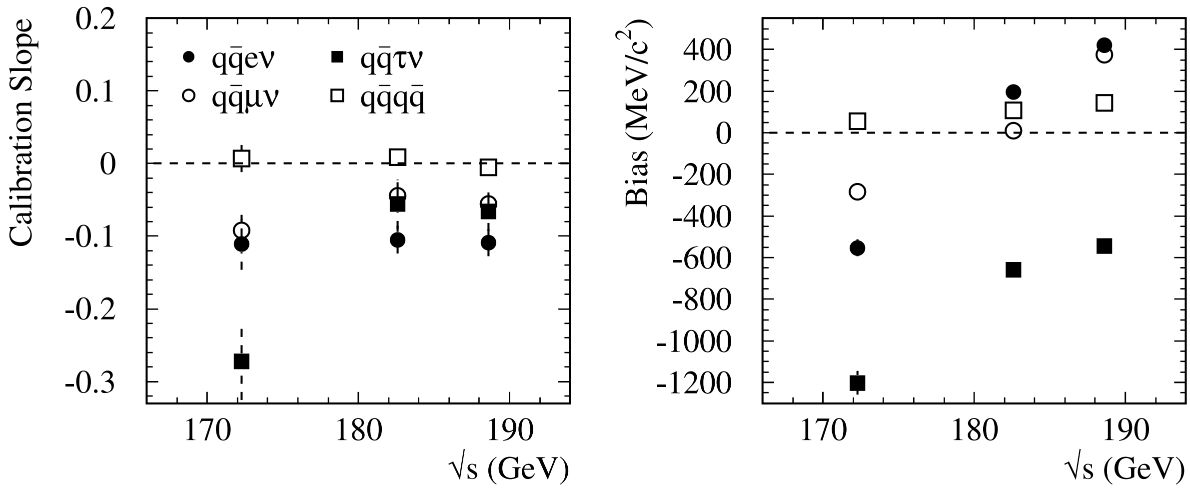

Figure 6.19: *Slope and bias (see Figure 6.17 and 6.18) as a function of $\sqrt{s}$.*

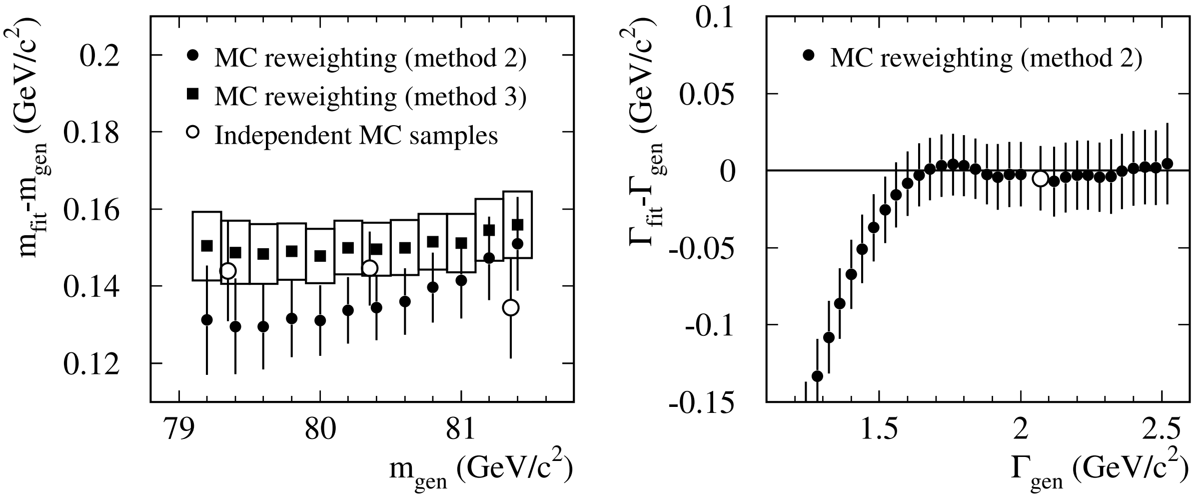

Figure 6.20: *The calibration curves obtained from MC reweighting for m_{W} (left) and Γ_{W} (right) in the $\mathrm{q\bar{q}q\bar{q}}$ channel at $\sqrt{s}$ =189 GeV. The statistical errors indicated for reweighting results are highly correlated from point to point. Two different methods to calculate the event weights (section 4.3) are shown as a cross-check of the linear fit to independent samples used to calibrate the m_{W} result. For the right-hand plot only the main MC sample (with $m_{\mathrm{gen}} = 80.35$ GeV/c^2 and $\Gamma_{\mathrm{gen}} = 2.07$ GeV/c^2) was used.*

precision on the statistical error is given by $\Delta\sigma/\sigma \sim \sqrt{\frac{1}{2n}}$ so in order to reach a precision better than 1%, more than 5,000 samples are needed. However, in practice the available MC statistics was typically limited to about 100 times the size of the data. Therefore a resampling method was used, using events more than once. The size of each sample was determined using Poissonian statistics with a mean equal to the expected number of WW and $\mathrm{q\bar{q}}\gamma$ events, picking the events randomly from the available sets of MC simulation.

Pull distribution and tuning of the analysis

Of interest for the estimation of the statistical error is the pull distribution, with the pull defined as:

$$\text{pull} \equiv \frac{m_{\mathrm{W}}^{\text{measured}} - m_{\mathrm{W}}^{\text{generated}}}{\sigma^{\text{estimated}}} \tag{6.28}$$

where $\sigma^{\text{estimated}}$ is the statistical error estimated from the likelihood curve (6.26). Equivalently pull distributions can be made for Γ_{W} and $\Delta m_{\mathrm{W^+W^-}}$. A few examples are shown in Figure 6.21. In order to optimise the likelihood model used in this analysis, two parameters $f_{\mathrm{q\bar{q}q\bar{q}}}$ (a scaling factor for the input errors of the constrained fit in equation (4.14)) and ϵ_{clus} (clustering efficiency in $\mathcal{P}_{\text{event}} = \epsilon_{\text{clus}} \cdot P^{4\text{f}}$ on page 112) were tuned so that

- the RMS of the pull distribution for the mass became one.
- the bias $\Gamma_{\text{fit}} - \Gamma_{\text{gen}}$ on the measured Γ_{W} became zero for $\Gamma_{\text{gen}} = 2.07$ GeV/c^2.

The values for ϵ_{clus} and $f_{\mathrm{q\bar{q}q\bar{q}}}$ found for the fully-hadronic channel were 0.7 and 1.1 respectively, at $\sqrt{s}$ =189 GeV. The same tuning was also used for the analysis at other centre-of-mass energies, with satisfactory pull and bias — as shown in Table 6.7. Both parameters are highly correlated to the estimation of the error on the mass but hardly influence the bias on the mass. In the semi-leptonic channel only the scaling factor for the input errors in the constrained fit $f_{\mathrm{q\bar{q}l\nu}}$ was tuned (to $f_{\mathrm{q\bar{q}l\nu}} = 1.4$), optimizing the overall agreement for the pulls in all channels. As visible in Table 6.7 the Γ_{W} measurement in the semi-leptonic channels after tuning shows a significant positive bias in all channels.

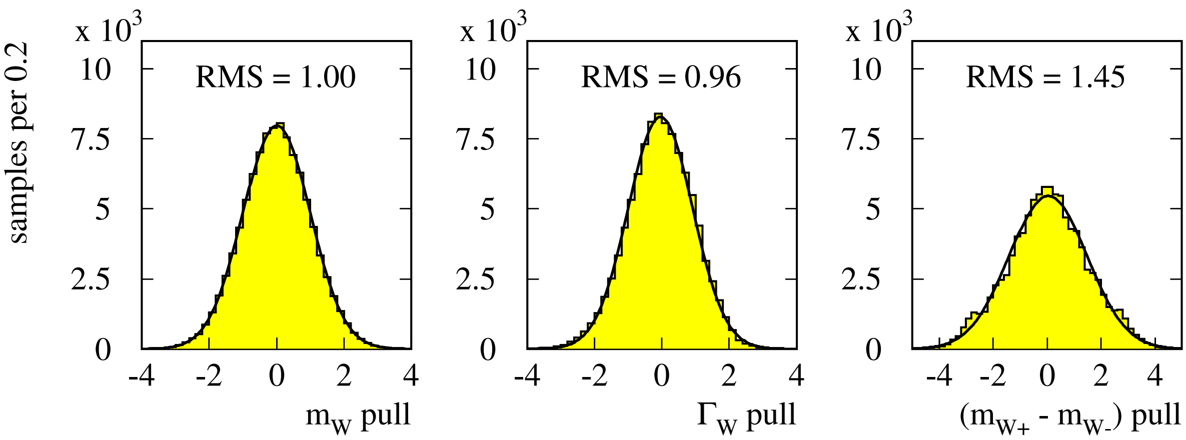

Figure 6.21: *Pull distributions for m_{W} (left), Γ_{W} (middle), and $\Delta m_{\mathrm{W^+W^-}}$ (right) for the fully-hadronic channel at $\sqrt{s}$ = 189 GeV; fitted with a Normal distribution. Each plot contains 100,000 samples.*

	RMS of m_W pull			Bias on Γ_W(GeV/c^2)		
	172	183	189	172	183	189
$q\bar{q}q\bar{q}$	1.05	1.02	1.00	-0.22 ± 0.09	0.032 ± 0.023	-0.003 ± 0.017
$q\bar{q}e\nu$	1.06	1.03	1.04	0.91±0.23	0.502±0.057	0.592±0.043
$q\bar{q}\mu\nu$	1.01	1.04	1.08	0.33±0.15	0.700±0.047	0.979±0.037
$q\bar{q}\tau\nu$	0.98	0.99	1.06	1.72±0.49	0.712±0.089	1.331±0.074

Table 6.7: *Width of the m_W pull distribution and Γ_W bias ($\equiv \Gamma_{fit} - \Gamma_{gen}$ for $\Gamma_{gen} = 2.07$ GeV/c^2) obtained after tuning of the analysis (see text).*

Pull as a function of estimated error

For small event samples (like the 172 GeV data sample) the accuracy of the measurement can show significant variations depending on the amount of 'luck' in the composition of the data sample that is actually obtained. In those cases the estimated statistical error from the data is a better estimator of the statistical accuracy than the average statistical error expected from MC simulation, provided that the method used to calculate this error is reliable. This can be tested by plotting the RMS of the pull distribution as a function of the estimated error per sample. An example is shown for the W mass in the $q\bar{q}q\bar{q}$ channel at $\sqrt{s} = 172$ GeV in Figure 6.22. Such plots were only used as a cross-check. For all measurements presented, the quoted errors have been corrected for the average width of the pull obtained from pull distributions as shown in Figure 6.21 (and listed in Table 6.7).

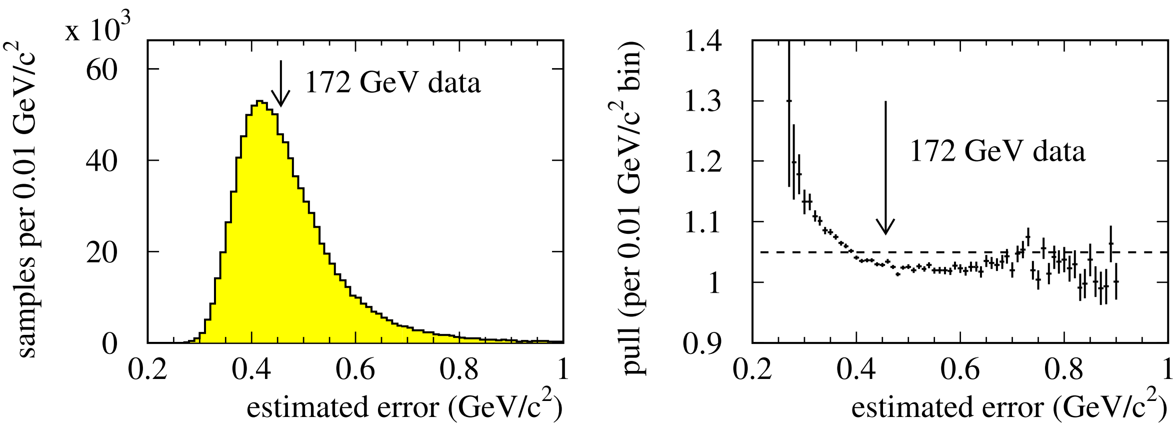

Figure 6.22: *Distribution of the estimated error per sample for 1 million MC samples (left) and the RMS of the pull as a function of the estimated error (right) for the W mass in the $q\bar{q}q\bar{q}$ channel at $\sqrt{s} = 172$ GeV. The arrows indicate the estimated error actually obtained with the DELPHI data. As the analysis was tuned at 189 GeV (see text), the behaviour of the pull is not optimal. The dashed line indicated the average width of the pull used for the correction of the quoted error.*

6.8 Summary

An overview of the results obtained with the 2D Ideogram analysis is shown in Table 6.8. The results for the W mass, width and difference of m_{W^+} and m_{W^-} are shown with statistical errors only, after full calibration. All quoted results and errors were corrected for bias and slope of the calibration curve and width of the corresponding pull distribution. In the next chapter a study of the systematic errors is presented, and the overall combination is done in chapter 8.

	Calibrated results		
Channel	172 GeV	183 GeV	189 GeV
m_W (GeV/c^2)			
$q\bar{q}q\bar{q}$	80.001 ± 0.475	80.224 ± 0.190	80.466 ± 0.106
$q\bar{q}\mu\nu$	80.370 ± 0.671	80.626 ± 0.309	80.048 ± 0.213
$q\bar{q}e\nu$	80.307 ± 0.971	80.661 ± 0.443	80.115 ± 0.290
$q\bar{q}\tau\nu$	81.25 ± 1.27	80.075 ± 0.577	80.075 ± 0.332
Γ_W (GeV/c^2)			
$q\bar{q}q\bar{q}$	1.61 (+1.32) (-1.01)	2.39 (+0.45) (-0.39)	2.08 (+0.23) (-0.21)
$q\bar{q}\mu\nu^*$		2.72 (+0.99) (-0.75)	1.98 (+0.52) (-0.46)
$q\bar{q}e\nu$	0.4 (+1.6) (-1.6)	3.0 (+2.0) (-1.2)	3.7 (+0.8) (-0.7)
$q\bar{q}\tau\nu^*$		3.8 (+3.8) (-1.9)	2.83 (+0.95) (-0.85)
$q\bar{q}l\nu$	0.4 (+1.6) (-1.6)	3.00 (+0.72) (-0.58)	2.75 (+0.41) (-0.37)
m_{W^+} - m_{W^-} (GeV/c^2)			
$q\bar{q}q\bar{q}$	7.2 ± 19.4	3.57 ± 3.29	2.06 ± 2.22
$q\bar{q}\mu\nu^*$		-0.87 ± 3.08	-1.67 ± 1.59
$q\bar{q}e\nu$	5.3 ± 7.7	-4.38 ± 3.48	-6.66 ± 1.98
$q\bar{q}\tau\nu^*$		-7.7 ± 6.8	2.38 ± 2.29
* At $\sqrt{s} = 172$ GeV the three semi-leptonic channels were combined for Γ_W and $\Delta m_{W^+W^-}$ before calibration in order to avoid large statistical fluctuations			

Table 6.8: *Results obtained with the 2D Ideogram analysis; with statistical errors only.*

Chapter 7

Systematic uncertainties

In the previous chapter the 2D Ideogram analysis was presented, including an investigation of its statistical properties. Since the likelihood expression used in the analysis was not complete, Monte Carlo simulation had to be used to calibrate the analysis. There the assumption was that the MC simulation gave an accurate description of all processes relevant to the production and detection of WW events, as recapitulated in Figure 7.1.

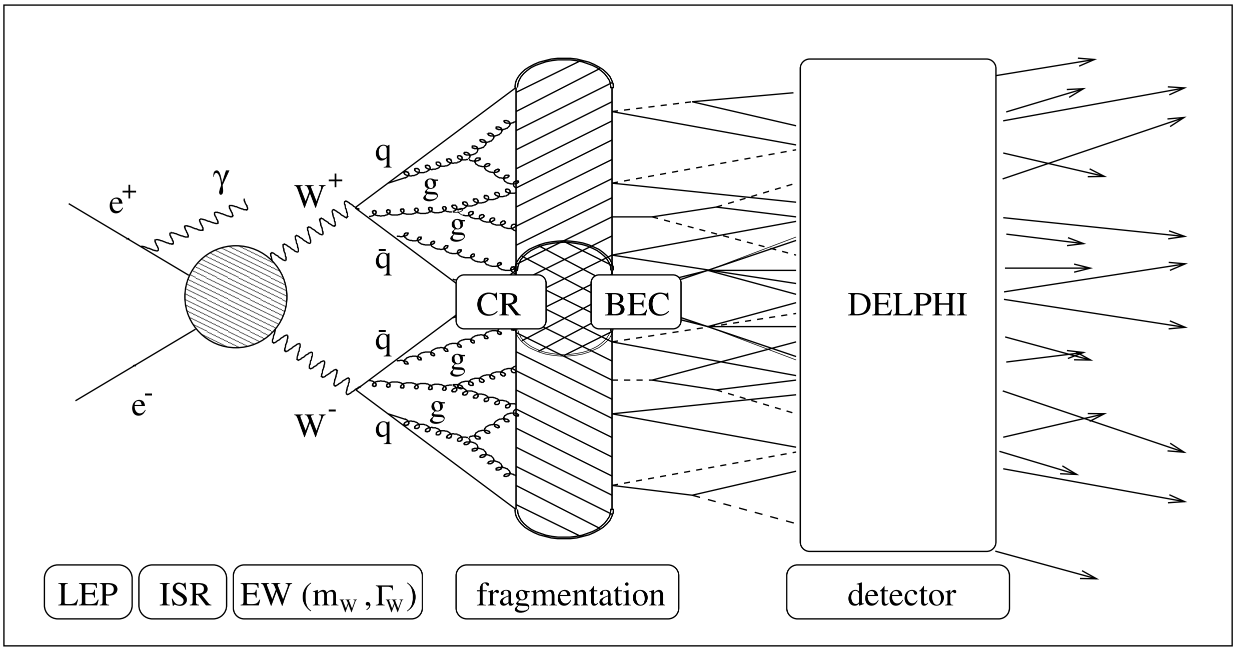

Figure 7.1: *Succession of phases in the production and detection of a W pair event, all to be accurately simulated by Monte Carlo simulation.*

In this chapter, the possibility will be considered that the MC simulation does not provide a complete and perfect description of reality. Thus, any discrepancy between the MC simulation and the 'truth' may lead to a systematic error on the W mass measurement. The difficult task of assigning systematic uncertainties therefore consists of checking all possible discrepancies between MC and reality and estimate to what extent such discrepancies might affect the measurement.

Statistical limitations

Since the cross-sections of interesting processes at LEP2 are relatively low, most measurements are limited by statistical uncertainties rather than systematic uncertainties. For the LEP combined measurement of the W mass the statistical error has become smaller than the quoted systematic uncertainty, but the understanding of the systematic errors is still improving and also there it is to be expected that the final systematic error will be smaller than the statistical uncertainty (maybe with exception of Colour Reconnection effects).

In the Γ_W and $\Delta m_{\mathrm{W^+W^-}}$ measurements statistical errors are even larger, so systematics play a smaller role. This is especially true for the $\Delta m_{\mathrm{W^+W^-}}$ case, where most of the systematic effects cancel out because they would affect $m_{\mathrm{W^+}}$ and $m_{\mathrm{W^-}}$ in the same way.

Method of determination of systematic errors

The limited amount of data available at LEP2 also has consequences for the method of determination of the systematic errors. Many of the possible systematic errors (like detector effects, or jet fragmentation modelling) cannot be studied on high energy data with sufficient precision. Therefore, one has to rely on Z peak data and use models to 'extrapolate' that knowledge to the simulation of high energy data.

The systematic error estimates presented here have all been determined using a large statistics MC sample; never on the data sample that was actually obtained. The goal is to obtain robust and 'universal' results that are meaningful, lead to an improved understanding and are not affected by the limited statistics of a small data sample.

The approach used in this chapter is to systematically go through all physics processes shown in Figure 7.1 and investigate all possible details where the MC simulation might fail to describe the 'truth'. Such a possible discrepancy is modelled, applied to the MC simulation, and the observed shift in the W mass or width is taken as a measure of the corresponding systematic error.

The modelling of possible discrepancies can be done in different ways:

- Sometimes it is straightforward to apply the effect 'by hand' to the MC simulation. For example, a mis-calibration of the jet energy scale, or a change in the length-to-width ratio of DELPHI can easily be implemented by applying the appropriate transformation to all measured 4-momenta in each event, either at the reconstructed jet or the measured particle level (section 7.5).

- Comparing models is another possibility. For example, to investigate jet fragmentation systematics one might replace the standard JETSET fragmentation by HERWIG fragmentation and see what the effect is (section 7.4).

- Similarly, one can vary the parameters inside one model within the range allowed by the (LEP1) data (this approach is used in section 7.4 as well).

Model dependence

A fundamental drawback of model comparisons is that the result is again model-dependent. It provides an indication of the *minimum* error, as common systematics do not show up in the difference. And it leads to an over-estimation of the minimum error in case the alternative model is believed to be 'worse' than the other, preferred, model that was actually used in the analysis.

One of the major advantages of the MLBZ technique (section 7.6) is the fact that with this method it is possible to compare the MC simulation *directly* to the *data*, thus providing a model independent estimate of the systematic errors related to jet reconstruction.

Relevance

The systematic studies presented in this chapter deal with more than twenty different topics. The focus is on the $\mathrm{q\bar{q}q\bar{q}}$ channel, where some of the estimations go beyond the level of detail that is achieved in the presently published W mass analyses. Thus they provide either a justification for being neglected or point towards solutions for the evaluation of the final LEP2 m_{W} systematics.

The majority of the results is believed to be relevant for other LEP W mass analyses as well, because to good approximation most effects play a very similar role for all W mass analyses in the different experiments. The $\mathrm{q\bar{q}l}\nu$ channel has been studied in less detail than the $\mathrm{q\bar{q}q\bar{q}}$ channel. Where results for the $\mathrm{q\bar{q}l}\nu$ ideogram analysis are missing, the corresponding numbers for the DELPHI $\mathrm{q\bar{q}l}\nu$ analysis [1, 2, 3] are quoted.

Central role of the constrained fit

As discussed in chapter 4 the use of a constrained kinematic fit gives a major improvement in the statistical precision. Furthermore, it significantly reduces the importance of detector related systematic effects, at the cost of introducing new dependencies of the reconstructed mass on the LEP beam energy and precise knowledge of Initial State Radiation through the kinematic constraints.

Outline of this chapter

It will be shown (section 7.2) that systematics related to LEP are well understood and can be studied with great precision using basic relativistic kinematics. The only remaining important uncertainty related to LEP is the energy scale.

The EW phase (section 7.3) is also well defined, but since ISR is by far the dominant correction it has to be taken seriously. The error quoted here for ISR effects is relatively large and may not be representative for other analyses, since a state-of-the art treatment for ISR should render a negligible effect, with the possible exception of non-factorisable $\mathcal{O}(\alpha)$ corrections.

More involved is the control of systematics related to jet fragmentation and possible final state cross-talk. Fragmentation models can be tuned on Z^0 data and are believed to cause negligible systematics, but it has proven to be a challenging task to substantiate and quantify this claim. Cross-talk due to Bose-Einstein (BE) correlations and Colour Reconnection (CR) can not be directly studied using Z^0's and large systematic effects (especially due to CR) in the $\mathrm{q\bar{q}q\bar{q}}$ channel cannot be excluded at present. Some 'classical' studies within the framework of available phenomenological models are presented in section 7.4.

Similarly, the knowledge of possible systematic effects related to the simulation of the DELPHI detector performance relies predominantly on Z^0 studies. In section 7.5, however, also high-energy data is used to study the jet energy response over an extended jet energy range, and the uncertainty associated with the length-to-width ratio of DELPHI is investigated.

In section 7.6 a refinement of jet fragmentation and detector effects is presented, based on the MLBZ method. In appendix A the method is described in detail. In this section the relevant results are shown, indicating that the jet fragmentation error which currently dominates the quoted systematic error on the combined LEP W mass measurement, most likely can be eliminated.

In section 7.7 a few internal consistency and stability checks are performed.

When differences in the data or in an improved model are established relative to the simulation, they can be corrected for by applying *minus* the shift to the measured m_{W}, and assign a suitable fraction of this shift as an additional systematic error. For corrections which are well under control this error will typically be the statistical error on the established difference, while it will be the full difference for corrections which cannot easily be understood.

To conclude, an overview is presented (section 7.8) of all systematic corrections and uncertainties reviewed in this chapter.

7.1 Finite MC statistics

Even in the hypothetical case of a perfect MC simulation, the calibration curves (see section 6.6) have a limited statistical precision due to the finite number of MC events generated. This uncertainty is quoted as a systematic error. At all energies care was taken to generate a number of simulated WW events equivalent to at least 100 times the integrated luminosity of the data, in order to keep this error smaller than 10% of the statistical uncertainty on the measurement. The values derived for the $\mathrm{q\bar{q}q\bar{q}}$ and the $\mathrm{q\bar{q}l}\nu$ channel for different $\sqrt{s}$ energies are listed in tables 7.14 to 7.17 at the end of this chapter.

The rest of this chapter will deal with the consequences of imperfections of the MC simulation.

7.2 LEP: preparation of the initial state

In the simulation the initial state consists of an electron and a positron that collide with opposite momentum parallel to the nominal beam axis and a centre-of-mass energy exactly equal to a fixed nominal value (e.g. 172, 183 or 189 GeV).

In reality, however, the initial state is prepared by LEP. This means that variations occur in the $\mathrm{e^+e^-}$ centre-of-mass energy and momentum and the exact location in space and time of the interaction point.

Variations of the interaction point

Space-time variations of the interaction point (the 'beam spot') are well known because they are of crucial importance for analyses that rely on the measurement of impact parameters and secondary vertices, like B physics measurements and Higgs boson searches [56]. The use of a fixed beamspot in MC simulation may lead to slight differences at the level of the particle reconstruction. These effects, however, are insignificant compared to the detector related systematics effects to be discussed in section 7.5.

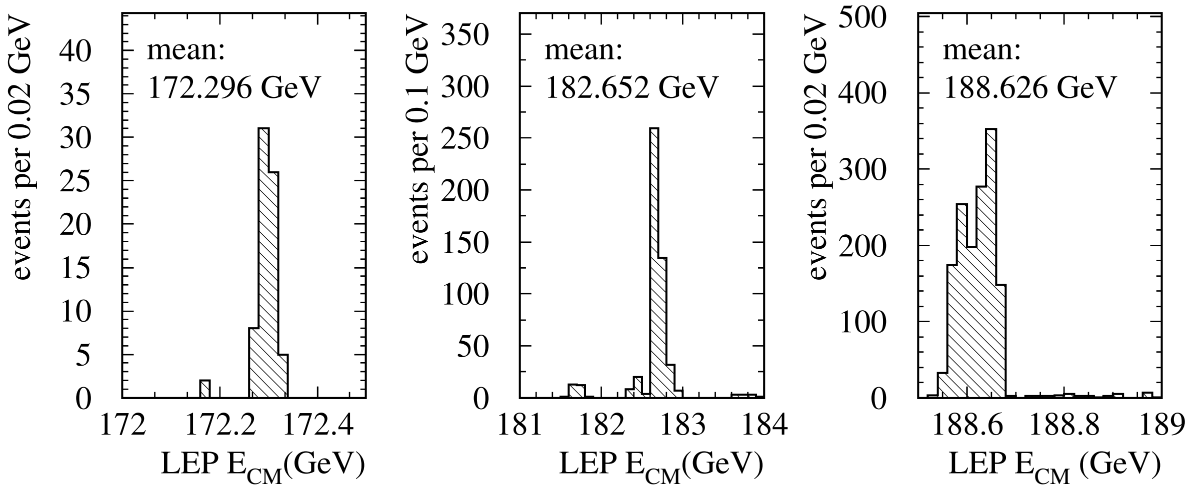

Figure 7.2: *LEP centre-of-mass energies used as constraint for all selected* $\mathrm{q\bar{q}q\bar{q}}$ *events at nominal LEP energies of 172(left), 183(middle) and 189(right) GeV.*

Known variations of $\mathrm{E_{beam}}$ in time

During physics running LEP continuously monitored the dipole bending field using 16 NMR probes located in main bend dipole magnets (as discussed in section 3.1) . After careful calibration the centre-of-mass energies for each of the 4 LEP interaction points were distributed to the LEP experiments via energy calibration files. These files give time-stamped estimates of the LEP beam energy at 15 minute intervals of running or anytime there is a significant change in the energy, e.g. due to an RF trip in one of the superconducting cavities.

The centre-of-mass energies that were read from this file and used as constraint for the events selected in the analysis are shown in Figure 7.2. Apparently the difference in centre-of-mass energy between data and simulation can be of the order of several hundred MeV. To first order this is excellently taken into account by using the correct energy value in the energy constraints. Higher order effects could however lead to a bias in the mass:

- The average ISR energy radiated and the associated positive bias on the mass depends on $\sqrt{s}$. In the $\mathrm{q\bar{q}q\bar{q}}$ analysis this dependence is expected to be reduced due to the event-by-event ISR treatment (which will automatically apply a stronger ISR correction when more events seem to have ISR). No ISR treatment has been included in the $\mathrm{q\bar{q}l}\nu$ analysis presented here, however, which may explain the much stronger dependence visible in Figure 7.3.

- Cross-sections and event topologies (e.g. the average boost of the W bosons) will slightly change and influence the W mass measurement indirectly. For example, an increase in the background cross-section will increase the (small) mass bias induced by the background. A more involved example is the negative mass bias which arises from the reconstruction of jets. The size of this effect, discussed in more detail in appendix A, depends on the average W boson boost and therefore on $\sqrt{s}$.

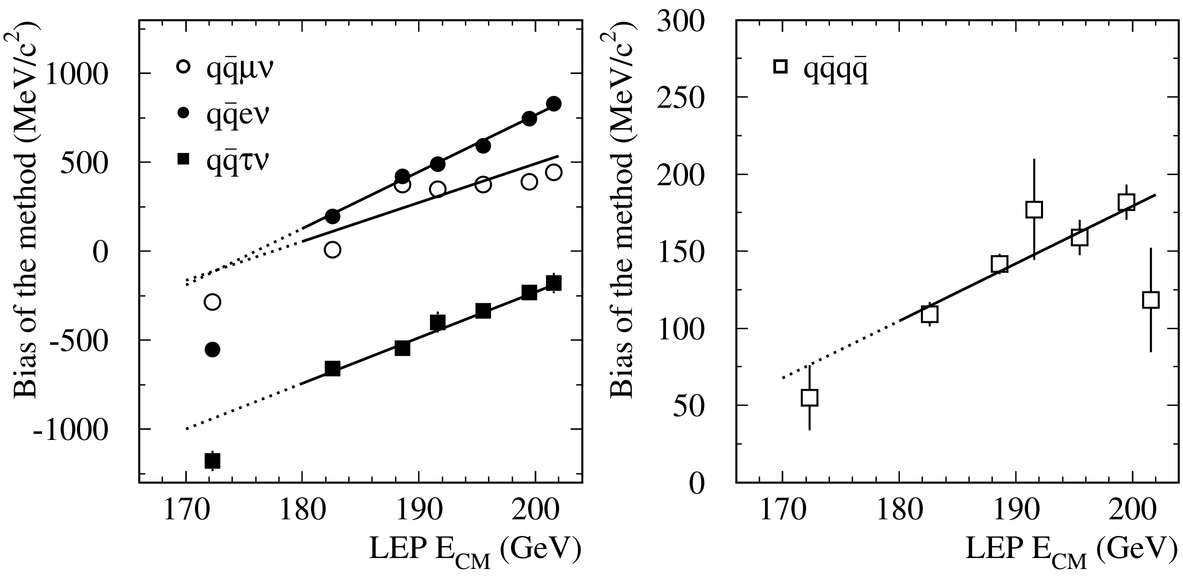

Figure 7.3: *Evolution of the mass reconstruction bias as a function of the LEP centre-of-mass energy, for the* $\mathrm{q\bar{q}l}\nu$ *channel (left) and the* $\mathrm{q\bar{q}q\bar{q}}$ *channel (right). In all cases the generated W mass was 80.35 GeV/*c^2*. The data points for 192-202 GeV are from [72].*

The size of these effects can be estimated from the evolution of the mass reconstruction bias $b \equiv (m_{\text{fit}} - m_{\text{generated}})$ for $m_{\text{generated}} = 80.35$ GeV/c^2 shown in Figure 7.3, where the analysis is kept fixed except for the tuning of the event-by-event purity estimator. In all channels the trend is clear: the bias becomes more positive with increasing $\sqrt{s}$ as expected from the dominating effect of ISR. Furthermore the behaviour in all channels except $\mathrm{q\bar{q}}\mu\nu$ is (surprisingly) linear for centre-of-mass energies above 180 GeV. The biases obtained at 172 GeV systematically fall below this linear trend, which is probably related to phase-space effects near the WW production threshold.

In order to take into account the deviation of the mean LEP centre-of-mass energy E_{CM} from the nominal value $E_{\text{CM}}^{\text{nominal}}$, first-order corrections were calculated as:

$$\Delta m_{\text{fit}} = \mathrm{d}b/\mathrm{d}E_{\text{CM}} \cdot (E_{\text{CM}}^{\text{mean}} - E_{\text{CM}}^{\text{nominal}}) \tag{7.1}$$

The values of $E_{\text{CM}}^{\text{mean}}$ are given in Figure 7.2. The slopes $\mathrm{d}b/\mathrm{d}E_{\text{CM}}$ at 183 and 189 GeV were obtained from the linear fit to the points above 180 GeV shown in Figure 7.3. To estimate the slope at 172 GeV the difference between the bias at 183 GeV and 172 GeV is used as an indication. The numerical values of $\mathrm{d}b/\mathrm{d}E_{\text{CM}}$ are shown in Table 7.1. The computed corrections are listed in Table 7.2, and systematic uncertainties of half their size are quoted in the Tables 7.14 to 7.17.

Uncertainty on the LEP energy scale

The most important uncertainty in the LEP beam calibration for the W mass measurement is the $\approx 0.02\%$ relative uncertainty on the overall energy scale. As was discussed in section 3.1, the dominant part of this uncertainty originates from the linear extrapolation of the RDP calibration at low energy (40-60 GeV) to the physics energies (86 GeV and higher).

$\mathrm{d}b/\mathrm{d}E_{\mathrm{CM}}$ (c^{-2})				
E_{CM}	$\mathrm{q\bar{q}}\mu\nu$	$\mathrm{q\bar{q}e}\nu$	$\mathrm{q\bar{q}}\tau\nu$	$\mathrm{q\bar{q}q\bar{q}}$
172 GeV	0.028	0.073	0.051	0.005
$\geq$ 183 GeV	0.022	0.032	0.026	0.004

Table 7.1: *Values of the slope* $\mathrm{d}b/\mathrm{d}E_{\mathrm{CM}}$ *of the curves in Figure 7.3.*

As the LEP energy is used as constraint in the kinematic fits, the measured mass is proportional to the LEP energy scale. Therefore the relative error on the mass is equal to the relative beam energy error:

$$\frac{\Delta m_{\mathrm{fit}}}{m_{\mathrm{fit}}} = \frac{\Delta E_{\mathrm{beam}}}{E_{\mathrm{beam}}} \tag{7.2}$$

For the measurement of the width the actual change of the overall scale is negligible, compared to the relative uncertainty on the measurement ($\approx 5\%$ LEP combined). However, since Γ_{W} is fitted using a 1-dimensional likelihood fit where the W mass in the analytical Breit-Wigner functions is fixed to 80.35 GeV/c^2, an indirect systematic bias could arise from a mismatch in the mass scales. To investigate the combination of the direct and indirect effect, MC reweighting was used to vary the 'true' value of the W mass and the measurement bias $\Gamma_{\mathrm{fit}} - \Gamma_{\mathrm{generated}}$ was plotted for $\Gamma_{\mathrm{generated}} = 2.07$ GeV/c^2 As shown in Figure 7.4 in all cases a quadratic dependence was found with a slope $d\Gamma/dm_{\mathrm{W}}$ at $m_{\mathrm{W}} = 80.35$ GeV/c^2 ranging from -1.4 to -0.3. An error in the LEP energy scale would change the scale of the reconstructed mass accordingly and therefore be equivalent to varying the reference mass by the corresponding amount given by relation (7.2), causing a systematic bias on the measured width equal to:

$$\Delta\Gamma_{\mathrm{fit}} = \mathrm{d}\Gamma/\mathrm{d}m_{\mathrm{W}} \cdot \frac{\Delta E_{\mathrm{beam}}}{E_{\mathrm{beam}}} \cdot 80.35 \quad \mathrm{GeV/c^2} \tag{7.3}$$

Two remarks should be made here:

- The uncertainty on the prediction for m_{W} from a SM fit using all experimental data[1] excluding direct m_{W} measurements, is of the same order of magnitude as the uncertainty on the LEP beam energy scale. Therefore, the quoted systematic error $\Delta\Gamma_{\mathrm{fit}}$ is also an indication of the systematic effect related to fixing the W mass to 80.35 GeV/c^2 in the Γ_{W} measurement (not quoted).

- Reversely, a possible bias on the W mass measurement caused by fixing Γ_{W} to 2.07 GeV/c^2 was found to be negligible. In all cases this effect turned out to be below 1 MeV/c^2.

The LEP E_{beam} errors, their correlation between years and the derived systematic uncertainties for mass and width are listed in Table 7.2. These errors become important in the LEP combined mass measurement as they are highly correlated between different years, channels and experiments.

[1] 80.373 $\pm$ 0.024 GeV/c^2, equation (1.34)

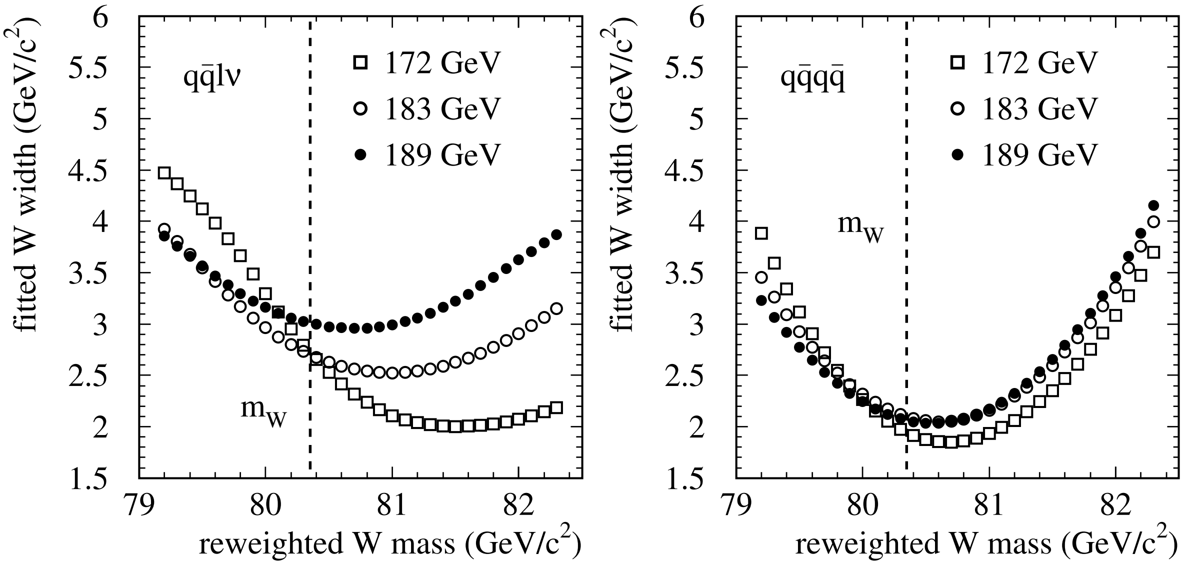

Figure 7.4: *Dependence of the fitted width (with a generated* Γ_W *equal to 2.07 GeV/*c^2*) on the reference mass for the* $q\bar{q}l\nu$ *channels combined (left) and* $q\bar{q}q\bar{q}$ *(right), determined by reweighting the reference MC sample. The dashed lines indicate the value to which* m_W *was fixed in the* Γ_W *measurement.*

Natural beam spread

The natural energy spread of electrons and positrons in each beam is of the order of 150 MeV, depending on the beam energy, the optics settings and frequency shift used. This leads to a statistical variation in centre-of-mass energy from event to event and corresponding boost of the event along the z-axis with a RMS spread of $\approx$ 200 MeV/c (more precise values are quoted in Table 7.2).

Since these boosts are practically non-relativistic ($\beta = p/E \approx$ 0.001) the effect of the boost can be studied separately from the spread in the energy, as the energy of the boosted system in the laboratory frame (= LEP energy calibration file) differs from the true centre-of-mass energy by only $\approx$ 100 keV — a negligible difference.

1. *Effect of the* e^+e^- *boosts:* Fully-hadronic W pair events from simulation were boosted along the z-axis at the reconstructed particle level with the size of the boost distributed according to a Gaussian with standard deviation varying from 200 MeV to 600 MeV. All shifts in the W mass and width were found to be compatible with zero. For the maximum spread of 600 MeV the observed shifts were +1.5 $\pm$ 1.6 MeV/c^2 for the mass and +2.3$\pm$3.3 MeV/c^2 for the width.

2. *Effect of the* e^+e^- *energy spread:* The latter study did not take into account the accompanying variations in centre-of-mass energy $\sigma_{\mathrm{natural}} \approx$ 200 MeV. It is evident that this will lead to an extra scatter in the fitted W mass and a bias on the width measurement. The

	Year			
	1996	1997	1998	
Nominal E_{beam}	86.0	91.5	94.5	(GeV)
Mean value of E_{beam}	86.148	91.326	94.313	
Correction to m_{W} bias				
$\mathrm{q\bar{q}q\bar{q}}$	+1	-1	-1	(MeV/c^2)
$\mathrm{q\bar{q}}\mu\nu$	+8	-8	-8	
$\mathrm{q\bar{q}e}\nu$	+22	-11	-12	
$\mathrm{q\bar{q}}\tau\nu$	+15	-9	-10	
Uncertainty E_{beam} scale	30	25	20	(MeV)
Correlation across years 1996	1.00	0.82	0.67	
1997	0.82	1.00	0.75	
1998	0.67	0.75	1.00	
Corresponding uncertainty on				(MeV/c^2)
m_{W}	28	22	17	
Γ_{W} $\mathrm{q\bar{q}q\bar{q}}$	17	8	5	
$\mathrm{q\bar{q}l}\nu$	39	13	5	
natural spread on $2\cdot E_{\mathrm{beam}}$	165 ± 8	219 ± 11	237 ± 12	(MeV)

Table 7.2: *List of uncertainties on the LEP beam energy currently quoted by LEP [46], and the corresponding impact on the* m_{W} *and* Γ_{W} *measurement.*

additional scatter $m_{\mathrm{W}} \cdot \sigma_{\mathrm{natural}}/\sqrt{s} < 100$ MeV/c^2 is small compared to the event-by-event resolution which is $\approx$3 GeV/c^2 ($\Gamma_{\mathrm{W}} \oplus$ measurement resolution). For n selected WW events it will lead to an additional statistical error on the effective LEP energy scale of $(m_{\mathrm{W}} \cdot \sigma_{\mathrm{natural}}/\sqrt{s})/\sqrt{n_{\mathrm{eff}}}$, where the effective number of participating events n_{eff} is estimated as the product of n and the selection purity. This additional uncertainty is quoted as systematic error on the LEP beam energy for each channel and each energy in tables 7.14 to 7.17 at the end of this chapter.

To estimate the effect on the measured width, the mass scatter $m_{\mathrm{W}} \cdot \sigma_{\mathrm{natural}}/\sqrt{s}$ should not be compared to the event resolution, but to the measured width Γ_{W}. The reason for this is that the analysis was calibrated to measure Γ_{W} with slope 1 and a bias equal to 0. The analysis cannot distinguish the extra mass scatter due to the LEP energy spread from an increased value of Γ_{W}. Therefore the analysis will overestimate the measured Γ_{W} according to:

$$\Gamma_{\mathrm{W}}^{\mathrm{fit}} \approx \sqrt{(m_{\mathrm{W}} \cdot \frac{\sigma_{\mathrm{natural}}}{\sqrt{s}})^2 + \Gamma_{\mathrm{W}}^2} \tag{7.4}$$

which predicts a positive bias of $\sim$+2.5 MeV/c^2 on all measurements of Γ_{W} — fully correlated across years, channels and experiments. This bias is applied as a correction.

RF asymmetries

An asymmetry in the RF voltage, caused e.g. by a trip of one of the RF units on one side of the experiment, can lead to a temporary boost of the e^+e^- centre-of-mass system in the direction of the beam axis. These boosts typically are 20 to 70 MeV/c [73]. Any accompanying change in centre-of-mass energy is properly corrected for by the LEP calibration files.

The influence of a boost along the beam direction on the measured mass (or width) has to be the same for positive and negative z direction because of the symmetry of the problem. This means that the effects of positive and negative boosts related to the 200 MeV natural beam spread (see above) do not average out but add up with the same sign. Therefore the small systematic effects quoted for the boosts related to the natural beam spread can be regarded as a conservative upper limit for the effect of a one-sided 70 MeV/c boost, which can thus safely be neglected.

7.3 ElectroWeak description and ISR

As discussed already in chapter 2, Electroweak theory provides a well-defined framework for the description of $e^+e^- \rightarrow$ 4-fermions(+photon(s)) production processes. The 4-fermion part and the description of photon radiation will be discussed separately.

4-fermion production

The EXCALIBUR MC generator used for the analysis at 183 GeV and 189 GeV includes all leading order 4-fermion production diagrams. The MC samples at 172 GeV, however, were generated with PYTHIA, only including the tree-level WW and ZZ diagrams (without taking into account their interference). Generator level studies [1, 31] have shown that this omission has a very small effect in all final states except for $\mathrm{q\bar{q}e}\nu$ where the interference with single W production is important. Therefore at 172 GeV a correction is applied and a systematic error is quoted to cover the effect of missing 4-fermion diagrams, with a numerical value of 10 MeV/c^2 in the $\mathrm{q\bar{q}q\bar{q}}$ and $\mathrm{q\bar{q}}\mu\nu$ channels, and 50 MeV/c^2 in the $\mathrm{q\bar{q}e}\nu$ channel. An uncertainty of 25 MeV/c^2 is quoted for the $\mathrm{q\bar{q}}\tau\nu$ channel, since the tau selection includes a significant fraction of $\mathrm{q\bar{q}e}\nu$ events (Tables 7.12 and 7.14).

Initial State Radiation

The only really large QED correction is related to Initial State Radiation (ISR), which has a direct influence on the measurement of the mass via the constraints used in the constrained fits. In about 10% of the events at 189 GeV an ISR photon of energy larger than 1 GeV is emitted and in 90% of those cases the ISR photons escape undetected inside the beam pipe. It is generally a good approximation to assume that the emitted ISR energy in an event is below the experimental resolution ($\sim$9 GeV in the $\mathrm{q\bar{q}q\bar{q}}$ channel (Figure 4.5) and worse for $\mathrm{q\bar{q}l}\nu$ events). In that case, the over-estimation of the effective centre-of-mass energy will not be noticeable, causing a positive bias on the reconstructed mass proportional to the total unseen energy loss E_γ in the event:

$$\Delta m_{\mathrm{W}} = E_\gamma m_{\mathrm{W}} / \sqrt{s} \qquad (7.5)$$

$m_{\rm W}$ and $\Gamma_{\rm W}$ shifts caused by ISR (MeV/c^2)								
$\sqrt{s}$, ISR model	$\rm q\bar{q}\mu\nu$		$\rm q\bar{q}e\nu$		$\rm q\bar{q}\tau\nu$		$\rm q\bar{q}q\bar{q}$	
$m_{\rm W}$	YB	full MC	YB	full MC	YB	full MC	YB	full MC
172 GeV QEDPS	407	373	383	274	433	255	410	252
183 GeV QEDPS	720	470	693	512	798	433	708	255
189 GeV QEDPS	872	567	857	609	944	507	829	291
YFS	838	547	836	589	909	467	799	275
YFS-QEDPS	-20 ± 5		-20 ± 7		-40 ± 8		-16 ± 3	
$\Gamma_{\rm W}$	full MC		full MC		full MC		full MC	
189 GeV YFS-QEDPS	-20 ± 10		-19 ± 13		-15 ± 16		-16 ± 5	

Table 7.3: *Comparison of the ISR shift predicted by the 'Yellow Book' formula (2.12) with the shift determined for the Ideogram analysis with full MC simulation. The values of the 'full MC' shifts at 172 GeV have a substantial statistical uncertainty. The difference between the QEDPS and YFS treatment of ISR (see text) serves as a basis for the systematic error estimate. All numbers have been corrected for the calibration slope.*

The average value $\langle E_\gamma \rangle$ at $\sqrt{s}$= 172, 183 and 189 GeV is equal to ≈ 0.88, ≈ 1.61 and ≈ 2.02 GeV. Replacing E_γ in equation (7.5) by the average ISR energy loss $\langle E_\gamma \rangle$ to obtain the overall mass shift leads to the 'Yellow Book' formula (2.12). This is a good approximation in the case that the overall measured mass is just the (unweighted) average of the masses of all events. In a real analysis, however, events with a high-energy ISR photon — if selected — will enter somewhere in the tail of the mass distribution and thus effectively have less impact on the measurement than events without ISR. Therefore, the mass shift caused by ISR is smaller than the shift predicted by equation (2.12).

$$\Delta m_{\rm W}^{\rm tot} < \langle E_\gamma \rangle m_{\rm W} / \sqrt{s} \tag{7.6}$$

This effect is illustrated in Table 7.3. The predicted mass shift shows small variations from channel to channel because $\langle E_\gamma \rangle$ for the selected events depends on the event selection. The 'true' ISR shift was obtained from WW simulation as the difference in fitted mass between the full sample and the sample containing only events without significant ISR (requiring $\sum E_\gamma < 10$ MeV). In all cases the actual ISR shift is considerably smaller than the predicted shift. In the $\rm q\bar{q}l\nu$ channels the observed shift is proportional to the Yellow Book formula. In the $\rm q\bar{q}q\bar{q}$ channel, however, the effect appears to be stable between 200 and 300 MeV/c^2, as expected for a successful event-by-event ISR treatment. In fact, this shift should show only a limited sensitivity to the amount of ISR radiation, and rather be a measure for the detector sensitivity to energy lost in the z direction, as given by a 3C constrained fit assuming a photon in the beam-pipe.

According to theoretical studies a correct implementation of currently available ISR models *should* result in a negligible systematic ISR uncertainty on the W mass. Nevertheless, for this analysis a cross-check was performed comparing the ISR model actually used with an independent theoretical model. The ISR uncertainty is deduced from the observed difference.

The standard DELPHI version of EXCALIBUR includes ISR photons with non-zero p_t (w.r.t. the beam axis) generated according to the QED Parton Shower (QEDPS) approach. WW events, generated with EXCALIBUR and analysed with the full Ideogram analysis were reweighted as a function of the total ISR energy in the events in order to correspond to the KORALW [74] ISR model, based on the YFS approach. The weights were derived from the ratio of the QEDPS and YFS ISR spectra at generator level. This was done for events generated at 189 GeV and the resulting shifts in the measured m_{W} and Γ_{W} are listed in Table 7.3.

Based on the differences between YFS and QEDPS found, an ISR uncertainty of 16 MeV/c^2 is quoted in the $\mathrm{q\bar{q}q\bar{q}}$ channel and 20 MeV/c^2 for all semi-leptonic channels at 189 GeV, both for the m_{W} and the Γ_{W} measurements; except for the $\mathrm{q\bar{q}}\tau\nu$ channel, where an uncertainty of 40 MeV/c^2 is quoted on the mass measurement. The corresponding numbers at 183 and 172 GeV were taken to be proportional to the 'true' ISR shift at each energy, with a minimum of 10 MeV/c^2.

Some other experiments currently quote ISR uncertainties of 5 MeV/c^2 and smaller in their 189 GeV papers [65], derived from the difference between a full $\mathcal{O}(\alpha^3)$ and $\mathcal{O}(\alpha^2)$ treatment or between an $\mathcal{O}(\alpha^2)$ and $\mathcal{O}(\alpha)$ treatment inside the KORALW ISR model. When QED radiative effects are to be controlled at a level below 10 MeV/c^2, however, other (non-factorisable) $\mathcal{O}(\alpha)$ effects may become important, and should be taken into account.

The ISR systematic error quoted here is assumed to be sizeable enough to cover all effects related to photon radiation inside the events.

7.4 QCD and jet production

The simulation of jet production and detection is arguably the most involved part of the simulation. As the W mass measurement is performed on final states with jets, this stage in the MC simulation is a quite important one. This section deals with systematic uncertainties related to the simulation of QCD processes, in four separate parts. First, the jet fragmentation of the individual W bosons (without considering possible cross-talk) is discussed in section 7.4.1. Then final state cross-talk via Bose-Einstein Correlations is the subject of section 7.4.2, followed by Colour Reconnection in section 7.4.3. Finally in section 7.4.4 the issue of the multi-jet rate in QCD background is addressed.

7.4.1 Jet fragmentation

The LEP2 data do not provide sufficient statistics to study fragmentation systematics from a MC/data comparison with the required precision.

Therefore the traditional approach relies on model comparisons and variation of tuning parameters inside a model, within the range compatible with the large statistics Z^0 data taken at LEP1 energies.

Model comparisons

The jet fragmentation model preferred by all LEP collaborations is JETSET with Lund string fragmentation. In DELPHI it has been tuned to the Z^0 data with more success than HERWIG 5.9, and reproduces the LEP1 event shapes and particle production rates excellently [41]. Recently a new tuning based on HERWIG 6.1 has become available in DELPHI that is able to describe the

DELPHI event shapes and multiplicities almost as well as JETSET, but at the time of writing of this thesis no simulation samples were available yet.

Event sample	detector simulation	shift (MeV/c^2)	
		m_{W}	Γ_{W}
ALEPH (HERWIG - JETSET)	DELSIM	-6 ± 18	-68 ± 38
(ALEPH - DELPHI) JETSET	DELSIM	$+3 \pm 18$	$+4 \pm 43$
DELPHI, JETSET			
"$\Lambda_{QCD} - 2\sigma$" - REFERENCE	FASTSIM	$+3 \pm 6$	-4 ± 12
"$\Lambda_{QCD} + 2\sigma$" - REFERENCE	FASTSIM	-7 ± 6	$+15 \pm 12$
"$\sigma_q - 2\sigma$" - REFERENCE	FASTSIM	-9 ± 6	-11 ± 12
"$\sigma_q + 2\sigma$" - REFERENCE	FASTSIM	-3 ± 6	-2 ± 12

Table 7.4: *A study of fragmentation effects on the m_{W} and Γ_{W} measurement in the $\mathrm{q\bar{q}q\bar{q}}$ channel at $\sqrt{s}$ = 189 GeV. All results are given with respect to the standard JETSET sample, the statistical error on the observed difference is also given.*

Instead a comparison between JETSET and HERWIG was done based on the event samples generated by ALEPH in the context of the LEP WW workshop [68]. The events were generated using ALEPH tuned JETSET and HERWIG, after which the full DELPHI detector simulation and W mass analysis were applied. The resulting difference for the $\mathrm{q\bar{q}q\bar{q}}$ channel at 189 GeV (see Table 7.4) is in excellent agreement with zero for m_{W}, while the Γ_{W} shift is 1.8 sigma away, with a large statistical error.

Tuning of parameters

Table 7.4 also shows the results of a comparison between the ALEPH tuning and the DELPHI tuning of JETSET, using the same event samples generated for the LEP WW workshop. In this comparison ZZ-like events were removed from the DELPHI EXCALIBUR simulation sample, as the ALEPH KORALW-based sample only contained doubly resonant WW-like (CC03) diagrams. This omission corresponds to a 120 MeV/c^2 shift in the width and 7 MeV/c^2 in the mass. Other differences that are thus cross-checked include the difference between the KORALW and EXCALIBUR treatment of ISR and FSR. Here the effect is remarkably consistent with zero.

Furthermore events were produced where the values of Λ_{QCD} and σ_q were changed with respect to the standard DELPHI tuned JETSET values by twice their estimated error. The estimated errors are ± 0.018 GeV for Λ_{QCD} and ± 0.007 GeV/c for σ_q, estimated by comparing a range of different fits, using different sets of input distributions [41]. These two parameters were chosen because they are expected to have the largest influence on the W mass. To obtain sufficient statistical precision, a million MC events per sample were needed. In order to speed up the generation, the DELPHI fast detector simulation package (FASTSIM) was used.

Fragmentation error

The results in table 7.4 are all compatible with zero. Based on these numbers and a similar study in the $\mathrm{q\bar{q}l\nu}$ channel, DELPHI [3] decided to quote a systematic error from fragmentation

Channel	m_W error (MeV/c^2)	Γ_W error (MeV/c^2)
$q\bar{q}l\nu$	20	42
$q\bar{q}q\bar{q}$	12	24

Table 7.5: *Systematic errors due to jet fragmentation quoted by DELPHI [3].*

reflecting twice the statistical precision of the JETSET tuning parameter studies in the combined semi-leptonic and fully-hadronic channels, listed in Table 7.5.

These numbers are believed to be conservative, which is an inevitable consequence of a lack of detailed understanding of the physics processes involved and modelling thereof.

As the other LEP collaborations currently also quote sizeable numbers for fragmentation systematics, and the LEP EW Working group takes all these numbers to be fully correlated between experiments, channels, and years, this has become the largest systematic contribution to the combined LEP W mass result [75]. In order to be able to make more precise estimates of this systematic error an improved understanding is needed.

The MLBZ method provides such precise and model-independent understanding and will be discussed in section 7.6.

7.4.2 Bose-Einstein correlations

Bose Einstein Correlations (BEC) are not described by the standard DELPHI MC simulation. This omission could lead to systematic errors on the W mass and width measurements if BEC leads to significant cross-talk between W bosons.

The main influence of BEC on the W mass measurement is expected to originate from a change in the fraction of mis-assigned particles. As discussed before, in $q\bar{q}q\bar{q}$ events the correct clustering of particles to jets and assignment to their parent W bosons is *already* one of the major difficulties. A BEC-induced enhancement of particles from different W bosons close in phase space could result in a fraction of mis-assigned energyflow which is different than expected (and simulated) from the independent decay of two superimposed W bosons.

A fundamental flaw of the majority of the available BEC models is that they do not have any relation with the quantum-mechanical origin of the effect. Rather, their aim is to reproduce the enhancement of pairs of identical bosons close in phase-space, which is only the most visible aspect of the BEC phenomenon. Therefore it is not clear what the predictive power of such models is. In addition to this drawback, other caveats exist:

- The framework used most frequently by the LEP experiments is the LUBOEI model, available as an option inside PYTHIA. It uses a local reweighting technique to move identical bosons closer to each other in phase space, and then offers different options to restore energy and momentum conservation. The danger of this procedure is that it (locally) violates energy and momentum conservation, and thereby changes invariant masses by construction. It is not clear how significant the resulting 'secondary' effects on the measured W mass are, and how to disentangle them from the W mass shifts caused by BEC.

- Models based on global reweighting of events in order to reproduce the two-particle correlation function ensure energy and momentum conservation, but in the process of reweighting they may change distributions of other variables, such as the invariant mass distributions (Breit-Wigner shapes) of the produced W bosons in the EW phase. Such a change is in contradiction with the factorisation ansatz that interference effects at the time-scale of hadron formation should not influence the hard EW scattering process. The latest global reweighting schemes [76] take care to minimise these secondary effects.

The reservations mentioned above should be kept in mind to properly assess the m_{W} and Γ_{W} shifts discussed below, which were observed with three different types of BEC models:

Local reshuffling of momenta

Several of the momentum reshuffling schemes of the LUBOEI model have been considered in this study. Full DELPHI simulation samples were produced only with the BE_0 reshuffling scheme. The more up-to-date BE_3 scheme and the recommended BE_{32} scheme have been produced in large statistics samples with the DELPHI FASTSIM simulation. Similarly, a BE_3 sample generated by ALEPH in the context of the Crete LEP WW workshop [68] was interfaced with the full DELSIM simulation and put through the W mass analysis. The resulting shifts on the W mass w.r.t. the corresponding JETSET reference samples are shown in Table 7.6. The shifts cover a large range, varying from 0$\pm$4 to -101$\pm$3 MeV/c^2. This shows that the size of these shifts critically depends on the values chosen for the parameters λ (the correlation strength) and the source size r. The size of the mass shift is expected to grow when λ/r increases. In order to obtain the most realistic estimate, it was decided to tune the values of λ and r on LEP1 data. For this exercise the BE_{32} model was chosen, because it gave the largest shift for the untuned values $\lambda = 1.6$ and $r = 0.33$ fm.

Global reweighting

The reweighting scheme considered here is the Kartvelishvili - Kvatadze - Møller (KKM) reweighting scheme described in [77]. Generator level studies show that the predicted multiplicity changes can be made compatible with LEP2 data, when the appropriate way of normalising the event weights is chosen. In this study unwanted changes in the generated mass distribution (at 4-fermion level) were strongly reduced by generating events according to a reduced Γ_{W} of 0.2 GeV/c^2, with ISR switched off. Using a 1-dimensional approximation of the full analysis after applying the fast detector simulation, shifts on the mass were found compatible with zero at the 10 MeV/c^2 level (see Table 7.6).

The quantum-mechanical approach

A model that is based more directly on quantum-mechanics is the ST model [78]. It calculates quantum-mechanical interferences for 2-particle and 3-particle final states in the framework of the LUND string model. It is thus based on the assumption that the LUND string fragmentation model (used in JETSET) is able to describe not only the development of the parton shower in momentum space (which is experimentally constrained by the data), but also the space-time evolution (about which little is currently known). A confirmation of the validity of this approach is the fact that it predicts the enhancement of like-sign pion pairs close in phase space as observed in LEP1 data to within the experimental statistical precision. Similarly the ST model can predict the effects of

1D approximation of 183 GeV analysis

'reference' ≡ BEC switched off
'BEA' ≡ BEC inside and between W's
'BEI' ≡ BEC only inside W's

model	$\sqrt{s}$	λ	r (fm)	m_{W} shift (MeV/c^2)	Γ_{W} shift (MeV/c^2)
ST BEI - reference *	183	not applicable		-4 ± 9	-
ST BEA - reference *	183			-1 ± 8	-
ST BEA - BEI *	183			+3 ± 11	-
KKM global - reference *	183	1.00	0.50	-10 ± 10	-

Full 2D 189 GeV analysis

model	$\sqrt{s}$	λ	r (fm)	m_{W} shift (MeV/c^2)	Γ_{W} shift (MeV/c^2)
BE_0 BEI - reference **	189	1.00	0.50	-134±38	-
BE_0 BEA - reference **	189	1.00	0.50	-100±38	-
BE_0 BEA - BEI **	189	1.00	0.50	+34±43	-
BE_0 BEI - reference **	200	0.85	0.50	-2±34	-33±74
BE_0 BEA - reference **	200	0.85	0.50	+30±34	-56±74
BE_0 BEA - BEI **	200	0.85	0.50	+32±34	-23±74
BE_3 BEI - reference ***	189	2.10	0.77	+1±14	+46±31
BE_3 BEA - reference ***	189	2.10	0.77	-2±14	+99±32
BE_3 BEA - BEI ***	189	2.10	0.77	-3±14	+53±31
BE_3 BEI - reference °	189	1.00	1.00	-1±10	+0±20
BE_3 BEA - reference °	189	1.00	1.00	-1±10	+2±20
BE_3 BEA - BEI °	189	1.00	1.00	+0±4	+2±8
BE_3 BEI - reference °	189	1.60	0.33	+22±4	-31±8
BE_3 BEA - reference °	189	1.60	0.33	-51±4	+60±8
BE_3 BEA - BEI °	189	1.60	0.33	-73±4	+90±8
BE_{32} BEI - reference°	189	1.60	0.33	+35±4	-15±7
BE_{32} BEA - reference°	189	1.60	0.33	-63±4	+85±7
BE_{32} BEA - BEI °	189	1.60	0.33	-101±3	+102±6
BE_{32} BEI - reference°°	189	1.35	0.60	+18±5	+13±11
BE_{32} BEA - reference°°	189	1.35	0.60	-14±5	+39±11
BE_{32} BEA - BEI °°	189	1.35	0.60	-32±4	+26±8

* not retuned, no ISR, reduced Γ_{W}, FASTSIM
** not retuned, normal ISR and Γ_{W}, full DELSIM
*** ALEPH sample from Crete WW workshop, full DELSIM
° not retuned, normal ISR and Γ_{W}, FASTSIM
°° JETSET parameters retuned, normal ISR and Γ_{W}, FASTSIM

Table 7.6: *Shifts on W mass and width found for different BEC models and parameter settings. All studies were performed on CC03 WW events generated by PYTHIA (DELPHI samples) or KORALW (ALEPH samples).*

Bose-Einstein correlations when the particles originate from different W bosons. Earlier studies based on this model and the 183 GeV $q\bar{q}q\bar{q}$ analysis showed a shift in the mass of +3 $\pm$ 11 MeV/c^2.

Preliminary BEC conclusion

Table 7.6 gives a full list of models that have been checked and the shifts on the measured m_{W} and Γ_{W} they produced.

The ST and KKM model predict shifts compatible with zero at the 10 MeV/c^2 level. The only significant shifts were found with the LUBOEI model. Here the (BEA-BEI) are most relevant for the systematic uncertainty, since (BEI-reference) should be equal to zero when the BEI model is properly tuned on Z^0 data. BEC inside bosons should be part of the jet fragmentation studies, and is covered by MLBZs at the 5 MeV/c^2 level (section 7.6). Any significant (BEI-reference) shift therefore is an indication of an intrinsic systematic uncertainty in the BEC study at hand, rather than an estimate of a systematic error on the W mass measurement.

From the (BEI-reference) shifts in Table 7.6, an apparent intrinsic precision of 20-30 MeV can be deduced for the LUBOEI studies presented here. This lends support to the hypothesis that the shifts predicted by LUBOEI are secondary effects related to the reshuffling of momenta, rather than genuine predictions of BEC effects.

Nevertheless, DELPHI currently quotes a systematic uncertainty based on the LUBOEI (BE_{32}) shift for the values of λ and r that give the best fit to the 2-particle correlations observed in LEP1 data [3]: -32 MeV/c^2 for m_{W} and +26 MeV/c^2 for Γ_{W}.

However, a new development since the latest DELPHI W mass publication [3] is the fact that recently [43] the 4 LEP experiments unanimously concluded that there is no evidence in LEP2 data of any correlations between W's, which means that the effect is much smaller than would be expected on the basis of the correlations observed inside W and Z bosons.

In view of the above, a systematic uncertainty of 10 MeV/c^2 seems to be a realistic estimate for the m_{W} measurement. For Γ_{W} fewer results are available, so a 25 MeV/c^2 will be quoted, close to the shift found with LUBOEI.

7.4.3 Colour Reconnection

To study CR effects in the non-perturbative phase, one has to rely on the available phenomenological models. They implement CR inside existing fragmentation models:

- PYTHIA: In the Sjöstrand-Khoze (SK) model a reconnection of strings can occur when they overlap or cross in space-time.
  - SK1: The strings have a lateral dimension, and for each event a reconnection probability can be calculated which depends on the space-time overlap of the strings as:

    $$p_{CR} = 1 - \exp(-\kappa \cdot O) \tag{7.7}$$

    where O is the space-time integral of the string overlap and κ a free parameter.
  - SK2: Strings have a thin one-dimensional core. Reconnection only occurs when the cores intersect.

- SK2': Is based on 1-dimensional strings as in SK2, but reconnection only occurs when cores intersect *and* the string length is reduced.

- ARIADNE: Reconnection happens if this leads to a lower QCD potential (i.e. strings with a lower invariant mass).
  - AR2: Reconnection between strings from different bosons is only allowed below a user-supplied energy scale (usually Γ_W).
  - AR3: Reconnection is allowed at all energy scales, i.e. including the perturbative phase.

- HERWIG: Colour dipoles are rearranged before cluster formation, changing the size (in space-time) of the clusters. Multiple reconnections are allowed.

Colour Reconnection is not only expected to change the particle flow (and thus affect jet clustering), but it would actually act as an interaction between the two W bosons in a $q\bar{q}q\bar{q}$ event, directly affecting the invariant mass of the hadronic decay systems through the transfer of 4-momentum. This would obviously have an effect on the W mass measurement.

A very important feature, predicted by all CR computations, is that CR plays a role only in a rather small fraction of the events ($\sim 30\%$). Whether or not reconnection can take place

1D approximation of 183 GeV analysis			
model	$\sqrt{s}$	m_W shift(MeV/c^2)	Γ_W shift (MeV/c^2)
ARIADNE 1 (inside) *	183	+12 ± 7	-
ARIADNE 2 (all) *	183	+28 ± 6	-
ARIADNE 3 *	183	+55 ± 6	-
Full 2D 189 GeV analysis			
model	$\sqrt{s}$	m_W shift (MeV/c^2)	Γ_W shift (MeV/c^2)
SK1 full - reference **	189	+269±17	-
SK1 full - reference ***	189	+262±20	-
SK1 full - reference ****	189	+283±6	+144±23
SK1 improved full - reference ****	189	+258±6	+85±23
SK1 30% - reference ***	189	+5±7	+131±15
SK1 30% - reference ****	189	+46±2	+54±3
SK1 improved 30% - reference ****	189	+44±2	+32±3
SK2 - reference ****	189	-2±5	+37±10
* not retuned, no ISR, reduced Γ_W, FASTSIM			
** Crete ALEPH retuned, FASTSIM			
*** Crete ALEPH retuned, full DELSIM			
**** not retuned, normal ISR and Γ_W, FASTSIM			

Table 7.7: *Shifts on the W mass and width found for different CR models.*

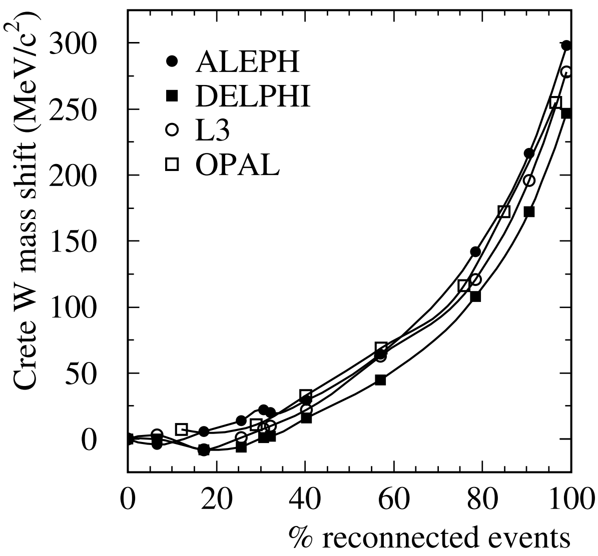

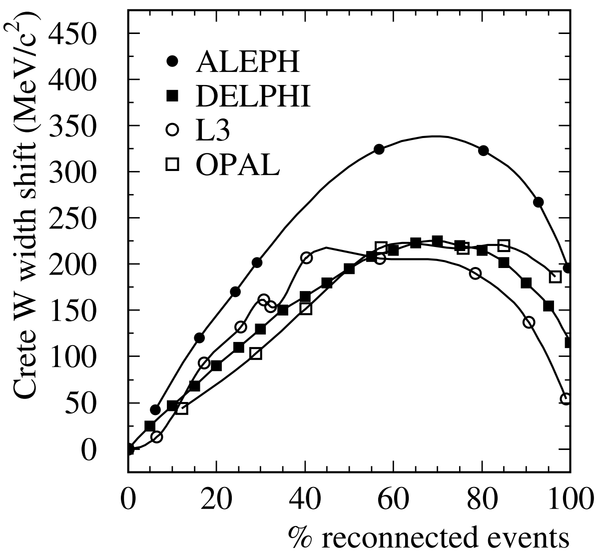

Figure 7.5: *Observed shift in the fitted mass (left) and width (right) as a function of the fraction of reconnected events, using the CR event samples generated for the Crete workshop (see text).*

depends on the configuration of the colour flow inside the event, determined by the directions and momenta of the primary quarks and anti-quarks.

The list of models that were tested and the corresponding shifts on the W mass and width as found with the Ideogram analysis are listed in Table 7.7.

Crete workshop results

In the context of the 'Crete' WW workshop the SK1 model was chosen to serve as a benchmark CR model for comparison between the LEP experiments. The free parameter κ can be tuned from zero to full reconnection, giving large ($\approx$ 300 MeV/c^2) measurable mass shifts for the full reconnection. Two samples of 100,000 events were generated using standard ALEPH KORALW+JETSET. Care was taken to make sure that the two samples were identical on the 4-fermion level. However, one sample was treated with standard JETSET while for the other sample JETSET was used with *full* SK1 colour reconnection. Subsequently both sets of events were passed through the full detector simulation and the $\mathrm{q\bar{q}q\bar{q}}$ W mass analysis of each of the 4 LEP experiments. The aim was to compare among different experiments the effect on the mass as a function of the *average* reconnection probability, which can be computed for a given value of κ. Using random numbers and formula (7.7) for each event either the reconnected or the original non-reconnected event was chosen, according to $p_{CR}(\kappa, O_{\mathrm{event}})$. By using a common set of random numbers it was ensured that each of the experiments used exactly the same mixed set of reconnected and non-reconnected events as a function of κ. In Figure 7.5 (left) the resulting curves of the mass shift are shown as a function of the average reconnection probability. The study shows that the m_{W} shifts are *identical* for the different experiments, within the statistical precision. This further supports the approach used by the LEP EW working group [75] to deter-

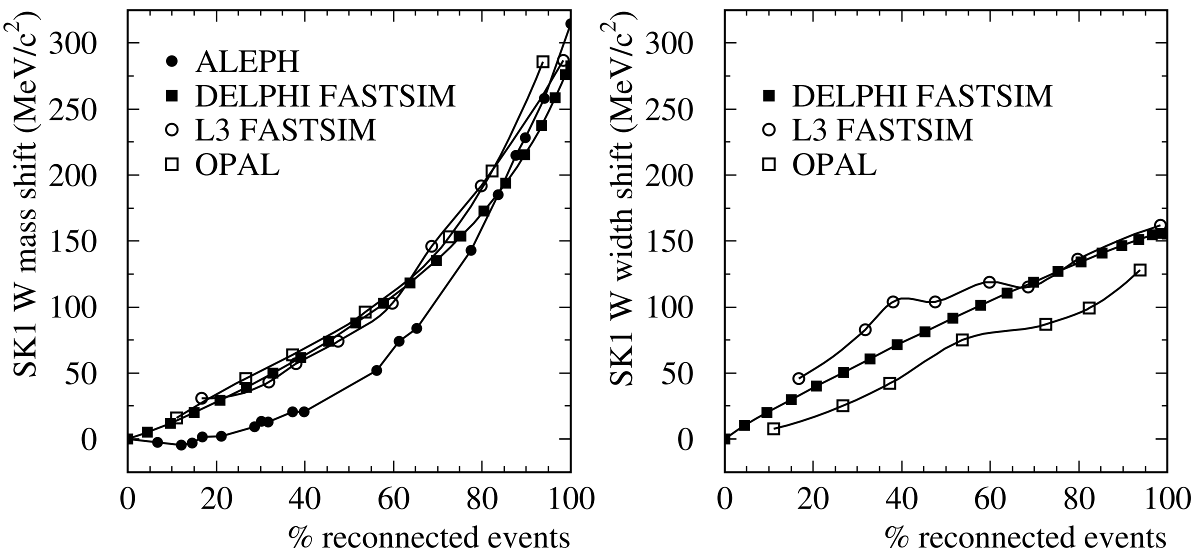

Figure 7.6: *Observed shift in the fitted mass (left) and width (right) as a function of the fraction of reconnected events, where each experiment used its own SK1 implementation. The ALEPH curve still shows the typical shape observed with the Crete samples (the most recent ALEPH curves agree with those of the other experiments).*

mine a common FSI error in the LEP W mass and width combination, taken (and believed) to be fully correlated and equal in size for the different LEP analyses.

DELPHI refinements

In DELPHI the Crete study was extended, applying the following refinements:

- First, an improved statistical treatment was implemented combining for each event the CR and non-CR event likelihood curves with relative weights p_{CR} and (1-p_{CR}) where p_{CR} reflects the probability of reconnection for the event as given by equation (7.7). Also for each point of the curve an automated Jackknife procedure was used to calculate the statistical errors (shown only in Figure 7.7). The procedure of combining weighted events instead of rejecting either the reconnected or the non-reconnected version of each event from the sample was found to give an improvement in the statistical precision of up to a factor $\sqrt{2}$ at 50% reconnection, and the continuous way in which all available information is used results in smoother curves.

- A similar study was done of the effect on the measured W *width* as a function of the reconnected fraction of events. A curve with a surprising shape was found (see Figure 7.5), which was later confirmed by the other experiments. Again the observed shift turned out to be identical for the 4 experiments (the statistical errors, not shown in Figure 7.5, are fairly large).

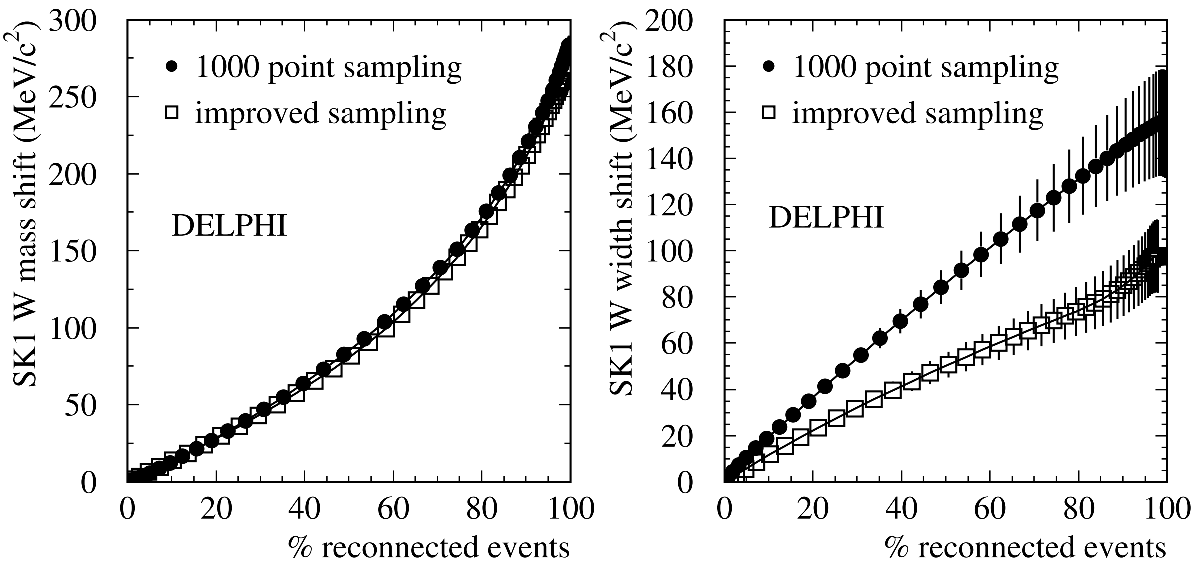

Figure 7.7: *Observed shift in the fitted mass (left) and width (right) as a function of the fraction of reconnected events, using the improved DELPHI SK1 implementations (see text). The statistical errors, indicated by the error bars, are almost fully correlated from point to point.*

- The exercise was repeated using DELPHI FASTSIM simulation instead of the full DELSIM detector simulation checking whether this would yield the same estimated systematic shifts. The FASTSIM curve turned out to agree perfectly with the DELSIM curve. Therefore all further SK1 studies were based on FASTSIM simulation.

- Figure 7.6 displays the curves obtained by each of the LEP experiments when using their own implementation of SK1 instead of the Crete SK1 events. Clearly, these curves are more linear (both for the mass and the width) than seen with the Crete samples. This led to the discovery that a mistake in the generation of the Crete samples led to an erroneous relation between the calculated reconnection probabilities and the actual colour flow in the events. Therefore the Crete samples do not represent the real 'SK1' behaviour, but it is still interesting to compare the response of the different analyses.

- The SK1 model uses a numerical sampling of phase space in order to integrate the string overlap. It was shown [79] that the standard sampling procedure is not sufficient to give a reliable calculation of the string overlap and that this can be significantly improved by using a more efficient choice of phase space sampling points. This improvement was implemented in the DELPHI SK1 routine. Also the possibility of multiple reconnections was added. The resulting curve is shown in Figure 7.7, together with the curve obtained with the standard SK1 model using 1000 instead of 100 sampling points, both based on DELPHI tuning of JETSET. The difference between the two curves turns out to be small for the mass, but significant for the Γ_W curve.

Preliminary CR conclusions

The DELPHI estimate of the systematic error due to CR is 46 MeV/c^2 (mass) and 54 MeV/c^2 (width). These values are based on SK1 with 30% reconnected events (Table 7.7). This is considered to be a realistic fraction by the author, Sjöstrand — in agreement with SK2 and HERWIG model predictions.

These values represent the largest shifts found with DELPHI tuned samples, apart from the ARIADNE 3 model, which never was regarded (or intended) as a serious physics model. It includes reconnections in the perturbative phase where calculations have shown these effects to be small (see discussion in section 2.7).

7.4.4 QCD background processes

As discussed in section 2.6 the main physics background process passing the event selection is two-fermion $q\overline{q}\gamma$(+ 2 gluons) production. Especially in the fully-hadronic channel this QCD background is significant. The requirement of 4 or more jets selects events with at least two hard gluons, which means that higher order diagrams are important. This leads to systematic uncertainties in both the topology and the cross-section of the accepted events.

Fortunately the influence of $q\overline{q}\gamma$ background on the mass is small: leaving out the $q\overline{q}\gamma$ events completely from the MC simulation changes the mass by +36 MeV/c^2 (at 172 GeV), decreasing to +15 MeV/c^2 (at 189 GeV) in the $q\bar{q}q\bar{q}$ channel. The corresponding numbers for all channels and energies are shown in Table 7.8. Features of the Ideogram analysis that help to reduce this impact are the inclusion of an event-by-event purity and a simple event selection which is not (or only very slightly) biased by the mass information in the event, giving a flat background shape.

Possible systematic effects are only a fraction of the overall impact mentioned above. They were assessed in the following way:

- The uncertainty on the accepted cross-section is estimated to be 5-7% [80]. A conservative change of 10% was applied and the shift in fitted mass and width quoted as systematic error. The results are listed in Tables 7.14- 7.17, at the end of this chapter.

- A possible imperfection in the description of the background shape was estimated by comparing different MC samples based on different fragmentation models. The reference MC based on PYTHIA + JETSET fragmentation was compared to ARIADNE + JETSET and HERWIG 5.9. The resulting shifts for 189 GeV are shown in Table 7.8. Since all shifts are compatible with zero, and the HERWIG 5.9 model with DELPHI tuning gives a slightly worse description of the Z^0 data than the JETSET models, the difference PYTHIA-ARIADNE was quoted as a systematic error on the background shape (see Table 7.8).

7.5 Detector effects

The last step in the measurement is the detection of the final state particles with the DELPHI detector. Also here Z^0 events play a crucial role in understanding possible systematic discrepancies. In addition to the LEP1 data, Z^0 events were available from the calibration runs that were taken

m_W and Γ_W shifts caused by $q\bar{q}\gamma$ background (MeV/c^2)								
$\sqrt{s}$, MC program	$q\bar{q}\mu\nu$		$q\bar{q}e\nu$		$q\bar{q}\tau\nu$		$q\bar{q}q\bar{q}$	
m_W	m_W	Γ_W	m_W	Γ_W	m_W	Γ_W	m_W	Γ_W
172 GeV JETSET*	+3		-82	+288	-180		-36	+323
(ARIADNE*	-7		-56	+297	-85		-65	+306)
183 GeV JETSET	-5	+56	-44	+351	+40	+735	-21	+377
189 GeV JETSET	-6	+78	-107	+433	+34	+1091	-15	+337
ARIADNE-JETSET	-	-	-	-	-	-	+5 ± 5	+22 ± 10
HERWIG-JETSET	-	-	-	-	-	-	-11 ± 11	+24 ± 23
* At $\sqrt{s}$ = 172 GeV the three semi-leptonic channels were combined for Γ_W in order to avoid large statistical fluctuations								

Table 7.8: *The impact of* $q\bar{q}\gamma$ *background on the* m_W *and* Γ_W *measurement bias (corrected for the calibration slope). For the* $q\bar{q}q\bar{q}$ *channel at 189 GeV numbers are shown for the differences when using JETSET, ARIADNE or HERWIG fragmentation to describe the* $q\bar{q}\gamma$ *background.*

at least once a year, providing tens of thousands of events to be used for detector alignment and calibration.

This section describes the specific detector systematics checks that have been done. Some of the results only serve as a cross-check and will be superseded by MLBZ results [2], to be presented later in section 7.6. Others are complementary sources of systematic errors and will be treated as separate contributions to the systematic uncertainty (and/or applied as correction where appropriate).

7.5.1 Jets

The detection of jets is a complicated process, as discussed before. Here a study is presented of possible discrepancies between data and MC, identified using hadronic Z^0 events from the two 1998 Z^0 calibration runs. Not only 2-jet, but also 3-jet $Z^0 \to q\bar{q}g$ events were selected, in order to study jets with energies below 45.6 GeV as well. In all cases a constrained fit was used to estimate 'true' jet energies and directions, and a jet energyflow efficiency was defined as $\varepsilon = E_{\text{measured}}/E_{\text{fitted}}$. In order to extend the jet energy range to include energies above 45.6 GeV, 2- and 3-jet hadronic events from the 189 GeV data were added to the study. The majority of radiative $Z^0\gamma \to q\bar{q}\gamma$ was removed by requiring a reconstructed $\sqrt{s'}$ above 180 GeV.

In addition to the energyflow efficiency scale, also the resolution was compared between data and MC, in terms of the RMS of ε. Furthermore a comparison of the angular resolutions was performed, based on the acollinearity of 2-jet events. Finally each estimated discrepancy was applied to 189 GeV WW simulation, at the level of reconstructed particles or jets, in order to study the effect on the measured m_W and Γ_W. This gave the following results in the $q\bar{q}q\bar{q}$ channel:

- *overall jet energy scale*
  The average jet energyflow efficiency in DELPHI is around 85%, and the agreement between data and MC simulation is of the order of 1%. This can be derived from the plots in

[2] So far MLBZ results are only available for m_W; not yet for Γ_W.

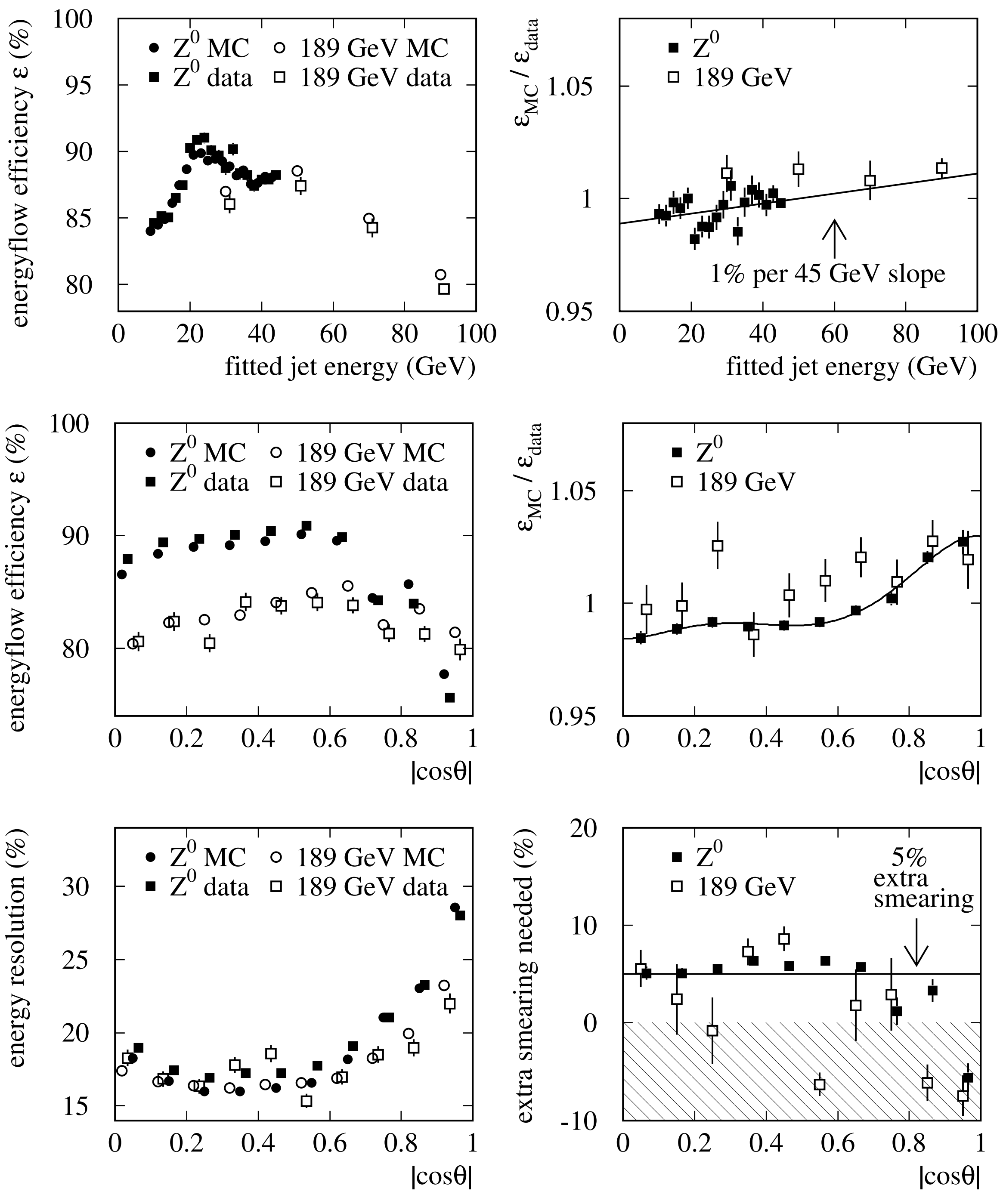

Figure 7.8: *Jet systematics study, comparing 189 GeV and Z peak data with the corresponding MC simulation (left), selecting hadronic events with 2 or 3 jets. In general a fair agreement between data and MC can be seen. The parameterisations shown in the right-hand plots were used to estimate possible systematics due to data/MC discrepancies (see text).*

Figure 7.8, and is confirmed by the difference between the fitted W mass with and without constrained fit in Figure 5.1.

The effect of an overall mismatch in energy scale on the $m_{\rm W}$ measurement is small, since this scale is fixed by the value of $\sqrt{s}$ in the constrained fit. Applying a +1% scaling of all measured jet energies at 189 GeV induced a shift of +3.0±0.3 MeV/c^2 on $m_{\rm W}$ and -0.5±0.3 MeV/c^2 on $\Gamma_{\rm W}$.

This effect is not taken into account separately because (in case of $m_{\rm W}$) it is covered by the MLBZ method, and also included in one of the effects discussed below (energy scale versus cosθ).

- *energy scale versus energy (i.e. non-linearity)*
  Since in WW events the jet energies range from 25 to 75 GeV, it is interesting not only to check the average jet energyflow efficiency, but also the response as a function of the jet energy. In Figure 7.8 (top left) the energyflow efficiency is plotted as a function of the fitted jet energy in order to investigate the non-linearity of the energy response. The non-linearity in data is well described by the MC. In the ratio $\varepsilon_{\rm MC}/\varepsilon_{\rm data}$ (top right) no evidence for a dependence as a function of energy was found, although the high-energy data systematically give a higher ratio than the $\rm Z^0$ peak results. The effect of an additional non-linearity slope of 1% per 45 GeV was investigated using MC simulation, and the results are listed in Table 7.9.

  This effect is only partly covered by MLBZs, and will be quoted separately.

- *energy scale versus* cosθ
  A clear dependence of the energyflow reconstruction efficiency can be seen as a function of the polar angle θ of the jet (Figure 7.8, middle plots). The ratio $\varepsilon_{\rm MC}/\varepsilon_{\rm data}$ was parameterised and applied to MC simulation to estimate the corresponding shifts in W mass and width. The results are shown in Table 7.9.

  This effect should be covered by MLBZs, and serves as a cross-check (for $m_{\rm W}$).

- *energy resolution versus* cosθ
  The jet energy resolution also varies as a function of the polar angle. Here the MC simulation is a bit too optimistic in the barrel region, while overestimating the errors in the very forward directions. In Figure 7.8 (bottom right) the mismatch in resolution $(\sigma^2_{\rm data} - \sigma^2_{\rm MC})^{1/2}$ (or, in case $\sigma_{\rm MC} > \sigma_{\rm data}$, $-(\sigma^2_{\rm MC} - \sigma^2_{\rm data})^{1/2}$ in the shaded area) is plotted. The corresponding systematic uncertainty was estimated by adding an extra Gaussian smearing of 5% to the jet energies in the MC simulation.

  The results are shown in Table 7.9. The $m_{\rm W}$ numbers serve only as a cross-check, because this effect is covered in a superior way by the MLBZ method.

- *resolution on the jet angles*
  Similarly, a systematic uncertainty was estimated by applying an extra smearing of 5 mrad to the jet directions (based on a data/MC comparison of the acollinearity of 2-jet $\rm Z^0 \to q\bar{q}$ events). The results are shown in Table 7.9. Also in this case the MLBZ method should take the effect into account in more detail.

Study of Jet systematics in the $q\bar{q}q\bar{q}$ channel			
simulated discrepancy	m_W shift (MeV/c^2)		
	172 GeV	183 GeV	189 GeV
introducing +1% per 45 GeV non-linearity slope	-3.6±0.5	-6.0±0.3	-13.7±0.2
applying energy-scale versus cosθ correction	+3.0±1.2	+9.2±0.4	+10.7±0.3
5% extra smearing jet energies	-2.0±6.3	-2.1±2.3	-1.6±1.4
5 mrad extra smearing jet angles (θ and ϕ)	-3.5±4.5	+4.0±2.0	+0.8±1.3
0.1% increase in DELPHI length	+1.0±1.8	-3.1±0.7	-4.2±0.6
simulated discrepancy	Γ_W shift (MeV/c^2)		
	172 GeV	183 GeV	189 GeV
introducing +1% per 45 GeV non-linearity slope	+6.5±0.8	+6.3±0.4	+6.8±0.2
applying energy-scale versus cosθ correction	-7.8±2.3	-9.6±1.0	-8.3±0.6
5% extra smearing jet energies	+7.8±12.1	+13.0±5.0	+2.6±3.3
5 mrad extra smearing jet angles (θ and ϕ)	+3.4±9.3	+5.0±4.4	+24.0±3.0
0.1% increase in DELPHI length	+2.2±3.4	+1.4±1.7	+3.1±1.1

Table 7.9: *Shift in W mass ($\equiv m_{\rm new} - m_{\rm reference}$) and width when different sources of jet systematics are introduced in a MC sample (and the MC sample is fitted as if it was data). Since the simulated effects generally induce only small disturbances to the events, the obtained shifts are small and have a high statistical precision. The statistical errors were evaluated using the Jackknife method.*

The above study was restricted to the $q\bar{q}q\bar{q}$ channel. For the $q\bar{q}l\nu$ channel the overall results were adopted from a similar jet reconstruction systematics study performed for the main DELPHI analysis [3] (Tables 7.14-7.16).

7.5.2 Leptons

The Z^0 calibration data also contain $Z^0 \rightarrow \mu^+\mu^-$ and $Z^0 \rightarrow e^+e^-$ events. Those events were used to do similar studies for the lepton reconstruction systematics as presented above for the jet response of the main DELPHI $q\bar{q}l\nu$ analysis [1, 2, 3]. The lepton systematics numbers quoted by DELPHI are adopted for the $q\bar{q}l\nu$ study presented here. No particular reasons are known to expect a different systematic behaviour, but since no dedicated cross-checks have been performed, the quoted values were multiplied by a factor 2 (Tables 7.14-7.16), to reflect an increased level of uncertainty.

7.5.3 Aspect ratio of DELPHI

The uncertainty on the length to width ratio (aspect ratio) of DELPHI could lead to systematic distortions in the reconstructed polar angle θ. Whereas a relative alignment of detector parts is possible with great precision using calibration data, it is virtually impossible to extract information about the absolute ratio of the length scale and the radial scale of the detector from reconstructed tracks. Hence the aspect ratio must be derived from the knowledge of the absolute positions and geometry of sub-detectors. In the DELPHI alignment this ratio is mainly determined by the Vertex Detector. The dominant uncertainty on its geometry is the uncertainty on the radius, which is known with a precision slightly better than 0.1% (during data taking conditions).

The effect of this aspect ratio uncertainty was estimated by varying the scale of the z-momenta of all measured particles (in MC simulation). This was done on the level of the reconstructed particles. The resulting effects on m_{W} and Γ_{W} are listed in Table 7.9.

Shifts corresponding to a change of 0.1% are quoted as a systematic error (or the statistical error on the shift; whichever is larger). The size of the effects decreases for lower $\sqrt{s}$ values because near WW threshold the jets of the W bosons are almost back-to-back, so that the effect of the aspect ratio on the mass vanishes. At higher energies an effect of the angular distortion on the mass becomes possible, but as long as the angular distribution of the W bosons has a uniform component the (positive and negative) mass shifts will partly cancel out on average. The systematic effect grows for increasing values of $\sqrt{s}$ as the angular distribution becomes more peaked in the forward direction (section 2.1).

7.6 Refinement based on MLBZ

In the previous sections (7.4.1 and 7.5) jet fragmentation and reconstruction systematics were investigated using the traditional approach. By comparing Z^0 data and Z^0 MC simulation possible systematic discrepancies were identified and applied to WW simulation to investigate their effects on m_{W} and Γ_{W}. This was a tedious job, requiring the simulation and subsequent analysis of millions of WW MC events. The number of possible effects studied was therefore limited, and each effect had to be simplified in order to apply it to the WW simulation (e.g. a variation of a single JETSET parameter; a comparison of two fragmentation models; a 1-dimensional correction to the jet energies as function of cosθ). In many cases the result still contained a significant model-dependence, and the question remains how to combine the list of correlated m_{W} (or Γ_{W}) shifts.

A faster and more straight-forward approach, which does not require any additional MC simulation, is the Mixed Lorentz Boosted Z^0 (MLBZ) method.This method uses the Z^0 data events themselves to produce a 'simplified' WW simulation (see also the introduction in section 5.6). By applying the Ideogram analysis directly to the 'emulated' WW events, a mass is extracted. The same procedure is applied to Z^0 events from MC simulation — already available in large quantities. By comparing the reconstructed MLBZ mass between data and MC, a a model-independent and statistically precise estimate of a subset of systematic errors due to jet fragmentation and reconstruction is obtained.

Z^0 data taking period	1997	May 1998	October 1998
$(m_{\mathrm{data}} - m_{\mathrm{simulation}})\vert_{\mathrm{udsc}}$ (MeV/c^2)	-0.3 $\pm$ 2.8	-1.0 $\pm$ 1.5	-4.7 $\pm$ 2.9

Table 7.10: *Systematic fitted mass difference between data and MC simulation for the different* Z^0 *data taking periods in 1997 and 1998, estimated using the MLBZ technique.*

The results shown in Table 7.10 have been corrected for the difference in W and Z^0 mass scale, and the sensitivity to the difference in flavour composition was reduced (and does not have a significant effect). A detailed description is given in Appendix A. The remainder of this section will focus on the main features of the MLBZ method and give a further explanation and interpretation of the results presented above.

MLBZ essentials

A crucial piece of knowledge which is exploited when performing the simplified WW emulation, is the fact that all Z^0 events are produced at rest — both in MC and in data. Thus their Lorentz boost is well defined. The WW emulation used in the MLBZ results presented here is indeed extremely simplified, retaining only the most basic properties of a WW event. Two Z^0 events are boosted in opposite direction, and superimposed. The direction of the boosts is randomly chosen giving a uniform angular distribution, while the magnitude of the boosts is kept fixed to the average value for W's in a WW event.

It is perfectly possible to improve the emulation, because the (EW) production of W bosons is a well-defined process. Rescaling the Z^0 events to reproduce a proper Breit-Wigner distribution, and taking into account ISR and the angular distributions of the W bosons is trivial. It is even possible to choose Z^0 events in such a way that after the boost *one* of the jets of each Z^0 points in the direction in the detector where it was originally detected. However, with these requirements all degrees of freedom have been used, and the other jets are forced to point to the 'wrong' regions inside the detector. Also the energies and momenta of the particles after the boost are different from the original ones with which they were detected. Therefore MLBZ events can *not* be regarded as a WW simulation with full description of detector effects (The study in appendix A shows that these limitations play a negligible role as long as the detector discrepancies are known to be small and the Z^0 events are selected such that the overall angular distribution of jets in the detector resembles the distribution of jets in WW events).

While the WW emulation is only an approximation, the MLBZ method does not compromise the completeness or detail with which the systematic jet discrepancies are taken into account. Since the main MC model is directly compared to data, all imperfections in the simulation of Z^0 events are included and probed, automatically taking correlations into account. The difference between the Z^0 and W fragmentation scale is expected to be eminently treated by the Parton Shower models. Thus it is believed that fragmentation systematics are fully covered, while detector effects are partly included as well.

Improved understanding

The Z^0 events are used more than once, boosting them in different directions and mixing them with different Z^0 events. Thus an excellent statistical precision of the order of 2 MeV/c^2 can be reached on the systematic bias for a typical Z^0 calibration run with an integrated luminosity of 2.5 pb^{-1}. This level of statistical precision allowed a detailed study of the W mass reconstruction bias as a function of Z^0 event variables, and confirmed the following expectations:

- Non-perfect jet reconstruction causes the W jet-jet angle to be under-estimated on average, thus leading to a negative bias on the reconstructed mass.
- Deterioration of the jet reconstruction quality leads to a more negative bias
- This bias is excellently described by the MC simulation

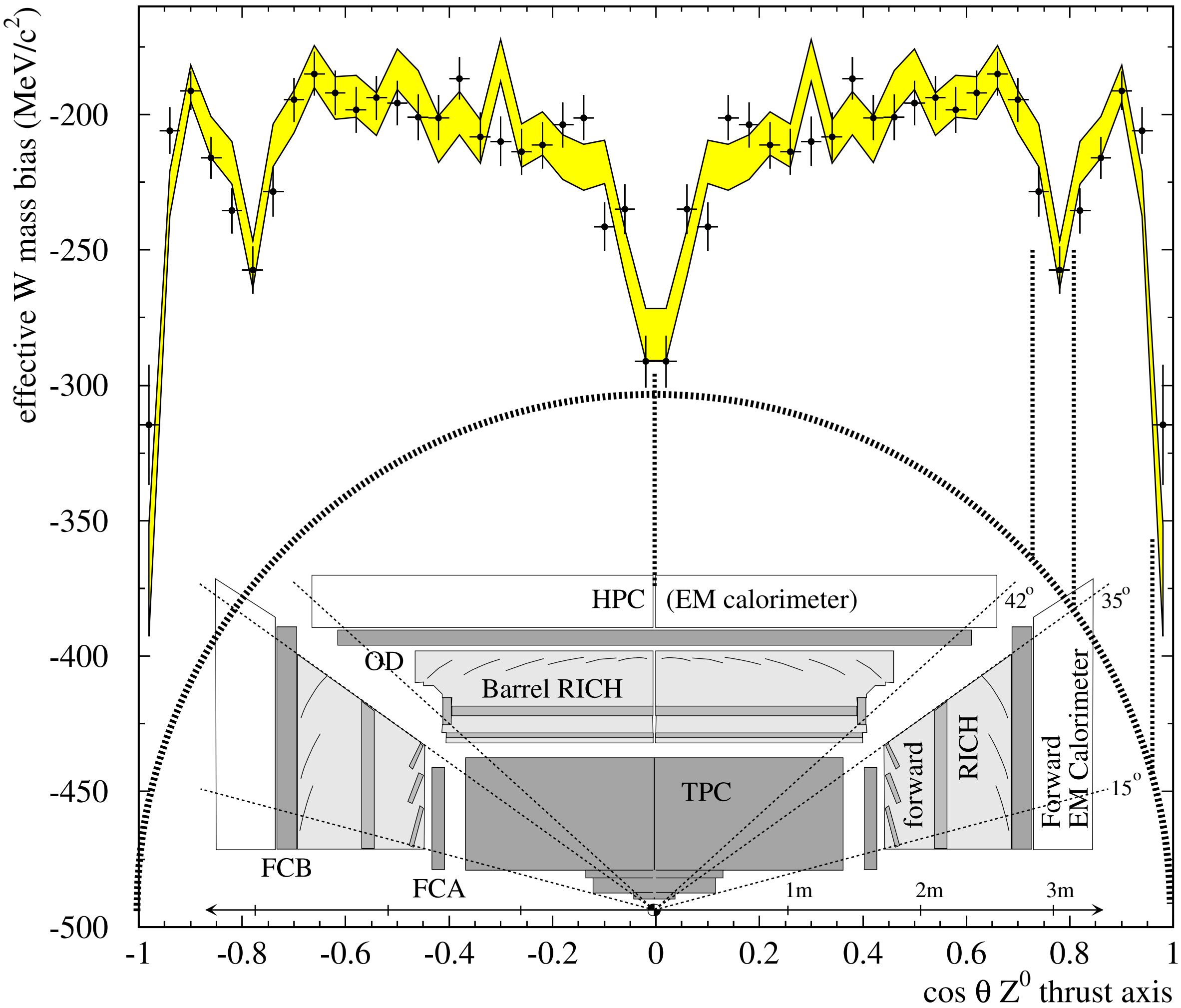

Figure 7.9: *The effective W mass bias (see text) is shown as a function of the polar angle of the* Z^0 *thrust axis. Points with error bars represent 1997* Z^0 *data, while the shaded band indicates MC simulation with statistical error. Several DELPHI subdetectors have been superimposed to illustrate their angular coverage.*

These findings are illustrated in Figure 7.9 and 7.10. In these plots the 'effective W mass bias' is to be interpreted as follows: it would be the overall reconstruction bias on the mass ($m_{\mathrm{fit}} - m_{\mathrm{true}}$) if the average quality of jet reconstruction for all jets would be as good as the average jet reconstruction quality of the Z^0 events in the corresponding bin. An exact description is given in the appendix (page 189), and relies among others on the linearity which is cross-checked on page 204. The statistical errors were estimated using the Jackknife method.

Figure 7.9 clearly shows that the W mass bias indeed becomes more negative in the regions where the detector is less efficient. The dip near $|\cos\theta| \approx 0.8$ is more pronounced than in the corresponding plot based on 1998 data in Figure 7.10. One major difference is that the 1998 Z^0

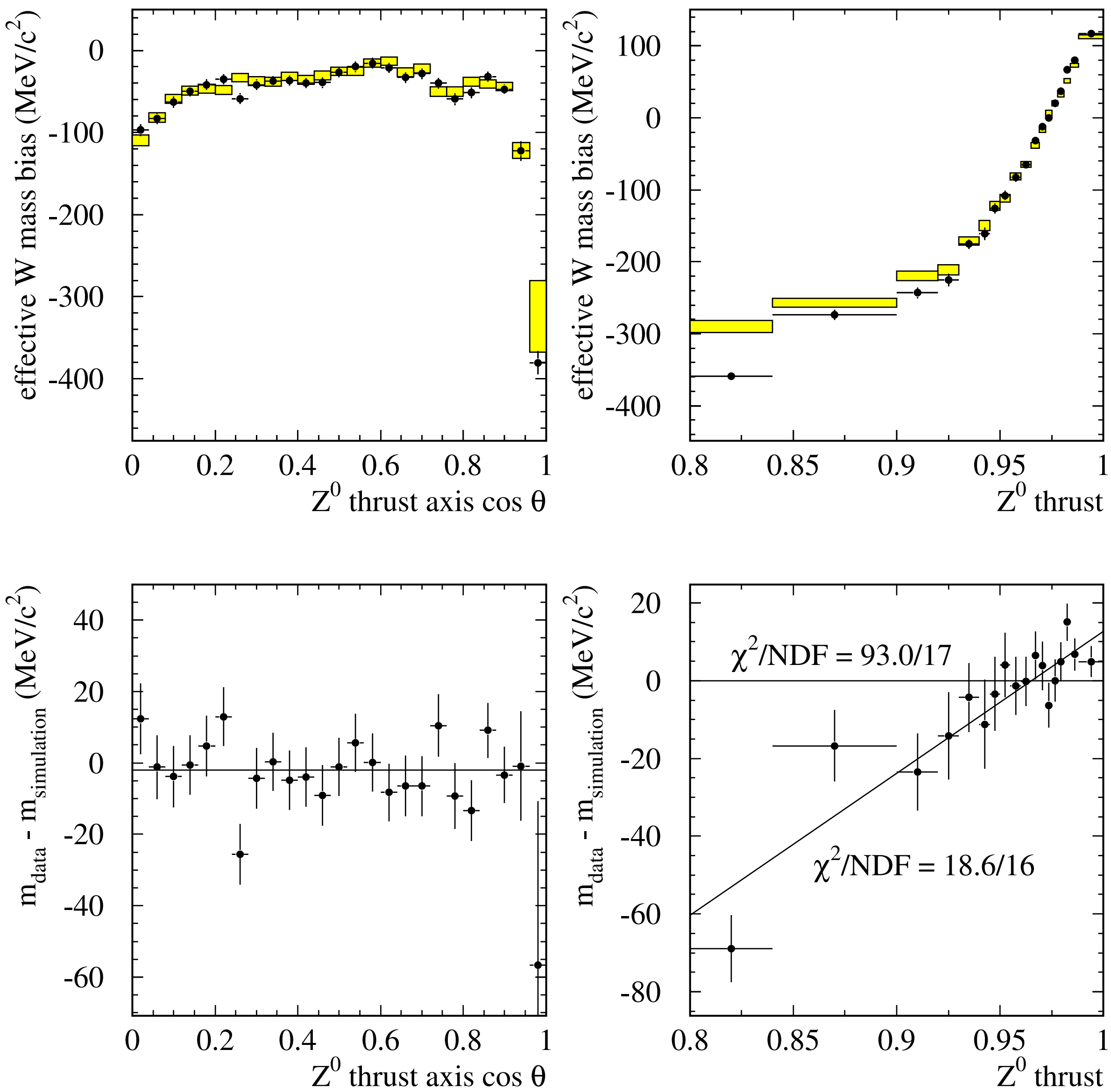

Figure 7.10: *Effective W mass bias as a function of the polar angle of the* Z^0 *thrust axis (left) and thrust value (right), for 1998 data (points with error bars) and MC simulation (shaded band). In the bottom plots the corresponding difference between data and MC is shown.*

events were analysed with the 189 GeV $q\bar{q}q\bar{q}$ Ideogram analysis, while the results on 1997 Z^0's were obtained with the 183 GeV $q\bar{q}q\bar{q}$ Ideogram analysis.

Data / MC agreement

Important for the systematic error on the W mass is the difference between data and MC simulation. In Figure 7.10 a discrepancy is visible in the bias for Z^0 events with low values of the thrust

— i.e. broad (spherical) events with a high gluon activity. A similar trend was already visible in the 1997 study, but less pronounced. The overall effect of this discrepancy for the W mass, however, is at the level of only ~ 4 MeV/c^2. This observed discrepancy does however not allow us to conclude whether the effect comes from fragmentation or a detector effect. More detailed studies would be needed to clarify this, which is beyond the scope of this thesis.

Time stability

In Figure 7.11 the average difference between data and MC is shown as a function of time during the Z^0 calibration runs that where taken in 1998. The statistical error on the difference *per hour* is of the order of 20 MeV/c^2, which is already better than the overall LEP fragmentation error. From these plots one can study the long-term and short-term stability of the DELPHI detector, in terms of the W mass. The overall measured values were already listed in Table 7.10.

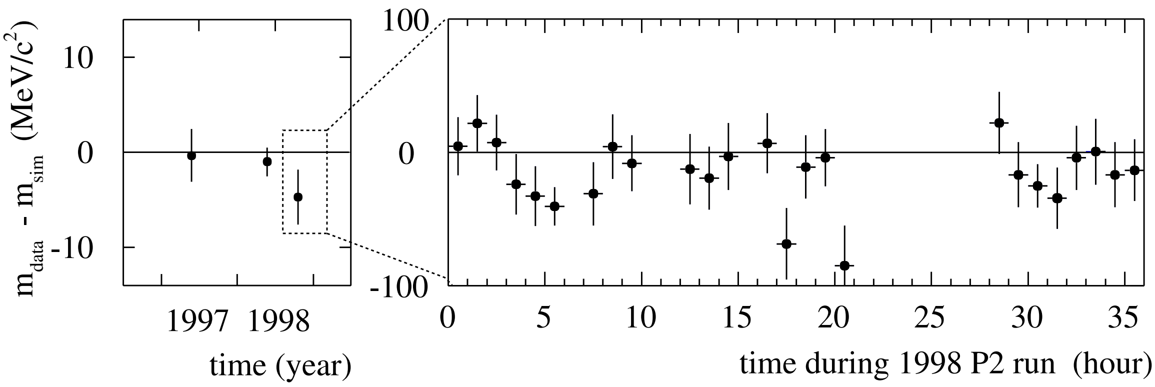

Figure 7.11: *Stability of the difference between data and MC simulation on a long time scale (left) and a short time scale (right).*

Coverage and limitations

A detailed discussion about the coverage and limitations of the MLBZ method can be found in the appendix. The MLBZ bias is believed to cover all fragmentation effects, including internal BEC correlations and CR effects *inside* bosons. Also many detector related effects and their internal correlations are treated correctly to first order. Some detector effects, however, are not (fully) covered and have to be estimated separately. Examples are the non-linearity of the jet energy response and the DELPHI aspect ratio discussed before (section 7.5), as well as the time stability (outside Z^0 calibration data taking periods). It can be noted however, that *none* of the other LEP experiments quote results for these effects, and that the non-linearity and aspect ratio studies in DELPHI were originally inspired by discussions about MLBZ limitations.

MLBZ conclusion

The MLBZ method has led to new insights regarding jet reconstruction systematics and a wealth of statistically very precise quantitative results. DELPHI currently quotes MLBZ results (both in

$\mathrm{q\bar{q}q\bar{q}}$ channel	$\sqrt{s}$		
(MeV/c^2)	172 GeV	183 GeV	189 GeV
Systematic correction according to MLBZ:			
$m_{\mathrm{data}} - m_{\mathrm{simulation}}$	-	0	-2
Uncertainties on MLBZ correction:			
MLBZ statistics	-	3	1
MLBZ reducible:			
No ISR		2	
No BW width		2	
MLBZ irreducible:			
Particle masses		<2	
Quark flavour		<1	
LEP E_{beam}		0.5	
Back-to-back correlations		1	
Track density		3	
total MLBZ uncertainty	10	6	5
Uncertainties not covered by MLBZ:			
DELPHI aspect ratio	2	3	4
Jet energy bias vs. angle	3	9	11
Jet energy non-linearity	4	6	14
Time dependence	<5	<5	<5

Table 7.11: *Complete set of systematic uncertainties on jet reconstruction for the mass measurement in the* $\mathrm{q\bar{q}q\bar{q}}$ *channel. An explanation and discussion of the various entries in the table can be found in appendix A.*

the $\mathrm{q\bar{q}q\bar{q}}$ and the $\mathrm{q\bar{q}l}\nu$ channel) as a confirmation that the quoted fragmentation error (12 MeV/c^2) is conservative [3], and in the $\mathrm{q\bar{q}q\bar{q}}$ channel it is used as a (2 MeV/c^2) correction on the W mass bias to take into account fragmentation and jet smearing effects.

In this thesis the MLBZ result is considered to be a measurement of all jet reconstruction systematics for the mass in the fully-hadronic channel, including fragmentation and all 'conventional' detector systematics. A summary is shown in Table 7.11.

Although the jet energy bias as a function of cosθ *should* be covered by the MLBZ method (appendix A), the conventional estimate indicates an effect of 11 (9) MeV/c^2 in the fully-hadronic channel at 189 (183) GeV (Table 7.9), which appears to be large compared to the *overall* shifts found by the MLBZ method. Since this difference is not fully understood, the conventional estimate is quoted as an additional systematic uncertainty on the jet energy response.

No MLBZ results in the semi-leptonic channel or for the Γ_{W} measurement have been obtained so far with the analysis presented in this thesis (but first results for the $\mathrm{q\bar{q}l}\nu$ channel are available [3]). Therefore the MLBZ method is used only in the fully-hadronic channel to refine the systematic error on m_{W}.

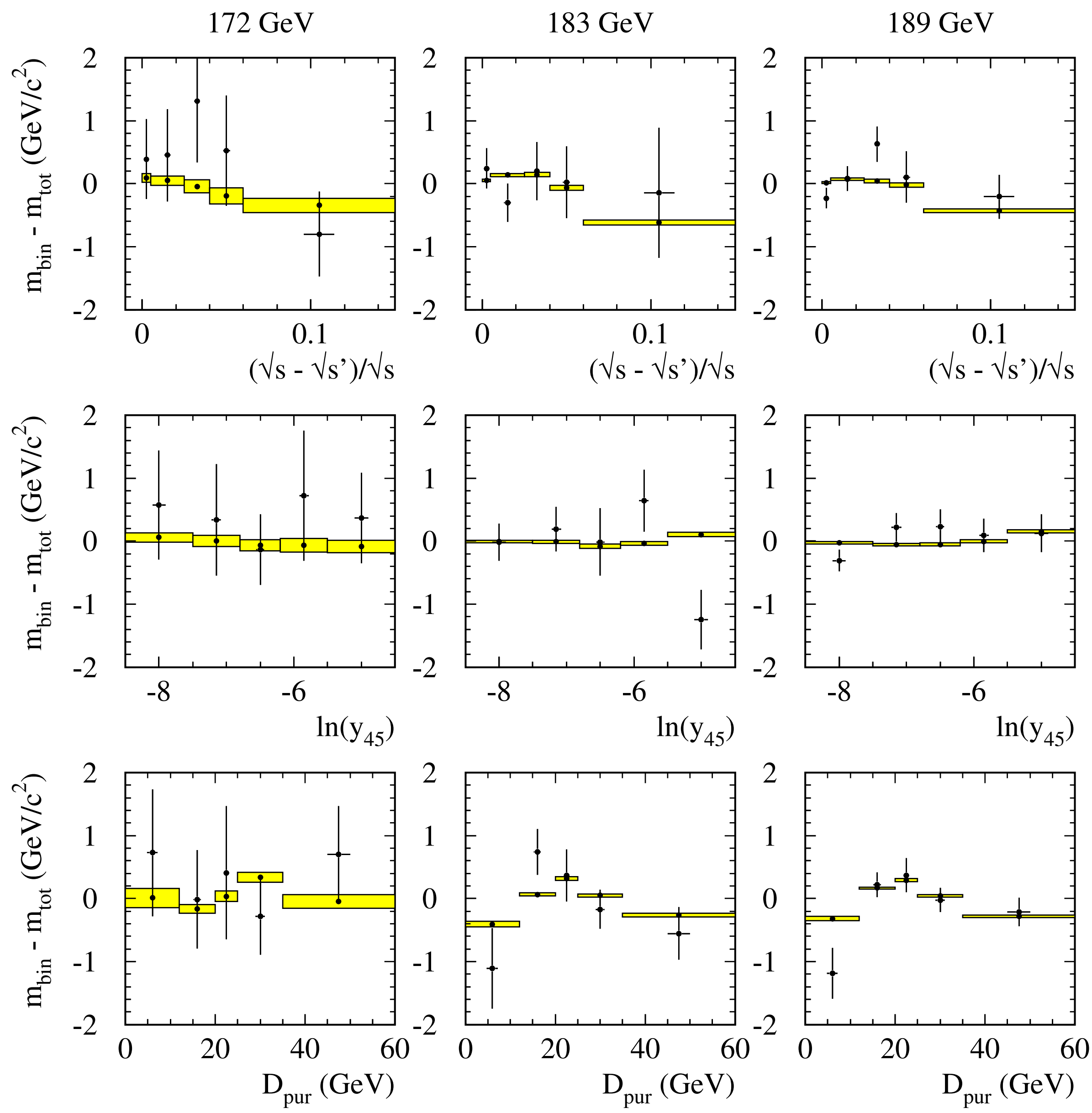

Figure 7.12: *Dependence of the fitted mass on a selection of event variables (see text), in bins of approximately equal statistics, for the* $q\bar{q}q\bar{q}$ *channel. Points with error bars represent data, while the shaded bands indicate the MC prediction. The average fitted mass for each energy (in MC and data) was subtracted from the fitted masses, to remove the difference between the measured W mass and the generated value of* m_W *used in the MC simulation.*

7.7 Consistency cross-checks

In Figure 7.12 the stability of the mass reconstruction bias is investigated as a function of a few observables, which are closely related to the m_W measurement: the reconstructed $\sqrt{s'}$, the value of the DURHAM y variable when going from 5 to 4 jets y_{45}, and the D_{pur} variable used to estimate the purity.

The overall data/MC agreement is satisfactory. For the D_{pur} a discrepancy of slightly more than 2 sigma is observed in the first bin, where more than 50% of the events are $\mathrm{q\bar{q}}\gamma$ background. If this effect would be due to a wrong background shape or level (not supported by the full mass spectrum), this discrepancy would require the description of the background shape (or level) to be wrong by a factor 10 more than estimated from the model comparisons. It is therefore compelling to conclude that most of the effect is due to a statistical fluctuation.

This feature illustrates the weakness of relying on data/MC discrepancies for estimating systematic errors when analysing data with limited statistics. Such a procedure will in many cases produce 2 sigma effects for which one cannot predict the reliability. It often means that one includes systematics where there was a statistical fluctuation and ignore other systematics when the fluctuation is in opposite direction of the systematic bias.

Notice also the fact that at 172 GeV the average of the masses of the data bins is not equal to the mass of the whole sample. This is probably due to the extremely small data size of only 15 events per bin on average, leading to asymmetric likelihood curves also for the mass. Nevertheless, for all variables the stability is good.

7.8 Corrections, correlations and combination

Some of the systematic effects discussed in this chapter are understood sufficiently well to correct for the discrepancy to first order. Table 7.12 gives an overview of the corrections applied to the measured m_{W} and Γ_{W} results (Table 6.8).

Fully-hadronic channel

For the $\mathrm{q\bar{q}q\bar{q}}$ channel a complete set of systematic uncertainties is available. All sources of systematic uncertainties considered in this chapter have been studied at all energies, except for the effects of jet fragmentation on the Γ_{W} measurement at energies below 189 GeV. There the 189 GeV error is quoted for all energies. Tables 7.14 to 7.17 give an overview of all systematic uncertainties.

Semi-leptonic channel

For the $\mathrm{q\bar{q}l}\nu$ Ideogram study the systematics evaluation was limited to the effects related to LEP, backgrounds, ISR and the statistical error on the calibration. Systematics that have not been studied specifically in the framework of the $\mathrm{q\bar{q}l}\nu$ Ideogram analysis are: jet fragmentation, detector response to leptons and jets and the DELPHI aspect ratio. For these sources of systematics a best estimate was made, based on previous DELPHI publications [1, 2, 3] and a detailed study of the 189 GeV DELPHI main $\mathrm{q\bar{q}l}\nu$ analysis presented in [81]. The errors were estimated as follows:

- The reconstruction of muons in DELPHI is well understood, and the standard treatment in the Ideogram analysis included smearing and momentum scale corrections to improve the agreement between data and MC. The electron treatment, however, is more involved and there the lack of systematic studies should be reflected in an increased systematic uncertainty. Therefore the lepton reconstruction errors quoted by DELPHI were conservatively doubled in size.

- Since the MLBZ study presented here did not include the $\mathrm{q\bar{q}l}\nu$ channel, the fragmentation errors have to be derived from model comparisons and variations. As discussed in section 7.4.1 no significant effects were found for the main DELPHI $\mathrm{q\bar{q}l}\nu$ analysis, and the conservative numbers quoted in Table 7.5 are adopted and assumed to be independent of the energy.

- The jet treatment in the Ideogram analysis is well under control, and the response of the analysis to systematic discrepancies is expected to be similar to the response of the main DELPHI $\mathrm{q\bar{q}l}\nu$ analysis. The dominating jet uncertainty quoted for the $\mathrm{q\bar{q}l}\nu$ channel corresponds to the overall jet energy scale (due to the missing neutrino, the effect can be much larger than in the $\mathrm{q\bar{q}q\bar{q}}$ channel). The effects on m_{W} quoted by DELPHI show a consistent increase from 15 MeV/c^2 at 172 GeV to about 30 MeV/c^2 for an energy scale uncertainty of 1%. Those numbers have been adopted here, scaled to correspond to a 1.5% uncertainty on the energy scale for all energies.

  The numbers quoted for the effect of a 1% non-linearity slope in the jet energy response (at 189 GeV) have been adopted without change. The scale as a function of cosθ was investigated in [81], and found to be negligible in all channels ($<$ 5 MeV/c^2 for m_{W} and $<$ 10 MeV/c^2 for Γ_{W}). Here a 5 MeV/c^2 is quoted for the mass and 10 MeV/c^2 for the width. The non-linearity and cosθ-dependent uncertainties are assumed to be fully correlated with the numbers quoted for the $\mathrm{q\bar{q}q\bar{q}}$ channel, and scale down at lower energies proportional to the $\mathrm{q\bar{q}q\bar{q}}$ numbers.

  Finally, in the main DELPHI $\mathrm{q\bar{q}l}\nu$ analysis corrections were applied to improve the data/MC agreement regarding the resolution on the jet energy and angles. In the Ideogram analysis only the largest correction was applied (Table 7.12), corresponding to the effect of the angular resolution on Γ_{W}. To take this omission into account (without MLBZ results as a cross-check), twice the values quoted by DELPHI at 189 GeV are adopted here, and taken to be independent of the energy.

- The effect of the DELPHI aspect ratio in the $\mathrm{q\bar{q}l}\nu$ channel is assumed to be identical in size and fully correlated to the $\mathrm{q\bar{q}q\bar{q}}$ channel, even though DELPHI quotes a smaller number at 189 GeV [3].

An overview of all errors is shown in the Tables 7.14 to 7.17. In the semi-leptonic channel the numbers for the Γ_{W} measurement have been evaluated and are listed only for the combined $\mathrm{q\bar{q}l}\nu$ channels, because the combination was done on the level of the likelihood curves to improve the treatment of the asymmetric errors.

W mass and width systematics combination

The systematic errors of the measurements in the different WW decay channels and years are correlated. In the combination of the error contributions the following correlations were used:

Source of systematic effect	correction to m_{W} (MeV/c^2) $\mathrm{q\bar{q}q\bar{q}}$	$\mathrm{q\bar{q}}\mu\nu$	$\mathrm{q\bar{q}e}\nu$	$\mathrm{q\bar{q}}\tau\nu$	correction to Γ_{W} (MeV/c^2) $\mathrm{q\bar{q}q\bar{q}}$	$\mathrm{q\bar{q}l}\nu$
172 GeV						
LEP energy known*	-1	-9	-25	-21	-	-
LEP energy spread	0	0	0	0	-1.4	-1.4
jet scale vs. cos θ + smearings	0	-	-	-	-3.4	*-10******
4-fermion correction**	*-10*	*-10*	*-50*	*-25*	-	-
overall correction 172 GeV	-11	-19	-75	-46	-5	-11
183 GeV						
LEP energy known*	+1	+8	+12	+10	-	-
LEP energy spread	0	0	0	0	-2.2	-2.2
jet scale vs. cos θ + smearings	0	-	-	-	-8.4	*-44******
MLBZ correction	0	-	-	-	-	-
overall correction 183 GeV	+1	+8	+12	+10	-11	-46
189 GeV						
LEP energy known*	+1	+8	+13	+11	-	-
LEP energy spread	0	0	0	0	-2.5	-2.5
jet scale vs. cos θ + smearings	0	-	-	-	-18.3	*-60******
MLBZ correction	+2	-	-	-	-	-
overall correction 189 GeV	+3	+8	+13	+11	-21	-63
* from Table 7.2, after correction for calibration slope ** from [1, 31] *** from [81]						

Table 7.12: *Systematic corrections applied to the measured values of* m_{W} *and* Γ_{W}.

- Uncorrelated between channels and years are
  - The statistical error on the calibration curve
  - The effect of the natural spread of the LEP energy on the mass
  - The systematic error from not including all 4-fermion diagrams and interferences at 172 GeV.
- For the combination of the uncertainties on the LEP energy scale the correlation matrix(shown in Table 7.2) provided by LEP was used. All the remaining LEP errors were assumed to be fully correlated between channels and years.
- The errors due to ISR were based on the 189 GeV estimates, and scaled down for the other centre-of-mass energies proportionally to the overall shift induced by ISR. This error is assumed to be fully correlated across years and channels.

- Effects related to fragmentation (covered by MLBZ in the $\mathrm{q\bar{q}q\bar{q}}$ channel), jet systematics and the DELPHI aspect ratio were conservatively taken to be fully correlated between years and channels.
- The background description and lepton modelling were treated as correlated between years, but uncorrelated between the $\mathrm{q\bar{q}q\bar{q}}$ and the $\mathrm{q\bar{q}l\nu}$ channel.
- Final State Interference effects in the fully-hadronic channel were assumed to be energy independent and fully correlated for all energies.

$\mathrm{W^+}$ - $\mathrm{W^-}$ mass difference

Practically all possible systematic discrepancies discussed so far in this chapter are expected to have an identical influence on the mass reconstruction of $\mathrm{W^+}$ and $\mathrm{W^-}$ bosons, and will therefore vanish in the $\Delta m_{\mathrm{W^+W^-}}$ measurement. Furthermore the statistical errors are much larger, so that the measurement is evidently statistically dominated.

The measurements in the $\mathrm{q\bar{q}q\bar{q}}$ and $\mathrm{q\bar{q}l\nu}$ channel are fundamentally different:

- The $\mathrm{q\bar{q}q\bar{q}}$ $\Delta m_{\mathrm{W^+W^-}}$ measurement is quite involved, relying on jet charge separation to construct a likelihood curve for the mass difference in each event. The jet-charge distributions are well described by the MC. Wrong pairing background and $\mathrm{q\bar{q}}\gamma$ background may influence the results. All of these effects should be well under control using MC reweighting to do a calibration of the analysis, though.
- The $\mathrm{q\bar{q}l\nu}$ study, on the other hand, is simple. It is based on the usual mass fit, and relies on dividing the events in a $\mathrm{W^+}$ and a $\mathrm{W^-}$ sample using the charge of the leptons. The measurement assumes that the measured mass is fully determined by the hadronic system in a $\mathrm{q\bar{q}l\nu}$ event. Since this is not perfectly true, a calibration curve is needed here as well.

An interesting consequence of this fundamental difference is illustrated by the statistical error due to the LEP beam energy spread: in the $\mathrm{q\bar{q}q\bar{q}}$ channel this error cancels, like the other systematic effects. In the $\mathrm{q\bar{q}l\nu}$ channel, however, this error becomes twice as large, because the event sample is divided in two and the difference of the masses is taken.

In both measurements, a source of systematics that can be envisaged would be a large forward-backward asymmetry of the DELPHI detector. This could affect $\mathrm{W^+}$ and $\mathrm{W^-}$ bosons differently because of the angular distributions with which they are produced. But it is hard to imagine that such an effect could be large enough to be significant. A 100 MeV/c^2 error on the mass difference has been assigned both to the lepton and the jet forward-backward asymmetries.

Another possible systematic deviation could originate from a wrong estimation of the slope of the calibration curve. Due to the large instrinsic statistical uncertainty of this measurement, the statistical uncertainty on the calibration slope is significantly larger than achieved for the W mass analysis. Also the background from $\mathrm{q\bar{q}}\gamma$ processes, or a wrong description of the lepton or jet charge separation could affect the calibration slope. The effect of the uncertainty on level and shape of the $\mathrm{q\bar{q}}\gamma$ background has been checked for the $\mathrm{q\bar{q}q\bar{q}}$ analysis and the effect was always below a 3% change of the slope.

In view of the above a short list of conservatively estimated systematic errors has been assigned and is shown in Table 7.13. This simplified estimation of systematic errors should be regarded as preliminary. To obtain a detailed understanding of all possible systematic effects relevant especially for the calibration slopes would require more work.

$\Delta m_{\mathrm{W^+W^-}}$ all energies combined				
Sources of systematic error	$\mathrm{q\bar{q}}\mu\nu$	$\mathrm{q\bar{q}e}\nu$	$\mathrm{q\bar{q}}\tau\nu$	$\mathrm{q\bar{q}q\bar{q}}$
Effect on calibration bias (MeV/c^2)				
LEP energy spread (statistical)	8	10	14	0
Lepton reconstruction F/B asymmetry	100	100	100	-
Jet reconstruction F/B asymmetry	100	100	100	100
Overall uncertainty bias	142	142	142	100
Effect on calibration slope (change in %)				
Statistical uncertainty calibration	10%	12%	18%	6%
Lepton / jet charge confusion	1%	1%	5%	5%
Background shape (JETSET - ARIADNE)	-	-	-	2%
Background level (± 10%)	1%	2%	2%	3%
Overall uncertainty slope	10%	12%	19%	9%

Table 7.13: *Overview of systematic errors on the* $\Delta m_{\mathrm{W^+W^-}}$ *measurement.*

m_W	$\sqrt{s} = 172$ GeV				
Sources of systematic error (MeV/c^2)	$q\bar{q}\mu\nu$	$q\bar{q}e\nu$	$q\bar{q}\tau\nu$	$q\bar{q}l\nu$	$q\bar{q}q\bar{q}$
Statistical error on calibration	33	46	85	26	23
Lepton corrections	*20*	*30*	-	14	-
Fragmentation	*20*	*20*	*20*	20	*
Jet energy scale	*16*	*21*	*29*	19	*
Jet energy + angular resolutions	*14*	*32*	*24*	20	*
Jet reconstruction (MLBZ)	*	*	*	*	10
Jet energy bias vs. angle	1	1	1	1	3
Jet energy non-linearity	5	6	7	6	4
Jet energy time stability	-	-	-	-	5
Aspect Ratio	*2*	*2*	*2*	2	2
Background shape	-	-	-	-	10
Background level	1	8	18	6	4
I.S.R.	10	10	18	11	14
4-fermion correction	*10*	*50*	*25*	15	*10*
LEP energy known	5	13	11	8	1
LEP energy unknown	28	28	28	28	28
LEP energy spread (statistical)	19	21	22	13	11
Colour reconnection	-	-	-	-	46
Bose Einstein correlations	-	-	-	-	10

Γ_W	$\sqrt{s} = 172$ GeV				
Sources of systematic error (MeV/c^2)	$q\bar{q}\mu\nu$	$q\bar{q}e\nu$	$q\bar{q}\tau\nu$	$q\bar{q}l\nu$	$q\bar{q}q\bar{q}$
Statistical error on calibration	-	-	-	180	63
Lepton corrections	-	-	-	*56*	-
Fragmentation	-	-	-	*42*	24
Jet energy resolution (+ scale)	-	-	-	*30*	10
Jet angular resolution	-	-	-	*10*	10
Jet energy scale vs. angle	-	-	-	*10*	8
Jet energy non-linearity	-	-	-	-	7
Aspect Ratio	-	-	-	-	3
Background shape	-	-	-	-	21
Background level	-	-	-	29	32
I.S.R.	-	-	-	10	14
4-fermion correction	-	-	-	*100*	20
LEP energy unknown	-	-	-	39	17
Colour reconnection	-	-	-	-	54
Bose Einstein correlations	-	-	-	-	25

Table 7.14: *Contributions to the systematic error at 172 GeV. Numbers in italics are based on previous DELPHI publications (see text).*

m_{W}	$\sqrt{s} = 183$ GeV				
Sources of systematic error (MeV/c^2)	$\mathrm{q\bar{q}}\mu\nu$	$\mathrm{q\bar{q}e}\nu$	$\mathrm{q\bar{q}}\tau\nu$	$\mathrm{q\bar{q}l}\nu$	$\mathrm{q\bar{q}q\bar{q}}$
Statistical error on calibration	14	19	25	10	8
Lepton corrections	*70*	*80*	-	45	-
Fragmentation	*20*	*20*	*20*	20	*
Jet energy scale	*23*	*31*	*42*	28	*
Jet energy + angular resolutions	*14*	*32*	*24*	21	*
Jet reconstruction (MLBZ)	*	*	*	*	6
Jet energy scale vs. angle	3	3	3	3	9
Jet energy non-linearity	7	9	11	8	6
Jet energy time stability	-	-	-	-	5
Aspect Ratio	*3*	*3*	*3*	3	3
Background shape	-	-	-	-	7
Background level	1	4	4	2	2
I.S.R.	17	16	34	20	14
LEP energy known	4	6	5	5	1
LEP energy unknown	22	22	22	22	22
LEP energy spread (statistical)	9	9	13	6	5
Colour reconnection	-	-	-	-	46
Bose Einstein correlations	-	-	-	-	10

Γ_{W}	$\sqrt{s} = 183$ GeV				
Sources of systematic error (MeV/c^2)	$\mathrm{q\bar{q}}\mu\nu$	$\mathrm{q\bar{q}e}\nu$	$\mathrm{q\bar{q}}\tau\nu$	$\mathrm{q\bar{q}l}\nu$	$\mathrm{q\bar{q}q\bar{q}}$
Statistical error on calibration	-	-	-	41	23
Lepton corrections	-	-	-	*56*	-
Fragmentation	-	-	-	*42*	24
Jet energy resolution (+ scale)	-	-	-	*30*	10
Jet angular resolution	-	-	-	*44*	5
Jet energy bias vs. angle	-	-	-	*10*	10
Jet energy non-linearity	-	-	-	-	6
Aspect Ratio	-	-	-	-	2
Background shape	-	-	-	-	25
Background level	6	35	74	26	38
I.S.R.	-	-	-	17	14
LEP energy unknown	-	-	-	13	8
Colour reconnection	-	-	-	-	54
Bose Einstein correlations	-	-	-	-	25

Table 7.15: *Contributions to the systematic error at 183 GeV. Numbers in italics are based on previous DELPHI publications (see text).*

m_W	$\sqrt{s} = 189$ GeV				
Sources of systematic error (MeV/c^2)	$q\bar{q}\mu\nu$	$q\bar{q}e\nu$	$q\bar{q}\tau\nu$	$q\bar{q}l\nu$	$q\bar{q}q\bar{q}$
Statistical error on calibration	13	16	23	9	7
Lepton corrections	*22*	*58*	-	19	-
Fragmentation	*20*	*20*	*20*	20	*
Jet energy scale	*32*	*42*	*57*	40	*
Jet energy + angular resolutions	*14*	*32*	*24*	21	*
Jet reconstruction (MLBZ)	*	*	*	*	5
Jet energy scale vs. angle	*5*	*5*	*5*	5	11
Jet energy non-linearity	*16*	*22*	*26*	20	14
Jet energy time stability	-	-	-	-	5
Aspect Ratio	*4*	*4*	*4*	4	4
Background shape	-	-	-	-	5
Background level	1	10	3	4	2
I.S.R.	20	20	40	24	16
LEP energy known	4	7	6	5	1
LEP energy unknown	17	17	17	17	17
LEP energy spread (statistical)	5	6	7	3	3
LEP boost asymmetry	-	-	-	-	1
Colour reconnection	-	-	-	-	46
Bose Einstein correlations	-	-	-	-	10

Γ_W	$\sqrt{s} = 189$ GeV				
Sources of systematic error (MeV/c^2)	$q\bar{q}\mu\nu$	$q\bar{q}e\nu$	$q\bar{q}\tau\nu$	$q\bar{q}l\nu$	$q\bar{q}q\bar{q}$
Statistical error on calibration	-	-	-	26	17
Lepton corrections	-	-	-	*56*	-
Fragmentation	-	-	-	*42*	24
Jet energy resolution (+ scale)	-	-	-	*30*	3
Jet angular resolution	-	-	-	*60*	24
Jet energy bias vs. angle	-	-	-	*10*	8
Jet energy non-linearity	-	-	-	-	7
Aspect Ratio	-	-	-	-	3
Background shape	-	-	-	-	22
Background level	8	43	109	34	33
I.S.R.	-	-	-	20	16
LEP energy unknown	-	-	-	5	5
LEP boost asymmetry	-	-	-	-	1
Colour reconnection	-	-	-	-	54
Bose Einstein correlations	-	-	-	-	25

Table 7.16: *Contributions to the systematic error at 189 GeV. Numbers in italics are based on previous DELPHI publications (see text).*

m_W all energies combined			
Sources of systematic error (MeV/c^2)	$q\bar{q}l\nu$	$q\bar{q}q\bar{q}$	$q\bar{q}q\bar{q} \oplus q\bar{q}l\nu$
Statistical error on calibration	7	6	4
Lepton corrections	26	-	9
Fragmentation (MLBZ)	20	5	11
Jet energy + angular resolution	21	*	8
Jet energy scale (vs. angle)	35	10	15
Jet energy non-linearity	16	12	13
Jet energy time stability	-	4	2
Aspect Ratio	4	4	4
Background	4	6	4
I.S.R.	22	15	18
4-fermion correction	1	0	0
LEP energy known	5	1	3
LEP energy unknown	18	17	18
LEP energy spread (statistical)	3	3	2
LEP boost asymmetry	-	1	0
Colour reconnection	0	46	29
Bose Einstein correlations	0	10	6
Γ_W all energies combined			
Sources of systematic error (MeV/c^2)	$q\bar{q}l\nu$	$q\bar{q}q\bar{q}$	$q\bar{q}q\bar{q} \oplus q\bar{q}l\nu$
Statistical error on calibration	22	14	12
Lepton corrections	56	-	15
Fragmentation	42	24	29
Jet energy response + angles	62	21	32
Jet energy scale vs. angle	10	8	9
Jet energy non-linearity	-	7	5
Aspect Ratio	-	3	2
Background	28	41	38
I.S.R.	19	16	16
4-fermion correction	4	1	1
LEP energy unknown	8	6	6
LEP boost asymmetry	-	1	1
Colour reconnection	-	54	40
Bose Einstein correlations	-	25	18

Table 7.17: *Contributions to the systematic error on the W mass and width measurements for $\sqrt{s}$ = 172-189 GeV combined.*

Chapter 8

Results and Conclusion

The previous chapters described the analysis used and the systematic errors associated with the measurement. Here an overview of the measurement results is given, together with its interpretation and a comparison with other existing measurements.

8.1 W mass

Fully-hadronic results

The 2D Ideogram analysis as presented in chapter 6 was not only applied to the 189 GeV data, but also used to update the 172 and 183 GeV results that were already published before. In figure 8.1 the new results are compared to the published results. The agreement is good. At 189 GeV, the only difference in mass comes from a slightly different treatment of the systematic corrections. The published versions of the Ideogram analysis at lower energies differ from the 'final' analysis in quite a number of points (chapter 5). Main differences are the cut at 25% purity, the 4C approximation while at 183 GeV still the full 6C 2D Ideograms were used, and the event-by-event ISR treatment. Considering these changes in the analysis, the difference in measured mass at 183 GeV is not surprising.

To appreciate the development of the $\mathrm{q\bar{q}q\bar{q}}$ analysis it is illustrative to compare the expected statistical sensitivity on MC, and the development of the quoted systematic errors, as shown in Table 8.1

m_{W} $\mathrm{q\bar{q}q\bar{q}}$ channel (MeV/c^2)				
	Expected statistical error		Quoted systematic error	
	'New' Ideogram	Published	'New' Ideogram	Published
172 GeV	510	520	33	50
183 GeV	189	193	23	32
189 GeV	104	104	27	28

Table 8.1: *Comparison of the expected statistical errors and quoted systematic errors (excluding the systematic error due to the LEP beam energy scale, and FSI).*

In spite of the fact that more possible sources of systematic errors have been studied and are included, the overall systematic uncertainties have decreased compared to the published numbers. It is clear that the understanding of the systematic has improved considerably. The improvement on the expected statistical errors is small, which is no surprise because the 172 GeV analysis already took into account 5-jet topologies, the event purity and event resolution.

The overall combination of the $\mathrm{q\bar{q}q\bar{q}}$ results obtained at 172, 183 and 189 GeV gives:

$$m_W^{\mathrm{q\bar{q}q\bar{q}}} = 80,395 \pm 91 \text{ (stat)} \pm 25 \text{ (syst)} \pm 47 \text{ (FSI)} \pm 17 \text{ (LEP) MeV}/c^2 \tag{8.1}$$

This result is shown together with the published results from the 4 LEP experiments for the 172-189 GeV data sets in Figure 8.2. The L3 result has not been published, but is based on the numbers used by the LEP EW working group in the Summer 2000 EW fit.

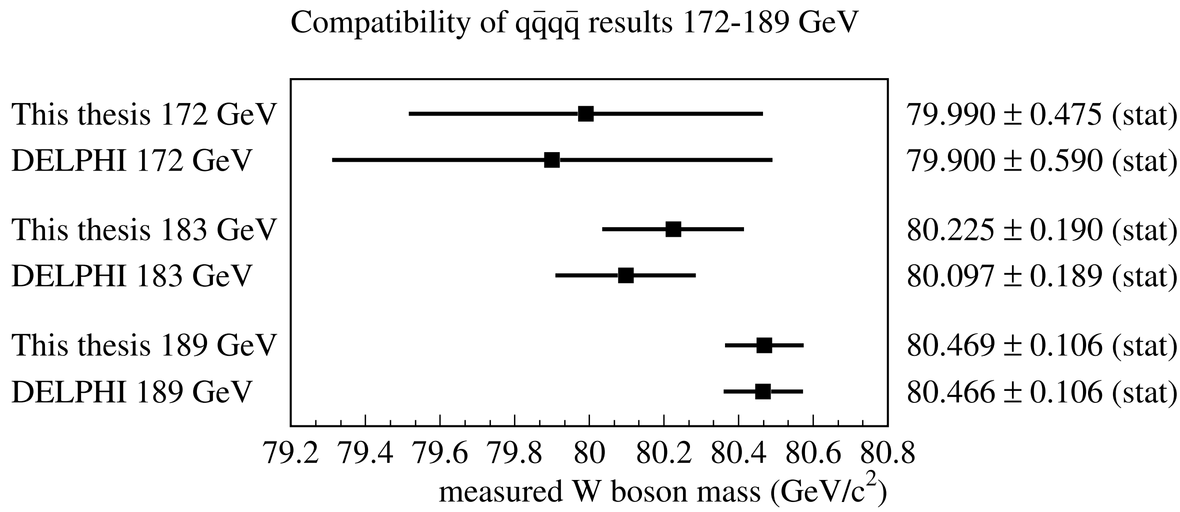

Figure 8.1: *W mass measurement results obtained with the final 2D ideogram analysis (from Table 6.8, with the corrections listed in Table 7.12), compared to the published DELPHI results. Only the statistical errors are shown*

Semi-leptonic results

The $\mathrm{q\bar{q}l}\nu$ results obtained with the 2D Ideogram analysis are compared to the DELPHI published numbers in Figure 8.3. The analyses are independent, but they were applied to the same data sets. Thus the Ideogram results can be considered as an independent cross-check. At 183 and 172 GeV the agreement is excellent. At 189 GeV, however, both the results of the $\mathrm{q\bar{q}}\mu\nu$ and the $\mathrm{q\bar{q}e}\nu$ channels deviate more than expected. To quantify the statistical significance of the observed differences would require more work, taking into account the correlations between the analyses. The largest deviation is seen in the $\mathrm{q\bar{q}e}\nu$ channel, where the reconstructed equal-mass spectrum (Figure 6.11) already showed a deficit of events exactly at the peak. This deficit can also be

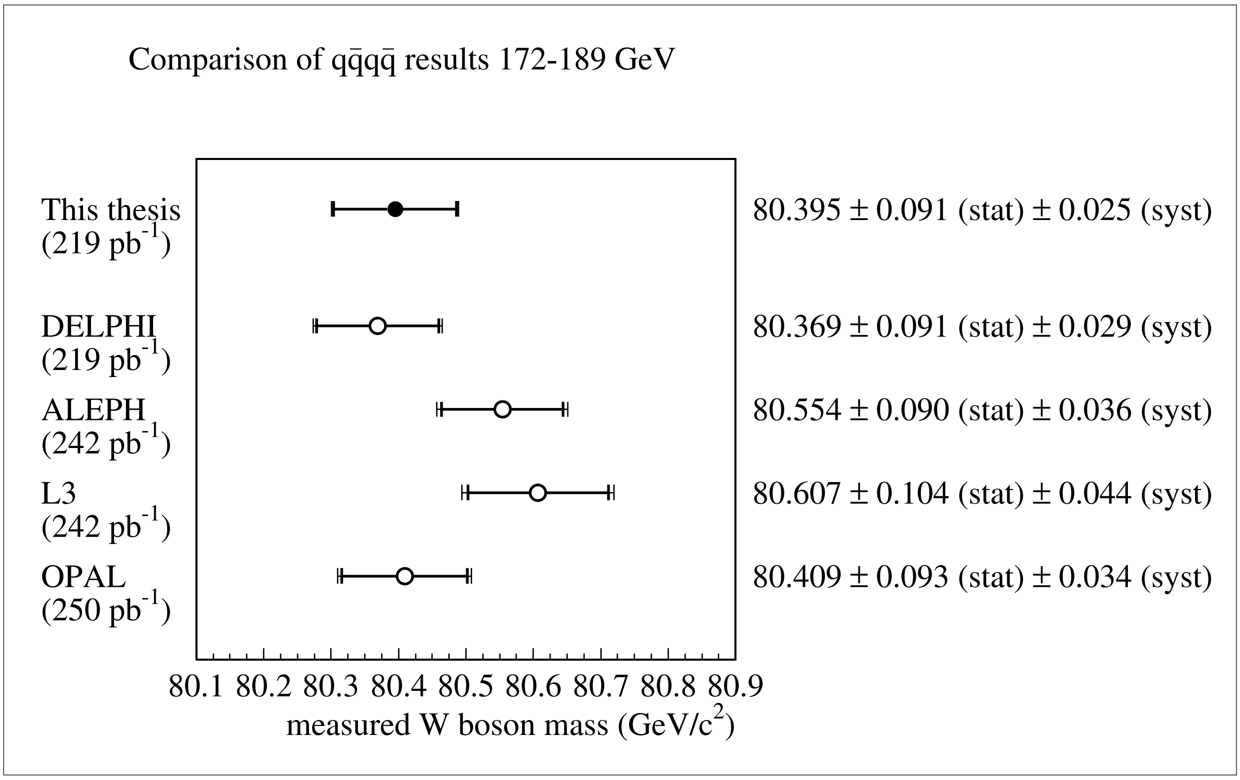

Figure 8.2: *Comparison of* $\mathrm{q\bar{q}q\bar{q}}$ m_{W} *results. The systematic errors shown do not include the error due to the LEP beam energy scale (~17 MeV/c^2) and FSI (~56 MeV/c^2 [75]).*

seen in the corresponding mass spectrum for the main DELPHI $\mathrm{q\bar{q}l}\nu$ analysis [3], however. At that time the unexpected peak structure inspired an intensified cross-check of possible systematic problems in the electron channel at 189 GeV, but nothing was found that could explain the effect. It therefore had to be interpreted as a statistical fluctuation. In addition to this hitherto unexplained effect, another possible source of a systematic bias may be an incomplete simulation of the backgrounds in the Ideogram analysis. The plots in Figure 6.6 show some indication that a few background events not included in the MC simulation (probably Bhabha events) are selected in the $\mathrm{q\bar{q}e}\nu$ channel. The possible effects of such a background have not been studied. A detailed systematic investigation was considered to be beyond the scope of the $\mathrm{q\bar{q}l}\nu$ Ideogram study.

The principal aim of the $\mathrm{q\bar{q}l}\nu$ project reported here, was to investigate the statistical sensitivity of the Ideogram analysis in the $\mathrm{q\bar{q}l}\nu$ channel. From Table 8.2, it is clear that the Ideogram study can match the statistical sensitivity of the main DELPHI $\mathrm{q\bar{q}l}\nu$ analysis, despite its preliminary character.

The overall combination of the $\mathrm{q\bar{q}l}\nu$ results obtained at 172, 183 and 189 GeV gives:

$$m_W^{\mathrm{q\bar{q}l}\nu} = 80,239 \pm 124 \text{ (stat)} \pm 60 \text{ (syst)} \pm 18 \text{ (LEP) MeV}/c^2 \tag{8.2}$$

This result is shown together with the published results from the 4 LEP experiments for the 172-189 GeV data sets in Figure 8.4. The L3 number is based on the numbers (up to 189 GeV) used by the LEP EW working group in the Summer 2000 EW fit.

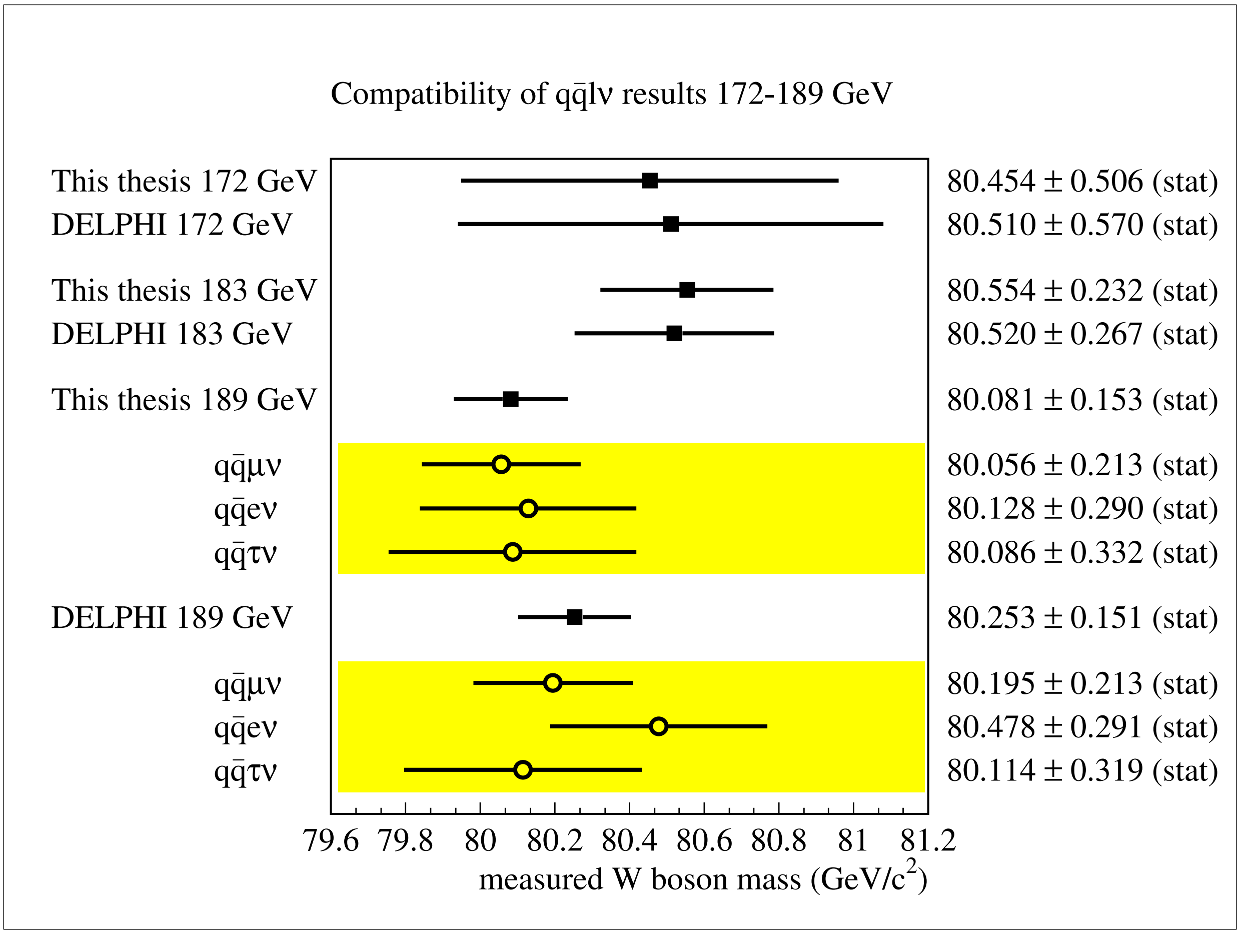

Figure 8.3: *W mass measurement results obtained with the final 2D ideogram analysis (from Table 6.8, with the corrections listed in Table 7.12), compared to the published DELPHI results. Only the statistical errors are shown.*

m_W $q\bar{q}l\nu$ channel (MeV/c^2)		
	Expected statistical error	
	'New' Ideogram	Published
172 GeV $q\bar{q}l\nu$	592	623*
183 GeV $q\bar{q}l\nu$	235	259*
189 GeV $q\bar{q}l\nu$	142	143
* The DELPHI published $q\bar{q}l\nu$ measurements at energies below 189 GeV did not include the $q\bar{q}\tau\nu$ channel.		

Table 8.2: *Comparison of expected statistical errors in the* $q\bar{q}l\nu$ *channel.*

Overall combination and interpretation of the W mass result

Combination of the $q\bar{q}l\nu$ and $q\bar{q}q\bar{q}$ channel gives the following overall measurement of the W boson mass:

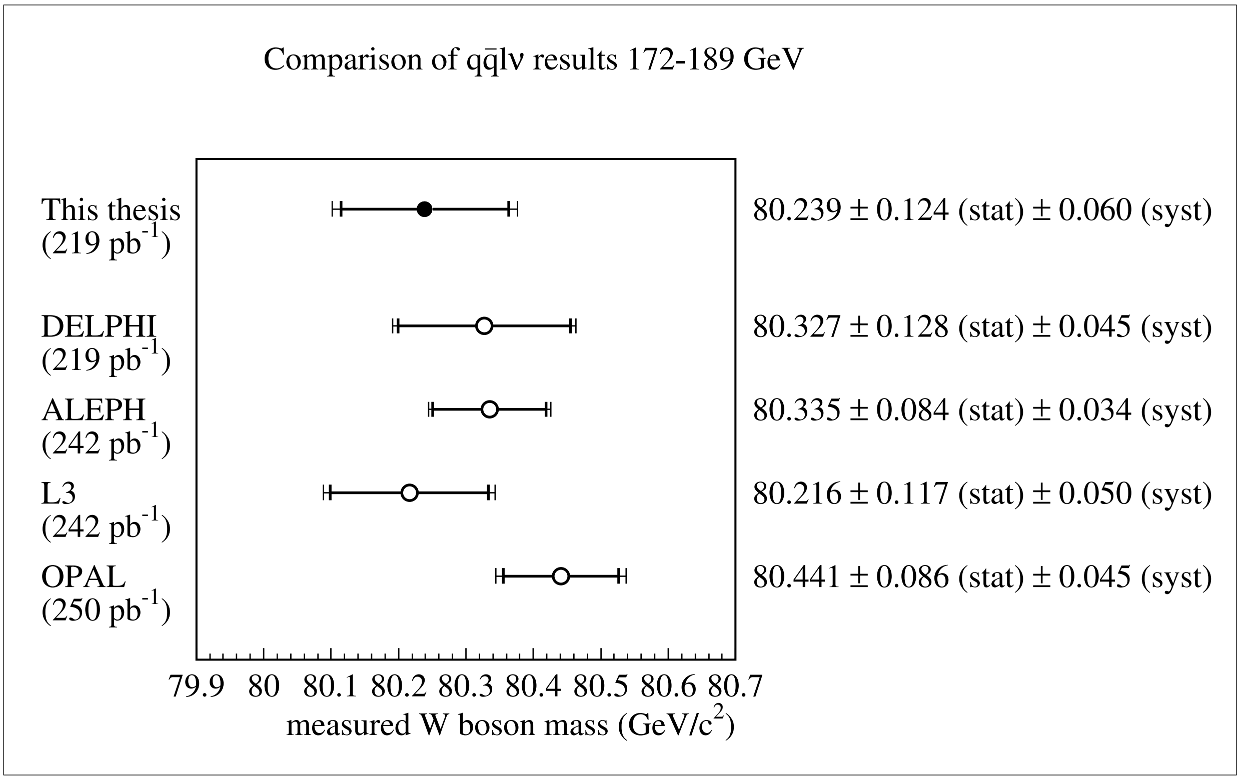

Figure 8.4: *Comparison of the* $\mathrm{q\bar{q}l}\nu$ m_{W} *result obtained in this thesis with the published results of the LEP experiments used in the LEP EW combination. The systematic errors shown do not include the error due to the LEP beam energy scale.*

$$\boxed{m_W^{\mathrm{all}} = 80,339 \pm 73 \text{ (stat)} \pm 32 \text{ (syst)} \pm 30 \text{ (FSI)} \pm 18 \text{ (LEP) MeV}/c^2}$$

This result is in excellent agreement with the standard model expectation (equation (1.34)): $m_{\mathrm{W}} = 80.373 \pm 0.024$ GeV$/c^2$, and also with the combined direct measurement of LEP (Summer 2000, including energies up to 202 GeV [75]): $m_{\mathrm{W}} = 80.428 \pm 0.047$ GeV$/c^2$. The good agreement of the measured W mass also means that the corresponding value of Δr:

$$\Delta r \;=\; 0.0377 \;\pm\; 0.0052 \tag{8.3}$$

agrees with the SM prediction [11] $\Delta r = 0.0357 \pm 0.0014$. Subtracting the term due to the running of α, $\Delta\alpha = 0.0664 \pm 0.0002$ (equation (1.32)), the result is:

$$\Delta r_{\mathrm{W}} \;=\; -\,0.0287 \;\pm\; 0.0052 \tag{8.4}$$

which demonstrates the existence of purely EW radiative corrections (of the type discussed in chapter 1) by 5.5 standard deviations. These quantum fluctuations cause the measured value of the ρ parameter to deviate from unity:

$$\rho = 1.0096 \pm 0.0022 \tag{8.5}$$

but taking into account the effect from radiative corrections on ρ predicted by the SM (as in equation (1.39)), one obtains the following measurement of ρ_0:

$$\rho_0 = 0.9989 \pm 0.0022 \tag{8.6}$$

The agreement of the measured value of ρ_0 with unity reflects the compatibility of the measurement with the assumption that the Higgs field is limited to the SM Higgs doublet.

This agreement has been confirmed already with better precision by the combination of the LEP and Tevatron results. It is therefore interesting to use the above assumption and predict the Higss mass indirectly from a SM fit. The results of this world combined EW fit are shown in Figure 8.5 (and Figure 8.9 at the end of this chapter). As an illustration the direct W mass measurement presented in this thesis is superimposed [1] on the plots.

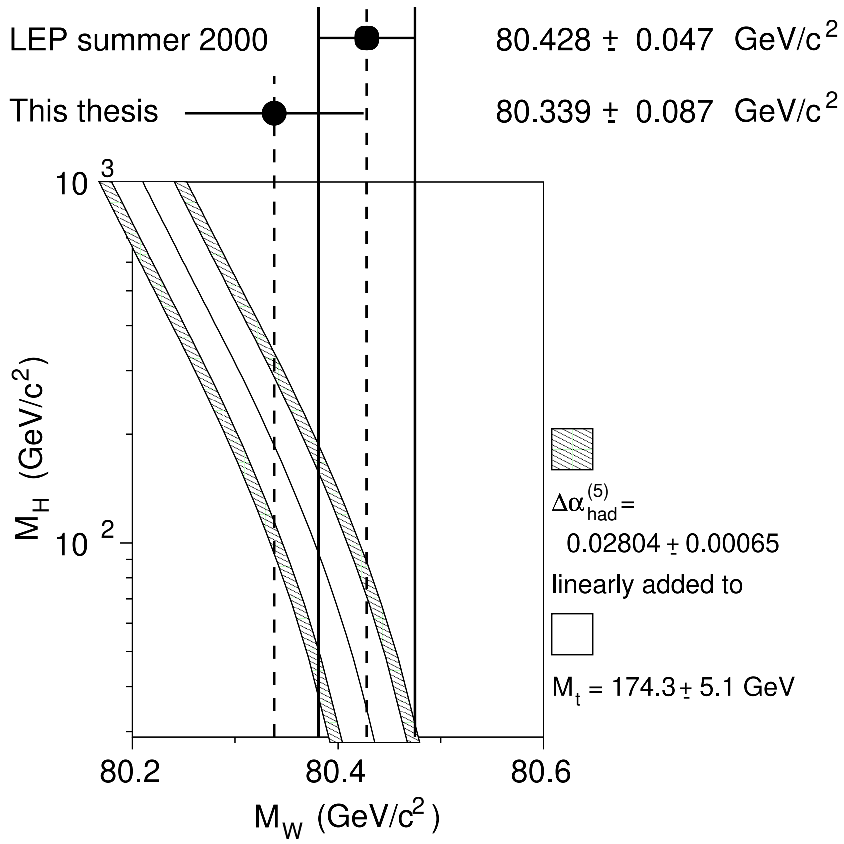

Figure 8.5: *Prediction of the SM Higgs boson mass as a function of the W mass. Based on a Summer 2000 EW working group plot [75].*

[1]The result of this thesis is correlated to the overall direct m_W measurement shown, through the DELPHI m_W results already included in the world average.

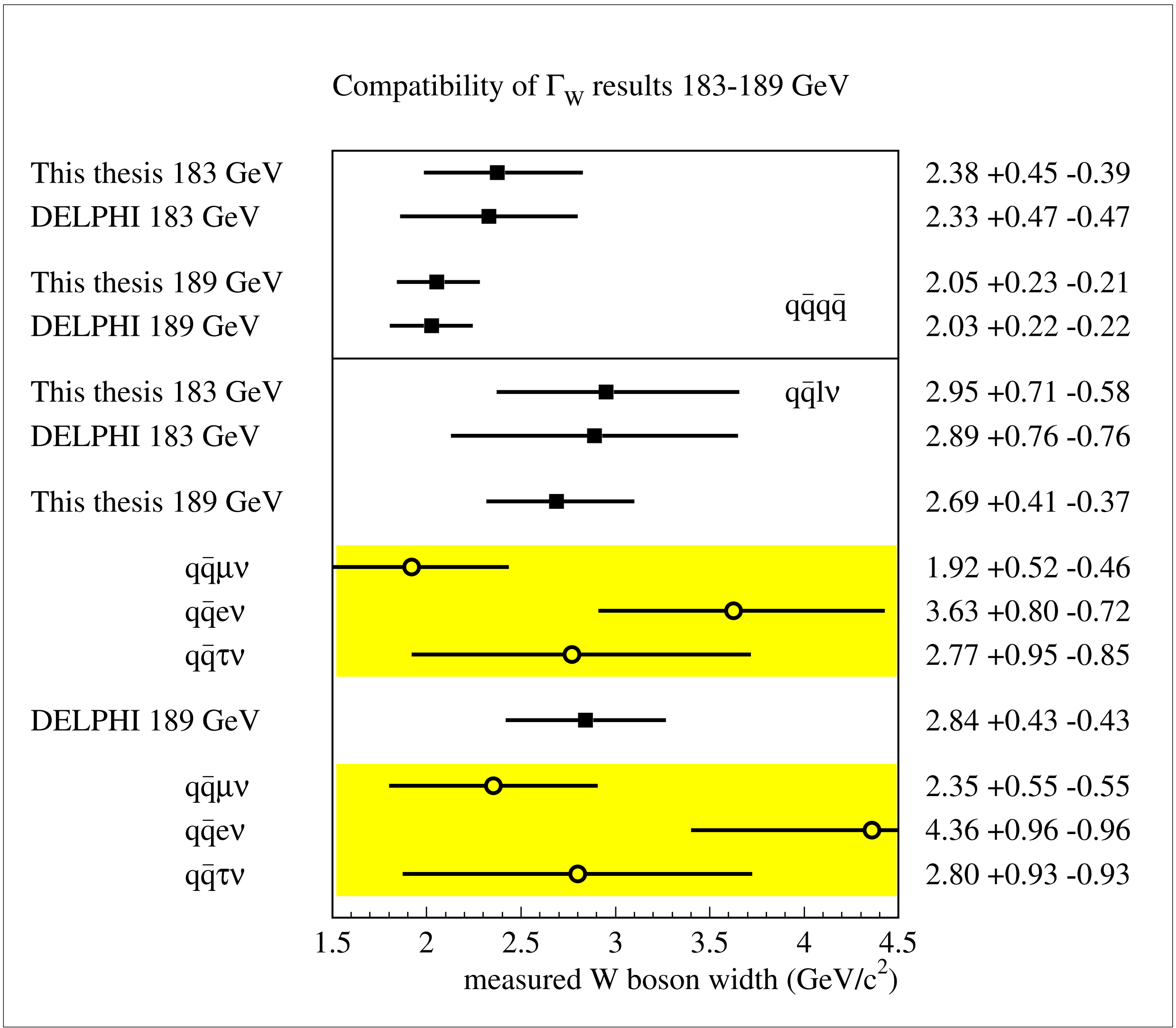

Figure 8.6: *Comparison of the Γ_W results obtained in this thesis with the 183 and 189 GeV results published by DELPHI. Only the statistical errors are shown.*

8.2 W width

Combination of results

W width results have also been published by DELPHI before, but only for 183 and 189 GeV data. The updated Ideogram results show an excellent agreement with the published DELPHI results, as shown in Figure 8.6. Again the 189 GeV numbers are shown separately for the different $q\bar{q}l\nu$ channels. Both in the $q\bar{q}l\nu$ Ideogram study and in the main DELPHI analysis the measured width in the $q\bar{q}e\nu$ channel is high compared to the other results. This is consistent with the deficit of events seen in the mass peak, as discussed in relation with the m_W measurement in the previous section.

The combination of the different semi-leptonic channels was done at the level of the likelihood

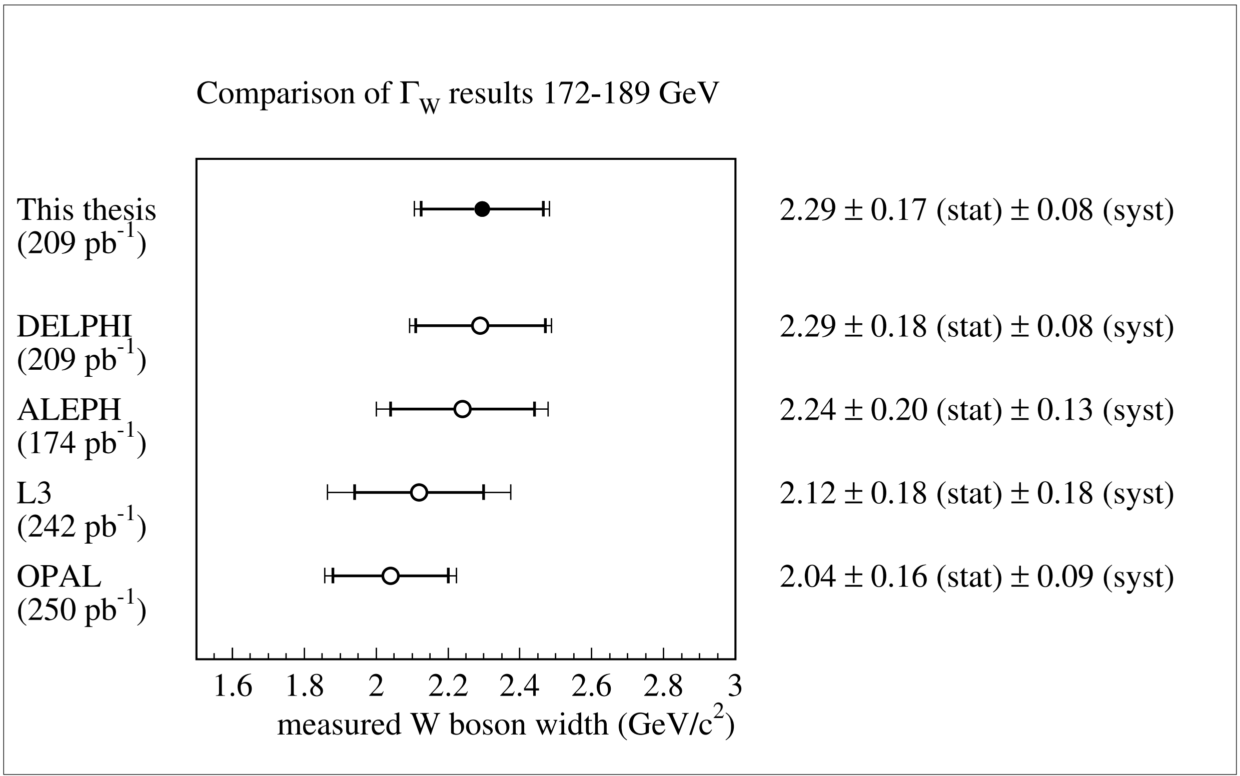

Figure 8.7: *Comparison of the $\Gamma_{\rm W}$ results obtained in this thesis with the 172-189 GeV results made available to the EW working group (and partly published) by the 4 LEP experiments. The systematic errors include the uncertainty due to CR, BEC and LEP.*

curves, in order to properly take into account the asymmetric errors. While the $\rm q\bar{q}q\bar{q}$ measurement of the W width:

$$\Gamma_W^{\rm q\bar{q}q\bar{q}} = 2,120^{+198}_{-186}\,\text{(stat)} \pm 58\,\text{(syst)} \pm 60\,\text{(FSI) MeV}/c^2 \tag{8.7}$$

is in perfect agreement with the SM prediction of 2.09 GeV/c^2, the combined semi-leptonic result is almost two standard deviations higher:

$$\Gamma_W^{\rm q\bar{q}l\nu} = 2,673^{+326}_{-303}\,\text{(stat)} \pm 103\,\text{(syst) MeV}/c^2 \tag{8.8}$$

The overall ideogram result for $\Gamma_{\rm W}$ is equal to:

$$\boxed{\Gamma_W \;=\; 2,295^{+173}_{-164}\,\text{(stat)} \;\pm\; 64\,\text{(syst)} \;\pm\; 44\,\text{(FSI)}\;\; \text{MeV}/c^2}$$

where the systematic uncertainties related to LEP are included in the ‘syst’ error quoted. This result is compared to the published results of the 4 LEP experiments in Figure 8.7.

Interpretation

The good agreement of the measured value in the $\rm q\bar{q}q\bar{q}$ channel with the SM prediction of $\Gamma_{\rm W}$ can be interpreted as a confirmation of our understanding of the detector resolution, and the correct propagation of errors in the 2D Ideogram analysis.

As mentioned already in the $q\bar{q}l\nu$ channel the agreement is not so good. In this case the results presented here provide an independent cross-check for the main DELPHI analysis confirming that the effects are really in the DELPHI data and are not restricted to a specific analysis.

The overall LEP summer 2000 combined result [75]:

$$\Gamma_W^{\rm LEP} = 2,120 \pm 80\ \text{(stat)} \pm 70\ \text{(syst)}\ \text{MeV}/c^2 \tag{8.9}$$

is in good agreement with the Standard Model and currently is the most precise direct measurement of $\Gamma_{\rm W}$. The final LEP2 combined measurement will be slightly more precise, but can certainly not match the precision of the indirect SM prediction (better than 0.003 GeV/c^2 [11]).

8.3 $\mathbf{m_{W^+} - m_{W^-}}$ results

Result and discussion

The measured differences between the W^+ and W^- boson masses are shown in Figure 8.8. All results are compatible with a zero mass difference, except the $q\bar{q}e\nu$ measurement at 189 GeV. This result is 3.1 sigma away from zero. This discrepancy calls for a detailed investigation. However, given the considerable effort already spent by the DELPHI $q\bar{q}l\nu$ mass group to understand the observed deviations in the $m_{\rm W}$ and the $\Gamma_{\rm W}$ measurement on the same data sample, this is not expected to be a simple task.

The possibility that this mass difference of 6.66 GeV/c^2 is due to a systematic effect is extremely unlikely as well. It cannot be explained by a wrong calibration slope. A forward-backward asymmetry of the electron reconstruction could in principle lead to such an effect, but would be required to be anomalously large.

The effects on $\Delta m_{\rm W^+W^-}$ of possible backgrounds like electrons from Bhabha scattering have not been investigated. Again it would require not only a significant background, but also a detector-related forward-backward asymmetry.

In view of the above, and in line with the approach followed in the DELPHI 189 GeV publication, the effect is taken as a so far unexplained, possibly statistical, fluctuation. Therefore the $q\bar{q}e\nu$ number is included in the combined result:

$$\boxed{\frac{m_{\rm W^+} - m_{\rm W^-}}{m_{\rm W}} = -0.013 \pm 0.011\ \text{(stat)} \pm 0.002\ \text{(syst)}}$$

The measurement is statistically dominated. The precision in the $q\bar{q}l\nu$ channel is better than in the $q\bar{q}q\bar{q}$ channel thanks to the easy separation between the W^+ and the W^- provided by the lepton. In the $q\bar{q}q\bar{q}$ channel resolution is lost due to non-perfect jet clustering, jet pairing, and limited separating power that can be achieved using jet charge information.

Discussion

It is interesting to see how much better one can measure the average W mass than the difference of the W^+ and the W^- mass. This is due to the nature of the kinematic constraints available at LEP, which cause $m_{\rm W^+}$ and $m_{\rm W^-}$ (in one event) to be anti-correlated in the constrained fit. This effect is visible as the elongated ellipses along the $m_{\rm W^+} - m_{\rm W^-}$ axis in the Ideograms (see e.g. Figures 5.5 and 6.14), and is strongest near the kinematical limit.

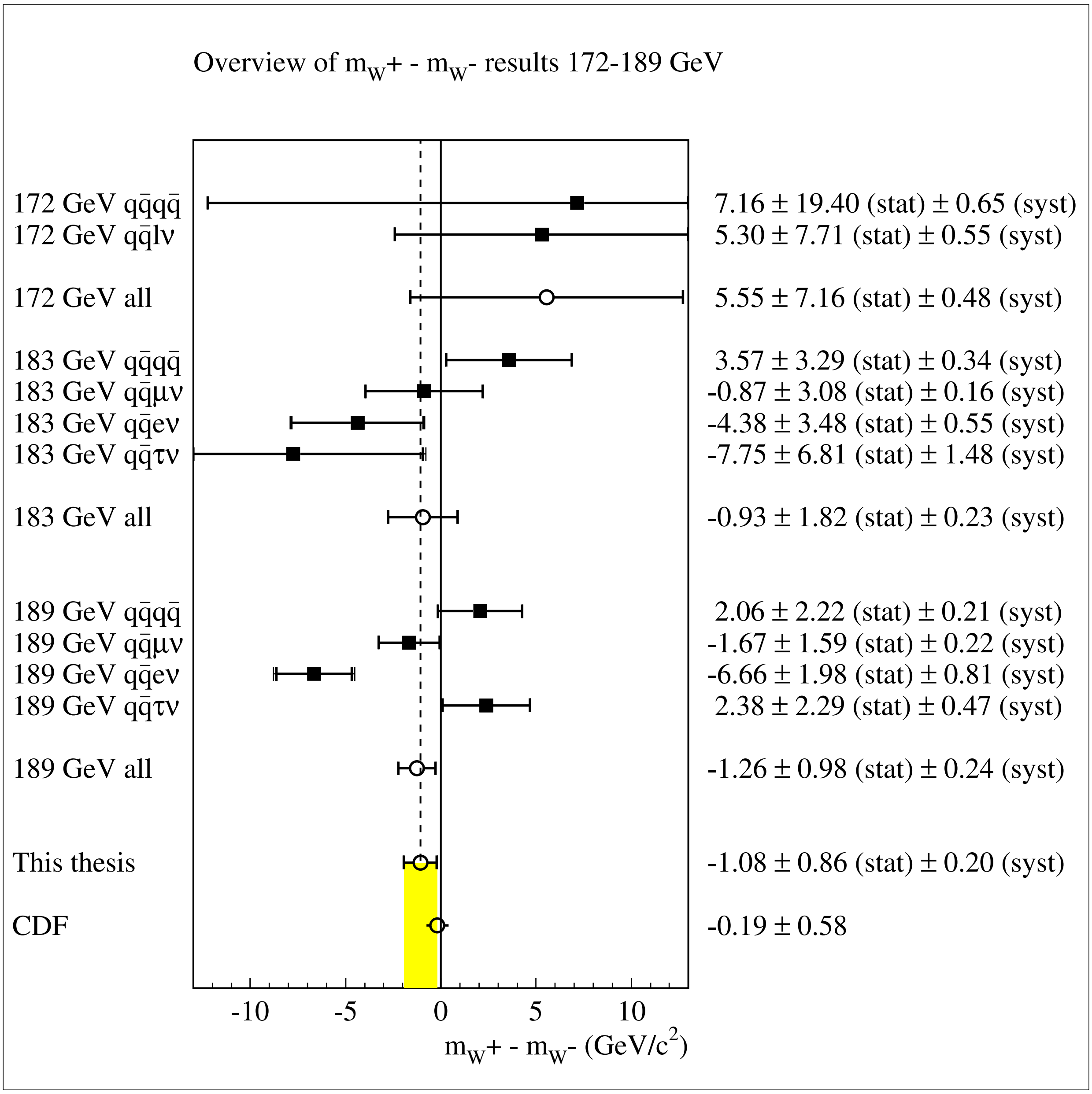

Figure 8.8: *Difference of W^+ and W^- boson mass measured with the 2D ideogram analysis.*

From a physics point of view the result is not surprising. As discussed in section 1.2 the masses of a particle and its anti-particle have to be equal in a relativistic quantum field theory. Since this fundamental prediction so far has only been experimentally tested in the Weak vector boson sector by the CDF collaboration [18], an additional independent measurement is worthwhile. Especially since it is possible to perform this measurement at LEP, with only a small change in the existing W mass analyses.

$m_{W^+} - m_{W^-}$ outlook

It will be hard to improve the Ideogram measurement in the $q\bar{q}q\bar{q}$ channel, unlike the $q\bar{q}l\nu$ measurement which can certainly be developed further. With some further improvements and the full LEP2 statistics DELPHI alone could probably obtain a final precision of the order of 0.50 GeV/c^2 on $\Delta m_{W^+W^-}$, and the LEP combination would allow a 0.3% measurement.

8.4 Conclusion and Outlook

The main result of the thesis research presented here is the development of the Ideogram analysis for the measurement of the W mass at LEP. As can be seen from the results presented in this chapter, the statistical performance and the control of the systematic uncertainties (both of crucial importance for the LEP W mass measurement) of the analysis have achieved an excellent level.

The main focus was on the W mass measurement in the $q\bar{q}q\bar{q}$ channel. But also in the $q\bar{q}l\nu$ channel and the measurement of Γ_W the statistical sensitivity of the Ideogram approach was demonstrated.

The W mass, width and m_{W^+} - m_{W^-} results presented were all in agreement with the current world averages and Standard Model expectations. The 172, 183 and 189 GeV data samples analysed correspond to approximately 1/3 of the LEP2 data taken by DELPHI. A final analysis of the full LEP2 data set is currently ongoing in DELPHI and the other LEP experiments.

Outlook Ideogram analysis and DELPHI W mass

The $q\bar{q}q\bar{q}$ Ideogram analysis is in good shape. Small improvements in the statistical sensitivity are still possible, but are not expected to make a big difference.

It is probably important to improve the description and understanding of the jet energy flow response (at least the part that is not covered by MLBZs); especially because some of these effects were found to increase for higher values of $\sqrt{s}$.

The $q\bar{q}l\nu$ Ideogram framework is ready to be used. To turn it into a full-fledged analysis, a further development of the event selection would be the first requirement. An improved identification of tau leptons and maybe an ISR treatment as used in the main DELPHI $q\bar{q}l\nu$ analysis could also help to further improve the statistical sensitivity.

LEP W mass and systematics

The combination of the W mass results of the 4 LEP experiments brings the overall statistical error down to a level where the understanding of the systematics becomes crucial. A detailed and careful study of systematics was presented in chapter 7. It is worthwhile to consider the three main sources of systematics in the LEP combination, and the prospects for possible improvements:

Jet fragmentation In the summer 2000 LEP combination the largest systematic uncertainty was quoted for fragmentation modelling. As argued in this thesis (chapter 7 and Appendix A), the true systematic effect is probably much smaller than that. Using the MLBZ method to compare the DELPHI fragmentation modelling directly with the data, possible systematic discrepancies were searched for with a high level of detail and statistical precision. A further development of the MLBZ method and use by the other experiments would lead to an improved understanding of this systematic effect and help to reduce the fragmentation uncertainty, possibly to a negligible level.

Final state cross-talk Only affecting the $\mathrm{q\bar{q}q\bar{q}}$ channel, the FSI error reduced the weight of the $\mathrm{q\bar{q}q\bar{q}}$ channel in the summer 2000 LEP combination to 27%, even though the statistical sensitivity for this channel is superior to that of the $\mathrm{q\bar{q}l}\nu$ channel. Thus the quoted systematic error for FSI was smaller, while its effective impact on the final precision of the W mass combination was actually bigger than the fragmentation error. A better understanding of this systematic effect will have to come from direct measurements constraining the available FSI models.

- Colour reconnection: So far the strongest experimental constraint on the size of the CR shift comes from the measured difference in m_W between the $\mathrm{q\bar{q}q\bar{q}}$ and the $\mathrm{q\bar{q}l}\nu$ channel. The LEP summer 2000 combination gave the following (preliminary) value: $\Delta m_\mathrm{W}(\mathrm{q\bar{q}q\bar{q}} - \mathrm{q\bar{q}l}\nu) = +5 \pm 51$ MeV/c^2. This result is model-independent and does not contradict the quoted systematic uncertainty. When all LEP2 data will be included the error may be reduced to to $\sim$42 MeV/c^2.

  For obvious reasons an independent and more precise experimental confirmation is wanted. But it turns out to be difficult to find observables more sensitive to CR than the W mass. A promising candidate is the measurement of the particle flow of low momentum particles in between jets (the 'string effect') using the L3 method [45]. It is hoped that this type of measurements can be used to constrain the available CR models (a factor ~ 2) better than the W mass. These constrained models can then be used to address the effect on m_W.

  Another viable option would be to trade statistical sensitivity for systematics, for example by ignoring low-momentum particles or discarding events that are expected to be most sensitive to CR reconnection, thus increasing the statistical error but reducing CR systematics. The danger of this approach is that it will certainly increase the statistical error, while it is not sure how much it might reduce the unknown CR effects.

  A more elegant way to sacrifice statistical sensitivity would be to perform a simultaneous measurement of W mass and CR shift (in the framework of the different models).

  Finally, the question needs to be answered whether the current estimation of the CR error is consistent with the way the other errors are quoted. While most of the other systematic errors are quoted as '1 sigma'-like two-sided uncertainties, the current quoted CR effect covers the full range of observed shifts, and its one-sided numerical value is quoted among two-sided numbers. Effectively, this leads to a factor 2^2 extra weight of the CR uncertainty with respect to the other errors. It might eventually be more consistent to perform 3 different LEP combinations: a conservative one, a 'best estimate', and a combination assuming only CR at the perturbative level ($\sim$5 MeV/c^2).

- BEC: As argued in chapter 7 the effect of BEC is probably smaller than 10 MeV/c^2. To come to a final estimation of systematics related to BEC it is important that the LEP experiments continue to pursue a direct measurement using an event-mixing technique, where the reference sample is produced by mixing the hadronic parts of $q\bar{q}l\nu$ events, to reduce model dependences in the analyses.

It is up to the W-mass measurement community to find a (preferably model-independent) way to translate the observed reduction of inter-W correlations in an uncertainty on the mass and width measurements.

LEP beam energy scale As discussed in chapter 3, several independent methods are being pursued to further cross-check and reduce the uncertainty on the extrapolation of the LEP energy scale. It is not yet clear whether the aim of 10 MeV will eventually be reached.

Extrapolating the currently available LEP results to the full LEP2 data set, the fully-hadronic channel is expected to achieve a statistical sensitivity of ∼28 MeV/c^2 compared to ∼30 MeV/c^2 for the semi-leptonic channel. Depending on the impact of the final estimation of the FSI errors, the combined statistical precision will be in the range from 21-24 MeV/c^2. Thus, in an optimistic scenario where the fragmentation error is strongly reduced and the FSI error reaches a level of 25 MeV/c^2 ($q\bar{q}q\bar{q}$ channel only), the final error on the LEP2 W mass could become better than 30 MeV/c^2; close to the uncertainty on the indirect prediction of the W mass.

Outlook m_W and the Standard Model

LEP finished data taking in 2000. The final analysis of the LEP2 data and subsequent combination is likely to take at least until 2003. The final LEP W mass result will set the standard for the nearby future.

The Tevatron collider recently started a new data taking period (RUN2) which will enable an improved, high statistics measurement of m_W using the transverse momentum spectrum of leptonically decaying W's. But Tevatron and LHC (its start foreseen in 2006) will certainly need a few years of running to achieve the level of understanding of the systematics required to reach a similar or better precision.

Another important next step in the EW precision measurements for the coming years is the expected improvement in the direct measurement of the mass of the *top quark*. A detailed study of the top quark which will be one of the main topics at the Tevatron. In Figure 8.9 the relation between the top mass, W mass and the prediction for the SM Higgs mass is illustrated. The improved knowledge of the W boson and top quark masses will further restrict the allowed region for the SM Higgs boson mass — and thus be a key ingredient in solving the mystery of mass generation in the Standard Model.

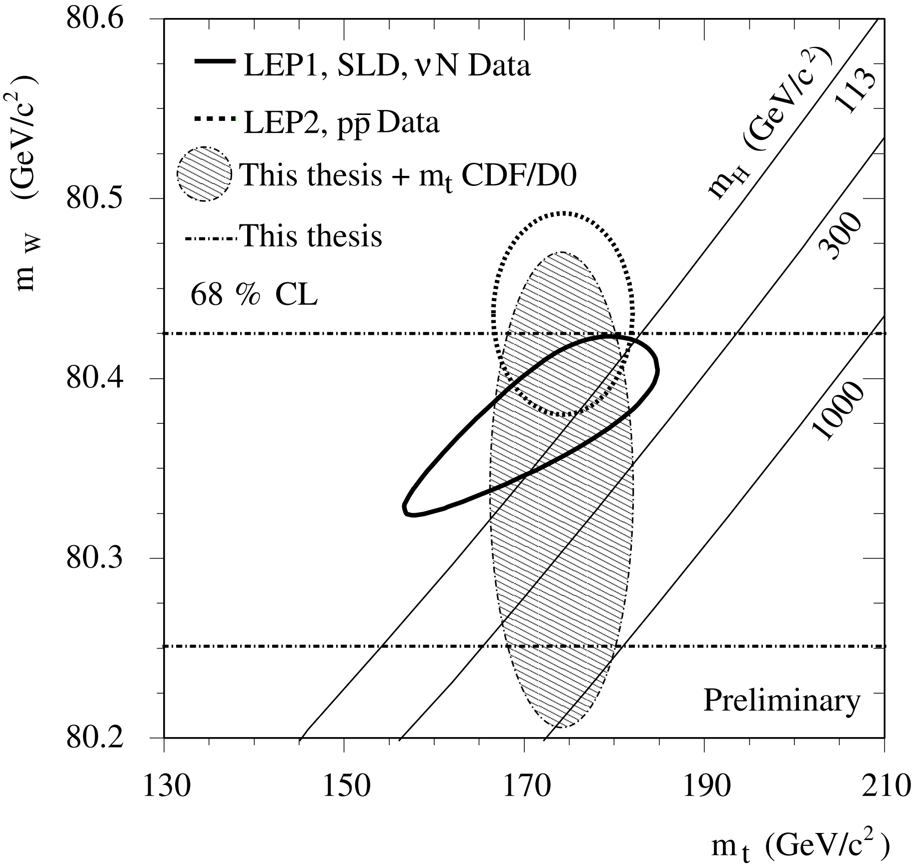

Figure 8.9: *The indirect SM prediction of the W mass and top quark mass (based on LEP1, SLD and neutrino scattering data), compared to different sets of direct measurements. The plot is based on the summer 2000 Standard Model fit performed by the LEP EW working group [75]. The final W mass result presented in this thesis is superimposed, both as a single measurement and in combination with the direct measurement of the top quark mass.*

Appendix A

Mixed Lorentz Boosted Z^0's

N.J. Kjær and M. Mulders,
CERN-OPEN-2001-026 (to be submitted to NIM)

Abstract

A novel technique is proposed to study systematic errors on jet reconstruction in W physics measurements at LEP2 with high statistical precision. The method is based on the emulation of W pair events using Mixed Lorentz Boosted Z^0 events. The scope and merits of the method and its statistical accuracy are discussed in the context of the DELPHI W mass measurement in the fully hadronic channel. The numbers presented are preliminary in the sense that they do not constitute the final DELPHI systematic errors.

A.1 Introduction

The measurement of the W boson mass is one of the major topics in LEP2 research. It provides a precision test of the Standard Model and a way to further constrain the predictions for the Higgs boson mass. With a final expected statistical error on the W mass of 20 MeV/c^2 for the four LEP experiments combined, it is very important to control systematic uncertainties to a level of 10 MeV/c^2 or -where possible- even lower. This paper focuses on systematic errors related to jet reconstruction, which have proven to be some of the most challenging systematic errors at the moment. Typical errors quoted for the W mass analyses of the four LEP collaborations at a centre-of-mass energy of 183 GeV [1-5], vary between 20 and 60 MeV/c^2 for jet fragmentation, and between 20 and 35 MeV/c^2 for detector effects.

Our knowledge about jet reconstruction errors is almost entirely based on Z^0 events. Events recorded at LEP1, or during the calibration runs at the Z^0 peak energy in between the high energy runs in 1997, 1998 and 1999 are used as 'template' to tune and check the detector alignment and calibration, efficiency and resolution, and to test and tune models describing jet fragmentation. The same models and detector simulation are then ported to the description of W pair events.

The conventional way to estimate errors on this description follows a similar approach: a 'realistic' uncertainty in the simulation of Z^0 data is derived from a comparison between Z^0 data and

Monte Carlo and translated into a realistic 'shaking' of the high energy WW simulation (detuning fragmentation parameters, using different models or varying the description of the detector, etc.). The shift in the W mass obtained from the Monte Carlo sample is used as an estimate for this source of systematic error. This is repeated for different possible sources of shaking, and the systematic errors are added in quadrature or somehow combined taking into account the correlations between the different estimates. The limitations to this approach are:

- Each of the individual systematic errors is typically close to statistical sensitivity. This means that we often have to include statistical errors on the individual errors in our estimate of the systematic error.

- To take into account a 'complete' set of systematic effects, a considerable number of different shifts has to be determined and combined.

- It is not always clear how different estimates of systematic effects are correlated. The question often is how complementary and how realistic different shakings are.

This necessarily leads to conservative estimates of the systematic error.

The philosophy of the Mixed Lorentz Boosted Z^0 (MLBZ) method presented in this paper is to use Z^0 events from data and Monte Carlo simulation (MC) to emulate WW events *first*, and *then* do a comparison of the reconstructed W mass, applying the analysis directly on the MLBZ events (see figure A.1). In this way a large subset of all possible detector effects and fragmentation model imperfections is probed at once, following a well-defined procedure that simplifies the intricate task of composing a complete, realistic list of effects and correctly handling the internal correlations to good approximation. It should be stressed already here, however, that not all effects are covered. A breakdown of the effects that are considered to be covered by the MLBZ method is given in table A.2 and discussed further in section A.4.

The effective statistical precision on a systematic shift in the W mass obtained with the MLBZ method with the example analysis described in this paper is around 300 MeV/c^2 per generated or detected Z^0 event [1], compared to a typical mass resolution of 3 GeV/c^2 per generated WW MC event [2] used in the conventional approach.

The aim of this paper is not to give definitive answers to all questions related to this new method, but merely to give a comprehensive description of a first implementation and present the first results. Hopefully this will serve as a basis for a fruitful discussion about this new and potentially very useful technique.

Section A.2 gives a description of the MLBZ method itself and appendix A.7 the technique used to determine the statistical precision. In section A.3 the first results are presented, followed by a discussion of the possible limitations of the method in section A.4. The final two sections contain an outlook and conclusions.

---

[1] A better resolution can be obtained by increasing the number of mixed pairs per Z^0 event (i.e. increasing the sample size) or the number of boosts for each mixed Z^0 event pair. For the analysis described here available CPU time was a limiting factor.

[2] The statistical resolution of 3 GeV/c^2 is a convolution of the Breit Wigner width of the W ($\approx$2 GeV/c^2) and the average resolution per event ($\approx$2 GeV/c^2).

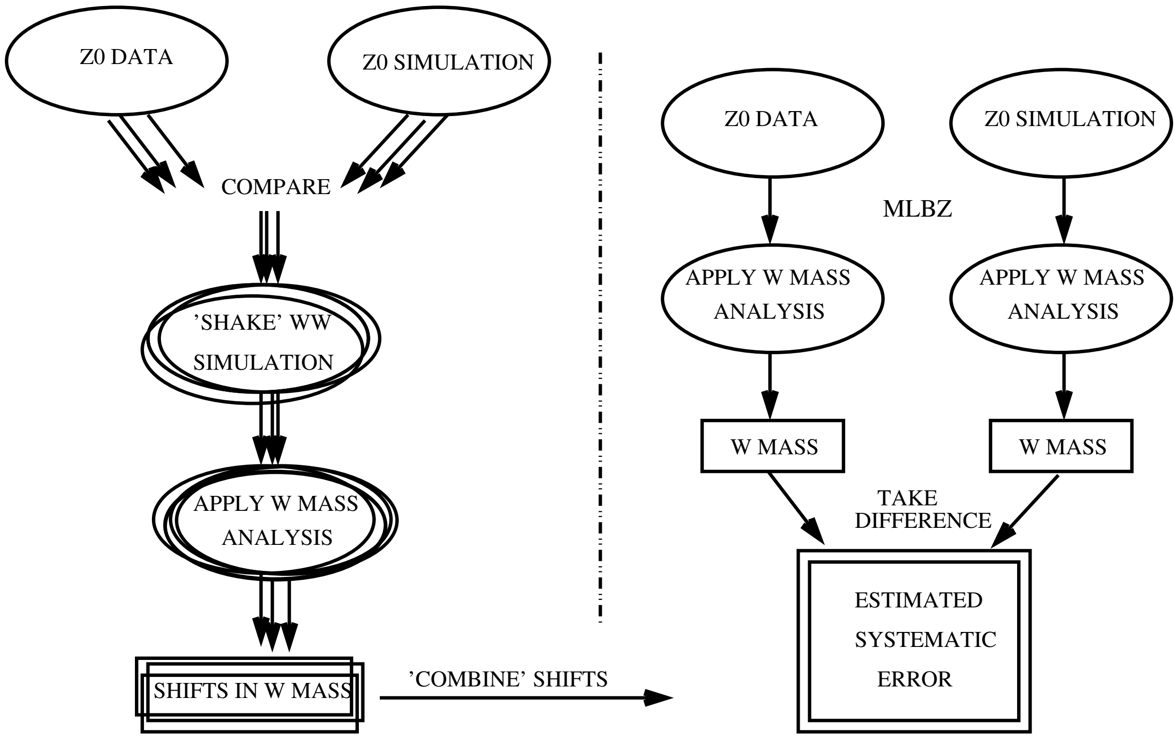

Figure A.1: Conventional approach to estimate systematic errors vs. MLBZ

A.2 Description of the MLBZ method

The general outline of the MLBZ method [3] is as follows:

1. Select hadronic Z^0 events taken during the Z^0 calibration runs
2. Superimpose the measured 4-momenta of the particles of two Z^0 bosons after Lorentz boosting them in opposite direction with a boost typical for W bosons in the high energy run, thus emulating the topology of a fully hadronic WW event.
3. To fully exploit the information in the calibration data, Z^0 events should be used more than once by mixing them more than once and using more than one (isotropically distributed) boost direction per mixed event pair.
4. Apply the WW analysis of which the systematic effects are to be studied to the MLBZ events thus created.
5. Do this both on Z^0 events from data and from MC simulation and study the observed differences to draw conclusions about systematic errors.

[3] Here only the emulation of fully hadronic WW events is mentioned. See section A.5.1 for other channels.

A.2.1 Details of event selection and MLBZ procedure

For this paper the DELPHI W mass measurement at 183 GeV [3] in the fully hadronic channel was used as an example. The Z^0 events were mixed and Lorentz boosted in the following way:

1. The Z^0 events were collected at the beginning of 1997 with a beam energy of $E_{\mathrm{beam}}(t)$, varying slightly as a function of time t. It is not necessary to know $E_{\mathrm{beam}}(t)$ to a high precision. Instead a fixed beam energy of $E_{\mathrm{bZ^0}} = 45.625$ GeV was assumed.

2. On applying the runquality selection as used in [3], 1.6 pb^{-1} of Z^0 data remained.

3. The Z^0 candidates were selected with hadronic cuts giving a purity exceeding 99%:

   - at least 8 charged particles
   - carrying at least 15 GeV total energy
   - of which at least 3 GeV per hemisphere

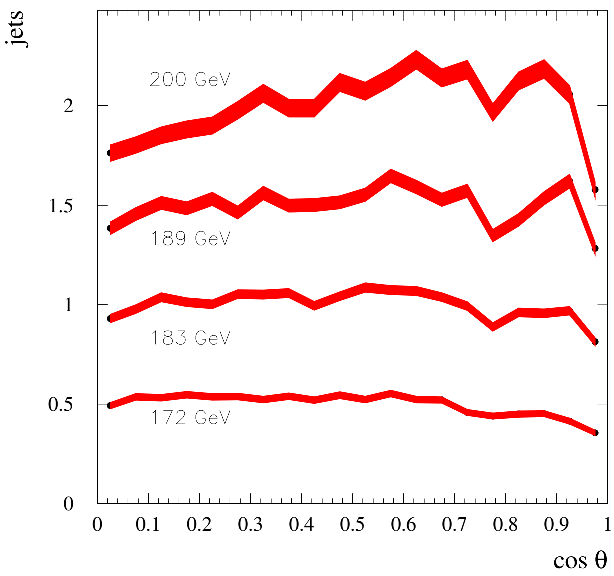

Figure A.2: The distribution of the measured jets in simulated WW events as a function of the cosine of the polar angle with the beam, with arbitrary normalisation for different values of the centre-of-mass energy. The thickness of the line indicates the statistical uncertainty.

The measured angular distribution of jets in W$^+$W$^-$ events is almost uniform (see figure A.2), while Z^0 jets are distributed according to $1 + (\cos\theta)^2$, where $\cos\theta$ is the polar angle with the LEP beam. In order to have the same angular distribution of jets in the Z^0 candidates and the W$^+$W$^-$ events, Z^0 events were randomly discarded according to the value of the polar angle of their thrust axis. 31557 events were selected in 157 samples of 201 events each, using approximately 94% of the data available. The sample size of 201 events was chosen as a compromise to have reasonable statistics but still be able to perform the full analysis (as described below) for one sample in a single 8 CPU-hour batch job. From Pythia/Jetset Z^0 MC 161 samples of the same size were selected. Some distributions of Z^0 event variables for data and MC are shown in figure A.3.

4. The 4-momenta [4] of the measured particles in the Z^0 event were Lorentz boosted in a single random direction with a boost given by $\gamma_{\mathrm{boson}} = \frac{\sqrt{s_{\mathrm{high}}}}{2\mathrm{m_W}}$, where $\sqrt{s_{\mathrm{high}}} = 182.7$ GeV is an approximation to the LEP centre-of-mass energy of the high energy data (at 183 GeV) and $m_{\mathrm{W}} = 80.35$ GeV/c^2 is a nominal value of the W mass.

5. Another Z^0 candidate was then treated in the same way except the opposite direction of the boost was chosen. The particles of both boosted Z^0 events were mixed and a new event created. Each event was used 400 times by mixing it k times (k different isotropically distributed boost directions) with every other event from the same sample of 201 events. k was chosen to be 2, giving 40200 MLBZ events per sample.

6. These MLBZ events have nearly the same kinematical properties as W^+W^- events. The main differences come from the overall energy scale and Initial State Radiation (ISR). The MLBZ events were then treated as W^+W^- events and a fitted mass $m^{\mathrm{sim}}_{\mathrm{MLBZ}}$ extracted from simulated Z^0s and $m^{\mathrm{data}}_{\mathrm{MLBZ}}$ from the Z^0 data, using the 183 GeV W mass analysis [3], assuming a centre-of-mass energy $\sqrt{s_{\mathrm{MLBZ}}} = 4\gamma_{\mathrm{boson}}\mathrm{E_{bZ^0}}$ in the constrained fits.

7. The difference of the fitted mass with respect to $2E_{\mathrm{bZ^0}}$ is interpreted as a measure for the experimental bias at the scale of $2E_{\mathrm{bZ^0}}$, the approximated Z^0 mass. Thanks to the use of relative errors on the jet energies in the constrained fit [6], the fit is largely invariant under a scale transformation of all energies and masses. Therefore the measured experimental bias is related to the experimental bias at the scale of the W mass by a factor $\frac{m_{\mathrm{W}}}{2E_{\mathrm{bZ^0}}} \approx \frac{m_{\mathrm{W}}}{m_{\mathrm{Z}}}$.

8. If the simulation of jet reconstruction in W^+W^- events is affected by systematic errors most of these will be the same for simulated MLBZ events. Thus the difference between the fitted mass on MLBZ data and MLBZ simulation, rescaled to the W mass scale,

$$\Delta m_{\mathrm{W}}^{\mathrm{MLBZ}} = \left(m^{\mathrm{data}}_{\mathrm{MLBZ}} - m^{\mathrm{sim}}_{\mathrm{MLBZ}}\right) \cdot \frac{m_{\mathrm{W}}}{m_{\mathrm{Z^0}}} \tag{A.1}$$

is a measure of the systematic error from non-perfect simulation on the W mass. This measure can be improved by taking into account the difference in flavour composition between Z^0 and W boson decay products, as will be discussed in section A.3.3.

A.2.2 Statistical accuracy

When applying the standard analysis to the MLBZ events as described in the previous subsection, the statistical error on the measurement can not be determined in the usual way assuming that

[4] Assuming pion masses for charged particles and photon masses for neutrals.

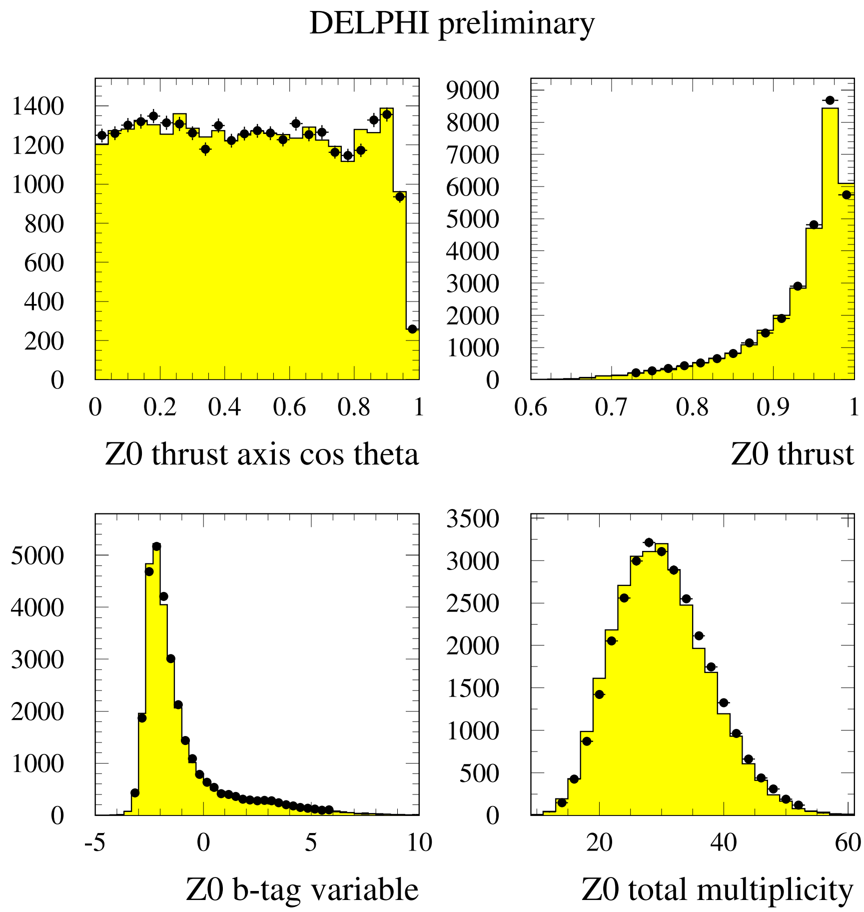

Figure A.3: Comparison between 1997 data (the points with error bars) and MC (the filled histogram) for different event variables of the selected Z^0 events. The total Z^0 multiplicity includes both charged and neutral particles. The MC plots are normalised to the number of data events.

events are uncorrelated observations of the quantity that is to be measured. The Z^0 events are independent, but the MLBZ events are not.

Therefore a resampling technique know as the 'Jackknife' method [7, 8, 9, 10] was used. A full description of its implementation is given in appendix A.7. As the data was treated in such a way that many samples of 201 events are independent, a comparison with the traditional RMS estimate can serve as a cross-check of the Jackknife method at the level of the measured MLBZ mass per sample. This comparison is shown in table A.1 and confirms that the Jackknife procedure used estimates the statistical errors correctly to within 10%.

For the example analysis discussed here the statistical precision on the fitted MLBZ mass turns out to be $1/\sqrt{n_{Z^0}} \cdot 300$ MeV/c^2 at the scale of the W mass, where n_{Z^0} is the number of selected Z^0 events. This allows a precise determination of various effects to a precision of typically order of 2 MeV/c^2 or better.

	Z^0 data	Z^0 simulation
number of samples n_{samp}	157	161
uncertainty on mass per sample (MeV/c^2)		
average Jackknife estimate $\langle\sigma^{\text{MLBZ}}_{sample}\rangle$	23.7 ± 0.2	22.3 ± 0.2
cross-check: RMS of sample masses	22.0 ± 1.3	20.3 ± 1.1
all samples combined; uncertainty on mass (MeV/c^2)		
Jackknife estimate $\sigma^{\text{MLBZ}}_{all}$	1.9	1.8
cross-check: RMS of samples $/\sqrt{n_{\text{samp}}}$	1.8	1.6

Table A.1: Comparison of different estimates of the statistical uncertainty on the mass measured with MLBZ events.

A.3 Results

In this section the expected experimental bias on the W mass is compared to the observed bias in data and simulation, and the results are briefly discussed.

A.3.1 Expected reconstruction bias

The – average – reconstructed W mass obtained through kinematical reconstruction is not equal to the average 'true' or generated W mass. The difference of the two will from now on be called reconstruction bias:

$$b_{\text{rec}} = m_{\text{reconstructed}} - m_{'\text{true}'} \tag{A.2}$$

This bias is caused by a range of many more or less correlated effects. It is known from MC studies that the following two dominating effects give the largest contribution to the reconstruction bias:

- A positive bias due to ISR photons that are lost inside the beam pipe and not taken into account in the kinematical fit. At 183 GeV this causes an average positive shift of the order of 300 MeV/c^2 on the reconstructed mass.
- A negative bias due to the imperfect reconstruction of jets, which smears the masses preferably downwards. As will be shown later in this section this bias turns out to be of the order of -200 MeV/c^2 at 183 GeV.

The treatment of ISR falls outside the scope of this paper, as its effects cannot be studied with the MLBZ method, and will not be discussed further. The negative bias due to jet misreconstruction, on the other hand, can be studied very well using MLBZs, and is the main subject of this paper.

Reconstructing a boosted Z^0

The origin of the negative reconstruction bias can already be demonstrated with the simple case of a single boosted Z^0. When a Z^0 boson, produced at rest, decays hadronically and is detected by the DELPHI detector, the main error on the measured direction and energy of the jets is caused by missing particles. In this way

- on average the measured energy is 10-20 % lower than the Z^0 boson mass
- when clustered in two jets, the jets are not exactly back-to-back which means that the measured boson is moving in the laboratory frame with a 'measured' velocity (or boost) β_{meas} .

This means that the invariant mass of the detected particles is typically 10-20% smaller than the 'true' Z^0 mass. When the Z^0 boson is boosted with a certain boost β_{boson} before or after the measurement, the detected invariant mass will remain the same [5]. This is no longer true, however, when applying a constrained fit to improve the measurement of the invariant mass beyond the detector resolution, irrespective of the specific analysis technique that is used. The DELPHI convolution method [3, 6] gives a bias in the reconstructed mass which is corrected for by calibration curves, while Monte Carlo reweighting methods [2, 4, 5] automatically correct for the bias in the procedure using simulation. The two methods behave very similar to deficiencies in the simulation, and are therefore affected by systematics in a comparable way.

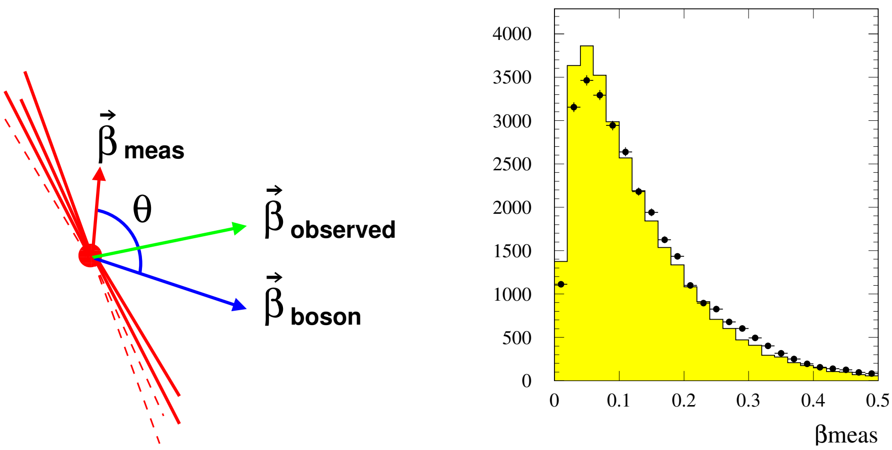

Figure A.4: The observed boost β_{observed} is a combination of the true boost of the boson β_{boson} and the mismeasurement of the event β_{meas} . The plot on the right shows the distribution of β_{meas} in data and MC.

To approximate the effect of a constrained fit, all particle momenta in our boosted Z^0 event are rescaled with a rescaling factor so that the total energy equals the 'expected' energy $\gamma_{\text{boson}}\mathrm{m}_{Z^0}$, with $\gamma_{\text{boson}} = 1/\sqrt{1-\beta^2_{\text{boson}}}$. In this overall rescaling procedure the directions of the observed particle momenta and therefore the ratio $|\mathbf{p}|/E = \beta_{\text{observed}}$ remain constant. The final observed invariant mass is then given by:

$$m_{\text{fit}} = \frac{E_{\text{observed}}}{\gamma_{\text{observed}}} = \frac{\gamma_{\text{boson}}\mathrm{m}_{Z^0}}{\gamma_{\text{observed}}} = \gamma_{\text{boson}}\mathrm{m}_{Z^0}\sqrt{1-\beta^2_{\text{observed}}} \tag{A.3}$$

[5]This is only perfectly true when the same particles are missed before and after the boost (uniformity of the detector), and assuming that the lack of Lorentz invariance of other resolution effects like momentum resolution on the reconstructed tracks is negligible.

which is thus fully determined by the observed boost γ_{observed} or equivalently β_{observed} which is the combination of the artificial boost β_{meas} due to the resolution of the detector and the true boost β_{boson} given to the boson (see figure A.4). The following expressions for γ_{observed} can be derived:

$$\gamma_{\text{observed}} = \gamma_{\text{boson}}\gamma_{\text{meas}}(1 + \beta_{\text{boson}}\beta_{\text{meas}}\cos\theta) \tag{A.4}$$

and substitution of γ_{observed} in equation (A.3) yields

$$m_{\text{fit}} = \frac{m_{Z^0}}{\gamma_{\text{meas}}(1 + \beta_{\text{boson}}\beta_{\text{meas}}\cos\theta)} \tag{A.5}$$

where θ is the angle between the two boosts in the laboratory frame. For two MC events the distribution of measured masses is shown in figure A.5, applying 100,000 boosts corresponding to different centre-of-mass energies in random directions (uniformly distributed in the laboratory frame). The peculiar 'box' shape is easily understood from equation (A.5), bearing in mind that

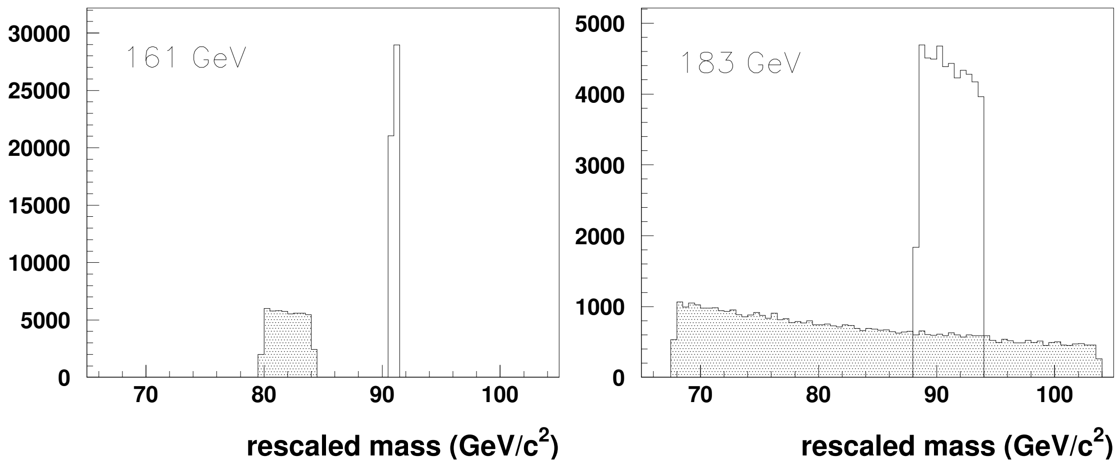

Figure A.5: For two MC Z^0 events the distribution of rescaled masses is shown after boosting each event a 100,000 times in random directions. This is done for a boost corresponding to a WW event at $\sqrt{s}$=161 GeV (left) and $\sqrt{s}$=183 GeV (right). One event is measured with large β_{meas} (shaded histogram); the other with small β_{meas} (open histogram).

$\vec{\beta}_{\text{boson}}$ has a uniform angular distribution, corresponding to a flat distribution in cosθ.

For a perfectly measured event $\beta_{\text{meas}} = 0$ and $\gamma_{\text{meas}} = 1$ so that equation (A.5) reduces to $m_{\text{fit}} = m_{Z^0}$. In other cases the average bias $m_{\text{fit}} - m_{Z^0}$ and the RMS of this bias can be calculated analytically:

$$m_{\text{fit}} - m_{Z^0} = \frac{m_{Z^0}}{2\alpha\gamma_{\text{meas}}}\ln(\frac{1+\alpha}{1-\alpha}) - m_{Z^0} = m_{Z^0}\left[(\frac{\beta^2_{\text{boson}}}{3} - \frac{1}{2})\beta^2_{\text{meas}} + \mathcal{O}(\beta^4_{\text{meas}})\right] \tag{A.6}$$

and

$$\sigma^2_{m_{\text{fit}}} = \frac{m^2_{Z^0}}{\gamma^2_{\text{meas}}}\left[\frac{1}{1-\alpha^2} - \left(\frac{1}{2\alpha}\ln\left(\frac{1+\alpha}{1-\alpha}\right)\right)^2\right] = \frac{m^2_{Z^0}}{\gamma^2_{\text{meas}}}\left[\frac{\beta^2_{\text{boson}}}{3}\beta^2_{\text{meas}} + \mathcal{O}(\beta^4_{\text{meas}})\right] \tag{A.7}$$

where $\alpha = \beta_{\text{meas}}/\beta_{\text{boson}}$.

These formulas are in good agreement with the plots shown in figure A.6 generated by boosting 500 Z^0 events from MC 50,000 times each. They show an *increasing negative bias* for *increasing* values of β_{meas} (corresponding to worse jet reconstruction), and they also show that this effect becomes *less pronounced* for *increasing* values of the boson boost β_{boson} . When extracting

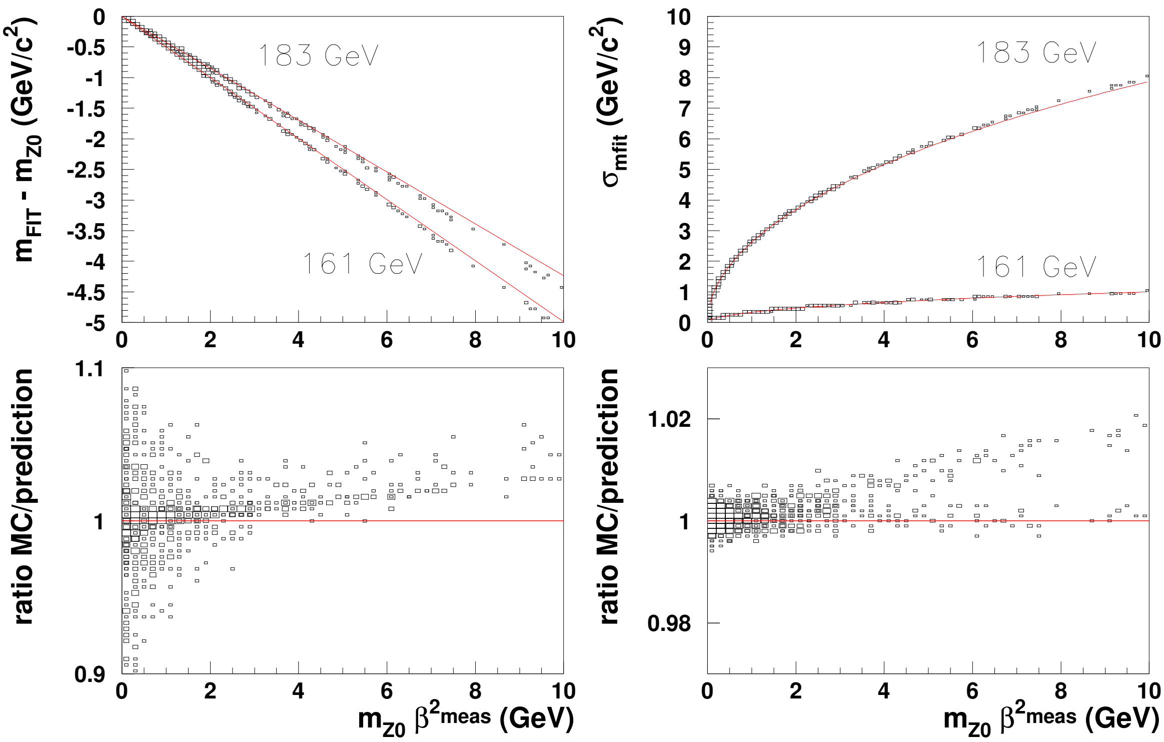

Figure A.6: The bias (left) and error on the bias (right) as a function of the measurement boost, compared to the analytical predictions up to $\mathcal{O}(\beta^2_{\text{meas}})$

information about jet reconstruction systematics, the interesting quantity to obtain from a Z^0 event is the average bias; not the measured mass obtained for a single boost. For a boost corresponding to 183 GeV, 400 boosts per Z^0 event and a typical value of $m_{Z^0}\beta^2_{\text{meas}}$ of 0.5 GeV (see figure A.4) the average bias is -210 MeV, and the relative precision per event on this bias is $\approx 50\%$. It can be seen from figure A.4 that the peak in the distribution of β_{meas} in data is shifted to slightly higher values compared to simulation. The shift of the peak corresponds to an average shift in $m_{Z^0}\beta^2_{\text{meas}}$ of ≈ 0.05 GeV, which in turn would be equivalent to a systematic shift of -21 MeV on the rescaled m_{Z^0} mass.

This simplified experiment is only an approximation of the full MLBZ analysis, as in a real constrained fit the rescaling factor is not the same for all jets, and jet masses and transverse errors on the jet momenta are taken into account. Furthermore additional statistical effects from the interaction of the two mixed events (e.g. jet clustering ambiguities) and more realistic analysis details play a role.

Reconstructing a W pair event

It is evident that at WW production threshold, when the true jets of the W bosons are strictly back-to-back, any imperfection in the mass reconstruction will lead to a negative mass bias (analogous to the reconstruction of the Z^0 bosons described previously). At a centre-of-mass energy of 183 GeV, still a negative shift remains.

That the negative bias from jet reconstruction depends both on the W boost and on the quality of the jet measurement can easily be checked using a simplified WW simulation. In figure A.7 the average bias is shown for 161 and 183 GeV, and jets generated as WW events with Breit-Wigner but without ISR. The measurement errors where assumed to be Gaussian according to the parameterisation as used in the fit of the 172 GeV analysis [6]. The transverse jet errors where multiplied with an additional factor X, and the bias plotted as a function of this factor (see figure A.7). For the most realistic value of X=1, the bias at 183 GeV was found to be ≈ -200 MeV/c^2, in agreement with the bias seen in MLBZ events (see section A.3.2).

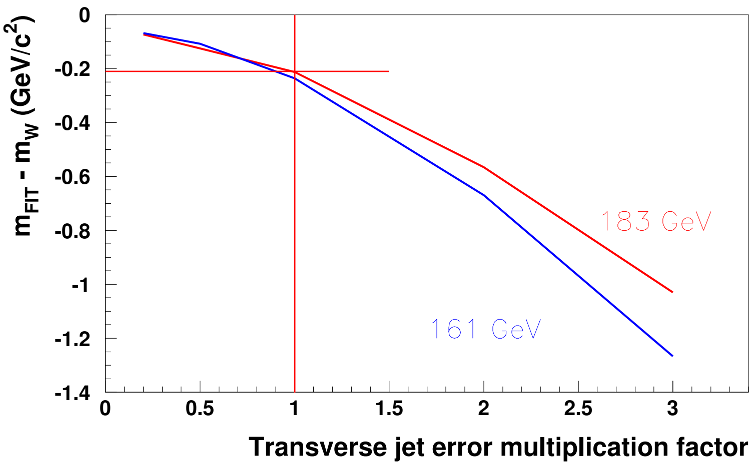

Figure A.7: Bias as a function of a transverse jet error scaling factor in a simplified WW simulation, for centre-of-mass energies of 161 and 183 GeV.

Again it is seen that the negative bias

- Is smaller for higher centre-of-mass energies (183 GeV compared to 161 GeV)
- Becomes larger when the jet reconstruction becomes worse.

A.3.2 Observed reconstruction bias

An interesting feature of the MLBZ method is that the mass bias can be studied as a function of properties of the *individual* bosons, rather than the usual *pairs* of W bosons. It can be shown (see appendix A.7 and A.8) that the MLBZ bias is a linear sum of the reconstruction biases of the individual Z bosons:

$$b^{kl}_{\mathrm{MLBZ}} \equiv \frac{b^k_{\mathrm{Z}} + b^l_{\mathrm{Z}}}{2} \tag{A.8}$$

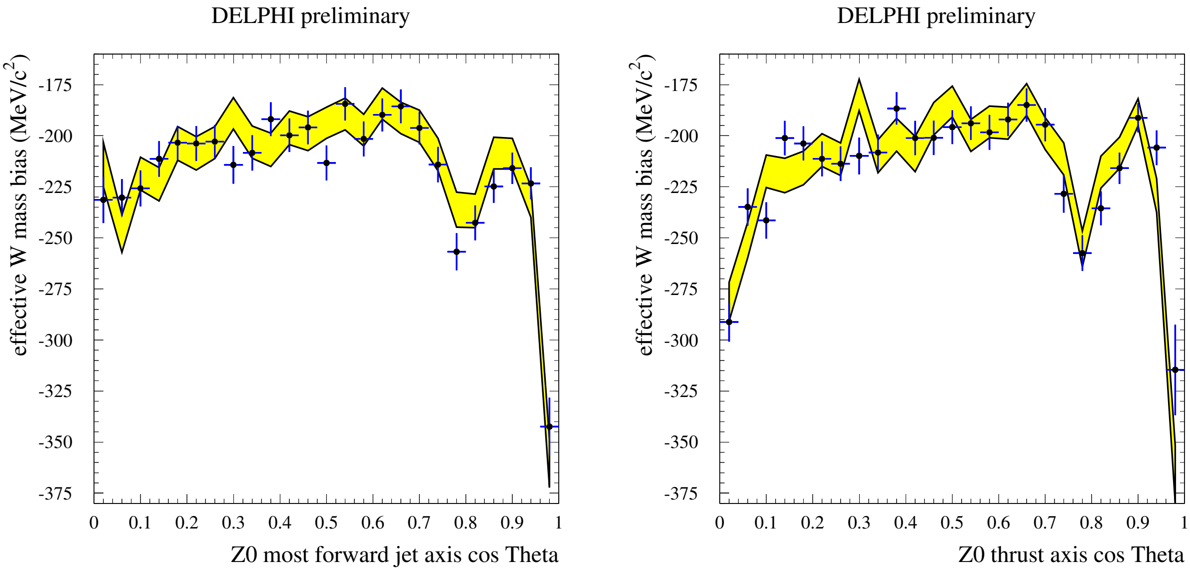

Figure A.8: Effective W mass bias as a function of the polar angle with the beam, for 1997 simulation (light shaded error band) and data (points with error bars).

Hence one can use the relation

$$b^i_{\mathrm{rec}} = \frac{\langle b_{\mathrm{Z}}\rangle^i + \langle b_{\mathrm{Z}}\rangle}{2} \tag{A.9}$$

to define an individual boson bias $\langle b_{\mathrm{Z}}\rangle^i$ in terms of measurable quantities:

$$\langle b_{\mathrm{Z}}\rangle^i = 2b^i_{\mathrm{rec}} - b_{\mathrm{rec}} \tag{A.10}$$

where b_{rec} ((A.2)) is the overall MLBZ reconstruction bias and b^i_{rec} the reconstruction bias obtained when mixing only Z^0 events with a certain property i with all other Z^0 events (including the ones with property i). $\langle b_{\mathrm{Z}}\rangle^i$ should be interpreted as the average individual boson bias of all Z^0 events in bin i, while $\langle b_{\mathrm{Z}}\rangle$ is the average of this bias over all bins and has to be equal to b_{rec} by definition.

In figures A.8 to A.10 $\langle b_{\mathrm{Z}}\rangle^i$ is plotted as a function of individual Z^0 event variables. In all cases the bias has been rescaled to the W mass scale as in equation ((A.1)) and is denoted as 'effective W mass bias'.

In figure A.8 the bias is shown as a function of the cosine of the polar angle with the beam. It is clearly visible that the reconstruction of jets in the forward region ($|\cos(\theta)| > .7$) is worse than in the barrel region, corresponding to a larger negative bias. The large negative bias for the most central bin ($|\cos(\theta)|$ close to 0) was unexpected and has not yet been understood. It is comforting, however, that all features in the data are described very well by the MC simulation, taking into account many effects of alignment, energy calibration, acceptance and detection efficiencies for all particle types integrated over the whole momentum range.

The reconstruction of jets is not only hampered by detector effects, but also by the broadening of jets due to soft and hard gluon radiation. Broader jets will be detected with larger uncertainties on the jet direction and therefore cause larger negative shifts on the mass. In addition broader jets will cause more confusion in the jet clustering effectively leading to a further deterioration of the jet reconstruction. As shown in figure A.9 the reconstruction bias depends very strongly on the Z^0 event thrust and particle multiplicity. The negative bias increases with almost 20 MeV/c^2 per extra particle. There is a positive correlation between the amount of gluon radiation and the number of particles, giving broader jets (i.e. a lower thrust value) for larger multiplicities. Again the behaviour of the data is excellently described by the simulation, except for a significant discrepancy for very low thrust events which however corresponds to an overall shift in the W mass of only 2 MeV/c^2.

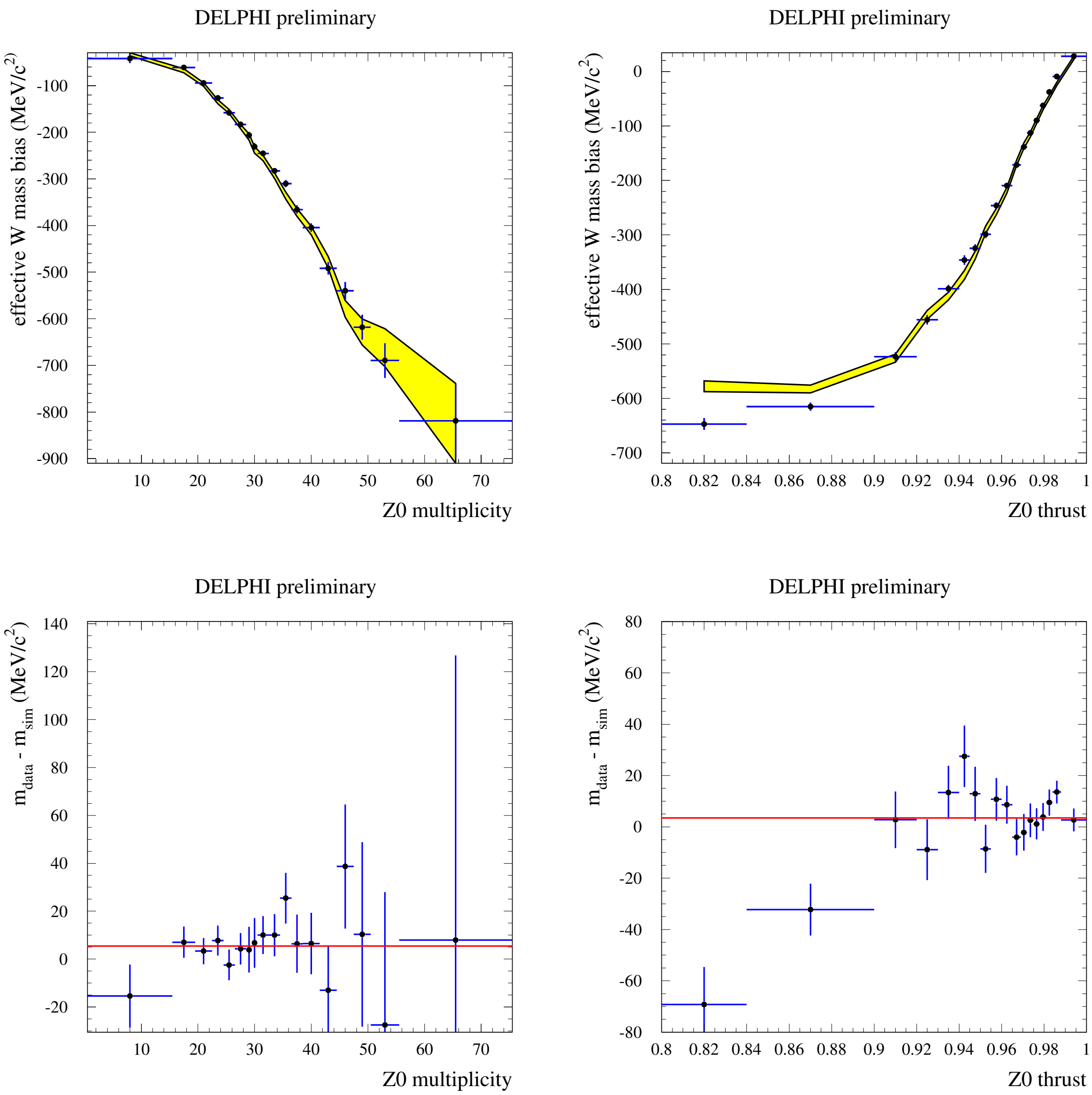

Figure A.9: Effective W mass bias as a function of the multiplicity (charged + neutral) and the thrust of the Z^0 event, for 1997 simulation (light shaded error band) and data (points with error bars).

Another important variable is the DELPHI combined b-tag variable that will prove to be useful in studying light-quark jets and heavy-quark jets separately. Again the dependence visible in the data is followed nicely by the simulated event bias (see figure A.10). Extended study revealed that the dependence of $\langle b_{\mathrm{Z}}\rangle^i$ on the b-tag should not be ascribed to the true b-quark content, but rather to indirect correlations through the strong dependence on average multiplicity and thrust. When the expected bias is calculated from the average multiplicity of all the events in the corresponding b-tag bin using the dependence shown in figure A.9, the main features of the shape of the curve are reproduced well in all bins except for the lowest and the highest b-tag bins, where the higher value of $\langle b_{\mathrm{Z}}\rangle^i$ is correlated with the lower than average fraction of low-thrust Z^0 events.

A.3.3 Comparison between data and Monte Carlo

As was shown in this section, the behaviour of the individual boson mass reconstruction bias $\langle b_{\mathrm{Z}}\rangle^i$ ((A.10)) in MLBZ events has been understood qualitatively, and is quantitatively described by the simulation to excellent precision.

Relevant for the final systematic error on the W mass is the average difference in reconstruction bias between data and MC simulation. Combining all analysed 1997 MLBZ data the overall difference $b_{\mathrm{rec}}^{\mathrm{data}} - b_{\mathrm{rec}}^{\mathrm{sim}} = \Delta m_{\mathrm{W}}^{\mathrm{MLBZ}}$ is equal to :

$$\Delta m_{\mathrm{W}}^{\mathrm{MLBZ}} = \left(m_{\mathrm{MLBZ}}^{\mathrm{data}} - m_{\mathrm{MLBZ}}^{\mathrm{sim}}\right) \cdot \frac{m_{\mathrm{W}}}{m_{\mathrm{Z}^0}} = -1.9 \pm 2.6\ \ \mathrm{MeV/c^2} \tag{A.11}$$

This value has been scaled to the W mass scale as in equation ((A.1)).

As W bosons hardly ever decay into b quarks, it is interesting to determine $\Delta m_{\mathrm{W}}^{\mathrm{MLBZ}}|_{\mathrm{b}}$ for b-quark jets and $\Delta m_{\mathrm{W}}^{\mathrm{MLBZ}}|_{\mathrm{udsc}}$ for light-quark (u,d,s,c) jets separately. The following model, based on a linear dependence on the b-quark purity P_{b} was used:

$$\Delta m_{\mathrm{W}}^{\mathrm{MLBZ}}(P_{\mathrm{b}}) = P_{\mathrm{b}} \cdot \Delta m_{\mathrm{W}}^{\mathrm{MLBZ}}|_{\mathrm{b}} + (1 - P_{\mathrm{b}}) \cdot \Delta m_{\mathrm{W}}^{\mathrm{MLBZ}}|_{\mathrm{udsc}} \tag{A.12}$$

The dependence of P_{b} as a function of b-tag as known from MC simulation was used to fit this model to the difference between data and simulation of b_{rec} as a function of the b-tag (see figure A.10) giving the following values for the heavy-quark and light-quark systematic MLBZ shifts:

$$\Delta m_{\mathrm{W}}^{\mathrm{MLBZ}}|_{\mathrm{b}} = -5.7 \pm 5.7\ \ \mathrm{MeV/c^2} \tag{A.13}$$

and

$$\Delta m_{\mathrm{W}}^{\mathrm{MLBZ}}|_{\mathrm{udsc}} = -0.3 \pm 2.8\ \ \mathrm{MeV/c^2} \tag{A.14}$$

The latter number is to be used as 'best MLBZ estimate' of the systematic bias on the W mass, even though the difference in systematic bias between light-quark and heavy-quark jets is not statistically significant.

A.4 Coverage and possible limitations

This section will start with some comments on the coverage of the MLBZ method as presented in table A.2, then concentrate on possible limitations and finally propose a scheme for a complete treatment of the systematic errors.

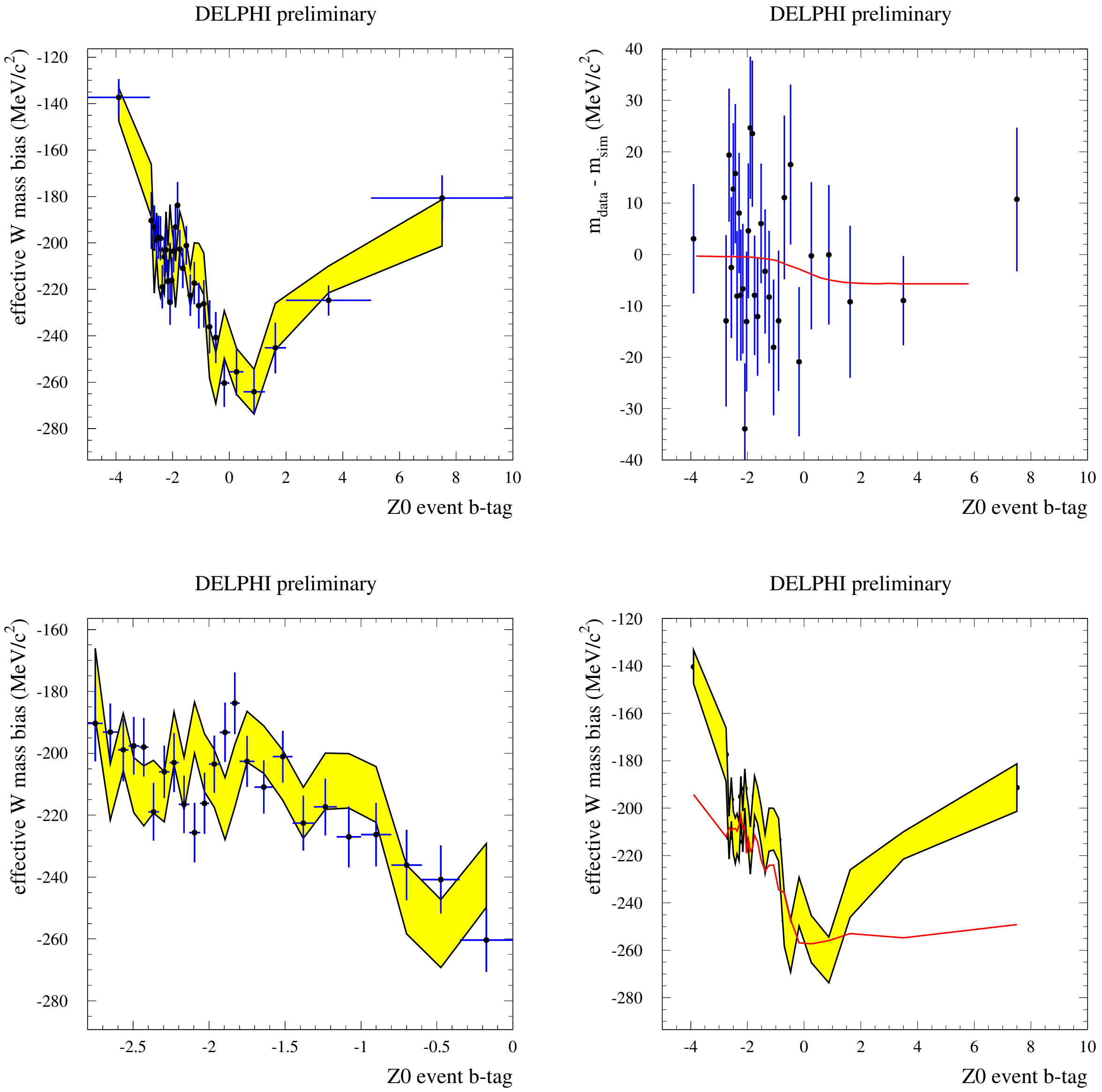

Figure A.10: Effective W mass bias as a function of the b-tag variable, for 1997 simulation (light shaded error band) and data (points with error bars) on the left, the difference between simulation and data (top right), and the expectation from the average multiplicity in each bin superimposed on the MC result (bottom right). The bottom left plot zooms in on central part of the top left plot.

A.4.1 Coverage of the MLBZ method

As listed in table A.2 the MLBZ technique is expected to give relevant information about the modelling of jet fragmentation and detection. The method constitutes a stringent test on many aspects of the simulation of jets that may influence the W physics measurement. The basic idea is that imperfections in the WW simulation that bias our measurement will also be present in the Z^0 simulation and thus give a measurable difference between MLBZ data and Monte Carlo.

Fragmentation effects covered	'fully'	partly	not at all
Hard gluon radiation	X		
Soft gluon radiation	X		
Fragmentation functions	X		
(+ detector response)			
2-particle correlations inside W's/Z^0's	X		
(+ detector response)			
FSI between W's/Z^0's			X
Detector effects covered	**'fully'**	**partly**	**not at all**
Jet energy scale at 45 GeV	X		
Jet energy versus (θ,ϕ)		X	
Jet energy non-linearity			
below 45 GeV		X	
above 45 GeV			X
Jet direction syst. bias			
asymmetric		X	
back-to-back symmetric			X
Track density		X	
Most other effects		X	

Table A.2: Summary of systematic effects covered by the MLBZ method.

As long as the emulation of the WW event topologies is reasonable, with a realistic coverage of phase space, this difference is believed to represent the actual systematic error to first order, automatically including

- practically all fragmentation effects with their internal correlations and the bulk of 'known' detector systematics
- and possible 'unknown' additional systematic effects that are not covered by traditional error estimates and would otherwise have escaped attention.

The advantage of such an 'inclusive' approach is that with one well-defined measurement the combined systematic effect is determined with excellent precision. In addition to this inclusive measurement different contributions to the systematic error can be studied as a function of relevant event variables (as discussed in section A.3.2), providing a highly sensitive test to disentangle more exclusive effects. This is important to

- improve our understanding of the different contributions that play a role
- to spot hypothetical large systematic discrepancies that accidentally cancel in the inclusive measurement but could render the result unstable for imperfections in the WW emulation by MLBZ events.

Systematic effects that are obviously NOT covered include the LEP beam energy calibration, the description of the ISR spectrum in WW events, Final State Interference (FSI) effects between particles from different W bosons and the description of background from non-WW physics processes. Those effects have to be taken into account separately.

A.4.2 Limitations

The MLBZ events contain the full information of any systematic bias in the description of the fragmentation, thanks to the fact that practically all processes involved are Lorentz invariant.

This is less true for the detector response for which, however, the main features are still expected to be the same in MLBZ and W^+W^- events except for higher order (non-linear) corrections.

To estimate how much a certain imperfection in the MLBZ description might affect the MLBZ measurement we will use the following approach: if there is a systematic deficiency in the detector description it will turn up in an (independent) data/MC comparison when this effect is larger than x_{local}. For effects smaller than x_{local} we have to rely on the MLBZ correction, so it has to be investigated to what precision $p\%$ of the effect the linear model is precise on the range up to $x = x_{\mathrm{local}}$. This will then give a maximal possible contribution of $y = p \cdot x_{\mathrm{sum}}$ MeV/c^2 to the W mass, where x_{sum} is the linear sum of the local deficiencies x_{local}, again known from independent study. The x, p and y have to be determined for the individual problems.

Detector-related limitations:

- *Back-to-back detector holes*
  The Z^0 events are produced back-to-back unlike the jets from W pair production. This could lead to correlations in MLBZ events not present in WW decays. This effect was studied by applying possible deteriorations to the simulation of the Z^0 events before and after they have been mixed and Lorentz boosted. We have put a hole in $|\cos(\theta)|$ varying the hole from 0.795-0.800 (realistic) to 0.700-0.800 (unrealistic). Applying the hole before Lorentz boosting corresponds to a discrepancy in the description of the detector during the Z^0 data taking, while applying the hole after Lorentz boosting corresponds to the effect of this additional hole on the kinematical reconstruction of WW events. As shown in figure A.11 the estimated systematic shift agrees better than $p = 15\%$ up to an additional artificial hole of 0.02 in cosθ for the two cases. The overall acceptance of DELPHI is known from independent studies to an accuracy of $x_{\mathrm{sum}} = 0.01$ (conservative), giving a maximal effect of these correlations of the order of $y = 0.9$ MeV/c^2.

- Another consequence of the back-to-back topology of the Z^0 events is that the MLBZ result is highly insensitive to certain systematic biases in the reconstruction of the jet direction only rotating the thrust axis direction (e.g. always 1 degree away from the beampipe). This kind of biases on the direction of the jets has to be investigated separately.

- *Track density and detector occupancy*
  The tracking efficiency depends on the track density. This effect is covered by MLBZ events, but only for particles originating from the same vector boson. It was seen by analysing the bias as a function of the thrust of the individual Z^0 events used in the MLBZ events (see previous chapter) that the bias depends highly on this quantity since events with gluon radiation have a low thrust value and give a much larger negative bias than events where the jets are slim. This was shown to be correctly described by the simulation. To

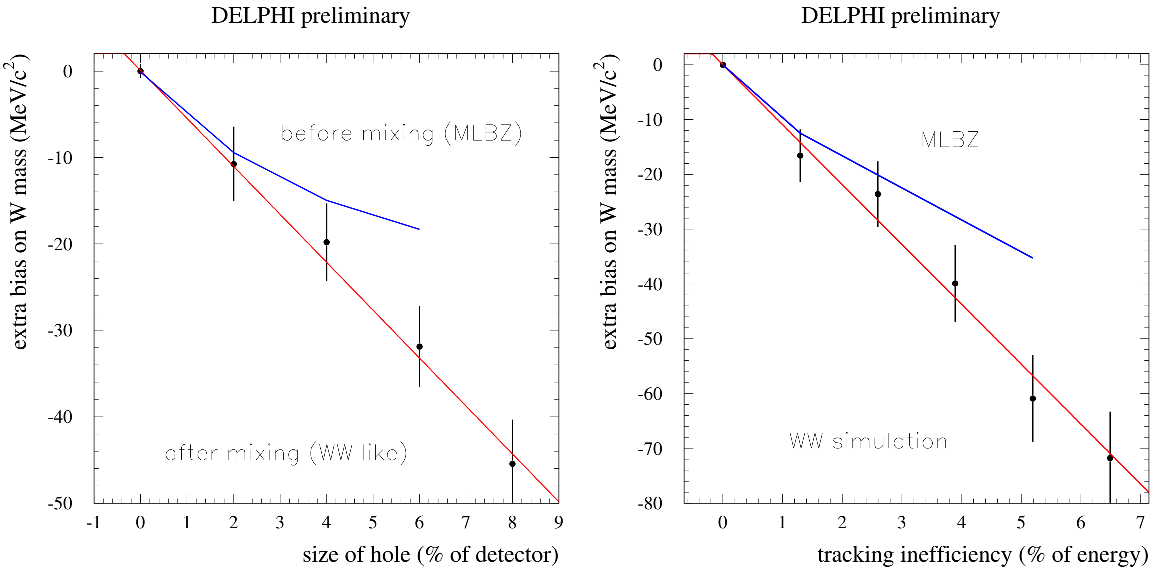

Figure A.11: The left plot shows the effect of an additional back-to-back symmetric hole in the detector, applying the hole before and after Lorentz boosting. The right plot compares the extra bias induced in MLBZ events and WW events from standard simulation introducing an additional track-density dependent tracking inefficiency.

study the effect of increased particle density for a 4-jet event with boosted jets, an additional particle inefficiency was artificially introduced as a function of the track density. This was studied on 1998 Z^0 simulation. Tracks that are close to each other were discarded according to a Gaussian with width of 5 mrad in $R\phi$, leading to a total loss of particles up to 7%. This change is applied both in MLBZ events before boosting, and in fully simulated WW events as shown in figure A.13. A linearity agreement of $p \approx 20\%$ can be derived, giving a maximum additional systematic of $y = 2.4$ MeV/c^2 for a track density discrepancy of $x_{\mathrm{sum}} = 1.0\%$ (conservative).

- The energy spectrum of jets in $\mathrm{W}^+\mathrm{W}^-$ events is quite different from Z^0 decays. Any non-linearity in the energy response could become a systematic error in m_{W}. This effect is partly covered for jet energies below 45 GeV in 3-jet (low-thrust) Z^0 events but not at all for jet energies above 45 GeV. This requires separate study.

- The distribution and correlation of jet directions are not completely identical. As a cross-check the bias was estimated as a function of the polar angle of the Z^0 thrust (see section A.3.2) with excellent agreement between simulation and data.

- A final detector-related point is the time dependency of the bias. By definition the data used for the MLBZ measurement is taken during the Z^0 calibration runs outside the high energy data taking periods. Therefore the conclusions about detector performance and description have to be extrapolated and/or interpolated in time. In 1997 on-pole Z^0 events were only recorded at the start of data taking while in 1998 Z^0 data were taken both at the beginning

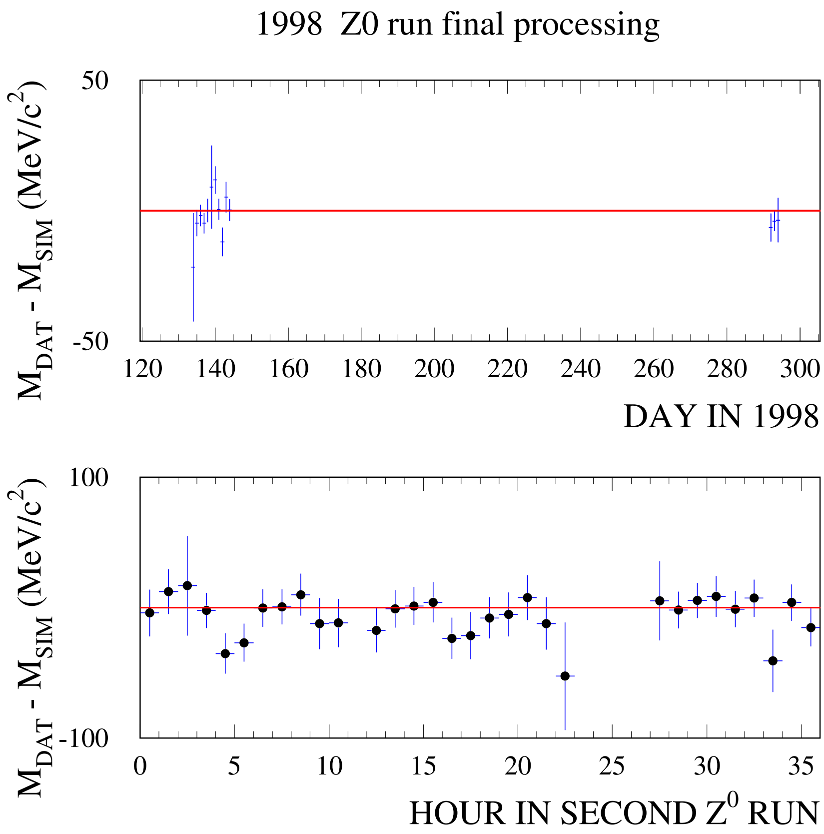

Figure A.12: Experimental stability of the systematic difference in W mass bias between data and simulation for 1998 Z^0 data.

and towards the end of the year. In order to illustrate both the short term and the long term stability 1998 data was analysed and the MLBZ mass plotted as a function of time in figure A.12. The measured overall mass differences between data and Monte Carlo are listed in table A.3. From these numbers and the fact that the stability plot in figure A.12 is compatible with a fully stable detector, a preliminary estimate for this effect is 5 MeV/c^2. By studying the detector stability over the years taking into account also the calibration

Z^0 data taking period	$\Delta m_{\mathrm{W}}^{\mathrm{MLBZ}}\|_{\mathrm{udsc}}$ (MeV/c^2)
1997	-0.3 $\pm$ 2.8
1998 P1	-1.0 $\pm$ 1.5
1998 P2	-4.7 $\pm$ 2.9

Table A.3: Measured systematic mass difference between data and Monte Carlo simulation for the different Z^0 data taking periods in 1997 and 1998.

data of 1999 and with additional studies (e.g. using Z^0s from radiative returns during the high energy data taking) one can probably draw more firm conclusions.

Fragmentation-related limitations:

- The flavour composition is different in Z^0 and W decays. A non-perfect simulation of the b decays would then lead to wrong estimation of the bias. As a function of the event b-tag variable the simulation describes the data perfectly and an upper bound of 1 MeV/c^2 is estimated.

- The fragmentation of Z^0 events happens at a scale 13% larger than W^+W^- decays. This has negligible impact on the bias since the simulation is adequately able to describe this energy evolution.

- When boosting the particles in the MLBZ procedure the particle masses are not precisely known. The approximation used (no mass for neutral particles, pion mass for charged particles) was compared to the all-photons and all-kaons hypothesis, giving a maximal effect of xx MeV on the W mass.

General limitations:

- *No-width approximation (reducible)*
  The MLBZ events produced in the analysis reported here have no width of the boson masses. This is a 'reducible' limitation, as it can be solved by using a more complete algorithm (see section A.5.2). By using only simulated WW decays where the two masses are within 2 GeV$/c^2$ of $m_{\rm W}$, it was verified that the bias from undescribed (tracking) inefficiencies of the detector was the same for WW event samples with the nominal W width and samples with the low width within the statistical error (see figure A.13). With a precision p equal to 15% over a large range, this approximation leads to an estimated systematic error of 1.8 MeV/c^2 for a conservative $x_{\rm sum} = 1.0\%$.

- *No-ISR approximation (reducible)*
  Unlike WW events MLBZ events contain hardly any ISR. Like the previous point this problem can be solved using the algorithm described in section A.5.2. It was verified that WW events without ISR responded in the same manner as the full sample to additional tracking inefficiencies, requiring a generated effective centre-of-mass energy less than 0.5 GeV away from 2 times the LEP beam energy. As shown in figure A.13 the deviation y for a discrepancy $x_{\rm sum} = 1.0\%$ and a precision $p = 20\%$ is again of the order of 2 MeV/c^2.

- The true LEP beam energy during Z^0 data taking is not exactly the same in simulation as in data. The only way this difference enters in the MLBZ measurement is through the measured Z^0 energy. As the energy uncertainty (10-20%) is very large compared to the fluctuations and the calibration uncertainty on the beam energy, this influence is hardly significant. By varying the assumed LEP beam energy ($E_{b{\rm Z}^0}$) in the MLBZ analysis we have found that this effect amounts to 0.5 $\pm$ 0.2 MeV/c^2 using a conservative uncertainty of 100 MeV on the average LEP beam energy during the Z^0 calibration runs.

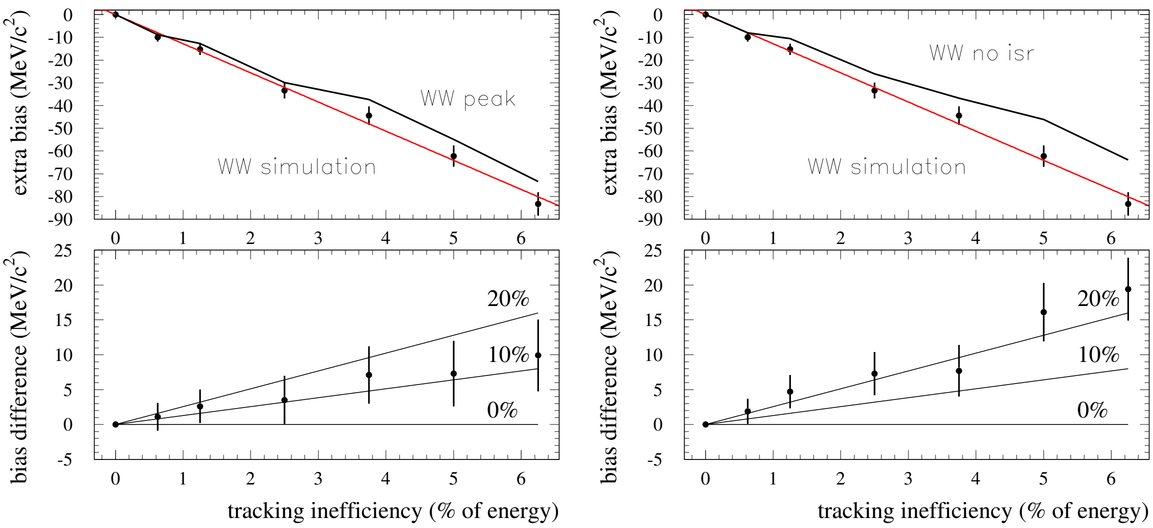

Figure A.13: The effect of an additional track-density dependent tracking inefficiency is shown for WW events from standard simulation compared to WW events with both generated masses less than 2 GeV/c^2 away from m_{W}(left) and events without ISR radiation (right). The different points are highly correlated within each plot.

A.4.3 Towards a complete estimate of the systematic error

From this study and other studies that are ongoing at the moment it can be concluded that the MLBZ method *can* be used to measure the combined systematic error from jet fragmentation and detector description, provided that the following additional effects are taken into account separately:

- non-linearity in jet energy response
- systematic bias in the jet directions
- stability in time

It is recommended to use the full 4-fermion MLBZ emulation (see section A.5.2) if CPU time allows that. Otherwise the effect of neglecting ISR and the W decay width have to be re-investigated for other analyses. When there is reason to believe that another detector or analysis will have a significantly different response to the back-to-back correlations present in Z^0 events, the cross-checks as presented in this paper have to be repeated.

A.5 Outlook

A.5.1 Semileptonic channel

MLBZs can also be applied to the semileptonic channel [6]. There the jets can be taken from hadronic Z^0 events, while the lepton can either be constructed by taking half a leptonic Z^0, or can be generated artificially, as the only information in the lepton is its energy and direction. By using artificially generated leptons one can statistically optimise the study of the systematics of the hadronic part, and later fold in the knowledge of the full energy and momentum spectrum of the lepton.

For the semileptonic channel systematic shifts from the reconstruction of the hadronic part of the event are expected to be larger than in the fully hadronic channel, because mass shifts are less strictly controlled by the constraints in the constrained fit. The final statistical sensitivity should be of the same order of magnitude, as it depends purely on the number of hadronic Z^0 events available and the resolution of the boost in the Z^0 events.

A.5.2 Improved emulation

The method described in this paper can be extended in order to improve the emulation of WW events. In DELPHI an algorithm is being developed (by Chris Parkes [11]) in which the Z^0 events can be rotated, rescaled and boosted reproducing the 4-fermions taken from WW simulation, thus including the effects of Initial State Radiation, a Breit-Wigner with the correct Γ_W, helicity structure and proper energy scale in the MLBZ topology [7]. This will emulate WW events closer to the truth, thus further improving the reliability of the measured systematic shift. The only drawback is that more mixings and boosts will be needed to obtain the same statistical precision because of the Breit-Wigner mass distribution and ISR.

The greatest virtue of such an improved emulation is that it will allow the use of analyses that are not easily scalable with energy, are sensitive to the helicity structure (TGC analyses) or e.g. contain neural networks that have been trained with WW simulation.

This was not needed for the DELPHI analysis used in this paper as it has a very simple cut based selection and kinematic fits that are very well scalable with energy.

A.6 Conclusion

A new technique to measure systematic errors from jet reconstruction in W physics measurements at LEP2 has been presented: the MLBZ method. A full description of the method itself and the procedure to determine the statistical precision has been given.

Some results relating to the W mass measurement on 1997 DELPHI data in the fully hadronic channel were shown and discussed. They give a consistent picture and show that the combined systematic error on jet fragmentation and a large fraction of detector effects in the fully hadronic channel is around 5 MeV/c^2, which is a factor 4 smaller than so far quoted by DELPHI [3] for

[6] The method can also be of use for other 4 fermion final states like ZZ or HZ.

[7] The package already includes the possibility to emulate ZZ and semileptonic WW final states.

fragmentation only (20 MeV/c^2). For a precise estimate of the jet energy response error more work is needed, as outlined in this paper.

The coverage and limitations of the MLBZ method were discussed, leading to the conclusion that it can be used for a complete estimate of the systematic error due to jet reconstruction effects, provided the method is complemented with separate studies of non-linearity in the jet response, back-to-back symmetric systematic biases in reconstructed jet directions, and a sound estimate of time stability of the detector.

One of the main worries, being the back-to-back correlation of Z^0 event topologies with the detector symmetry, was shown to have a negligible influence for realistic uncertainties on the DELPHI detector simulation.

Thus the method seems to be a very promising candidate to replace a number of existing methods thanks to its better precision, greater coverage and ease of use and definition.

Our understanding of the MLBZ method and its merits is rapidly improving, and will certainly benefit when it is further tested, used and improved in other analyses, including W physics analyses other than the W mass measurements. In particular it would be interesting to compare results obtained for different LEP experiments.

A.7 The Jackknife method

The statistical errors on the measured MLBZ masses were estimated using the 'Jackknife' resampling method [7, 8, 9, 10]. It is a non-parametric statistical method, i.e. a technique that can be used to estimate a statistical quantity without assuming knowledge about the underlying probability distribution. These methods have become more and more popular with the advance of modern computers. A well-known example of a rather advanced (and CPU time consuming) non-parametric technique is the Monte Carlo technique.

The Jackknife is a method for estimating the bias and standard error of an estimate. Here we are interested in the standard error. For a sample $\mathbf{x} = (x_1, x_2, ...x_n)$ and an estimator $\hat{\theta} = f(\mathbf{x})$, the method focuses on samples that *leave out one observation at a time*:

$$\mathbf{x}_{(i)} = (x_1, x_2, ..., x_{i-1}, x_{i+1}, ..., x_n)$$

for $i = 1, 2, ..., n$. These samples are called Jackknife samples. The ith Jackknife sample consists of the data set where the ith observation is removed. Now $\hat{\theta}_{(i)} = f(\mathbf{x}_{(i)})$, is called the ith Jackknife replication of θ, with a replication average

$$\hat{\theta}_{(\cdot)} = \sum_{i=1,n} \hat{\theta}_{(i)}/n$$

The Jackknife estimate of the standard error on $\hat{\theta}$ is then defined as

$$\hat{s}_{Jack} = \sqrt{\frac{n-1}{n} \sum_{i=1,n} (\hat{\theta}_{(i)} - \hat{\theta}_{(\cdot)})^2} \tag{A.15}$$

and is known to be a reliable estimator of the standard deviation provided that the distribution of $\hat{\theta}_{(i)}$ is smooth (in our case it turns out to be a Gaussian distribution). For non-smooth statistics, other methods like the Bootstrap [9, 10] can be used. In the central limit theorem the Jackknife error is shown to be equal to the Minimum Variance Bound for uncorrelated measurements.

The main building block for the technical implementation of the Jackknife method in the MLBZ analysis is the summed log-likelihood curve

$$\mathrm{L}^{\mathrm{mlbz}}_{j,k}(m_{\mathrm{W}}) = \sum_{m=1,n_{\mathrm{boost}}} \mathrm{L}^{\mathrm{mlbz}}_{j,k,m}(m_{\mathrm{W}})$$

where

$$\mathrm{L}^{\mathrm{mlbz}}_{j,k,m}(m_{\mathrm{W}}) = -2 \cdot \log(\mathcal{L}^{\mathrm{mlbz}}_{j,k,m}(m_{\mathrm{W}}))$$

with the event likelihood curve $\mathcal{L}^{\mathrm{mlbz}}_{j,k,m}(m_{\mathrm{W}})$ calculated for the MLBZ event consisting of Z^0 event no. j mixed with Z^0 event no. k using random boost no. m. In order to reduce the number of possible combinations to a managable level the data is divided in independent samples of $n = 201$ Z^0 events, and each event is mixed and Lorentz boosted $n_{\mathrm{boost}} = 2$ times with all other events from the same sample.

Taking the sum over all MLBZ events that contain event j, one obtains the Z^0 event likelihood curve

$$\mathrm{L}^{\mathrm{Z}^0}_{j}(m_{\mathrm{W}}) = \sum_{k=1,j-1} \mathrm{L}^{\mathrm{mlbz}}_{k,j}(m_{\mathrm{W}}) + \sum_{k=j+1,n} \mathrm{L}^{\mathrm{mlbz}}_{j,k}(m_{\mathrm{W}})$$

and combining all MLBZ events from the whole samples gives the overall sample likelihood curve

$$\mathrm{L}^{\mathrm{sample}}(m_{\mathrm{W}}) = \sum_{j=1,n} \sum_{k=j+1,n} \mathrm{L}^{\mathrm{mlbz}}_{j,k}(m_{\mathrm{W}}) = \sum_{j=1,n} \mathrm{L}^{\mathrm{Z}^0}_{j}(m_{\mathrm{W}}) \cdot \frac{1}{2}$$

For each sample the mass can be extracted by finding the minimum of the overall sample likelihood curve.

To calculate for each sample the Jackknife estimate of the statistical error on the fitted mass m_{fit}, we need the Jackknife replications $m_{\mathrm{fit(i)}}$ obtained by minimising $\mathrm{L}^{\mathrm{sample}}(m_{\mathrm{W}})_{(i)}$ given by

$$\mathrm{L}^{\mathrm{sample}}(m_{\mathrm{W}})_{(i)} = \mathrm{L}^{\mathrm{sample}}(m_{\mathrm{W}}) - \mathrm{L}^{\mathrm{Z}^0}_{i}(m_{\mathrm{W}})$$

thus totally removing event no. i from the sample.

As the shape of the summed log-likelihood curve $\mathrm{L}^{\mathrm{sample}}(m_{\mathrm{W}})$ around the minimum is very close to a parabola, the influence of event i on the fitted mass $m_{\mathrm{fit(i)}} - m_{\mathrm{fit}}$ can be approximated by

$$\Delta_i = \left. \frac{\frac{\delta \mathrm{L}^{\mathrm{Z}^0}_{i}(m_W)}{\delta m_{\mathrm{W}}}}{\frac{\delta^2 \mathrm{L}^{\mathrm{sample}}(m_W)}{\delta m_W^2}} \right|_{m_W = m_{\mathrm{fit}}} = \left. \frac{\delta \mathrm{L}^{\mathrm{Z}^0}_{i}(m_W)}{\delta m_{\mathrm{W}}} \right|_{m_W = m_{\mathrm{fit}}} \cdot \frac{1}{2} \sigma^2_{m_{\mathrm{fit}}} \tag{A.16}$$

where $\sigma_{m_{\mathrm{fit}}}$ is the standard likelihood error on the fitted sample mass. The average Jackknife replication $m_{\mathrm{fit}(\cdot)}$ is then given by

$$m_{\mathrm{fit}(\cdot)} = \sum_{i=1,n} m_{\mathrm{fit(i)}}/n = m_{\mathrm{fit}} + \left. \frac{\sum_{i=1,n} \frac{\delta \mathrm{L}^{\mathrm{Z}^0}_{i}(m_W)}{\delta m_W}}{n \cdot \frac{\delta^2 \mathrm{L}^{\mathrm{sample}}}{\delta m_W^2}} \right|_{m_W = m_{\mathrm{fit}}} = m_{\mathrm{fit}}$$

as

$$\sum_{i=1,n} \mathrm{L}^{\mathrm{Z}^0}_{i}(m_W) = 2 \cdot \mathrm{L}^{\mathrm{sample}}(m_W)$$

giving

$$\sum_{i=1,n} \left. \frac{\delta \mathrm{L}^{\mathrm{Z}^0}_{i}(m_W)}{\delta m_W} \right|_{m_W = m_{\mathrm{fit}}} = 2 \cdot \left. \frac{\delta \mathrm{L}^{\mathrm{sample}}(m_W)}{\delta m_W} \right|_{m_W = m_{\mathrm{fit}}} = 0$$

by definition. This means that we can substitute the *Jackknife influence value* $\hat{\theta}_{(i)} - \hat{\theta}_{(\cdot)}$ in equation (A.15) by Δ_i and use the following very simple formula

$$\sigma_{\mathrm{MLBZ}} = \sqrt{\sum_{i=1,n} \Delta_i^2} = \sqrt{\frac{n}{n-1}} \cdot \hat{s}_{\mathrm{Jack}}$$

as an excellent approximation of the Jackknife estimate (A.15) of the standard error on the fitted MLBZ mass for reasonably large values of n.

The same procedure applied to the whole data set of n_{samp} independent samples l used should give consistent results:

$$\sigma^{\mathrm{MLBZ}}_{all} = \sqrt{\sum_{l=1,n_{\mathrm{samp}}} \sum_{i=1,n} \Delta^2_{i,l}} \approx \frac{\langle \sigma^{\mathrm{MLBZ}}_{l} \rangle}{\sqrt{n_{\mathrm{samp}}}}$$

where $\Delta_{i,l}$ is calculated according to equation (A.16) replacing the sample error $\sigma_{m_{\rm fit}}$ by the overall likelihood error on the fitted mass when combining all samples.

In table A.1 a comparison of the different error estimates is given. It shows that for the number of events used the Jackknife method estimates the statistical error correctly to within 10%.

A.8 Linearity

Similarly to the Z^0 event influence Δ_i ((A.16)) one can define the MLBZ event influence Δ_{ij} as the change in the fitted sample mass when removing the MLBZ events containing the mixed pair of Z^0 events i and j:

$$\Delta_{ij} = \left.\frac{\delta \mathrm{L}_{i,j}^{mlbz}(m_W)}{\delta m_{\rm W}}\right|_{m_W = m_{\rm fit}} \cdot \frac{1}{2}\sigma^2_{m_{\rm fit}} \tag{A.17}$$

In figure A.14 the average Δ_{ij} is plotted as a function of the sum of the individual boson influences Δ_i and Δ_j of the constituent Z^0 events. The dependence is quite linear over the whole range, which means that linearity is conserved during the whole procedure of mixing and boosting the bosons, jet clustering, applying a constrained fit for each jet pairing and extracting the mass.

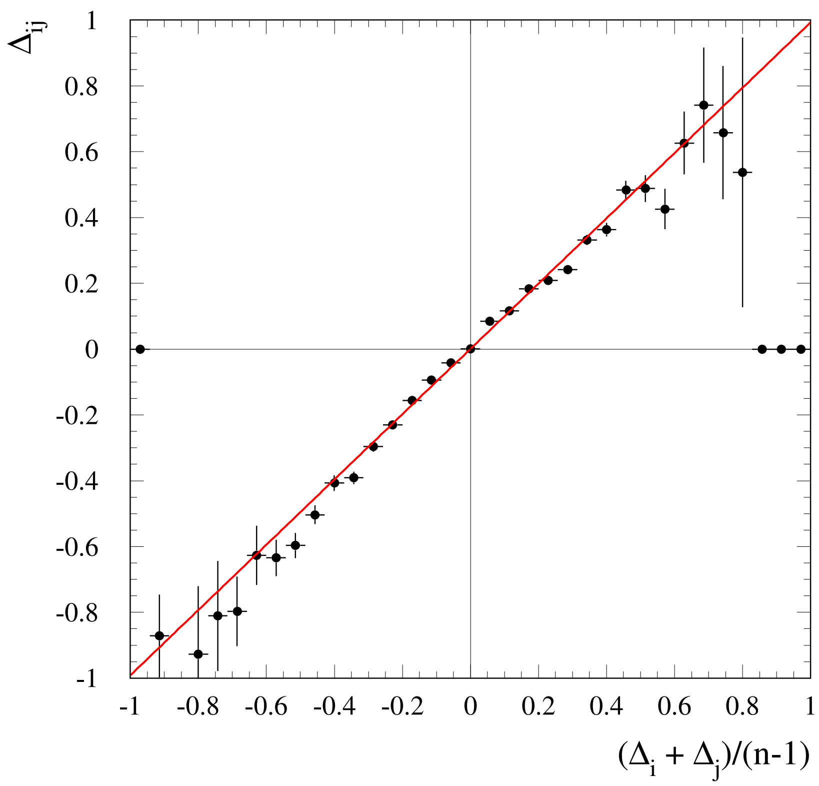

Figure A.14: The average MLBZ event influence as a function of the sum of the individual Z^0 event influences, in units of $\frac{1}{2}\sigma^2_{m_{\rm fit}}$.

MLBZ references

[1] LEP EW working group note, LEPEWWG/WW/99-01, revised 15/04/99.

[2] ALEPH Collaboration, Phys. Lett. **B453**(1999) 121.

[3] DELPHI Collaboration, Phys. Lett. **B462**(1999) 410.

[4] L3 Collaboration, Phys. Lett. **B454**(1999) 386.

[5] OPAL Collaboration, Phys. Lett. **B453**(1999) 138.

[6] DELPHI Collaboration, Eur. Phys. J. **C2**(1998) 581.

[7] B. Efron, Computers and the Theory of Statistics, SIAM Rev. **21**(1979) 460.

[8] P. Diaconis and B. Efron, "Computer-Intensive Methods in Statistics", Scientific American **248:5**(1983), 96.

[9] B. Efron, R.J. Tibshirani, "An Introduction to the Bootstrap", Chapman & Hall 1993. ISBN 0-412-04231-2

[10] A.C. Davison, D.V. Hinkley, "Bootstrap Methods and Their Application", Cambridge University Press, 1997. Hardback ISBN 0-521-57391-2 Paperback ISBN 0-521-57471-4

[11] A manual of the program can be found at `file://afs/cern.ch/delphi/tasks/wphysics/mlbz/mlbz_manual/mlbz_manual.html`, and more information can be obtained from Chris Parkes (Chris.Parkes@cern.ch).

Acknowledgements

We would like to thank Ahmimed Ouraou, Chris Parkes, Ivo van Vulpen, Jan Timmermans, Louis Lyons and Peter Renton for their help and many valuable suggestions. This work would not have been possible without the data and infrastructure provided by the DELPHI collaboration.

Bibliography

[1] DELPHI Collaboration, Measurement of the W-pair cross-section and of the W mass in e^+e^- interactions at 172 GeV, Eur. Phys. J. **C2**(1998) 581

[2] DELPHI Collaboration, Measurement of the mass of the W boson using direct reconstruction at $\sqrt{s} = 183$ GeV, Phys. Lett. **B462**(1999) 410

[3] DELPHI Collaboration, Measurement of the Mass and Width of the W boson in e^+e^- Collisions at $\sqrt{s} = 189$ GeV, CERN-EP/2001-029, Accepted by Phys. Lett. B

[4] N.Kjær and M.Mulders, Mixed Lorentz Boosted Z^0s, CERN-OPEN/2001-026 (2001)

[5] P. Abreu, A. De Angelis, G. Della Ricca, D. Fassouliotis, A. Grefrath, N. Kjær, R. Henriques, M. Mulders, M. Pimenta, and L. Vitale, The Estimation of the Effective Centre of Mass Energy in $q\bar{q}\gamma$ Events from DELPHI, Nucl. Instrum. Methods **A427**(1999) 487

[6] N. Kjær and M. Mulders, The ideogram technique for LEP2 analysis, DELPHI 97-55 PHYS 705

[7] S.L. Glashow, Nucl. Phys.**22**(1961) 579;
S. Weinberg, Phys. Rev. Lett.**19**(1967) 1264;
A. Salam, Elementary Particle Theory, proceedings 8^{th} Nobel Symposium Aspenäsgården, Ed: N. Svartholm, Almquist and Wiksells, Stockholm (1968), p.367

[8] F. Englert and R. Brout, Phys. Rev. Lett.**13**(1964) 321;
P.W. Higgs, Phys. Lett.**12**(1964) 132

[9] G. 't Hooft, Renormalization of Massless Yang-Mills Fields, Nucl. Phys. **B33**(1971) 173;
G. 't Hooft, Renormalizable Lagrangians for Massive Yang-Mills Fields, Nucl. Phys. **B35**(1971) 167;
G. 't Hooft and M. Veltman, Regularization and renormalization of gauge fields, Nucl. Phys. **B44**(1972) 189

[10] The LEP collaborations, Combination procedure for the precise determination of Z boson parameters from results of the LEP experiments, CERN-EP/2000-153 (2000)

[11] Particle Data Group, Review of Particle Physics, Eur. Phys. J. **C15**(2000) 1, in particular p. 73, 95-109 and 208.

[12] T. van Ritbergen and R.G. Stuart, On the Precise Determination of the Fermi Coupling Constant from the Muon Lifetime, Phys. Rev. Lett.**82**(1999) 488

[13] P.J. Mohr and B.N. Taylor, CODATA Recommended Values of the Fundamental Physical Constants: 1998, Rev. Mod. Phys.**72**(2000) 351

[14] Gargamelle Neutrino Collaboration, Observation of neutrino-like interactions without muon or electron in the Gargamelle neutrino experiment, Phys. Lett. **B46**(1973) 138

[15] UA1 Collaboration, Phys. Lett. **B122**(1983) 103;
UA2 Collaboration, Phys. Lett. **B122**(1983) 476;
UA1 Collaboration, Phys. Lett. **B126**(1983) 398;
UA2 Collaboration, Phys. Lett. **B129**(1983) 130

[16] C. Rubbia, Experimental Observation of the Intermediate Vector Bosons W^+, W^- and Z^0, Nobel lecture, Rev. Mod. Phys.**57**(1985) 699-722

[17] D.A. Ross and M. Veltman, Neutral currents and the Higgs mechanism, Nucl. Phys. **B95**(1975) 135

[18] CDF Collaboration, A Measurement Of The W Boson Mass, Phys. Rev. Lett.**65**(1990) 2243

[19] `http://www-cdf.fnal.gov/physics/ewk/wmass_new.htm`

[20] M. Veltman, Radiative Corrections To Vector Boson Masses, Phys. Lett. **B91**(1980) 95

[21] CDF Collaboration, Observation of top quark production in anti-p p collisions, Phys. Rev. Lett.**74**(1995) 2626;
D0 Collaboration, Observation of the top quark, Phys. Rev. Lett.**74**(1995) 2632

[22] BES Collaboration, Measurements of the Cross Section for $\mathrm{e^+e^-} \to$ hadrons at Center-of-Mass Energies from 2 to 5 GeV, hep-ex/0102003;
BES Collaboration, Measurement of the total cross-section for hadronic production by $\mathrm{e^+e^-}$ annihilation at energies between 2.6 GeV - 5 GeV, Phys. Rev. Lett.**84**(2000) 594

[23] H. Burkhardt and B. Pietrzyk, Update of the hadronic contribution to the QED vacuum polarization, LAPP-EXP-2001-03 (2001)

[24] J. Erler, Calculation of the QED Coupling $\hat{\alpha}(m_\mathrm{Z})$ in the Modified Minimal-Subtraction Scheme, Phys. Rev. **D59**(1999) 54008

[25] J.D. Bjorken, hep-ph/0008048

[26] S. Jadach et al., Precision Predictions for (Un)Stable $\mathrm{W^+W^-}$ Pair Production At and Beyond LEP2 Energies, hep-ph/0007012

[27] A. Denner et al., $\mathcal{O}(\alpha)$ corrections to $\mathrm{e^+e^-} \to$WW$\to$ 4 fermions(+γ), Phys. Lett. **B475**(2000) 127

[28] F.A. Berends, R. Pittau, R. Kleiss, EXCALIBUR: A monte carlo program to evaluate all four fermion processes at LEP-200 and beyond, Comput. Phys. Commun.**85**(1995) 437

[29] G. Gounaris et al., Triple Gauge boson Couplings in 'Physics at LEP2', CERN Yellow report **96–01**(1996) p. 525-576

[30] W. Beenakker et al., WW cross-sections and distributions in 'Physics at LEP2', CERN Yellow report **96–01**(1996) p. 79-140

[31] C.J. Parkes, P.B. Renton, and H.T. Phillips, A study of four fermion final state interference relevant to the measurement of the $\mathrm{W^+W^-}$ cross-section and the W-mass, DELPHI 97-96 PHYS 718

[32] V.S. Fadin, V.A. Khoze and A.D. Martin, On $\mathrm{W^+W^-}$ production near threshold, Phys. Lett. **B311**(1993) 311

[33] F.A. Berends, R. Pittau and R. Kleiss, Initial State QED corrections to four fermion production in $\mathrm{e^+e^-}$ collisions at LEP-200 and beyond, Nucl. Phys. **B426**(1994) 344

[34] Y. Kurihara, J. Fujimoto, T. Munehisha, Y. Shimizu, Hard Photon Distributions in e^+e^- Annihilation Processes by QEDPS, Progress of Theoretical Physics Vol. **96** (1996) 1223

[35] D.R. Yennie, S.C. Frautschi and H. Suura, The infrared divergence phenomena and high-energy processes, Ann. Phys. **13**(1961) 379

[36] M.W. Grünewald et al., Four-Fermion Production in Electron-Positron Collisions, report of the LEP-2 Monte Carlo Workshop 1999/2000, hep-ph/0005309, and references therein

[37] DELPHI collaboration, Measurement of the Gluon Fragmentation Function and a Comparison of the Scaling Violation in Gluon and Quark Jets, Eur. Phys. J. **C13**(2000) 573

[38] T. Sjöstrand, PYTHIA 5.7/JETSET 7.4, CERN-TH.7112/93 (1993)

[39] L. Lönnblad, Comp. Phys. Comm. **71** (1992) 15

[40] G. Marchesini et al., Comp. Phys. Comm. **67** (1992) 465

[41] DELPHI Collaboration, Tuning and Test of Fragmentation Models Based on Identified Particles and Precision Event Shape Data, Z. Phys. **C73**(1996) 11

[42] B. Andersson and M. Ringér, Bose-Einstein correlations in the Lund model, Nucl. Phys. **B513**(1998) 627

[43] N. van Remortel on behalf of the 4 LEP collaborations, Bose-Einstein correlations in WW events at LEP, talk at Moriond 2001, Les Arcs

[44] T. Sjostrand, V. Khoze, On Color rearrangement in hadronic $\mathrm{W^+\ W^-}$ events, Z. Phys. **C62**(1994) 281;
T. Sjostrand, V. Khoze, Does the W mass reconstruction survive QCD effects?, Phys. Rev. Lett.**72**(1994) 28

[45] T. Ziegler on behalf of the 4 LEP collaborations, Color reconnection at LEP, talk at Moriond 2001, Les Arcs;
P. de Jong on behalf of the 4 LEP collaborations, Color reconnection in W decays, talk at ICHEP2000, Osaka (hep-ex/0103018)

[46] LEP Energy Working Group, Evaluation of the LEP centre-of-mass energy above the W pair production threshold, Eur. Phys. J. **C11**(1999) 573;
LEP Energy Working Group, Evaluation of the LEP centre-of-mass energy for data taken in 1998, LEP Energy working group note 99/01;
LEP Energy Working Group, Evaluation of the LEP centre-of-mass energy for data taken in 1999, LEP Energy working group note 00/01

[47] L. Arnaudon et al., The effects of terrestrial tides on the LEP beam energy, Nucl. Instrum. Methods **A357**(1995) 249

[48] ALEPH Collaboration, Determination of the LEP center-of-mass energy from $Z\gamma$ events, Phys. Lett. **B464**(1999) 339;
G. W. Morton, Preliminary determination of $\sqrt{s}$ at LEP2 using radiative dimuon events in DELPHI, DELPHI 2000-134 CONF 433, contribution to ICHEP2000, Osaka

[49] DELPHI Collaboration, The DELPHI Detector at LEP, Nucl. Instrum. Methods **A303**(1991) 233;
DELPHI Collaboration, Performance of the DELPHI Detector, Nucl. Instrum. Methods **A378**(1996) 57

[50] DELPHI Collaboration, DELPHI Data Analysis Program (DELANA) User's Guide, DELPHI 89-44 PROG 137 (1989)

[51] V. Perevozchikov and N. Smirnov, PHDST Package Description V.3 VZD — Viewer of Zebra Data for DELPHI User's Manual, DELPHI 92-118 PROG 189

[52] Tz. Spassov and N. Smirnov, SKELANA — Skeleton Analysis Program, 1995;
F. Cossutti et al., Improvements to SKELANA for Version 2.0, DELPHI 99-175 PROG 239

[53] R. Chierici, C. Parkes and A. Tonazzo, WWANA: A standard package for W analysis, DELPHI 96-128 PROG 218

[54] DELPHI Collaboration, DELPHI event generation and detector simulation - User Guide, DELPHI 89-67 PROG 142 (1989)

[55] F. Cossutti, A. Tonazzo, F. Mazzucato, REMCLU : a package for the Reconstruction of Electromagnetic CLUsters at LEP200, DELPHI 2000-164 PROG 242

[56] G.Borisov, Combined B Tagging, Nucl. Instrum. Methods **A417**(1998) 384
DELPHI Collaboration, A precise measurement of the partial decay width ratio $R_b^0 = \Gamma_{\mathrm{b\bar{b}}}/\Gamma_{\mathrm{had}}$), Eur. Phys. J. **C10**(1999) 415

[57] N. Kjær, M. Mulders, M. Witek, VINCENT — Visual interface to Energyflow in Monte Carlo events, 1997, program can be obtained from the authors

[58] M. Witek, L. Pape, F. Carena, J.C. Marin, DELGRA — DELPHI Graphics for Interactive Event Viewing program, http://delphiwww.cern.ch/ delgra/

[59] A. Duperrin, Mesure de la masse du boson W dans la désintégration à quatre quarks dans l'expérience DELPHI au LEP, thesis, Université Claude Bernard, Lyon I (1999)

[60] S. Catani, Yu.L. Dokshitzer, M. Olsson, G. Turnock, B.R. Webber, New clustering algorithm for multi - jet cross-sections in e^+e^- annihilation, Phys. Lett. **B269**(1991) 432;
N. Brown, W. Stirling, Finding Jets and summing soft gluons: A new algorithm, Z. Phys. **C53**(1992) 629

[61] Yu.L. Dokshitzer, G.D. Leder, S. Moretti and B.R. Webber, Better Jet Clustering Algorithms, JHEP **08**(1997) 001

[62] L. Lönnblad, ARCLUS: A new jet clustering algorithm inspired by the colour dipole model, Z. Phys. **C58**(1993) 471

[63] N. Kjær and M. Mulders, PUFITC+: DELPHI constrained fitting package, available from the authors

[64] ALEPH Collaboration, Measurement of the mass of the W boson using direct reconstruction at $\sqrt{s} = 183$ GeV, Phys. Lett. **B453**(1999) 121;
L3 Collaboration, Measurement of the Mass and Width of the W boson at LEP, Phys. Lett. **B454**(1999) 386;
OPAL Collaboration, Measurement of the W mass and width in e^+e^- collisions at 183 GeV, Phys. Lett. **B453**(1999) 138

[65] The ALEPH Collaboration, Measurement of the W Mass and Width in e^+e^- Collisions at 189 GeV, Eur. Phys. J. **C17**(2000) 241;
The OPAL Collaboration, Measurement of the Mass and Width of the W Boson in e^+e^- Collisions at 189 GeV, CERN-EP/00-099, accepted by Physics Letters

[66] B. Efron, Computers and the Theory of Statistics, SIAM Rev. **21**(1979) 460;
P. Diaconis and B. Efron, "Computer-Intensive Methods in Statistics", Scientific American **248:5**(1983), 96;
B. Efron, R.J. Tibshirani, "An Introduction to the Bootstrap", Chapman & Hall 1993, ISBN 0-412-04231-2;
A.C. Davison, D.V. Hinkley, "Bootstrap Methods and Their Application", Cambridge University Press, 1997, Hardback ISBN 0-521-57391-2, Paperback ISBN 0-521-57471-4

[67] Z. Kunszt, W.J. Stirling et al., Determination of the mass of the W boson, hep-ph/9602352, printed in 'Physics at LEP2', CERN Yellow report **96–01**(1996) p. 141-206

[68] Workshops on WW physics at LEP2, see http://lepww.web.cern.ch/lepww/workshops/

[69] D.S. Sivia, “Data Analysis — a Bayesian Tutorial”
Oxford Science Publications, Clarendon Press, Oxford
ISBN 0-19-851889-7

[70] S. Ask et al., LEP machine background and noise in the DELPHI calorimeters, DELPHI 99-157 LEDI 12 (1999)

[71] DELPHI Collaboration, Search for the Standard Model Higgs boson at LEP in the year 2000, Phys. Lett. **B499**(2001) 23

[72] Joana Montenegro and Jörgen D'Hondt, private communication

[73] A. Müller, Precision Measurements of the LEP Beam Energy for the Determination of the W Boson Mass, thesis, Johannes Gutenberg-Universität, Mainz

[74] S. Jadach, W. Placzek, M. Skrzypek, B.F.L. Ward, Z. Was, Monte Carlo program KoralW 1.42 for all four-fermion final states in e^+e^- collisions, Comput. Phys. Commun.**119**(1999) 272

[75] LEP EW Working Group, Combined Preliminary Results on the Mass and Width of the W Boson Measured by the LEP Experiments, LEPEWWG/MASS/2000-01, ALEPH 2000-086 PHYSIC 2000-032, DELPHI 2000-165 PHYS 879, L3 Note 2617, OPAL TN-667

[76] V. Kartvelishvili, R. Kvatadze, Event weights for simulating Bose-Einstein correlations, hep-ph/0104314

[77] V. Kartvelishvili, R. Kvatadze, R. Møller, Estimating the effects of Bose-Einstein correlations on the W mass measurement at LEP2, Phys. Lett. **B408**(1997) 331

[78] S. Todorova, J.Rames Simulation of Bose-Einstein effect using space-time aspects of Lund string fragmentation model, IReS-97-29 PRA-HEP-97-16 (hep-ph/9710280)

[79] Sharka Todorova, private communication

[80] DELPHI Collaboration, W pair production cross-section and W branching fractions in e^+e^- interactions at 189 GeV, Phys. Lett. **B479**(2000) 89

[81] Laurent Simard, Mesure de la masse du W dans l'expérience DELPHI, thesis, Université de Paris-Sud UFR scientifique d'Orsay (2000)

Summary

In the press release for the Nobel Prize awarded to the Dutch high-energy physicists Gerard 't Hooft and Martinus Veltman in 1999, the Nobel Committee referred to the agreement between theoretical calculations made possible by their work and recent precise measurements of W and Z particle properties at LEP. In fact, the availability of a quantitative theoretical framework makes it meaningful to measure the free parameters of the theory with great precision, in order to test the theory for consistency and completeness and to search for phenomena beyond. One of these parameters is the mass of the W particle, the measurement of which is the main topic of this thesis.

The LEP collider at CERN in Geneva is the largest particle accelerator built to date. Thanks to its large circumference and the use of super-conducting accelerating cavities, a technology not yet established at the time of LEP's conception, LEP is the most powerful accelerator for electrons and their anti-particles, positrons. Colliding electrons and positrons yields clean events with well-defined kinematical properties, allowing precision measurements. During the years 1996 to 2000 the collision energy was larger than the threshold for the production of pairs of W bosons. In this period each of the four LEP experiments recorded about 10,000 W pair events. Since W particles are unstable and have a very short lifetime, only the decay products of the boson pairs were detected. From the measured invariant mass of the decay products, the mass of the W boson can be determined with high precision.

The analysis presented here is based on the data recorded by the DELPHI detector in the years 1996-1998, corresponding to about one third of the final statistics. From this data sample, the following W mass was measured:

$$m_{\mathrm{W}} \;=\; 80,339 \pm 73\ (\mathrm{stat}) \pm 47\ (\mathrm{syst})\ \mathrm{MeV}/c^2$$

where the first uncertainty is statistical and the second uncertainty accounts for possible systematic effects. In addition to the mass, also the natural mass spread (width) of the W bosons was measured. This width is related to the very short lifetime of the W bosons via the Heisenberg uncertainty principle, and was measured to be

$$\Gamma_{\mathrm{W}} \;=\; 2,295^{+173}_{-164}\ (\mathrm{stat})\ \pm\ 78\ (\mathrm{syst})\ \mathrm{MeV}/c^2$$

Finally the difference between the W^+ and W^- mass, predicted to be zero, has been measured for the first time at LEP, giving the following result:

$$\frac{m_{\mathrm{W}^+} - m_{\mathrm{W}^-}}{m_{\mathrm{W}}} \;=\; -\,0.013\ \pm\ 0.011\ (\mathrm{stat})\ \pm\ 0.002\ (\mathrm{syst})$$

All the above results are in agreement with existing direct measurements and predictions in the framework of the Standard Model.

These results will be superseded by the final analysis of all DELPHI data, which is currently in progress. Therefore the most valuable and long lasting contribution of the work presented here is the development of the new ideas and analysis methods.

The Ideogram approach aims at including the maximum attainable amount of information from each recorded event in order to minimise the statistical uncertainty. New ideas include a 5-jet treatment for events with 5 jets, the combination of different jet clustering algorithms, the inclusion of all possible jet pairings and the full description of the mass information of both W bosons in each event. The construction of a likelihood curve for each event has turned out to be a useful innovation allowing for further statistical analysis, for example by means of the Jackknife technique.

In addition to the statistical error, the systematic uncertainty on the measurement plays a significant role. In order to obtain a good understanding of the measurement and have confidence in the results, a detailed study of the systematic effects is presented. The study covers a wide range of possible sources of systematic errors, including an imperfect knowledge of the detector, the accelerator, and of the physics models used. In order to allow a model-independent investigation of possible systematics related to the hadronic decay of W bosons into jets, a novel technique is introduced known as the Mixed Lorentz-Boosted Z^0 technique. This method is shown to allow a study of fragmentation effects and part of the detector systematics with a precision of 5 MeV/c^2 or better.

The understanding of the statistical and systematic aspects of the W- mass analysis has almost reached the level required for an experimental determination of the W mass at the same level of precision as the Standard Model prediction, based on a global fit using all indirect measurements. Two systematic uncertainties, however, need further investigation: the LEP beam energy scale and the effects of final state cross-talk in the fully hadronic channel. These studies are expected to be completed in the coming years. A final uncertainty on the combined W mass measurement of all four LEP experiments better than 30 MeV/c^2 is within reach. Such a result will help to further constrain the allowed range for the mass of the so far elusive Higgs boson, and will possibly remain the most precise measurement of the W mass, a fundamental constant of nature, for many years to come.

Samenvatting

De Nobelprijs voor de natuurkunde werd in 1999 aan de Nederlanders Gerard 't Hooft en Martinus Veltman toegekend. Daarbij refereerde het Nobel Comité onder andere naar de overeenstemming tussen enerzijds de theoretische berekeningen die mogelijk zijn gemaakt door hun werk en anderzijds de precisiemetingen van de eigenschappen van W- en Z-deeltjes die recentelijk gedaan zijn bij LEP. Het bestaan van een kwantitatief theoretisch model maakt het zinvol om de vrije parameters van de theorie met grote precisie te meten, om zo de consistentie en volledigheid van de theorie te testen en te zoeken naar nieuwe, de bestaande theorie ontstijgende verschijnselen. Een van die vrije parameters is de massa van het W-deeltje, en de bepaling daarvan is het hoofd-thema van dit proefschrift.

De LEP versneller bij het Europese laboratorium CERN in Genève is de grootste deeltjesversneller ooit gebouwd. Het is tevens de krachtigste versneller voor elektronen en hun antideeltjes (positronen), dankzij de grote omtrek en het gebruik van supergeleidende versnellingselementen, een vooruitstrevende technologie op het moment dat LEP nog op de tekentafel stond. Het botsen van elektronen op positronen levert gebeurtenissen op met weinig achtergrondprocessen en goed gedefinieerde kinematische eigenschappen, waardoor precisiemetingen mogelijk zijn. Tijdens de jaren 1996 tot 2000 was de energie van LEP hoog genoeg om paren van W-deeltjes te produceren, en heeft ieder van de vier LEP experimenten bijna 10.000 van deze gebeurtenissen geregistreerd. Omdat de W deeltjes een uiterst korte levensduur hebben, zijn alleen de vervalproducten waarneembaar. Uit de invariante massa van die vervalproducten kan vervolgens de massa van de W- deeltjes afgeleid worden.

Bij de hier beschreven analyse wordt gebruik gemaakt van de meetgegevens die verzameld zijn door de DELPHI detector in de jaren 1996-1998, die samen ongeveer één derde vormen van de totale statistiek. Met deze gegevens werd de volgende W-massa gemeten:

$$m_{\mathrm{W}} \;=\; 80.339 \pm 73 \text{ (stat)} \pm 47 \text{ (syst) MeV}/c^2$$

waarbij de eerste onzekerheid statistisch is en de tweede onzekerheid alle systematische fouten bevat. Behalve de massa is ook de natuurlijke spreiding (breedte) van de massa van de W-deeltjes gemeten. Deze breedte hangt samen met de levensduur van het W-deeltje via de onzekerheidsrelatie van Heisenberg, en gaf het volgende resultaat:

$$\Gamma_{\mathrm{W}} \;=\; 2.295^{+173}_{-164} \text{ (stat)} \;\pm\; 78 \text{ (syst) MeV}/c^2$$

Tot slot is ook het verschil tussen de massa's van de W^+- en W^--deeltjes gemeten. Het is de eerste keer dat dit verschil bij LEP gemeten wordt, en de verwachte waarde is gelijk aan nul. Het volgende verschil werd gevonden:

$$\frac{m_{\mathrm{W}^+} - m_{\mathrm{W}^-}}{m_{\mathrm{W}}} \;=\; -\,0,013 \;\pm\; 0,011\,\text{(stat)} \;\pm\; 0,002\,\text{(syst)}$$

Alle bovenstaande resultaten komen overeen met reeds gepubliceerde directe metingen en voldoen aan de relaties met andere gemeten grootheden volgens de voorspellingen van het Standaard Model.

De resultaten zelf zullen pas definitief worden na de uiteindelijke analyse van alle DELPHI data. Daarom moet de belangrijkste bijdrage van het werk in dit proefschrift veeleer gezocht worden in de ontwikkeling van nieuwe ideeën en analyse methoden.

De in dit proefschrift ontwikkelde Ideogram benadering heeft als doel zoveel mogelijk statistische informatie uit iedere gebeurtenis te behouden om zo de totale statistische meetfout te minimaliseren. Nieuwe ideeën zijn onder andere het rekening houden met de 5$^{\mathrm{e}}$ jet in een 5-jet gebeurtenis, het combineren van drie verschillende cluster-algoritmen, het meenemen van alle mogelijke jet combinaties in de analyse en het beschrijven van de volledige massa-informatie van beide W-deeltjes in iedere gebeurtenis. Het bleek een nuttige verbetering te zijn om van iedere gebeurtenis een waarschijnlijkheidskromme te berekenen en die op te slaan voor nadere statistische analyse, bijvoorbeeld door middel van de 'Jackknife' techniek.

Behalve de statistische onzekerheid, is ook de systematische onzekerheid op de meting van groot belang. Om een goed begrip van de meting te verkrijgen en het vertrouwen in het resultaat te vergroten is een gedetailleerde studie van mogelijke systematische effecten uitgevoerd. Deze studie omvat een groot aantal mogelijke bronnen van systematische fouten, waaronder beperkingen in de kennis van de detector, de versneller, en van de gebruikte fysische modellen. Voor de model-onafhankelijke studie van mogelijke systematiek in relatie met het hadronische verval van W-deeltjes naar jets, wordt een nieuwe techniek geïntroduceerd met de naam 'Mixed Lorentz-Boosted Z^0 method'. Er wordt aangetoond dat deze methode effecten in de fragmentatie en detectie van jets aan het licht kan brengen met een nauwkeurigheid van 5 MeV/c^2 of beter.

De kennis van de statistische en systematische aspecten van de W-massa meting heeft hiermee bijna het niveau bereikt dat nodig is om een experimentele bepaling van de W-massa te doen met een nauwkeurigheid vergelijkbaar met die van de voorspelling op basis van een globale fit van het Standaard Model aan andere gemeten grootheden. Er zijn echter twee systematische onzekerheden die nog nadere studie vereisen: de energieschaal van LEP en de mogelijke onderlinge interacties van de vervalproducten van de twee W-deeltjes in volledig hadronische gebeurtenissen. De verwachting is dat deze studies binnen enkele jaren afgerond zullen worden. Een gecombineerde W-massa meting van de vier LEP experimenten met een uiteindelijke nauwkeurigheid van beter dan 30 MeV/c^2 behoort dan tot de mogelijkheden. Een resultaat met een dergelijke nauwkeurigheid zal ertoe bijdragen de massa van het tot nu toe ongrijpbare Higgs deeltje nog beter te voorspellen, en zal mogelijkerwijs nog vele jaren de meest nauwkeurige meting blijven van de W-massa, een fundamentele natuurconstante.